UNIVERSITÀ DEGLI STUDI DI CATANIA
FACOLTÀ DI SCIENZE MATEMATICHE, FISICHE E NATURALI
DOTTORATO DI RICERCA IN FISICA

Adriano Ingallinera

A Radio Characterization of Galactic Bubbles

PhD Thesis

COORDINATOR:
Prof. F. Riggi

SUPERVISOR:
Prof. F. Leone

TUTORS:
Dr. C. Trigilio
Dr. G. Umana

XXV ciclo

Contents

Chapter 1

Introduction

The Spitzer Space Telescope was launched in 2003 in an Earth-trailing orbit and, with important limitations, is still operating. It is the fourth telescope of the NASA Great Observatories program and represents a milestone for infrared astrophysics.

Among the several results achieved thanks to Spitzer instruments, two surveys (GLIMPSE and MIPSGAL) have observed most of the galactic plane portraying a six-band image (from 3.6 µm to 70 µm) of the Milky Way.

In particular, the MIPSGAL survey unveiled the existence of more than 400 diffuse roundish objects [1], most of them previously unknown; the characterization of the radio emission of these sources and its contribute to unveil their nature is the subject of this work.

1.1 The MIPSGAL survey

MIPSGAL is a 278° Galactic plane survey conducted through the Multiband Infrared Photometer for Spitzer (MIPS) instrument on the Spitzer Space Telescope [2][3]. The survey extends over $|b| < 1^\circ$ for $-68^\circ < l < 69^\circ$ and maps strips with $|b| < 3^\circ$ for $-8^\circ < l < 9^\circ$, at 24 µm and 70 µm [4].

From visual inspection of MIPSGAL mosaic images more than 400 compact roundish objects with a diffuse emission have been identified at 24 µm. These sources are characterized by a common morphology, as they appear as small nebulae with diameters usually below $1'$. They are divided in two groups: one characterized by nebulae which show a central object (54 objects) and another characterized by nebulae which do not show evidences of a central object. The nebulae are described as ring, disk or irregular and hereafter we will refer to them as “bubbles”. They turned out to be pervasive through the entire Galactic plane in the mid-infrared; their distribution is approximately uniform both in Galactic latitude and longitude, and the average density is found to be around 1.5 bubbles per square degree.

The bubbles were expected to be detected also at different wavelengths but a further analysis of the GLIMPSE[1] (for bands at 3.6, 4.5, 5.8 and 8.0 µm) and MIPSGAL (70 µm) images indicates that they were mostly detected only at 24 µm.

The absence, for most of these objects, of a counterpart at wavelengths shorter than 24 µm could be interpreted as a sign of extreme extinction, which would explain the non-detection of these objects in previous visible or near-infrared surveys.

Another interesting explanation could be that the emission only around 24 µm is an intrinsic property of this sources. It has been shown that some spectra (obtained with the Spitzer Infrared Spectrograph) present very strong [O IV], [Ne III], [Ne V], [S III] and [S IV] emission lines[2] with a very poor contribution from thermal dust [1][5]; other bubbles, instead, present a “classical” spectrum with an high thermal continuum.

However it cannot be ruled out also the possibility that such a peculiar emission could be due to a sensitivity limit of GLIMPSE and MIPSGAL. Very likely, all these three factors concur to explain what has been observed.

In the following images some bubbles are represented as an example. The images are obtained as an rgb superposition of monochromatic tiles at 24 µm (red), at 8 µm (green) and at 3.6 µm (blue). Other images of bubbles will be shown in chapter 7.

1.2 Hypotheses about the bubbles nature

The main hypothesis about the bubbles nature, driven by the morphology of these objects, is that they are the circumstellar envelopes of different kinds of evolved stars, such as planetary nebulae, supernova remnants, Wolf–Rayet

---

[1] GLIMPSE (Galactic Legacy Infrared Mid-Plane Survey Extraordinaire) is a survey of the inner Milky Way performed with the Spitzer Infrared Array Camera (IRAC) between 3.6 µm and 8.0 µm.

[2] All these lines occur between 10 µm and 35 µm [5], in particular [O IV] presents a line at 25.9 µm and [Ne V] at 24.3 µm, well inside the MIPS bandpass at 24 µm.

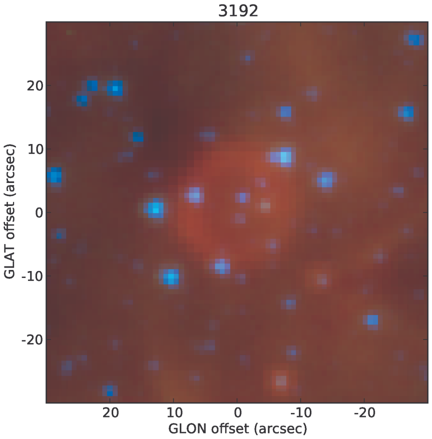

Figure 1.1: rgb image of the bubble 3192 at 24 µm (red), 8 µm (green) and 3.6 µm (blue). This bubbles shows a ring morphology.

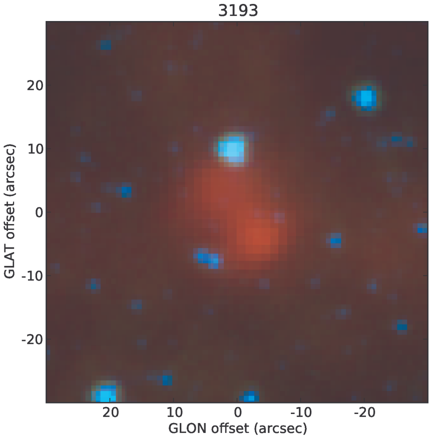

Figure 1.2: rgb image of the bubble 3193 at 24 µm (red), 8 µm (green) and 3.6 µm (blue).This bubbles shows a bipolar morphology.

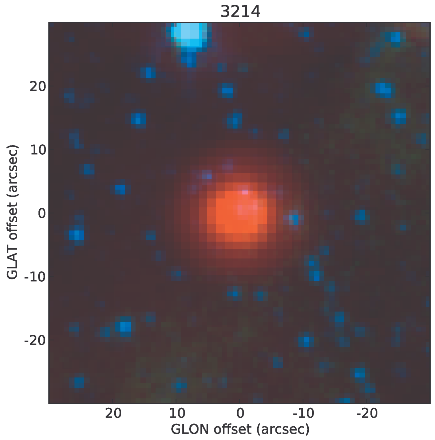

Figure 1.3: rgb image of the bubble 3214 at 24 µm (red), 8 µm (green) and 3.6 µm (blue). This bubbles shows a discoidal morphology and is classified as a planetary nebula.

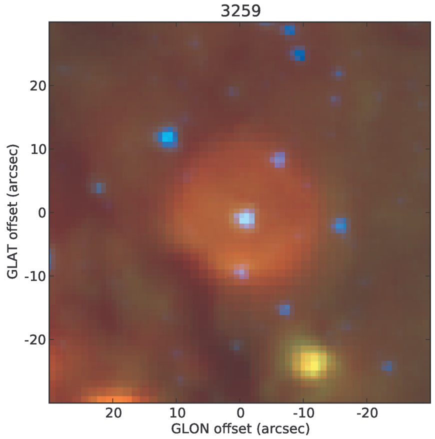

Figure 1.4: rgb image of the bubble 3259 at 24 µm (red), 8 µm (green) and 3.6 µm (blue). This bubbles shows a disk morphology in a very confused background; maybe an outer shell at 8 µm is visible.

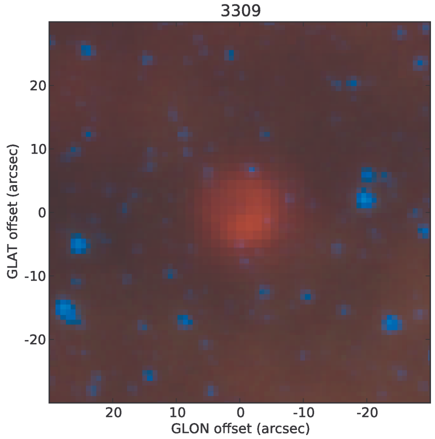

Figure 1.5: rgb image of the bubble 3309 at 24 µm (red), 8 µm (green) and 3.6 µm (blue). This bubbles shows an irregular disk morphology.

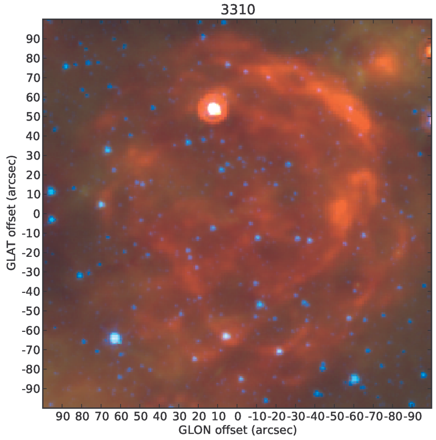

Figure 1.6: rgb image of the bubble 3310 at 24 µm (red), 8 µm (green) and 3.6 µm (blue). This bubbles shows a filamentary morphology and is very extended (notice the different scale); this bubble is classified as a supernova remnant.

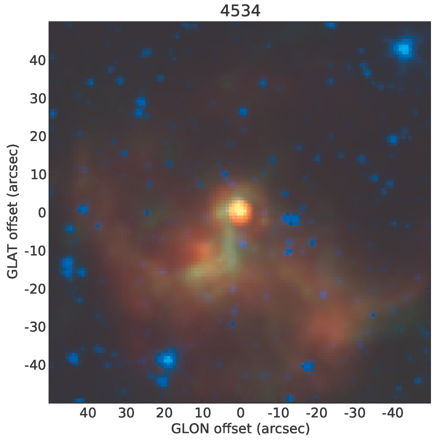

Figure 1.7: rgb image of the bubble 4534 at 24 µm (red), 8 µm (green) and 3.6 µm (blue). This bubbles is very extended and presents a very bright central source.

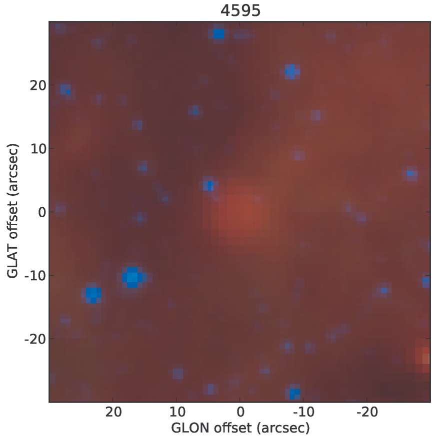

Figure 1.8: rgb image of the bubble 4595 at 24 µm (red), 8 µm (green) and 3.6 µm (blue). This bubbles shows a disk morphology but is surrounded by an extremely confused and bright background.

stars, Luminous Blue Variables, Asymptotic Giant Branch stars and so on. Archive searches have allowed to identify about the 10% of these objects, with the majority of the already known "bubbles" found to be planetary nebulae. Three supernova remnants and one post-AGB star were also identified. Therefore, about 90% of these bubbles are unclassified [1].

The efforts, by now conducted, to shed light on the nature of these objects, have been mainly aimed to the spectroscopy of the central source (where present) and of the nebula or to build an as much as extended spectral energy distribution (SED hereafter) of those bubbles observed with other instruments; very little has been done about the colors of both nebulae and central sources. In particular spectroscopy of central sources has produced some results. It is possible to see, in fact, that central sources are usually very bright at 24 µm and clearly detected toward shorter wavelengths typically down to 2MASS *H* band at 1.65 µm, with few sources detected indeed down to 500 nm.

Wachter et al. (2010) [6] showed that the spectroscopy of the central sources of 48 of the MIPSGAL bubbles[3] was usually compatible with evolved massive stars like Be, Oe/WNs and LBVs. They also pointed out that the lack of emission at wavelengths other than 24 µm could be mainly imputable to the [O IV] line at 25.89 µm, as supposed by Morris et al. (2006) for young supernova remnants [7]. The presence of very massive stars can also be inferred by the morphology of the nebula; Gvaramadze, Kniazev, & Fabrika (2010) [8] found that many bubbles resemble known nebulae surrounding LBV, BSG or WR stars. They confirmed the nature of some bubbles, inferred by morphological analyses, by means of spectroscopical identifications, showing that the mere presence and shape of the nebula can suggest the possibility of the presence of these massive stars.

Anyway, the spectra of these objects were found to be extremely different. Spitzer Infrared Spectrograph (IRS) high and low-resolution observations of a dozen of bubbles display an unexpected variety with a couple of spectra showing dust-free and highly-ionized-gas-rich objects. Some of our objects resemble spectroscopically LBVs or WR stars, but in the mid-IR they do not behave exactly as some of the classical examples. Whatever the nature of these 24 µm sources is, the implications of such a large number in the Galactic plane is remarkable, as we will explain in the next sections.

---

[3] Their work regarded a total of 62 objects.

1.3 The role of evolved massive stars

The importance of the discovery of several unknown massive stars relies on their pivotal role in the evolution of their host galaxies. In the galaxy context, massive stars are among major contributors to the interstellar ultraviolet radiation, because to their high surface temperatures; such a strong ultraviolet emission[4] is responsible for the excitation and ionization of the circumstellar matter which, in these states, subsequently undergoes longer-wavelength emission, allowing us to detect these source from optical to radio and to study the physical properties of these objects.

Massive stars are also characterized by strong stellar winds and, moreover, they may end their life in a final huge explosion. The last phases of their existence are, then, characterized by the dispersion of large amount of their mass in the circumstellar space (mass-loss phenomena). Since they are also the only objects in the universe where the nucleosynthesis is able to produce elements beyond the Neon and the only object capable to disperse elements heavier then Helium, they are the only objects that enrich the interstellar medium of processed material (as gas and dust). Also their explosions, from a purely mechanical point of view, could result extremely important in the evolution of their galaxy; it is vastly documented, for example, that the shocks on the interstellar medium, due to supernova episodes, can trigger local star formation.

From a theoretical point of view, the details of post-MS evolution of massive stars are still poorly understood. Indeed all theoretical models depend on the physical characteristics of the stars such as their chemical composition (mostly as metallicity), their mass and their rotational velocity; these quantities are very poorly constrained, because of the intrinsic difficulty of their measurements, but they greatly influence other measurable parameters like the mass-loss rate and the total mass-loss, which are characteristics "easily" derivable from the study of the ionized circumstellar envelopes. Unfortunately, empirical data, derived form observations, rely on a low-numbers statistics, because very few objects at different stages of post-MS evolution are known [9]; this is mainly due both to the short duration of these evolutionary phases of massive stars and also to the extreme extinction toward the Galactic plane, the place where the majority of these object is expected

---

[4] This emission is very often absorbed by circumstellar matter and interstellar medium, so it is indeed seldom detected.

to be located.
In this scenario, the contribution of infrared and radio observations is fundamental. In fact they allow to observe directly toward the galactic plane, since extinction is negligible or not present at all.

1.4 Missing planetary nebulae

As we have discussed, the MIPSGAL bubbles could represent a very important catalog where to look for evolved massive stars; however, it turns out that this catalog can be useful also to search for evolved lower-mass stars, in particular planetary nebulae. In particular, the MIPSGAL band at 24 µm is found to be, by now, the most sensitive for locating planetary nebulae [10][11], because of the peculiar emission of these objects.
It has been calculated that the total number of planetary nebulae in our galaxy should be around 23 000 [12]. Anyway, by now only about 2000 planetary nebulae has been discovered. This striking discrepancy is usually explained assuming, as the models predict, that the majority of the planetary nebulae lies in the galactic plane, and are more concentrated nearby the galactic center [13]. Observations toward this direction are heavily affected by the interstellar extinction, which could reach extremely high value from near infrared toward shorter wavelengths. Being, therefore, the planetary nebulae intrinsically faint objects, it is very likely that, at least in the optical and near infrared, the strong extinction causes that many of them are well below the sensitivity limits.
Other studies suggest that at least a part of these missing planetary nebulae could derive from the evolution of the most massive AGB stars, with masses above $2M_{\odot}$. These objects are thought to be embedded in thick circumstellar envelopes, resulting then to be heavily obscured. Their observation might, therefore, be fundamental to understand the late evolution of the most massive PNe progenitors.
One of the most important problem concerning planetary nebulae is that usually their distances are not known. Indeed, except the few planetary nebulae located in our prossimity for which parallax measurement is possible, the distance determination for these objects is extremely hard and, being observed mostly at high galactic latitudes, the galactic disk rotation model cannot be used.
For all these reasons, the observation of planetary nebulae lying in the galac-

tic plane can be very useful. In fact, using observations at long wavelengths (from mid infrared on) we can detect these objectes towards the galactic plane where they are extremely extinguished in the optical. The possibility to estimate also their distances would permit to obtain informations about their physical characteristics.

1.5 Radio observations

As reported above, many kinds of evolved stars are hot enough to ionize the gas (hydrogen, substantially) in their circumstellar envelope. This ionized medium is known to emit in the radio region of the electromagnetic spectrum, mainly via two mechanisms: thermal emission and non-thermal emission. The thermal emission is due to electrons in a thermal status (not accelerated) undergoing free-free transitions when they interact with positive ions, we will refer to this emission as to free-free (thermal) emission. The non-thermal emission arises when the relativistic electrons emit when they interact with magnetic fields spiralizing around its lines, we will refer to this emission as to synchrotron emission. The requirement of a magnetic field and the fact that electrons must be relativistic, in order to produce an observable effect, makes impossible for different kinds of object to show a synchrotron emission; indeed, in the galactic context, supernova remnants are the most prominent synchrotron emitters, along with objects like symbiotic stars or microquasars. These two kinds of emission model the spectral energy distribution of a radio source in two different, and characteristic, shapes. In particular if we suppose that the flux density is a power-law function of the observing frequency

$$F(\nu) \propto \nu^{\alpha(\tau)}$$

where exponent α is referred to as the radio spectral index and τ is the optical depth, then it is possible to show that for a thermal free-free emission the following relation holds

$$F(\nu) \propto \left\{ \begin{array}{ll} \nu^{2} & \text{for } \tau \gg 1 \\ \nu^{-0.1} & \text{for } \tau \ll 1 \end{array} \right. ,$$

while for a synchrotron emission

$$F(\nu) \propto \left\{ \begin{array}{ll} \nu^{5/2} & \text{for } \tau \gg 1 \\ \nu^{\alpha} & \text{for } \tau \ll 1, \ \text{with } \alpha \in (-1, -0.5) \end{array} \right. .$$

In principle, the reconstruction of a source radio spectral index could be easily done by means of multiwavelength observations. However there are different limitations that, in general, does not allow, in a realistic scenario, to observe in more than two bands.

First of all, in both the two emission types, the flux density of a generic source presents a peak value at a certain frequency. For a free-free emission spectrum the flux density value decreases slowly at frequencies greater then the peak one, while it drops very quickly at lower frequencies. For a synchrotron emission, the flux density value drop is quick in any direction away from the peak. This behavior implies that, unless a very bright source is observed, for many objects the flux density values at frequency too far from the peak can result below the sensitivity limit of an instrument, for a reasonable total integration time; since, for a given instrument, the sensitivity improves as the square root of the integration time (letting the bandwidth be constant), requesting a significant better sensitivity could be too much time-consuming to be accepted.

Another important limiting factor in a telescope sensitivity is the confusion limit, which introduces a natural source of noise. In particular the confusion noise ca be defined as the stochastic fluctuations of the background sky brightness below which sources cannot be detected individually [14]. This observing condition is related to the resolution of the instrument, since the poorer the resolution is the more sources will not be spatially separated. Also diffuse emission, in particular toward the galactic plane, can give significant contributions to the background level, limiting the sensitivity achievable. Using an interferometer instead of a single-dish telescope would permit to obtain a much higher resolution, possibly overcoming confusion problems; however, as we will see in the following chapters, an interferometer may not return a realistic image of a source when this is too much extended.

Another kind of useful radio observations are spectral line data searching for maser lines. Evolved stars, like AGB or post-AGB, are not expected to show a radio continuum, beacuse of their “low” effective temperature, but should present maser evidence on their spectrum originating from molecules such as OH, H_2O and SiO. Some of these lines are typical of only one kind of object and a particular combination of them is even able to give us informations on the evolutionary stage of each bubble.

Finally it is important to notice that the radio observation could suffer of different kinds of anthropic and Earth-based contaminations. Though the best radio telescopes are located relatively far from inhabited zones, interferences from human activities are pervasive in many radio bands, as we will see in chapters 3 and 5.

Taking into account what we have just discussed, radio observations of our bubbles can provide useful clues to understand their nature. The basic idea is to observe some of these bubbles at two different frequencies and then calculate their radio spectral index. The best instrument to achieve this goal is certainly the Very Large Array (VLA), that, after its upgrade (EVLA), combine a good resolution with an extremely high sensitivity. The observation we really made with the EVLA are reported in chapters 2 and 3. In chapter 4 we will discuss about observations of very extended bubbles with the Green Bank Telescope. In chapter 5 we will present some spectral line observations of a very large sample of bubbles, which where suspected to be AGB or post-AGB stars, searching for expected OH masers. The last chapters will deal with the data analysis and results.

Chapter 2

EVLA observation at 6 cm

The Very Large Array (VLA) is a well-known radio interferometer composed of 27 25-meter antennas located in New Mexico. The interferometer is presently in an enhancing state since 2002, under the project "Expanded VLA" (EVLA), which is scheduled to be complete by 2012. The EVLA improves several capabilities of VLA, like an up to 20 times higher sensitivity, a larger bandwidth (up to 8 GHz per polarization), a frequency resolution down to 1 Hz and other improvements concerning the imaging capability.
In the most compact configuration (D) and at an observing frequency of 5 GHz (corresponding to about 6 cm) the interferometer provides a $\sim 14''$ maximum resolution (HPBW) and a largest angular scale of about $2'$ for a snapshot observation. At that frequency, the system equivalent flux density is about 320 Jy and the theoretical thermal noise expected for a 1-minute long observation with a bandwidth of 128 MHz is about 0.15 mJy/beam [15].
The observations with the EVLA were the most important of this work, since they allowed us to characterize the radio emission of the bubble. In this chapter we will discuss about the observations in band C, pointing out, in particular, the observing strategy and data calibration process. In the next chapter we will talk about the observations in band L and the most important problematics (like data editing) connected to this band.

2.1 Preparing the sample

The set of bubbles listed in the Mizuno catalog comprises 428 sources distributed throughout the portion of the Galactic plane observed by MIPSGAL

[1]. Since we wanted to observe these objects with the EVLA, as a first step, from the original sample of MIPSGAL bubbles only sources with a declination above $-40°$ have been selected, in order to observe at an elevation of at the least 10°, resulting in a total "northern sample" of 367 sources. We checked a $1' \times 1'$ field centered on each of MIPSGAL positions in both NVSS catalog and in MAGPIS for radio emission[1] (see also section 6.1 for more details), ending up with a total of 22 (NVSS) plus 34 (MAGPIS) sources possibly detected at 20 cm. About 50% of the radio selected sources shows a 70 µm counterpart and every kind of 24 µm morphology (like disk, ring, shell and so on) is represented. Despite the fact that, for our targeted sources, either NVSS or MAGPIS (or both) data already exist, these cannot be used for the purpose of identifying the 24 µm MIPSGAL bubbles, mainly because of relatively poor sensitivity.

We then proposed observations whose main goal was to perform a spectral index analysis which would have allowed us to discriminate between thermal and non-thermal sources in the sample, hence shed light on the nature of the radio emission. To be able to carry out such an analysis we needed, for each source, data at the same angular resolution and a better signal-to-noise ratio. On the contrary, the existing NVSS/MAGPIS data suffer from three main issues: the available data have been obtained with a typical rms on average worst than what is achievable with EVLA; the existing observations have been taken at a different time with respect to ours and time variability effects could potentially affect the spectral index analysis; the combination of VLA and EVLA data could, in principle, be very problematic, while, for our analysis, we needed to combine maps obtained at different frequency and configurations to build spectral index maps or to provide zero-baseline information for higher angular resolution observations.

The available NVSS and MAGPIS data yet provided very useful indications regarding the size and flux of our selected sample of sources, and these informations were used to guide our observing strategy. Almost all the NVSS sources are compact at the $45''$ resolution. For these we assumed that their angular dimensions at 20 cm were comparable to their dimensions at 24 µm. The MAGPIS sources were observed in a multi-array survey with an angular resolution of $\sim 6''$ [16]. They mainly consist of weak, extended highly structured emission, which failed to be detected in the NVSS survey (limiting

---

[1] The sensitivity of this survey, expressed as map rms, is $\gtrsim 0.45$ mJy/beam for NVSS and $\gtrsim 1$ mJy/beam for the high-resolution 20-cm maps of MAGPIS.

peak source brightness of about 2.5 mJy/beam). As an example bubble 3736 is not reported in the NVSS catalog, while in the field from the MAGPIS survey a 20 cm morphology closely resembling that from MIPSGAL map is evident. Remarkably, 11 of the objects selected for EVLA observations have been already classified, according to the SIMBAD data base. These sources have been used as pathfinders for the rest of the sample, providing reference templates for the unclassified objects.

2.2 Observations details

Observations of the bubbles sample were made with the EVLA in configuration D at 6 cm during March 2010; the sample was split in four subset, observed in four different days. Each bubble has been observed for about 10 minutes and in two 128-MHz wide spectral windows (resulting therefore in a total bandwidth of 256 MHz) in order to achieve a theoretical noise level of about 10 μJy/beam. The observations have been carried out in "shared risk observation" mode with the EVLA not fully updated, hence the relatively narrow bandwith. However, we were conscious that calibration process errors and required flagging would have introduced further sources of noise that eventually would have dominated over the theoretical thermal noise.

The observing strategy adopted was the usual one. After that the sample has been divided in four observing blocks, in order to optimize their observation, the most convenient calibrators have been chosen to achieve the best results. In particular, the source 3C286 has been chosen as both flux and bandpass calibrator for all the four observing blocks, while four different complex gain calibrators were selected in order to minimize their distance from the targets. The table 2.1, lists all the calibrators chosen.

In table 2.2 all observed objects are reported along with their coordinates and the date and the approximate duration of each observation.

ID	RA (J2000)	DEC (J2000)	Obs. day (2010)	Obs. time (min)
3153	18:08:50.5	$-19^\circ\,47'\,39''$	13–Mar	12
3173	18:14:17.1	$-17^\circ\,02'\,16''$	14–Mar	12
3177	18:15:48.9	$-16^\circ\,38'\,27''$	14–Mar	12
3188	18:19:45.1	$-14^\circ\,48'\,02''$	14–Mar	10

3192	18:18:42.2	−14° 54′ 09″	14–Mar	12
3193	18:18:51.7	−14° 45′ 10″	14–Mar	12
3214	18:24:04.0	−11° 26′ 16″	14–Mar	10
3222	18:45:55.2	−02° 25′ 08″	14–Mar	10
3259	18:33:43.3	−08° 23′ 35″	14–Mar	10
3269	18:33:39.5	−08° 07′ 08″	13–Mar	10
3282	18:39:32.2	−05° 44′ 20″	14–Mar	10
3309	18:39:37.4	−04° 32′ 56″	14–Mar	10
3310	18:41:19.9	−04° 56′ 06″	13–Mar	5
3313	18:42:08.2	−03° 51′ 03″	14–Mar	10
3328	18:42:46.8	−03° 13′ 17″	14–Mar	10
3333	18:41:16.0	−03° 24′ 11″	14–Mar	10
3347	18:45:12.0	−01° 30′ 32″	14–Mar	10
3354	18:46:45.2	−00° 45′ 06″	13–Mar	10
3362	18:50:18.3	00° 03′ 48″	13–Mar	10
3367	18:50:04.3	−00° 18′ 45″	13–Mar	10
3384	18:53:56.8	01° 53′ 08″	13–Mar	10
3438	19:06:24.6	08° 22′ 02″	13–Mar	10
3448	19:06:33.6	09° 07′ 20″	13–Mar	10
3558	19:55:02.4	29° 17′ 20″	13–Mar	10
3654	19:06:45.8	06° 23′ 53″	13–Mar	10
3706	18:50:40.1	−01° 03′ 09″	13–Mar	6
3724	18:46:35.9	−03° 20′ 43″	14–Mar	10
3736	18:42:22.5	−05° 04′ 29″	14–Mar	10
3866	18:21:36.9	−14° 59′ 41″	14–Mar	10
3910	18:11:28.9	−19° 25′ 29″	13–Mar	6
3915	18:11:30.8	−19° 59′ 41″	13–Mar	12
4409	17:55:43.1	−29° 04′ 04″	27–Mar	10
4422	18:03:18.4	−27° 06′ 22″	13–Mar	12
4436	17:44:29.6	−32° 38′ 11″	27–Mar	10
4443	17:48:46.6	−29° 53′ 34″	21–Mar	10
4452	17:54:23.6	−28° 34′ 51″	21–Mar	10
4463	17:54:34.4	−27° 42′ 51″	27–Mar	10
4465	17:57:03.9	−27° 51′ 30″	27–Mar	10
4467	17:57:42.5	−26° 32′ 05″	13–Mar	12
4473	18:02:48.4	−24° 40′ 54″	13–Mar	12
4479	18:11:10.6	−21° 23′ 15″	13–Mar	12
4485	17:23:04.4	−36° 18′ 20″	21–Mar	10

4486	17:29:58.3	−35° 56′ 56″	21–Mar	10
4497	17:39:21.3	−31° 50′ 44″	27–Mar	10
4530	18:00:35.2	−23° 16′ 18″	21–Mar	5
4534	17:17:59.3	−37° 26′ 09″	21–Mar	5
4552	17:35:54.5	−32° 10′ 35″	27–Mar	10
4555	17:34:35.2	−32° 26′ 58″	27–Mar	10
4580	17:45:40.7	−27° 09′ 15″	21–Mar	10
4583	17:49:32.1	−27° 07′ 32″	21–Mar	10
4584	17:49:04.9	−27° 24′ 47″	21–Mar	10
4589	17:56:13.4	−24° 13′ 13″	27–Mar	10
4595	18:01:06.4	−22° 56′ 05″	21–Mar	10
4602	18:04:38.9	−20° 37′ 27″	13–Mar	12
4607	18:04:36.3	−21° 05′ 26″	13–Mar	12

Table 2.2: Observations summary for band *C*.

2.3 Data reduction

The entire data reduction process has been performed using the package CASA, an open-source C++ based software released by NRAO and aimed to ALMA and other radio-astronomy telescopes data analysis.

As a first step, the data were edited and flagged in order to identify and delete not properly working antennas, bad baselines and border (and usually noisy) channels; the editing process revealed no great corruptions in our data. As we will see in the next chapter, the data we acquired at 1.4 GHz were instead greatly affected by interferences, so in section 3.3 a detailed exposition of the editing process will be given.

The data calibration followed the guidelines explained by the NRAO staff during the 12th Synthesis Imaging Workshop, and reported in the CASA web tutorial for EVLA. For all the observations, the source 3C286 has been chosen as flux and bandpass calibrator, while as phase calibrator different sources have been observed in order to obtain a better calibration. It has also been observed the source BL Lacertae as polarization angle calibrator, even if, for the moment, no polarization calibration has been performed.

The bandpass calibration has been done using 3C286 as calibrator. Since its phase fluctuations with time were not neglectable and much greater than fluctuations with frequency, a preliminary correction of the phase variations

Obs. day	Gain cal.	Flux cal.	Bandpass cal.	Pol. angle cal.
13–Mar	J1820–2528 J1822–0938 J1856+0610 J1953+3537	3C286	3C286	BL Lac
14–Mar	J1822–0938	3C286	3C286	BL Lac
21–Mar	J1751–2524	3C286	3C286	*none*
27–Mar	J1751–2524	3C286	3C286	*none*

Table 2.1: Calibrators used for observations at 6 cm.

with time has been done (see figure 2.1). This was indeed a phase-only gain self-calibration, since it used the baseline-dependent channel-averaged data of the bandpass calibrator to determine the phase gain for itself. This process relies on the hypothesis that the channel-averaged phase for a given baseline is costant with time in an ideal receiver; it is also important that the calibrator must not be resolved (baseline-independent phase). The phase solution found was applied on the fly while determining the bandpass solutions. This calibration is aimed to determine the scan-averaged antenna-based complex gain as a function of the frequency, by means of baseline-based channel-wise value of the chosen bandpass calibrator; it is important therefore that this source has a very flat spectrum (i.e. no lines) and be very brigth, since high signal-to-noise ratio for each channel is required for a good calibration. After the application of the bandpass solutions, both the amplitude and phase variations of the data with frequency result flatter (figures 2.2 and 2.3), with the instrumental frequency-dependent response taken, therefore, into account.
The gain calibration has been done using different standard calibrators (table 2.1) in order to achieve a better calibration result. In fact, as usual, the gain calibrators have been chosen to be as close as possible to the targets; in this way phase distorsions due to atmosphere were minimized. The observing strategy was to acquire a phase calibrator scan before and after each target observations, so that if n targets were to be calibrated with the same gain calibrator, then this source was to be observed $n + 1$ times (see also section 3.3). Not only the calibrator visibilities vary (mainly in phase) between one scan and another but also within each scan (figure 2.4). It is to be kept in mind that the target gain correction is obtained interpolating the two calibrator adjacent scan; this rises two main issues: first this kind of calibration

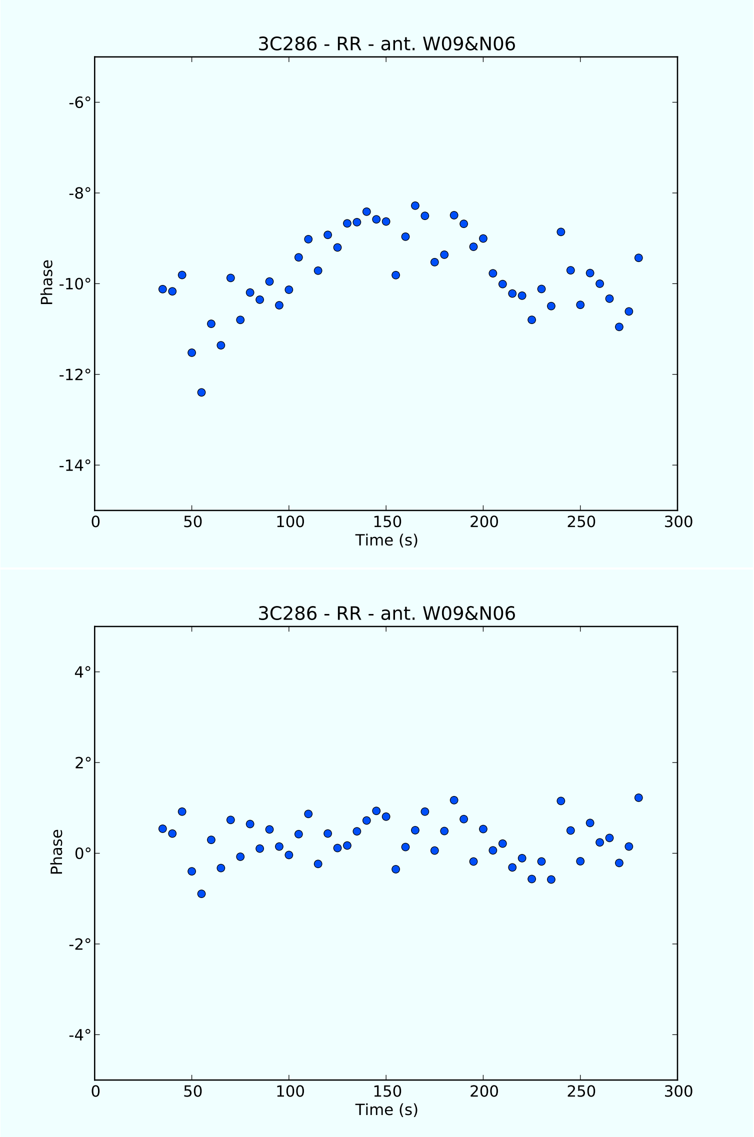

Figure 2.1: (top) raw data of the bandpass calibrator (only correlation RR and only one baseline are shown, border data are flagged). It is possible to notice that the phase values fluctuate of about 4° during the acquisition time. (bottom) after phase calibration the fluctuations are reduced by a factor 2.

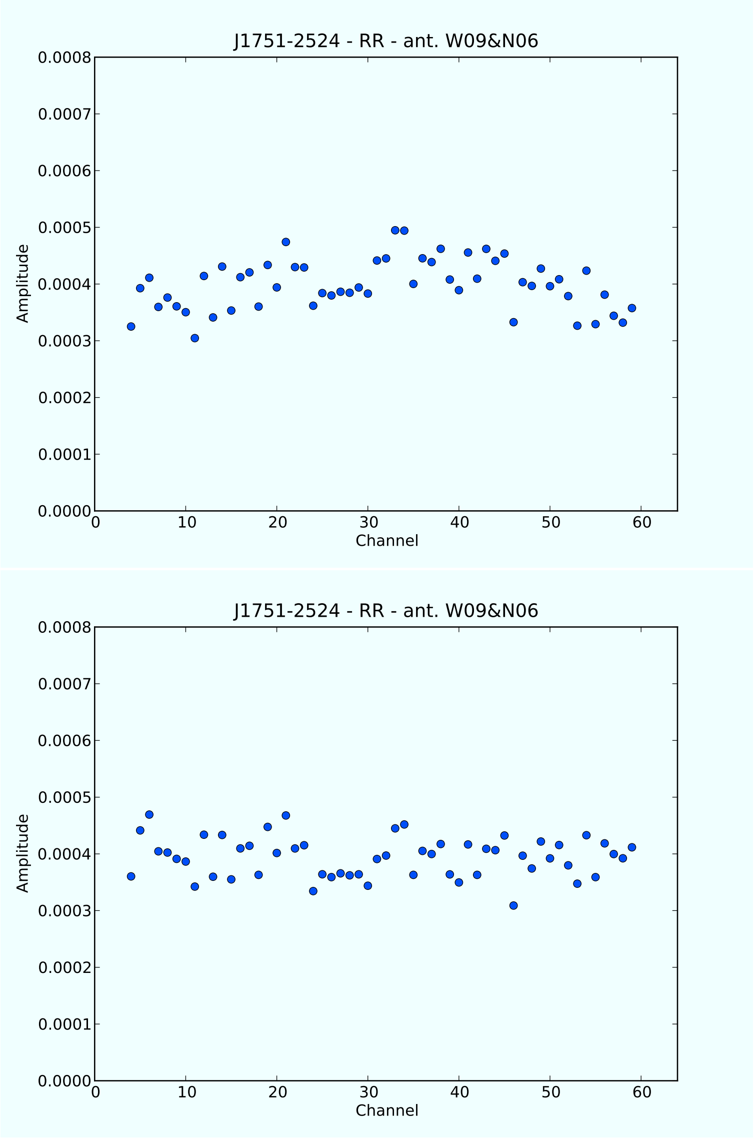

Figure 2.2: (top) raw amplitude values of the gain calibrator J1751–2524 (only correlation RR and only one baseline are shown, border channels are flagged). It is possible to notice that the amplitude variations with channel are indeed quite restrained, thanks to clean data and very good receivers. (bottom) after the bandpass calibration the fluctuations are further reduced.

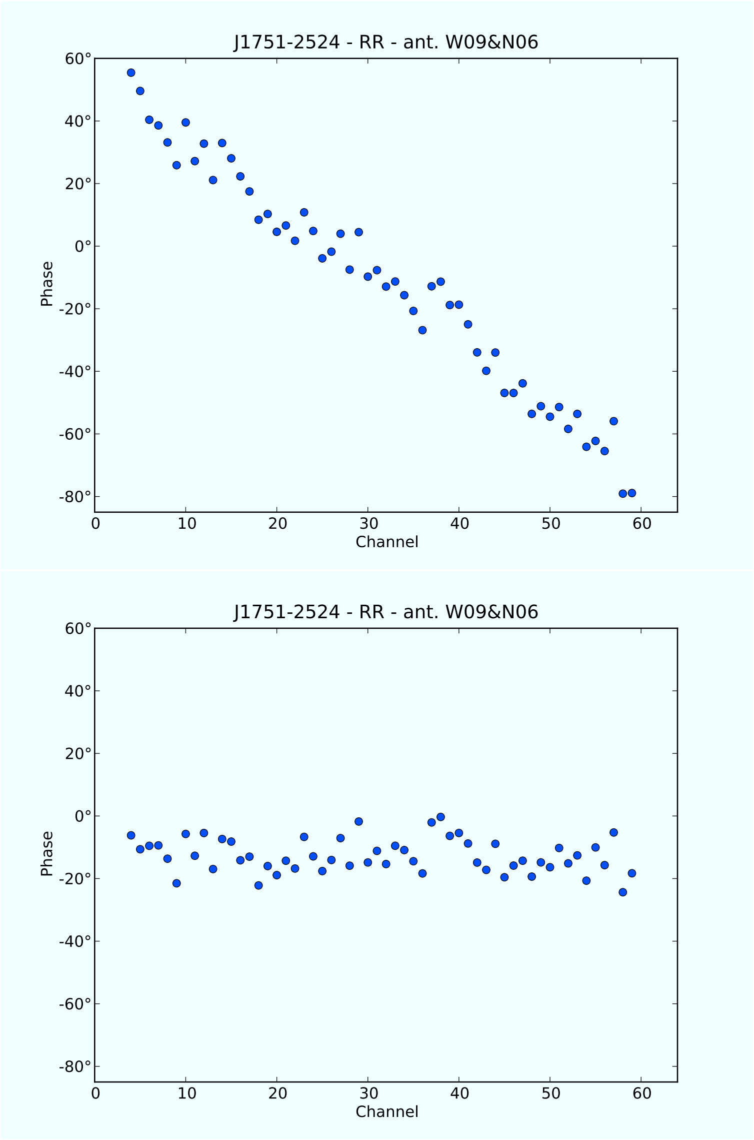

Figure 2.3: (top) raw phase values of the gain calibrator J1751–2524 (only correlation RR and only one baseline are shown, border channels are flagged). It is possible to notice that the phase values with channel extend over about 140°. The complessive slope is due to the delay. (bottom) after the bandpass calibration the phase appears flat with fluctuations under 30° and the delay slope is corrected (flat behavior).

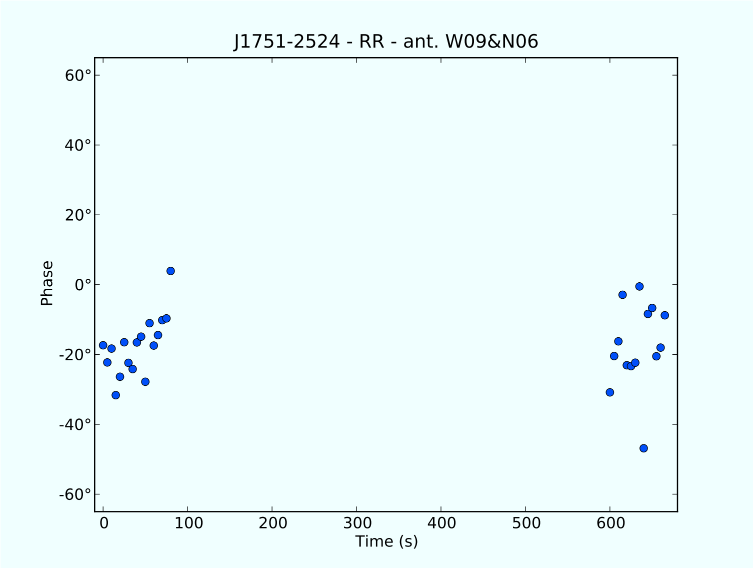

Figure 2.4: phase variations for two adjacent scans of the gain calibrator (the target source was acquired between this two scans). It is possible to notice that the phase fluctuations within one single scan are not completely negligible.

cannot correct amplitude and phase variation within the target scan (but target self-calibration can) and second that if a time-dependent solution is obtained every integration time, "rapid" phase fluctuations (amplitude is less affected) at the end of calibrator scans could lead to a biased interpolated solution (and the target calibration would not be good). Therefore, for every gain calibrator, two phase solutions have been derived: with the first one a solution every integration time is obtained in order to take into account rapid phase variations (useful to derive amplitude solutions), while with the second one a solution for each scan is derived in order to have a fluctuation-free interpolation between scans (useful to calibrate the targets); in both these two operations the bandpass solutions were applied on the fly. The amplitude solutions have then been derived applying both the bandpass solutions and the phase solution (first method). The flux calibration has been done using the standard calibrator 3C286, and the flux of the other calibrators has been found. The calibration solutions were then applied to all calibrators and to all the objects. In figure 2.5 we report, as an example, the calibrated phase values of the gain calibrator J1751–2524, where it is possible to notice that the phase fluctuaions are reduced within 10°. Since the calibration procedure is complex but could be easily automated, it has been performed by means of a single Python script, executable by CASA; the script is reported in section C.1.

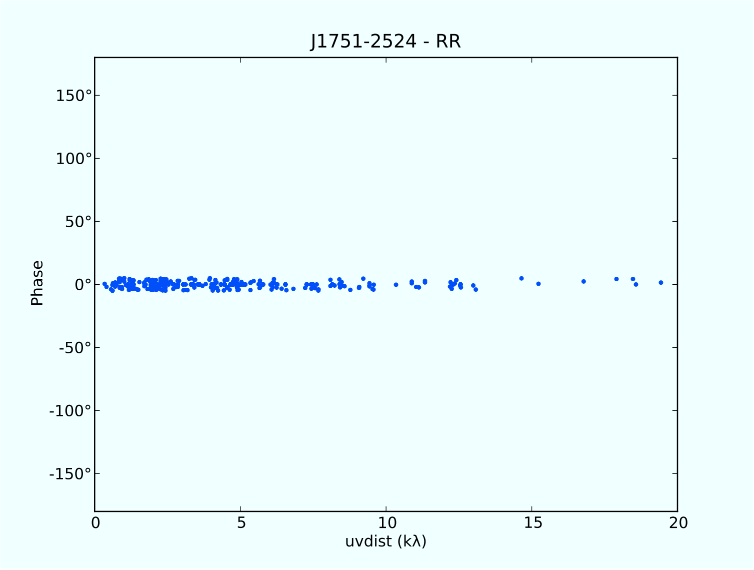

Figure 2.5: calibrated phase values for the gain calibrator J1751–2524 (only one spectral window and polarization are shown).

Data imaging has been made using the Clark implementation [17] of the CLEAN algorithm [18], convolving the resulting “clean components” with a Gaussian PSF. Since all observations have been carried out with the EVLA in the same configuration, no significant differences have been found in synthesis beam sizes, except for that group of bubbles with a very low declination, for which a more elongated beam resulted; anyway beam dimensions ranged from 10.7″ (minor axis of bubble 3910) to 74.4″ (major axis of bubble 4436), with a typical size of 25″ × 15″. Therefore all the images have been built using a 4″ pixel and a total size of 256 × 256 pixels, in such a way that each map covers approximately a 17′ × 17′ area (the primary beam is about 9′ FWHM).

For two bubbles, namely 3384 and 4607, it has also been performed a self-calibration process in order to improve the signal-to-noise ratio; these two sources were chosen as an example of the self-calibration capabilities thanks to their relatively high flux density and simple structure (the 4607 was not resolved at all).

2.4 First results

Almost all the bubbles in our sample proved to be well detected, with 44 clear dectection over 55; there were, anyway, some bubble not detected and others whose detection is unclear.

Since one main goal of this work was to characterize the radio emission of the bubbles as an important aid to their classification, a very accurate flux densities determination was needed. In order not to introduce systematic errors or biases, a unique procedure in this calculation has been adopted. First of all the sources have been divided into two classes depending on whether they were resolved or not.

For point sources (not resolved) the flux density has been determined using the CASA task `imfit`, which fits one elliptical Gaussian component on an image region. Given that the maps measure units were janskys per beam, the total flux density for a point source was numerically equal to the peak value of the fitted Gaussian component. The total error, ε, was computed as the quadratic sum of the fit error ε_f, the map rms, σ, and the error introduced in flux calibration (negligible indeed in both bands, ranging from 3% to 5%), ε_c

$$\varepsilon = \sqrt{\varepsilon_f^2 + \sigma^2 + \varepsilon_c^2}.$$

The flux density calculation for extended sources proved much more difficult. For extended sources detected in one only band, the strategy was to localize the source boundary as the lowest brightness level at which we were confident to encompass only our object; theoretically, one should descend down to 1σ, below which the source becomes indistinct with respect to background. The interferometric images artifacts, however, usually do not allow to look so deeply and, for many bubbles, we were forced to stop at higher levels. Selected then this appropriate region for each object, the flux density has been calculated by means of an integration over the area, performed directly with the CASA `viewer`. The total error was estimated as the map rms multiplied by the square root of the integration area expressed in beams.

If the source appeared extended not only in band C but also in the following

images in band L, a slightly modified version of the flux density procedure has been adopted; it is described in details in section 3.4.
The results obtained are listed, along with some useful characteristic of each map, in the table 2.3.

ID	Map rms (mJy/beam)	Beam	PA	Flux density (mJy)	Resolved?
3153	2.40	$29.9'' \times 13.9''$	20°	–	–
3173	0.16	$26.8'' \times 14.6''$	−29°	1.0 ± 0.3	no[2]
3177	0.90	$24.6'' \times 14.8''$	−23°	–	–
3188	0.24	$23.6'' \times 15.8''$	−5°	1.0 ± 0.3	no?
3192	0.53	$26.7'' \times 15.5''$	−34°	1.2 ± 0.6	yes
3193	0.61	$22.5'' \times 15.0''$	−18°	1.4 ± 0.6	no
3214	0.11	$22.4'' \times 16.0''$	0°	4.0 ± 0.2	no
3222	0.82	$21.3'' \times 14.4''$	41°	22.9 ± 1.5	no
3259	1.02	$20.6'' \times 15.4''$	7°		yes
3269	1.13	$22.2'' \times 16.6''$	28°	–	–
3282	0.83	$19.9'' \times 15.5''$	10°		ext[3]
3309	0.21	$19.8'' \times 15.5''$	14°	3.4 ± 0.4	yes
3310	7.23	$21.0'' \times 14.0''$	25°		ext[4]
3313	0.30	$19.6'' \times 15.1''$	24°	5.1 ± 0.7	yes
3328	0.97	$19.5'' \times 14.0''$	34°	114.8 ± 5.3	ext[5]
3333	0.15	$19.3'' \times 15.1''$	22°	6.4 ± 0.3	yes
3347	0.14	$20.2'' \times 14.1''$	40°	1.5 ± 0.3	no
3354	0.04	$21.1'' \times 18.5''$	51°	12.3 ± 0.1	yes
3362	2.35	$21.8'' \times 15.6''$	34°	12.1 ± 2.5	no
3367	0.79	$21.3'' \times 15.4''$	31°	4.7 ± 0.9	no
3384	0.16	$27.2'' \times 21.4''$	−2°	17.8 ± 0.4	yes[6]
3438	0.09	$19.8'' \times 16.1''$	46°	10.5 ± 0.1	no?
3448	0.13	$20.6'' \times 16.1''$	51°	12.7 ± 0.4	no
3558	0.05	$21.9'' \times 14.3''$	−7°		ext[4]
3654	0.18	$22.8'' \times 16.2''$	52°	59.7 ± 0.5	yes

---

[2] Not reliable.

[3] Maybe resolved-out, see chapter 4. This bubble is also discussed in detail in the appendix B.

[4] Resolved-out, see chapter 4.

[5] Maybe resolved-out, see chapter 4.

[6] Self-calibrated.

3706	0.40	23.1″ × 15.7″	37°	19.6 ± 0.8	yes
3724	0.18	19.9″ × 14.0″	36°	?	?
3736	0.14	20.2″ × 14.9″	27°	18.1 ± 0.5	yes
3866	0.30	24.0″ × 16.0″	−1°	10.3 ± 0.6	no
3910	6.47	30.5″ × 10.7″	28°		ext[3]
3915	2.88	31.2″ × 13.7″	26°	–	–
4409	0.03	68.2″ × 12.7″	−25°	7.3 ± 0.1	no
4422	0.06	35.1″ × 13.5″	15°	40.3 ± 0.2	no
4436	0.06	74.4″ × 11.3″	−15°	5.8 ± 0.1	no
4443	0.28	46.2″ × 15.0″	−35°	–	–
4452	0.18	39.6″ × 13.9″	−30°	2.1 ± 0.4	yes?
4463	0.03	10.0″ × 10.0″	0°	?	yes
4465	0.04	52.3″ × 12.2″	−13°	1.6 ± 0.1	no
4467	0.07	33.3″ × 13.2″	11°	–	–
4473	0.52	31.8″ × 13.4″	−12°	38.1 ± 0.8	no
4479	0.08	31.2″ × 13.5″	23°	16.0 ± 0.2	no
4485	0.83	43.6″ × 14.7″	−16°		ext[7]
4486	0.58	43.9″ × 14.2″	−16°	15.5 ± 0.9	no
4497	0.18	63.8″ × 11.7″	−16°	15.1 ± 0.4	no
4530	1.37	34.3″ × 13.1″	−30°	–	–
4534	9.11	48.7″ × 14.2″	−19°	?	?
4552	0.48	66.0″ × 11.7″	−18°	15.0 ± 0.7	no
4555	0.38	69.6″ × 11.9″	−20°	–	–
4580	0.35	46.5″ × 14.2″	−37°	2.0 ± 0.4	no
4583	0.86	39.8″ × 13.7″	−31°	?	?
4584	0.32	41.0″ × 14.5″	−33°	2.1 ± 0.5	yes?
4589	0.08	47.4″ × 12.3″	−15°	9.0 ± 0.2	no
4595	0.29	29.9″ × 13.3″	−25°		ext[6]
4602	0.25	30.1″ × 13.8″	18°	17.7 ± 0.7	no
4607	0.26	29.6″ × 13.7″	16°	8.2 ± 0.4	no[8]

Table 2.3: Flux densities and useful map parameters of all the observed bubbles.

As it is possible to see in the table 2.3, we were able to detected 44 bubbles over 55 observed with also 3 uncertain detections (flux density columns

---

[7] Maybe resolved-out, see chapter 4.

[8] Self-calibrated.

marked with a "?") and 8 non-detections (flux density columns marked with a "–"). A possible explanation of why we did not detect all the bubbles could be that they are quite bright at 20 cm but less at 6 cm, maybe due to a steep negative spectral index. Some other bubbles (with the resolved column marked with an "ext") resulted to be as extended as or more extended than the largest angular scale of the EVLA; for these sources single-dish observations were needed and we will discuss on this in chapter 4.
In the following pages some contour maps will be plotted. Some bubbles will be treated in detail in chapter 7; for those bubbles the relative contour map will be shown there.

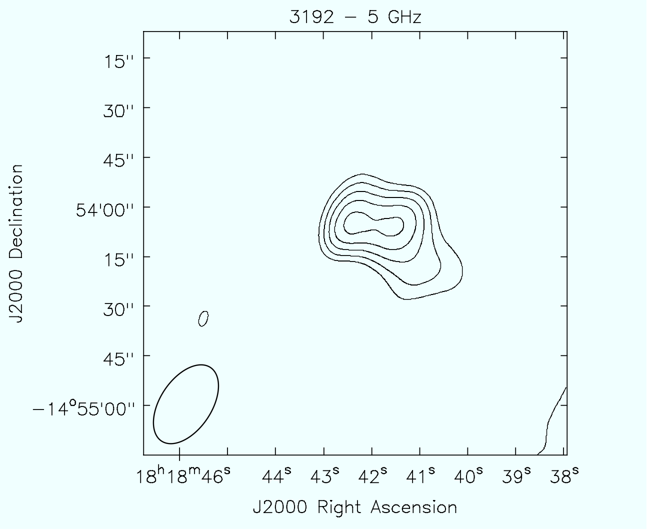

Figure 2.6: radio contour image of the bubble 3192 from our data at 5 GHz. Contours are 0.8, 0.9, 1.0, 1.1 and 1.2 mJy/beam.

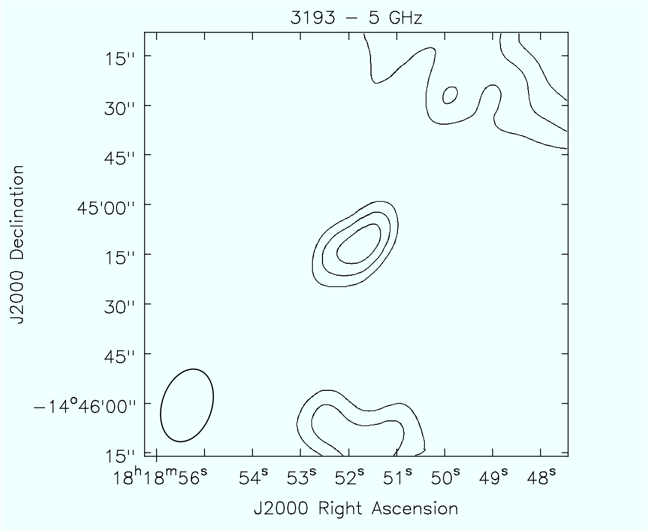

Figure 2.7: radio contour image of the bubble 3193 from our data at 5 GHz. Contours are 1.2, 1.4 and 1.6 mJy/beam.

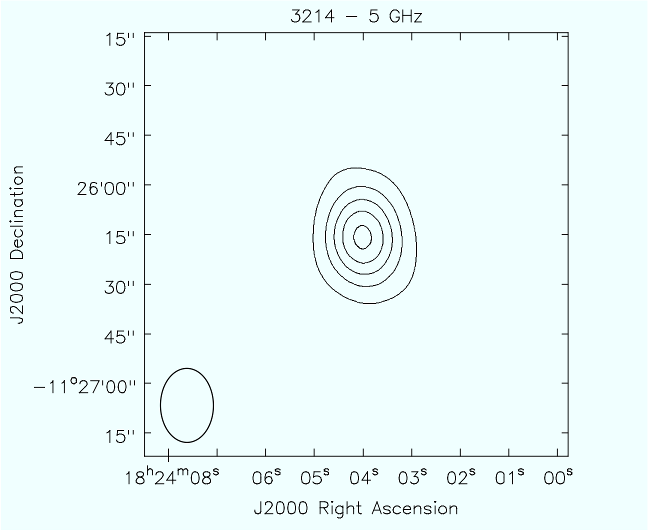

Figure 2.8: radio contour image of the bubble 3214 from our data at 5 GHz. Contours are 0.8, 1.6, 2.4, 3.2 and 4.0 mJy/beam.

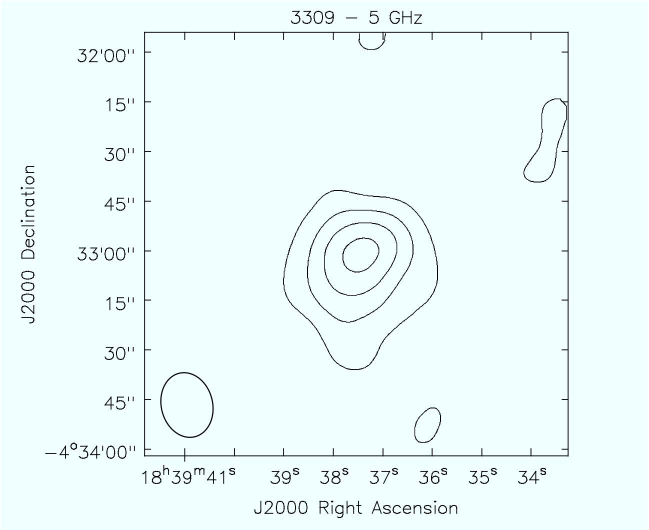

Figure 2.9: radio contour image of the bubble 3309 from our data at 5 GHz. Contours are 0.4, 0.8, 1.2 and 1.6 mJy/beam.

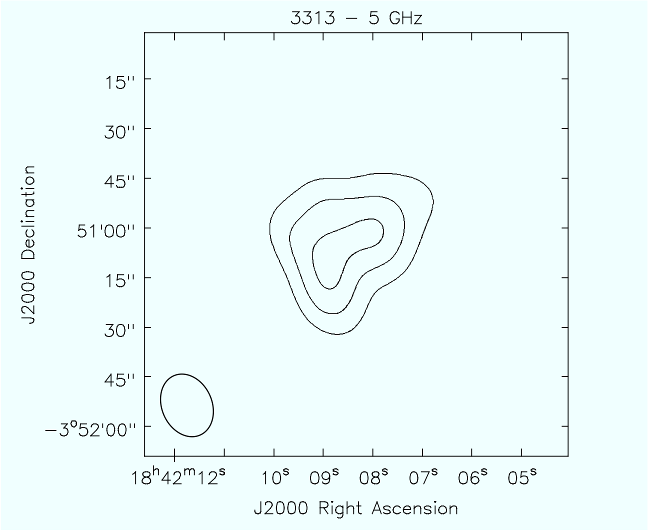

Figure 2.10: radio contour image of the bubble 3313 from our data at 5 GHz. Contours are 0.6, 1.0 and 1.4 mJy/beam.

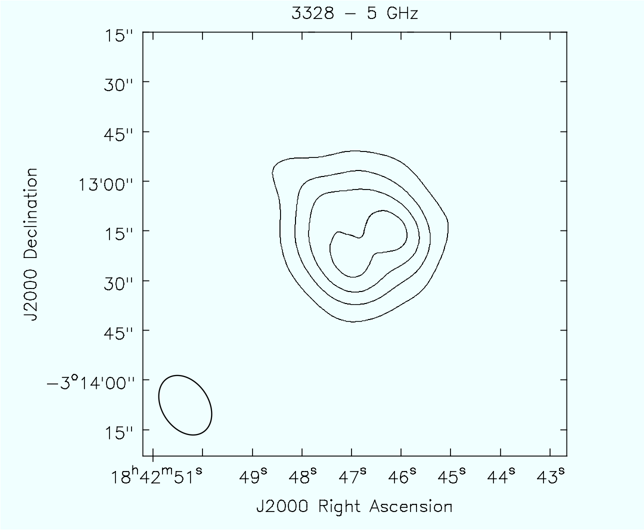

Figure 2.11: radio contour image of the bubble 3328 from our data at 5 GHz. Contours are 8, 16, 24 and 32 mJy/beam.

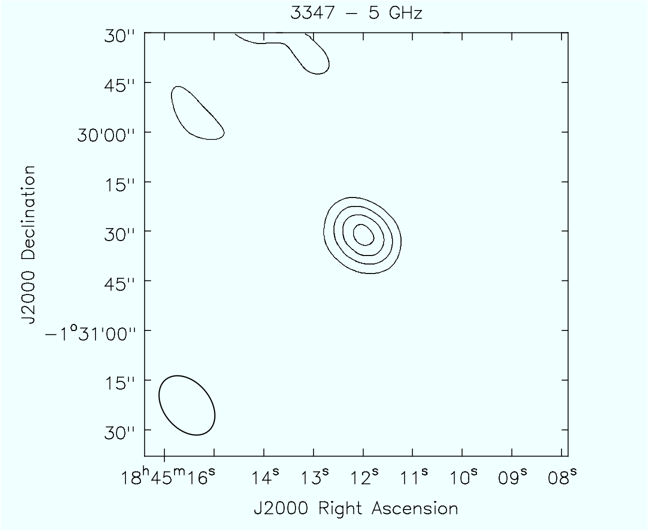

Figure 2.12: radio contour image of the bubble 3347 from our data at 5 GHz. Contours are 0.3, 0.6, 0.9 and 1.2 mJy/beam.

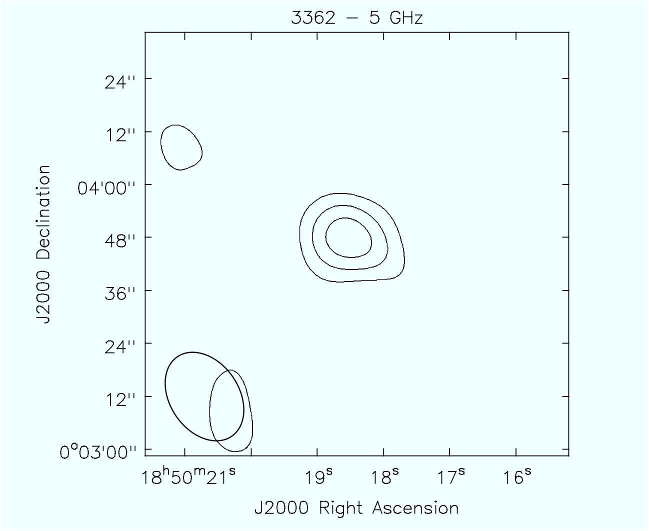

Figure 2.13: radio contour image of the bubble 3362 from our data at 5 GHz. Contours are 0.3, 0.6 and 0.9 mJy/beam.

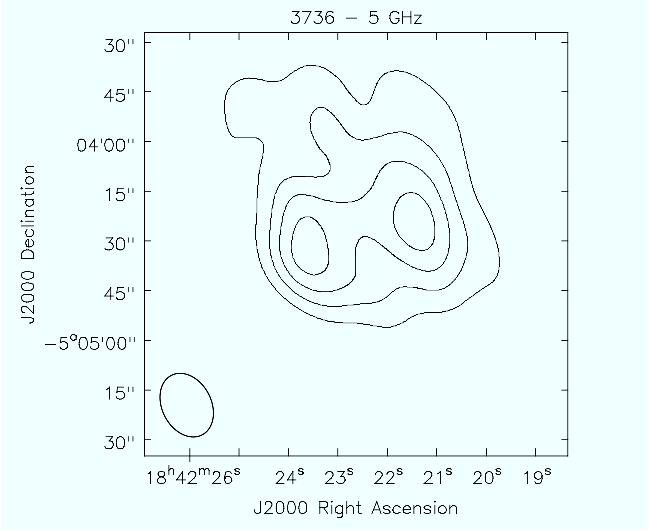

Figure 2.14: radio contour image of the bubble 3736 from our data at 5 GHz. Contours are 0.6, 1.2, 1.8 and 2.4 mJy/beam.

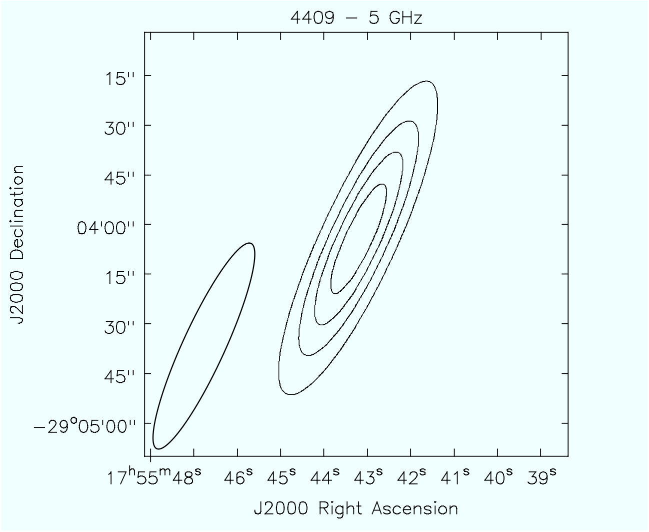

Figure 2.15: radio contour image of the bubble 4409 from our data at 5 GHz. Contours are 1.5, 3.0, 4.5 and 6.0 mJy/beam.

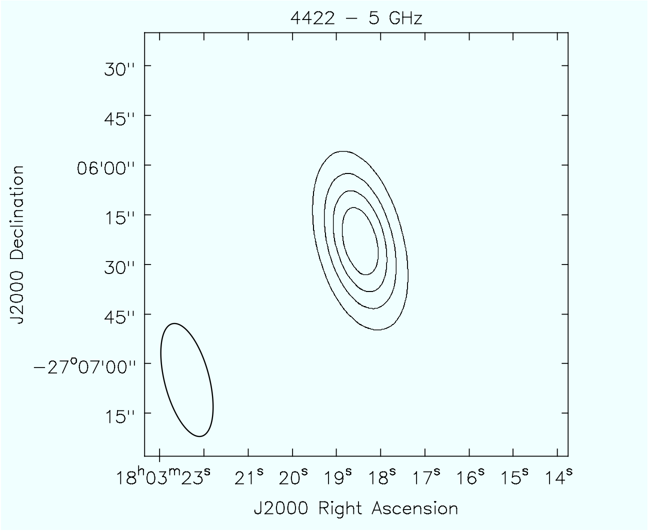

Figure 2.16: radio contour image of the bubble 4422 from our data at 5 GHz. Contours are 8, 16, 24 and 32 mJy/beam.

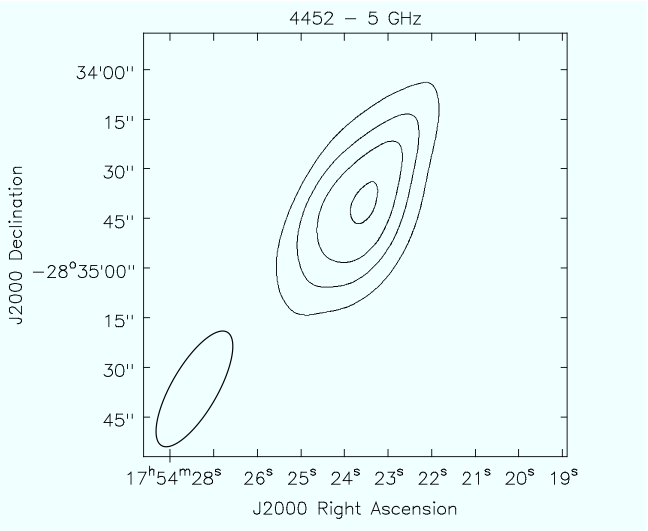

Figure 2.17: radio contour image of the bubble 4452 from our data at 5 GHz. Contours are 0.24, 0.48, 0.72 and 0.96 mJy/beam.

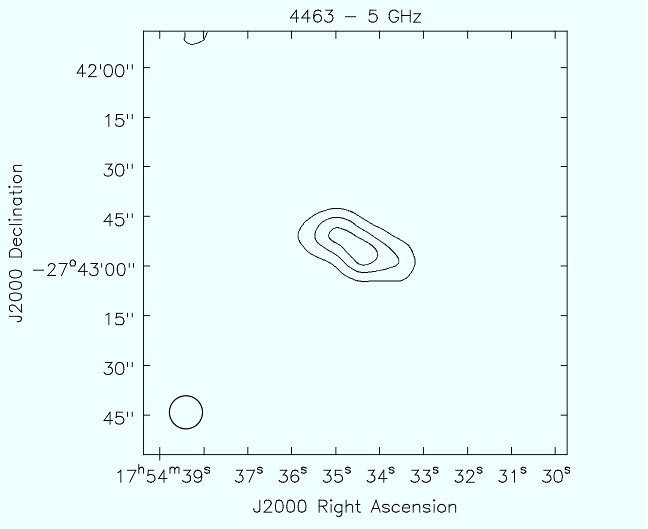

Figure 2.18: radio contour image of the bubble 4463 from our data at 5 GHz. Contours are 0.6, 1.2 and 1.8 mJy/beam. For this bubble deconvolution problems occurred.

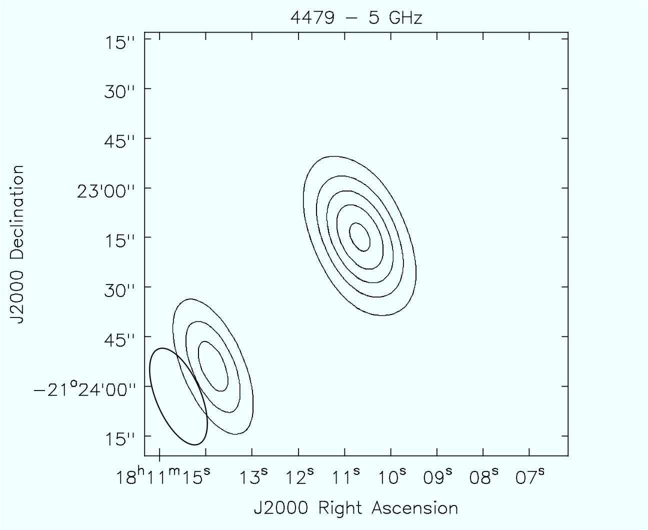

Figure 2.19: radio contour image of the bubble 4479 from our data at 5 GHz. Contours are 3, 6, 9 and 12 mJy/beam.

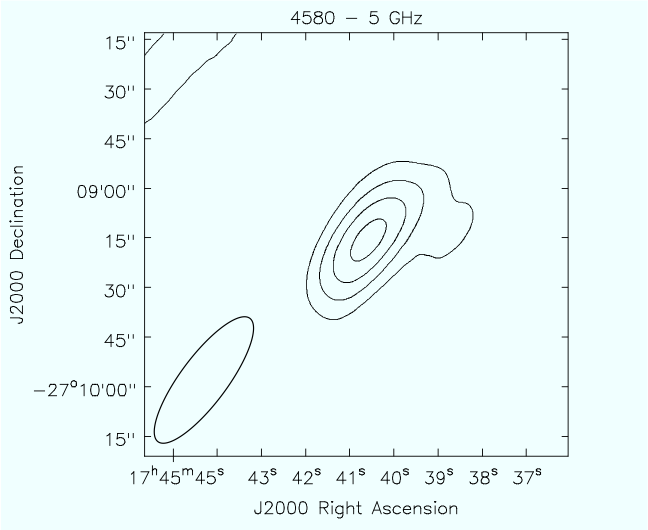

Figure 2.20: radio contour image of the bubble 4580 from our data at 5 GHz. Contours are 0.8, 1.2, 1.6 and 2.0 mJy/beam.

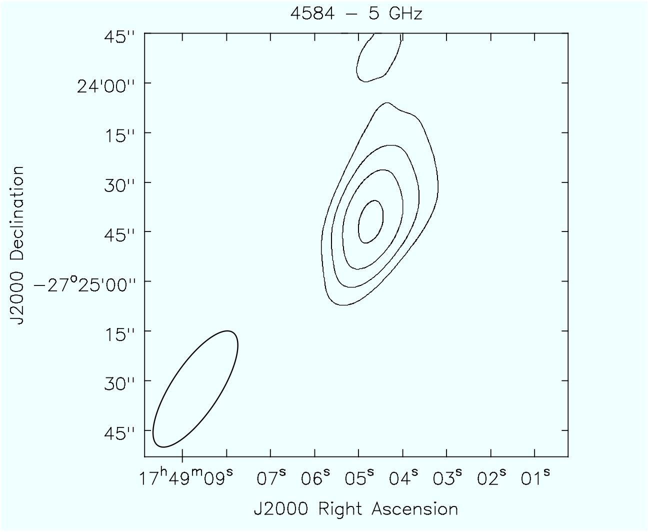

Figure 2.21: radio contour image of the bubble 4584 from our data at 5 GHz. Contours are 0.4, 0.8, 1.2 and 1.6 mJy/beam.

Chapter 3

EVLA observations at 20 cm

As explained in the previous chapter, our main purpose, which led to radio observations at 6 cm, was to unveil the nature of the radio emission of the MIPSGAL bubbles by deriving their radio spectral index. To meet this intent we needed observations also, at least, at another frequency; we then propose to carry out observations, again with EVLA, at 20 cm.

In order to obtain a resolution comparable to the other radio observations, we chose to observe with the EVLA in configuration C; anyway, since low declination sources showed in band C very elongated beams, we also proposed to observe some sources in configuration CnB to obtain a better coverage of the uv plane.

Our initial calculations showed that, using a bandpass of 500 MHz (the half of the real one), we could have achieved a noise level of only about 40 μJy/beam with an integration time of 10 min; however, as we will see, very pervasive interferences prevent us to reach this limit.

3.1 Preparing the observations

In the previous observations, from the original sample of MIPSGAL bubbles only sources with $\delta \geq -40^\circ$ and with radio emission in either NVSS or MAGPIS were selected, resulting in a sample of 57 sources. From the analysis of our band-C data, we found that eight sources were too extended to actually recover all the flux density, preventing to determine an accurate spectral index. As explained in the next chapter, to get zero-baseline flux density, we observed these sources with the GBT, in June 2011, in both bands.

Despite the fact that with only one frequency dataset was not possible to reach our main scientific goal, some interesting results have come out from the analysis of the obtained band-C data. Among the selected targets, nine were known PNe; all of them have been detected in band C, and, for many of them, it constituted their first detection at this frequency. For 34 of our targeted sources, MAGPIS data already existed. We have retrieved them and attempted to use them to perform a spectral index analysis. While for three of our bubbles, namely 3282, 3310 and 3910, the MAGPIS data were good enough to obtain a spectral index, in general, the available data were very noisy, with a typical rms of 1 mJy/beam, on average much worst than what could be achievable with EVLA and were not suitable to reach our scientific goal.

Since we expected that the flux densities of many sources could be very low (about 1 mJy), resulting in heavily time consuming observations, we decided not to observe all the sources observed at 6 cm, deleting the non-detected sources and the ones with good archive data. Therefore, to complete our project, we proposed band L observations for 34 sources, with no good available data at 20 cm.

3.2 Observations details

Observations of the bubbles sample were made with the EVLA in configuration C at 20 cm during March 2012 and in configuration CnB during May 2012 for a total of 8 hours; the sample was split in three subset, observed in three different days. Each bubble has been observed for about 10 minutes, and four of them were observed in both configurations (for these sources the total observing time was greater); three sources had not been chosen as targets for observations but where observed anyway as field sources in other bubbles observations. The total bandwidth benefitted the full expanded capabilities of the VLA, being as wide as 1 GHz and it was divided in 16 spectral windows. Unfortunately, we knew that band-L frequencies were very affected by RFI and we did not expect a total bandwidth greater than 500 GHz, but, as it will be shown later, the situation was even worse and the bandwidth was reduced to less the one third. For this reason, but also for other unavoidable error sources, the noise level we were conscious to achieve was several times worse than the predicted one.

Also for these observations the observing strategy adopted was the usual

one. After that the sources have been divided in three observing blocks, the most convenient calibrators have been chosen to achieve the best results. In particular, the source 3C286 has been chosen as both flux and bandpass calibrator for all the three observing blocks, while four different complex gain calibrators were selected in order to minimize their distance from the targets. The table 3.4, in the next section, lists all the calibrators chosen.
In table 3.1 all observed objects are reported along with the date and the approximate duration of each observation.

ID	Obs. day (2012)	Obs. time (min)	Configuration
3188	06–Mar	10	C
3193	06–Mar	10	C
3222	06–Mar	10	C
3309	06–Mar	9	C
3313	06–Mar	9	C
3333	06–Mar	10	C
3347	06–Mar	10	C
3354	06–Mar[1]	18	C/CnB
3362	06–Mar	10	C
3367	06–Mar[1]	15	C/CnB
3384	06–Mar[1]	18	C/CnB
3438	06–Mar[1]	21	C/CnB
3448	13–May	9	C
3654	13–May	4	C
3706	13–May	4	C
3724	06–Mar	10	C
3736	06–Mar	10	C
3866	06–Mar	5	C
4436	08–May	10	CnB
4452	08–May	10	CnB
4463	08–May	10	CnB
4465	08–May	10	CnB
4473	08–May	10	CnB
4485	08–May	10	CnB
4486	08–May	10	CnB

---

[1] Observed also on 13–May.

4497	08–May	10	CnB
4552	08–May	10	CnB
4580	08–May	10	CnB
4583	08–May	10	CnB
4584	08–May	10	CnB
4589	08–May	10	CnB
4595	08–May	10	CnB
4602	08–May	10	CnB
4607	08–May	10	CnB

Table 3.1: Observations summary for band L.

3.3 Data reduction

With respect to the data reduction process performed with band-C data, the data reduction of the data at 20 cm proved much harder mainly because of the diffuse presence of RFI.

As a first step the three datasets were split into their constituting spectral windows, not only in order to reduce the computational load but also to perform a more accurate flagging. Each spectral window was made of 64 channels and the width of each channel was 1 MHz. Indeed, some spectral windows appeared very affected by RFI while others appeared cleaner; in table 3.2 we list the spectral windows and an upper limit for the percentage of useful data after our flagging, given by the fraction of unflagged channel in the gain calibrators. As it is possible to notice, five spectral windows were so affected that no data could be used.

However, the possibility to observe in pseudo-continuum mode, that is with a huge number of channels, allowed us to perform a surgical flagging to maintain as many data as possible. The nature of the RFI affecting our data was various; indeed, it was possible to identify five different main interference types listed in table 3.3.

The philosophy behind data flagging was that it was better to delete a good, but suspected, datum rather than retain a suspected bad one; anyway it was a crime to blindly flag the data, and the entire flagging process was aimed to keep as many good data as possible. Since no reliable flagging algorithm exists, at least for such a contaminated dataset, all the editing process was conducted manually, using the CASA task `plotms`.

spw	Frequency (MHz)	Useful data
0	994 – 1057	< 52%
1	1058 – 1121	< 23%
2	1122 – 1185	0%
3	1186 – 1249	0%
4	1250 – 1313	< 8%
5	1314 – 1377	< 41%
6	1378 – 1441	< 72%
7	1442 – 1505	< 78%
8	1494 – 1557	0%
9	1558 – 1621	0%
10	1622 – 1685	0%
11	1686 – 1749	< 35%
12	1750 – 1813	< 79%
13	1814 – 1877	< 81%
14	1878 – 1941	< 53%
15	1942 – 2005	< 6%
total	994 – 2005	< 33%

Table 3.2: spectral window extensions and upper limit for useful data.

As a first step, for each spectral window the bandpass calibrator was edited. What we expect from the observation of a bandpass calibrator is to derive the bandpass solution for our dataset, that is to derive channel-wise coefficients that allow to take into account the different responses of the receivers for each channel; this is to say that we suppose that the antenna-based gain is frequency dependent and we want to determine this dependency. To achieve this goal, the observed bandpass calibrator is required to have a well known flat spectrum, above all free from emission or absorption lines, with a very high flux density, since we need to have a good signal-to-noise ratio even in a 1-MHz wide band (a channel). Under this conditions, an ideal receiver should measure the same flux density for all the channels for all the duration of the scan[2]; of course no ideal receivers exist but a good one is capable of very small gain variation with frequency. The extreme channels of each spectral

---

[2] The source chosen must not vary its intensity with time then.

Type	Characteristics
1	Localized both in frequency and in time
2	Extending over few channels but affecting all the scan
3	Lasting few tens of seconds but spreading over all the spw
4	Not 1, 2 or 3 but affecting only few baselines
5	Extending over entire spw, scan and baselines

Table 3.3: RFI types.

window are indeed usually characterized by a significant lower response, and they are flagged in all the fields. In figure 3.1 we report a real example of our data for the bandpass calibrator for a very clean spectral window, where it is possible to notice the dependency on frequency.

Even if the case presented was a real case, among our observation was the luckiest one, without any interference. For the other spectral windows, in fact, pervasive interferences required a more accurate flagging or, in the worst cases, the complete discarding of entire spectral windows. When an interference was suspected to affect the data, the preliminary move was to see if it was localized in frequency (i.e. it affected only few channels) and/or in time (types 1, 2 and 3 of the table 3.3). The measured amplitude of clean spectral windows can be used as a reference for the other to look for interferences (visible as amplitude spikes), given that the response of the receiver between spectral windows does not vary greatly; anyway most interference patterns are so impressive that no reference is needed to identify them.

As an example, let us consider the situation represented in figure 3.2. Two interferences occur in the same dataset, field, correlation and baseline (with respect to the previous example) but in the spectral window 15. The analysis of the amplitude versus the frequency reveal that the values recorded by the central channels are noticeably higher and show a non-casual pattern, with a double peaked structure. It is, in fact, possible to notice a broad and high interference between channels 24 and 40 and a narrow, and lower, one between channel 42 and 44. If we focus on the broad interference we can see that the majority of the points lie indeed in a value range comparable to that of RFI-free zone (blue points), and this could lead us to suspect that this interference is well localized not only in frequency but in time (type 1 interference), since only few points appear contaminated. Plotting the amplitude

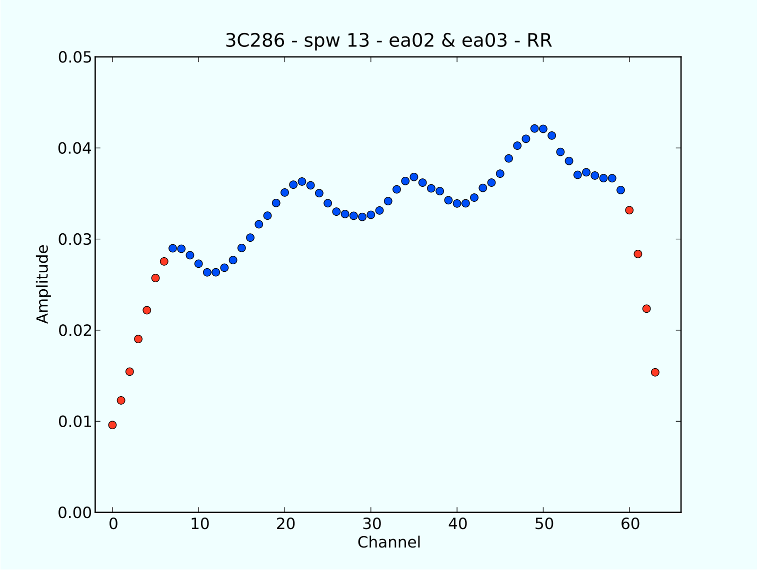

Figure 3.1: amplitude of raw data for 3C286 as a function of channel for the RFI-free spectral window 13. Only the baseline formed by the antennae ea02 and ea03 and only RR polarization have been plotted; the data were averaged for all the scan. It is possible to notice that, except for border channels, the variation of the measured amplitude with frequency is very small and smooth. Though, in theory, also border channels could be well calibrated, their very low gain would result in an amplification of the noise and so they are safely flagged (red circles).

against the time[3] makes our suspect become reality, as we can see that the same interference (recognizable by the same amplitude peak value) occupies a well determined time interval (yellow points). The other interference, on the contrary, shows a more uniform value distribution, and in fact we cannot see an analog structure in the second plot, but the interference is spread over the whole scan.

Let us start with the first interference; since we want to obtain an antenna-based gain, in principle, the exclusion of some baselines does not affect too much the calibration process. So, before we flag the interference, it is a good

---

[3] In this plot the red points of the previous plot are not reported since they are intended flagged.

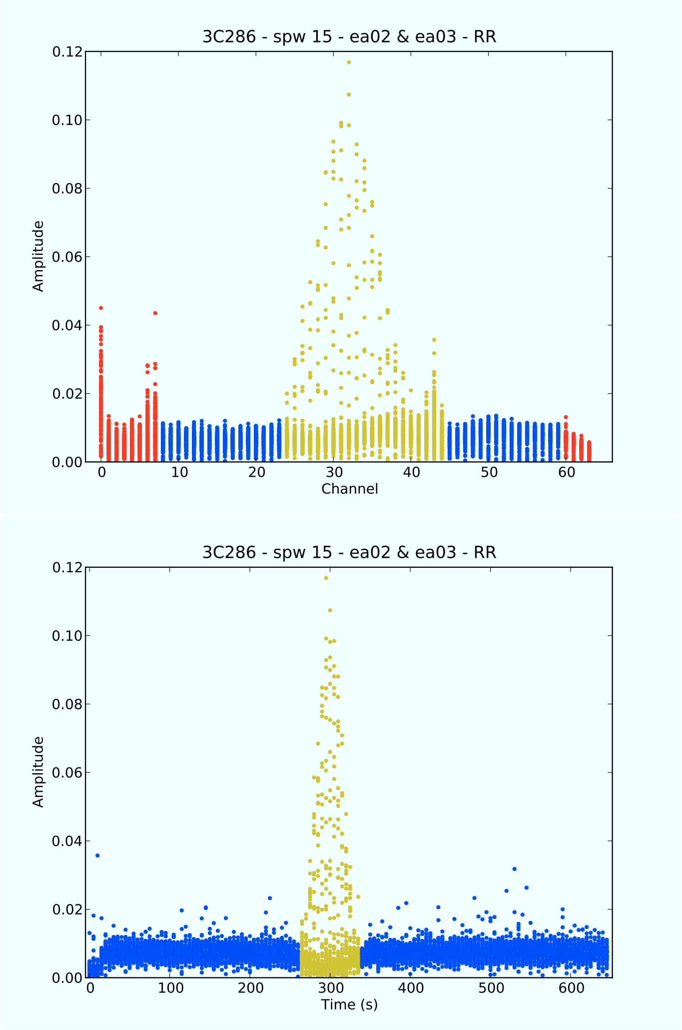

Figure 3.2: (top) amplitude versus channel plot. First of all, the border channels are flagged (red points); two prominent interference are recognizable between channels 24 and 44 (highlighted with yellow points). (bottom) Plotting amplitude versus time (excluding the red flagged points) it is possible to see the one interference (highlighted in yellow) is localized with time while the other is spread over the entire scan.

custom to see if the interference is present in all the baselines. Unfortunately both our interferences affect all the baselines, two of them (there are 325 baselines) are shown in figure 3.3. Therefore, filtering the first interference is quite simple, since it is sufficient to flag all the data between channels 24 and 40 acquired in the appropriate time interval (highlighted in the second plot of figure 3.2). This operation, like all the other flagging, has been performed manually, directly in the `plotms` plot. In figure 3.4 it is shown what we obtained after this flagging. It is possible to notice that the channels where the first interference appeared are now clean; in the amplitude-time plot, however, the time interval affected by the interference shows significantly lower value for amplitude. These low data along with initial data are flagged. The second interference is highlighted in yellow in both the plots; it is now possible to see that this interference affects all the duration of the scan.

Filtering out the second interference requires, therefore, the complete flagging of the channels 42, 43 and 44. Refining the temporal flagging we eventually obtain, in figure 3.5, a mean amplitude versus channel plot in the same fashion of the one in figure 3.1.

The procedure described was applied for all the 16 spectral windows and for all the three observations of the bandpass calibrator (one per each observing block). This allowed us to remove as many interferences as possible, preserving a good fraction of the data. Since the inspections were not automatic, only for the bandpass calibrator the plots in channels examined were one per each of the 325 baseline per each of the 16 spectral window per each of the three observations plus one in time per each of the 16 spectral window per each of the three observations, resulting in a total of 15 648 examined plots, with indeed plots examined more than once.

After that the flagging of bandpass calibrator was complete, all the channels which have been totally flagged were totally flagged in the rest of observed objects too. This operation was not strictly necessary since it would have been possible to interpolate solution in missing channels, anyway the non-negligible intrinsic variation in bandpass gain made it safe to delete them completely. Furthermore, it has been observed that contaminated channels in the bandpass calibrator often affect also the other objects, since their observed just after the calibrator and, as shown before, many interferences lasted more than a scan duration. The example shown above illustrates well how the spectral line observation mode has revealed extremely useful in detect and carefully and effectively delete the interferences; a limited number of channels, or worse only one, would have resulted in a more heavy flag with a

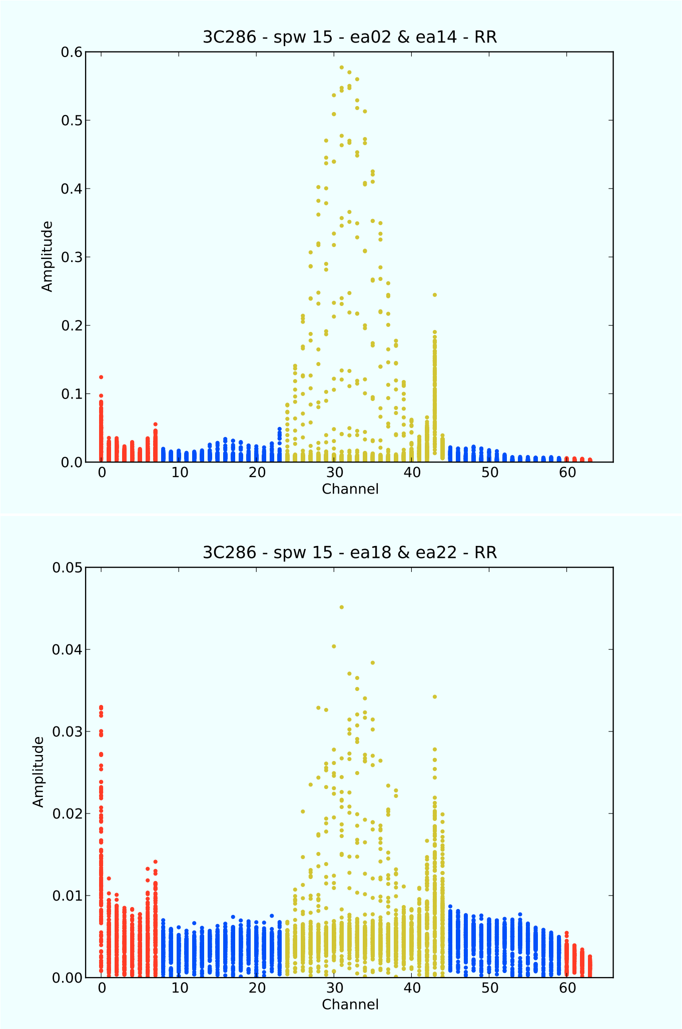

Figure 3.3: plots of amplitude versus channel for other two baselines; the two interferences are well visible also in these plots, as in all other 322 baselines not shown.

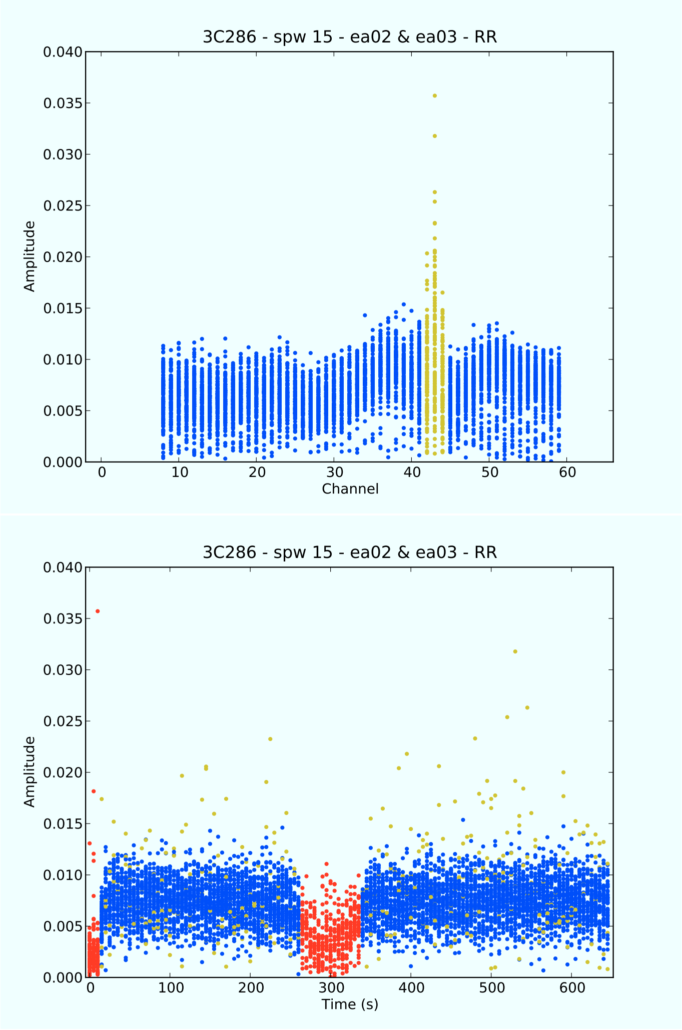

Figure 3.4: (top) amplitude versus channel plot after that the first interference has been flagged; the second one is still highlighted in yellow. (bottom) Once the first interference has been filtered out, the amplitude-time plot shows that the interval when that interference occurred is indeed totally corrupted (lower values) and so it has been flagged along with the initial acquisitions (red points); the second interference is marked in yellow and it affects, as expected, the whole scan.

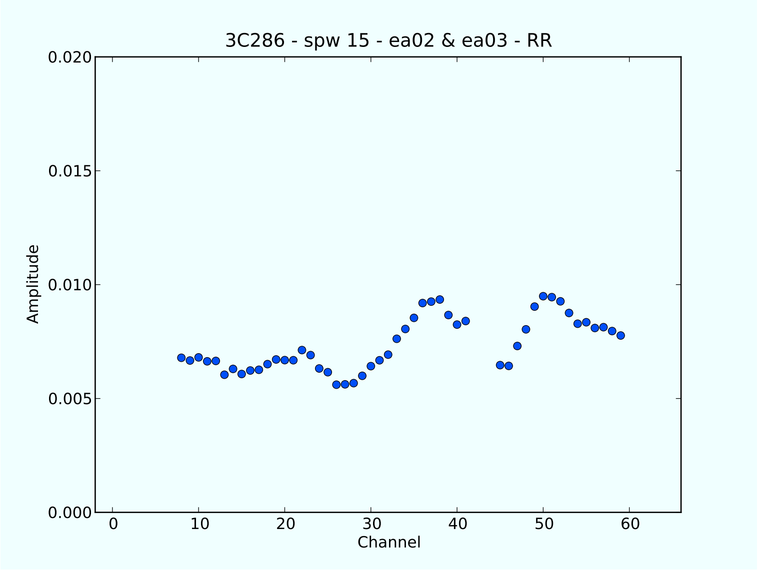

Figure 3.5: same as for figure 3.1 but for spectral window 15 after all the flagging operation. It is possible to see that the points show a regular and smooth behavior with mean amplitudes comparable to those of spectral window 13.

more conspicuous data loss and it was also possible that some contaminating interferences had not been detected at all.

The second step of the editing process regarded the complex gain calibrators. Since these calibrators are used to determine the time solutions for gain calibration, which usually vary greatly with time, a good flagging of bad data in these objects results even more critical than for bandpass calibrator. One of the most important constraint when we observe a gain calibrator, at least at 20 cm, is that it is unresolved by choice; this implies that each baseline should measure the same amplitude and phase difference within the shifts produced by the gain and its variation with time.

The procedure adopted for each gain calibrator consisted in an inspection of the amplitude as a function of frequency, as for bandpass calibrator, but also a deepest study of variation with time per each baseline. In fact, even if no interferences were found, or they simply were flagged out, it was possible to notice that the shortest baselines were often noisier than the longest one. This is a well known behavior, mainly due to antenna cross-talking. However, in a such a critical situation, many shortest baselines of gain calibrators have been flagged, preserving of them, anyway, a sufficient number per each antenna. The inspection of the frequency dependent behavior was necessary because, as discussed before, many interferences were localized in time, so some of them may not occur in the bandpass calibrator observation but be present in the following scans.

The gain calibrator observations were carried out in the usual and safest way; it was observed before and after the observation of each target object (our bubbles). Not only this observation strategy allowed a better interpolation of time-dependent gain, thanks to shorter intervals between two gain calibrator observations, but it also permitted to reduce the target data to be deleted when a massive flagging was required in gain calibrator. Sometimes, in fact, it could happen that, despite of any effort, one or more entire scans of a gain calibrator needed to be flagged. If n scans were completely deleted then $n + 1$ targets remained without at least two adjacent, in time, calibrator observations. Even in this case, in principle, if target data had resulted unaffected, a calibration could have been obtained by an interpolation of the farther calibrator observation; anyway, since that also in this case the gain variations (most important its phase variations) were rather quick, a good calibration could not be achieved and all the $n + 1$ target scans (at least for all the contaminated channels and baselines) were also flagged.

The final step was to edit also the target data. The flagging process was conducted as usual but the single baselines were not involved, since the *uv* data could show structure (more than one source, or resolved target). Since all previous flagging were also applied to target data, they resulted the most reduced by editing operations; this has to be taken into account to correct the theoretically expected map noise level.

To carry out the entire flagging process more than 50 000 plots were visually inspected in order to look for corrupted data. This could be a good indicator of how much complexity the expanded VLA carried and how it would be important to get to a completely automatic editing process.

The calibration process was performed as described for band C. The calibrator used at 20 cm are listed in table 3.4. Since each spectral window has been calibrated separately, the use of the calibration pipeline mentioned in section 2.3 proved extremely useful and time-saving.

After the calibration, the datasets were split into single objects, and the datasets of bubbles observed in both configurations were concatenated.

Data imaging has been performed as described in section 2.3. The use of

Obs. day	Gain cal.	Flux cal.	Bandpass cal.
06–Mar	J1822–0938 J1856+0610	3C286	3C286
08–May	J1751–2524 J1820–2528	3C286	3C286
13–May	J1751–2524	3C286	3C286

Table 3.4: Calibrators used for observations at 20 cm.

two different configurations allowed us to obtain no significant differences in beam size, having observed the bubbles with a very low declination in the hybrid configuration CnB, with the extended northern arm compensating their low maximum elevation. Beam dimensions ranged from $10.4''$ (minor axis of bubble 4463) to $29.1''$ (major axis of bubble 3193), with a typical size of $20'' \times 12''$, slightly smaller then the beam at 6 cm. All the images have been built using a $3''$ pixel; their total size, however, varied from 128×128 to 4096×4096 pixels because sometimes very far field sources[4] produced high sidelobes which needed to be clean well.
For the bubble 4552 it has also been performed a self-calibration process in order to improve the signal-to-noise ratio.

3.4 First results

The percentage of detected bubbles for band-L observations was slightly lower than for band C. This could mainly due to both a worse sensitivity and to the fact that, for optically thick thermal emitters, some bubbles can be much fainter at 20 cm than at 6 cm (about a factor 10 for pure black-body emitters).
The flux density calculation was performed in the same way of band C, except for sources resolved in both bands, for which we proceeded as follows. First of all, among the two frequency images of the same bubble, the higher resolution map was degraded to the same resolution of the other, simply convolving its clean components with the beam of the other image and adding the residual

---

[4] The field of view of VLA at this frequency is in fact very large, about $45'$ at 20% of primary beam maximum, and so many field sources are detected in any observation; a significant part of these field source are first detection at this wavelength or in absolute.

map. Then, for each bubble, an appropriate region was chosen in order to encompass the source in both bands and over it we calculated the total flux and error as in the previous case. The flux densities at 6 cm listed in table 2.3, are already corrected for this method.
The results obtained are listed, along with some useful characteristic of each map, in the table 3.5.

ID	Map rms (mJy/beam)	Beam	PA	Flux density (mJy)	Resolved?
3177	2.19	$25.1'' \times 14.5''$	-22°	–	–[5]
3188	1.46	$25.1'' \times 14.4''$	-23°	–	–
3192	0.74	$29.1'' \times 14.1''$	-21°	–	–[6]
3193	0.74	$29.1'' \times 14.1''$	-21°	–	–
3222	2.26	$18.4'' \times 14.4''$	-17°	21.5 ± 3.1	no
3309	0.88	$19.0'' \times 14.2''$	-12°	–	–
3310	1.07	$20.8'' \times 14.6''$	-23°		ext[7]
3313	0.98	$18.7'' \times 14.2''$	-10°	–	–
3328	0.87	$20.1'' \times 14.5''$	-27°	11.3 ± 4.4	ext[8]
3333	0.69	$20.1'' \times 14.5''$	-27°	4.0 ± 1.2	yes
3347	1.88	$18.7'' \times 14.4''$	-21°	?	?
3354	0.58	$15.5'' \times 12.0''$	-36°	12.0 ± 1.1	yes
3362	1.88	$17.1'' \times 13.2''$	-4°	–	–
3367	0.92	$16.1'' \times 11.9''$	-42°	6.8 ± 0.9	no
3384	0.82	$15.6'' \times 12.0''$	-38°	2.1 ± 0.8	no?
3438	0.39	$15.0'' \times 12.0''$	-26°	10.2 ± 0.8	yes
3448	0.73	$14.9'' \times 10.7''$	-77°	12.8 ± 1.1	yes?
3654	0.24	$13.5'' \times 10.8''$	-43°	64.1 ± 0.8	yes
3706	1.93	$14.3'' \times 11.6''$	-63°	10.8 ± 3.7	yes
3724	1.50	$18.7'' \times 14.3''$	-8°	–	–
3736	0.64	$20.8'' \times 14.6''$	-23°	?	?
3866	3.31	$25.1'' \times 14.5''$	-22°	9.7 ± 3.5	no
4409	0.46	$17.3'' \times 12.0''$	-3°	–	–
4436	0.33	$21.0'' \times 12.2''$	-29°	6.6 ± 0.4	no
4452	0.57	$17.3'' \times 12.0''$	-3°	–	–

---

[5] As field source with targets 3188, 3193 and 3866.

[6] As field source with target 3193.

[7] As field source with targets 3309 and 3736.

[8] As field source with target 3333.

4463	0.43	28.2″ × 10.4″	−46°		yes
4465	0.55	18.4″ × 12.1″	−25°	1.0 ± 0.6	no
4473	3.94	16.8″ × 12.0″	5°	34.7 ± 3.9	no?
4485	4.06	27.3″ × 11.9″	−34°	–	–
4486	0.53	24.1″ × 12.1″	−30°	14.4 ± 1.0	no?
4497	0.62	21.0″ × 11.8″	−31°	15.0 ± 0.9	no
4530	3.27	16.2″ × 11.8″	0°	–	–
4552	0.66	23.9″ × 11.7″	−36°	12.2 ± 1.0	no?[9]
4580	1.00	17.5″ × 12.2″	−12°	?	?
4583	2.02	17.1″ × 12.0″	−5°	–	–
4584	1.21	17.4″ × 12.1″	−11°	–	–
4589	0.55	17.8″ × 11.7″	−29°	8.9 ± 0.6	no
4595	3.30	16.2″ × 11.8″	0°		ext
4602	1.16	15.7″ × 11.7″	18°	14.7 ± 1.7	no
4607	0.51	15.4″ × 11.7″	15°	5.9 ± 0.6	no

Table 3.5: Flux densities and useful map parameters of all the observed bubbles.

As it is possible to see in the table 3.5, we were able to detected 23 bubbles over 40 observed with also 3 uncertain detections (flux density columns marked with a "?") and 14 non-detections (flux density columns marked with a "–"). As already explained, the bubbles with the resolved column marked with an "ext" resulted to be as extended as or more extended than the largest angular scale of the EVLA at 6 cm.

---

[9] Self-calibrated.

Chapter 4

Continuum single-dish observations

The images of the bubbles obtained from our EVLA data revealed that few of them had noticeable dimensions that exceeded the VLA largest angular scale. For these object, our interferometric data were not sufficient to recover their total flux densities, resulting in an altered spectral index determination. Since for both bands we were already using the shortest baseline available for VLA, we needed to carry out single-dish observations. Even if, in theory, single-dish data can fill in the gap in the central zone of the *uv* plane, reducing single-dish data and combining with interferometric ones proved not so straightforward as it seemed, with several ancillary operations necessary to achieve our initial intents.

4.1 Need for single-dish observations

As known, when we observe a source with an interferometer, if the source is more extended than the largest angular scale of the interferometer we are not able to recover all its flux density, resulting then in a net flux loss. It is first necessary to understand the reasons why this phenomenon occurs in order to have the possibility to overcome it and restore the entire flux of the source.

An interferometer can be seen as an instrument capable to measure the correlation function, or visibility, $V(u, v)$ which is the Fourier transform of the true sky brightness. However an interferometer cannot be able to measure

$V(u,v)$ in each point of the uv plane, and indeed the visibility function is sampled only on a discrete set of (u,v) pairs. In particular, for any observation, there will be a minimum and a maximum value for $\sqrt{u^2+v^2}$, the distance of a (u,v) point from the uv plane origin. These extreme values are easily derived from the minimum and the maximum baseline (b_{min} and b_{max}) of our interferometer; in details we have

$$\min\{\sqrt{u^2+v^2}\} = \frac{b_{\mathrm{min}}}{\lambda}\cos\theta$$

and

$$\max\{\sqrt{u^2+v^2}\} = \frac{b_{\mathrm{max}}}{\lambda},$$

where λ is the observing wavelength and θ is the source elevation. The maximum value for $\sqrt{u^2+v^2}$ determines the interferometer resolution, which can be easily estimated (minimum angular separation) as

$$\frac{1}{\max\{\sqrt{u^2+v^2}\}} = \frac{\lambda}{b_{\mathrm{max}}};$$

this is not a surprising result since it simply states that the resolution of an interferometer is comparable to that of telescope whose diameter is equal to the maximum distance of the interferometer elements. The presence of a low value for $\sqrt{u^2+v^2}$ has, however, no a single telescope analogue. Since an upper limit for $\sqrt{u^2+v^2}$ meant that nothing can be said for physical structure with angular dimensions smaller than about λ/b_{max}, the existence of a lower limit implies that nothing can be said also for structure with angular dimensions larger than about λ/b_{min}; this is no a strict limit, instead an interferometer is progressively blinder to more extended sources.

An interferometer can, therefore, be seen as a filter on the spatial frequencies domain: it filters out both extremely large spatial frequency (limiting the resolution) and also extremely low spatial frequency (poor sensitivity to diffuse emission). In figure 4.1 an example of the effects, on the mere imaging, produced by low spatial frequency filtering out are illustrated. In this figure the right picture has been obtained filtering out a circle of 5 pixel in radius in the Fourier plane. It is important to see how the large Gaussian source is almost completely disappeared; more curious is the effect on the large disk source: since its border was very sharp (high-spatial-frequency variation) it resist in the filtered image while the “flat” zone disappeared. Negative pits

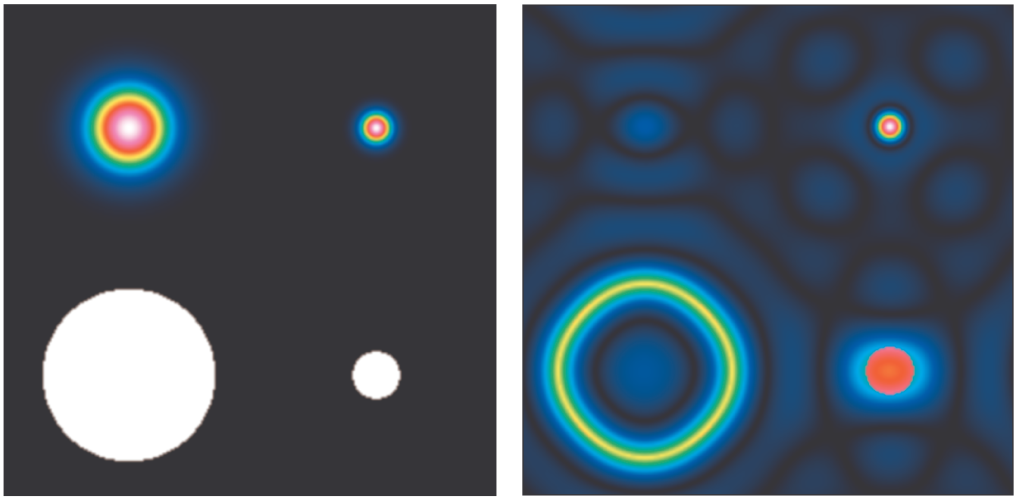

Figure 4.1: (left) simple sky model with two Gaussian sources (top) and two disk sources (bottom) of different dimensions. (right) The same image with low spatial frequency filtered out; it is possible to notice that the small sources are almost unaffected while large sources are dramatically transfigured.

become visible in the filtered image and they can be seen as warnings for lost diffuse emission.

Obviously the fact that missing low spatial frequency prevents the possibility of a satisfactory imaging, for interferometric data, is not simply an aesthetic problem. One of the major concern, as previously said, is that it is not possible to recover the entire flux density for an affected source; and more, any discussion about relative brightness is invalid since, as it is possible to notice in figure 4.1, this flux loss is not a simple brightness downscaling. An immediate evidence that we are not recovering all the flux density can be found using an "uvdist plot". This plot, in which the abscissa is $\sqrt{u^2+v^2}$, give us information about how much flux density we can recover at any $\sqrt{u^2+v^2}$ including angular scale up to its inverse; that is the ordinate value for $\sqrt{u^2+v^2}=0$ is the flux density obtainable including all angular scales (up to infinity), i.e. the total flux density recoverable from the image. In figure 4.2 we present an uvdist plot of a disc-like sky brightness model and the one obtained filtering out the low spatial frequency. It is possible to notice that the "real" flux density is much higher than the one recoverable from the filtered image; there is no way to know how much flux density you

ID	Right ascension	Declination	Flux density[a] at 5 GHz (mJy)	Dimensions[b] at 24 µm
3282	18:39:32.2	−05° 44′ 20″	140	100″
3310	18:41:19.9	−04° 56′ 06″	860	214″
3328	18:42:46.8	−03° 13′ 17″	130	58″
3558	19:55:02.4	+29° 17′ 20″	28	95″
3736	18:42:22.5	−05° 04′ 29″	15	109″
3910	18:11:28.9	−19° 25′ 29″	2300	248″
4485	17:23:04.4	−36° 18′ 20″	22	112″
4595	18:01:06.4	−22° 56′ 05″	46	74″
G79[c]	20:31:42.1	+40° 22′ 01″	560	210″

[a] Interferometric estimation.

[b] Intended as approximated mean angular diameter.

[c] Source from another project.

Table 4.1: selected sources for single-dish observations.

are loosing unless you know, a priori, the relative sky brightness, that is a perfect model of your source.

From the analysis of our EVLA data, we found that 8 sources seemed affected by this problem, since their maps at 5 GHz showed artifacts imputable to missing low spatial frequency or their dimensions and morphology at 24 µm, even if not strictly correlated to radio ones, suggested the possibility of an undetected diffuse emission. In table 4.1 all the suspected sources are listed along with their interferometrically estimated flux density and their dimensions at 24 µm (from MIPSGAL).

For these sources it was probable that we could only get a lower limit estimation of their flux density from the EVLA images. In fact the largest angular scale for EVLA at 5 GHz in configuration D is about 2′, while at 1.4 GHz is about 8′ in configuration C and 1′ in configuration B. Therefore, in order to recover all these bubbles flux density, also single-dish data were required. In particular, to fill in the gap in the *uv* plane, we needed a telescope with a diameter larger than the shortest baseline used in the EVLA observations (35 m). For this reason, we proposed observations of these 8 sources, both at 1.4 GHz and at 5 GHz, with the Green Bank Telescope.

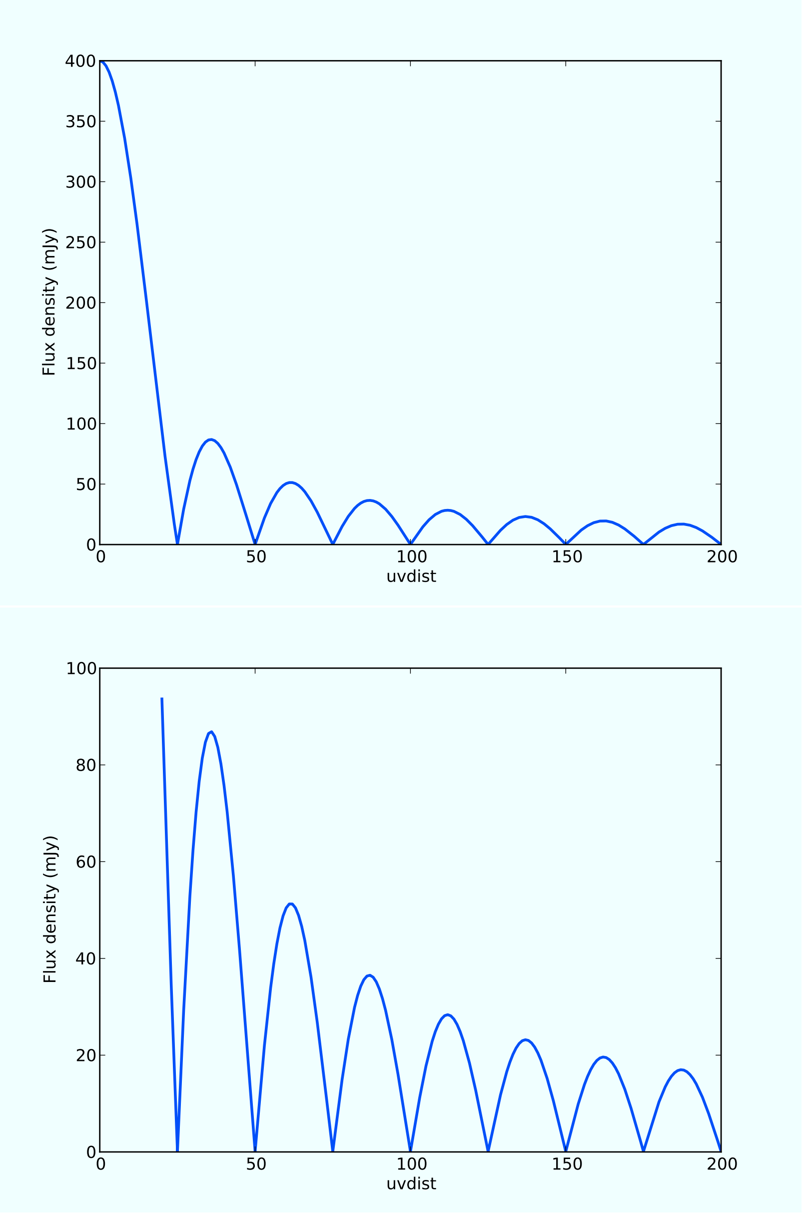

Figure 4.2: in the image above an uvdist plot of a disc-like sky brightness model is reported, with a supposed total flux density of 400 mJy. In the image below the low spatial frequency were filtered out and the total flux density recoverable is less than 100 mJy.

4.2 The Green Bank Telescope

The Green Bank Telescope (GBT hereafter) is the world largest fully steerable radio telescope, located at the National Radio Astronomy Observatory's site in Green Bank, West Virginia, with dimensions of the surface of 100 m × 110 m. The overall structure of the GBT is a wheel-and-track design that allows the telescope to view the entire sky above 5° elevation.

The GBT is of an unusual design. Unlike conventional telescopes, which have a series of supports in the middle of the surface, the GBT aperture is unblocked so that incoming radiation meets the surface directly. This increases the useful area of the telescope and eliminates reflection and diffraction that ordinarily complicate a telescope pattern of response. To accommodate this, an off-axis feed arm cradles the dish, projecting upward at one edge, and the telescope surface is asymmetrical. The primary mirror is actually a section of a conventional, rotationally symmetric 208-meter figure, beginning 4 m outward from the vertex of the hypothetical parent structure (figure 4.3). To maintain precise surface figures and pointing accuracy at high frequencies the telescope is equipped with a complex active surface. Finally, in order to reduce data contamination by RFI, the telescope is located in a radio-quiet zone.

4.3 Preparing the observation

Many of the sources we were proposing to observe with the GBT did not have a very high flux density; therefore, in order to obtain an appropriate signal-to-noise ratio for all the objects in our sample, we needed to achieve a sensitivity of a few millijanskys both at 1.4 GHz and at 5 GHz.

Both the receivers for band L and band C are collocated in the Gregorian focus of the GBT. For the band L we proposed to observe at a central frequency of 1475 MHz and with a bandwidth of 20 MHz; for the band C we chose a central frequency of 5100 MHz and a bandwidth of 80 MHz. As backend we chose to use the Digital Continuum Receiver since it was the only one suitable for our purpose.

Since one of our main goal was to combine the single-dish images with the interferometric ones, we needed to obtain also maps with GBT[1]. We then

---

[1] This was also necessary because some sources are so extended that they are resolved even with the GBT (at least in band C).

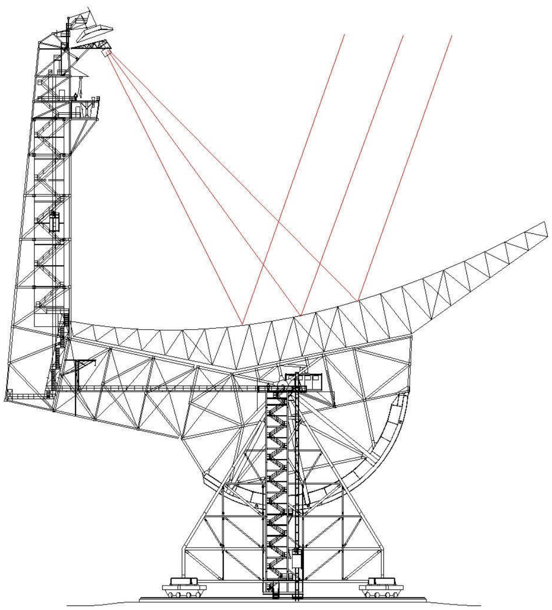

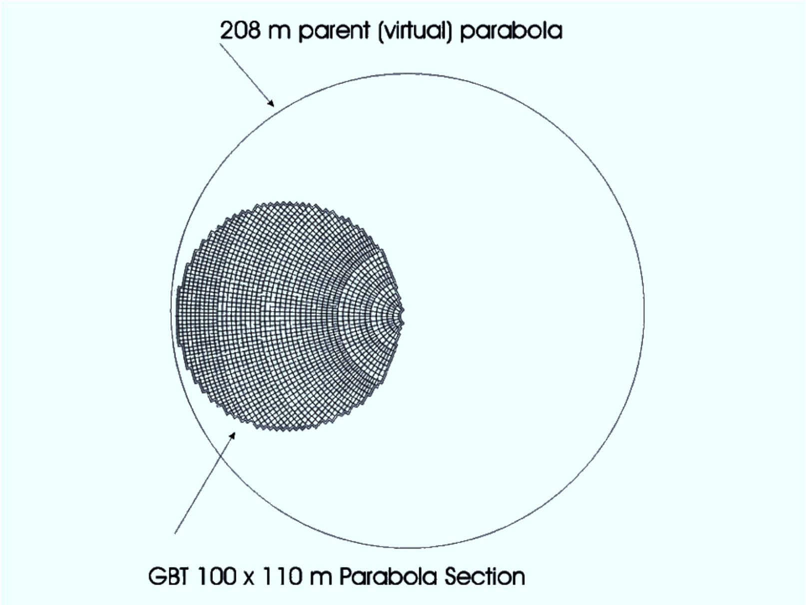

Figure 4.3: (top) a GBT side view; (bottom) the GBT primary mirror as seen from above, resulting in a small section of a larger virtual parabola [15].

	band L	band$C$
Scan direction	$150'$	$50'$
Orthogonal direction	$75'$	$25'$
Scan separation	$150''$	$50''$
Beam FWHM	$9'$	$2.6'$

Table 4.2: scan parameters.

proposed to map the fields with the "on-the-fly mapping" technique; in this mode, the telescope is slewed within a rectangular area of the sky while taking data [19]. In order to avoid background and instrumental fluctuations ("white error" mode) we proposed a slewing velocity high enough to execute scans of 0.3 s per beam (whose width was chosen to be 3 pixels); this allowed us to reach the desired sensitivity at 5 GHz (about 5 mJy/beam) and to observe at the confusion level ($\sim$ 20 mJy/beam) at 1.4 GHz. With this method we planned to obtain images slightly bigger than the EVLA field of view (about $9'$ at 5 GHz); so we set map dimensions of $25' \times 25'$ for the 5 GHz observations and $75' \times 75'$ for the 1.4 GHz ones.

It is known that mapping a sky region with a single-dish radio telescope produces an image in which each stripe of its along the scan direction has different values for error sources (for example the thermal noise) with respect to the other stripes, simply because each one of them was acquired at different times. We will discuss of this "stripe effect", which definitely is a systematic error, in section 4.6, where we will introduce a method aimed to remove the stripes. Since this method is applicable only if two image of the same field mapped along different directions are available, for each object we requested two orthogonal complete scans (`RaLongMap` and `DecLatMap` modes); to have also a better estimation of the background, we found more convenient to cross two rectangular maps with one side (the one along the scan direction) twice as long as the other (see figure 4.4 and table 4.3).

We found out that two sources, namely 3310 and 3736, were so close to each other that we could observe them at the same time; while band L map were large enough to contain both the source, we enlarged the relative band C map by a factor 1.5. The integration time for each map was about 1 h for band L and about 30 min for band C, with most of time spent to speed up and safely stop the telescope at each stripe.

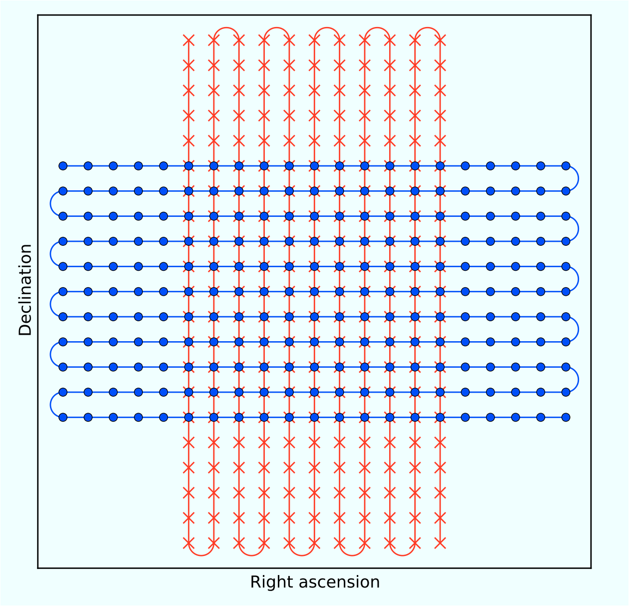

Figure 4.4: schematic example of the adopted map technique. Two rectangular maps are produced: one with the telescope slewing along the right ascension direction (blue lines) and the other along the orthogonal direction (red lines). During each scan, data are acquired at regular intervals (blue circle and red crosses). The entire map is acquired stripe by stripe.

4.4 Observations

All the observations were carry out on site; for our proposal we were awarded of 21.5 h of observing time, which was almost evenly parted between the two bands (table 4.4). Since no one of our sources was circumpolar and, worse, many of them had a low declination, an important study of the elevation of each source was done in order to observe at least at an elevation of 10° for both bands. The observing order was chosen in order to optimize the time we had with the minimum source elevations we required.
The observing operations are given to the telescope by means of a Python script describing what to observe and how. An example of a real script used during *L*-band observation is listed in section C.2. The observations followed the standard GBT procedure. Once an observing script has been created, it is possible to manage all the telescope operation via the Astronomer's

Day	Band	Time (h)
04–Jun–2011	L	4.5
05–Jun–2011	L/C	8.5
06–Jun–2011	C	8.5

Table 4.3: observations schedule.

Integrated Desktop (Astrid), a single, unified workspace that incorporates the suite of applications that can be used with the GBT. Astrid provides a single interface from which the observer can create, execute and monitor observations with the GBT. In particular, Astrid allows to create and execute scheduling blocks[2] (which perform astronomical observations) from observing scripts. It also provides a real time display of GBT data, an update on the status of the GBT and an area to edit observing scripts, which may be edited offline and saved before observing [20].
The observing operations can be summarized as follows. The first step is to select the requested receiver and back-end and set switches and frequencies; in fact, the routing of signals through the GBT system is controlled by many electronic switches which eliminate the need to physically change cables by hand. The GBT electronically configurable IF allows many, and more complicated, paths for the signals to co-exist at all times. This electronic control allows to configure the GBT IF in less then one minute, instead of the typical 30 minutes or more required for manual operations. This configuration step is executed via the function `Configure`, which needs as input a list[3] of configuration definitions; these include, for example, the selection of the receiver, the observation type, the back-end to use, the central frequency and the total bandwidth. As a next step, the function `Balance` is executed to change the various attenuator levels and gain levels in the GBT receivers, the IF and the back-ends so that each device is operating in its linear response regime. After this two preliminary steps the scanning sequence can start. First an utility scan is performed, thanks to the function `AutoPeakFocus`, to automatically peak and focus the antenna for the current location on the sky and with the current receiver, by means of the observation of a nearby calibration source; an example of this kind of calibration is shown in figure 4.5. Finally real

---

[2] A scheduling block consists of an observing script, where physical commands to the telescope are listed, and metadata containing informations such as the observer's name.

[3] A triple-quoted string indeed, see section C.2.

observing scans on target sources are executed with the commands, in our case, `RaLongMap` and `DecLatMap`, given as input the catalog of the desired objects.

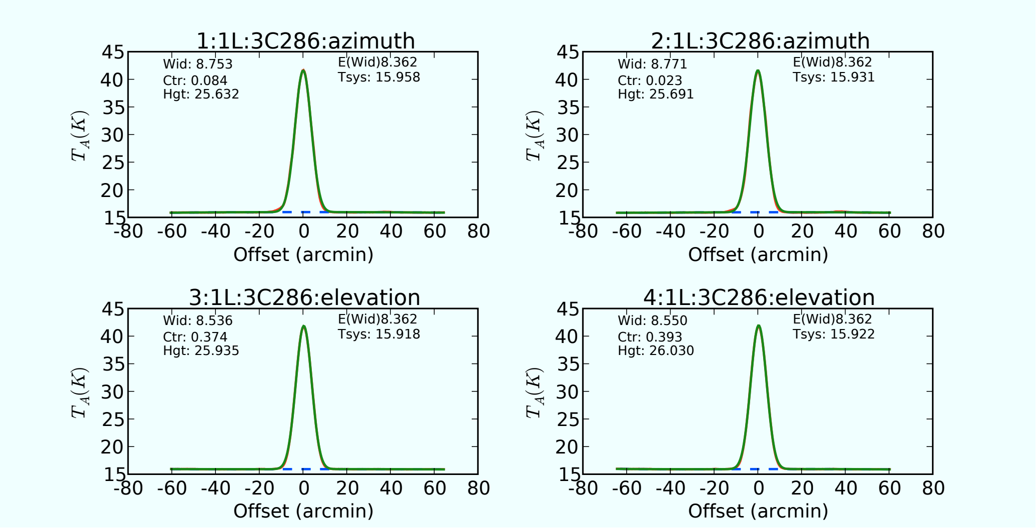

Figure 4.5: peak and focus on 3C286.

4.5 Data reduction

Unfortunately, no data reduction packages has yet been developed for GBT continuum observations. Therefore the entire data reduction process was performed using both simple routines provided by GBT staff and also by means of routines written by ourselves. The first step involves the use of the `sdfits` program, to convert the raw data from the telescope to SDFITS format, a particular FITS format explicitly designed to contain single-dish data.

Once produced a SDFITS file, it is processed by a routine which perform a flux calibration and write the FITS data in ASCII format. These data, along with the SDFITS header, are then used to build the map, as we are going to explain. For each source let us consider two orthogonal scans. For each one of them we have a series of flux density estimation, f_i, taken at the point (x_i, y_i); these points should the blue circles and red crosses of figure 4.4, they represent the points where the data were truly acquired. But, because of not avoidable pointing errors (due to many causes), they do not coincide with the theoretical points planned and instructed to the telescope with the observing script; much worse, since these errors are casual, our points (x_i, y_i) do not lie on a regular grid. So for each scan type the flux density estimation need to be reported on a regular grid through interpolation algorithm, and in particular via triangulation. Once regridded the data and created a regular grid for both the scan directions, the two sets of data are arithmetically averaged and written, with the appropriate header, to a standard FITS file.

4.6 Destriping

As previously discussed in section 4.3, and as for all single-dish maps, the images, produced by reduction routines, showed the so-called "stripe effect". This effect consists on prominent stripes, along the whole image, in the direction of the scan; the presence of these stripes is a systematic error introduced by instrumental noise shift and instability. Since this effect does not only scar the images but also prevent a current flux density calculation, a "destriping" procedure was needed.

There are few destriping algorithms available, one of them is described by Emerson and Gräve (1988) [21]. That algorithm can be described as follows: let us suppose to have a map obtained scanning the sky in a particular direction, let us say the horizontal direction; the image obtained would show horizontal stripes. Let us now calculate the Fourier transform of this image, since all stripes can be seen as (almost) zero-frequency oscillating signals in the scan direction, in the transformed map these error-affected regions will be confined in a single stripe passing through the center of the map and orthogonal to the scan direction (i.e. vertical). The Emerson and Gräve's algorithm averages two orthogonally-scanned Fourier-transformed images downweighting the affected regions; the inverse transformation of this averaged image should produce a "stripe-free" sky map.

The most problematic issue of this algorithm is that the central pixel of the transformed images is heavily downweighted; since the central pixel represents the zero-frequency oscillations on both directions, it contains information only of the total flux of the scanned sky. Not only it is therefore not affected by stripe effects but it is also essential for flux recovering from interferometric images, which was our purpose.

An alternative algorithm was then implemented. Let us suppose again to have the two orthogonally-scanned Fourier-transformed images; for both images the central pixel should not suffer of stripe contamination, the only possible difference in value should be a cumulative flux shift and since is not possible to determine which of the two images is more correct it is safe to rescale both for the mean value. As previously said, the transformed image of the horizontally-scanned map is contaminated in a single confined vertical stripe passing through the center; the very same region in the orthogonal transformed image should not be affected by stripe effect at all, we can then simply substitute the entire contaminated stripe with the unaffected one, and do the same for the orthogonal direction. We can now average the two transformed images and perform an inverse transformation to obtain a destriped sky map. In figure 4.6 an example of destriping process. If for a source more than one pair of orthogonal scans existed they have been first destriped and then averaged. The complete algorithm is listed in appendix section C.3.

4.7 Combining single-dish and interferometric data

As discussed at the beginning of the chapter, our main goal was to combine interferometric data, affected by flux density loss, with single-dish images, obtained with the GBT. This task proved much more complicated than we could have expected. In fact, despite the presence of several articles regarding the flux-loss problem and the combination of interferometric and single-dish data, only a few reliable implementation of the theoretical algorithm found in literature were available. We finally used the CASA task `feather` after its important improvement in version 3.4.

The theory behind the combination we aimed to perform is rather simple; definitively it is based on the fact that a single-dish telescope measures not only a single spatial frequency, but a whole range of continuous spatial frequencies up to a maximum one, which corresponds to the baseline equal to the diameter of the dish, D_s. Hence, a single-dish telescope behaves as an interferometer having a continuous range of baselines, from zero up to D_s [22].

So, let us suppose to have a single-dish image of a certain source. If we calculate the Fourier transform of this image we obtain a two-variable com-

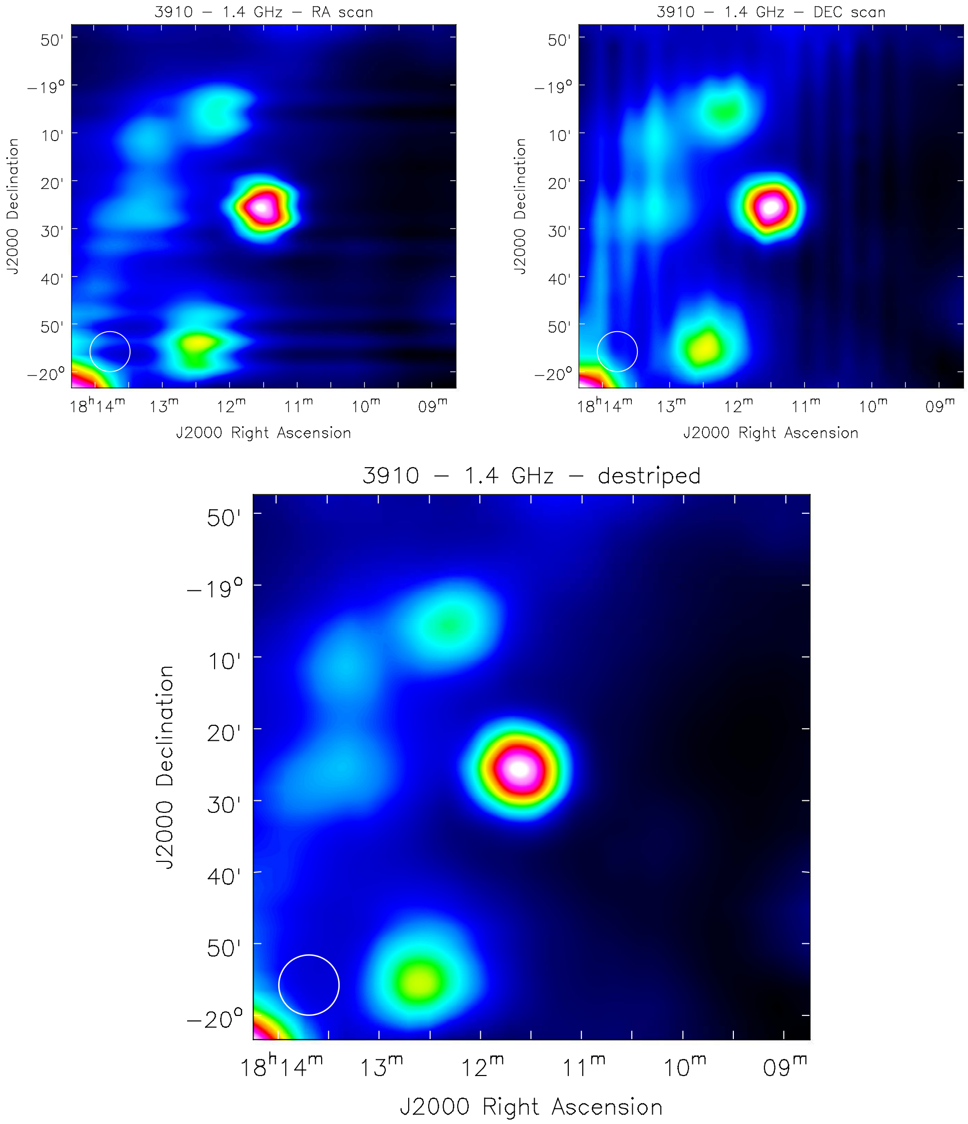

Figure 4.6: (top) two map of the same source acquired with orthogonal scans; it is easy to notice the prominent stripes along the scan direction. (bottom) After the destriping process the stripes are nearly disappeared.

plex function that can be interpreted as the “intensity” of each bidimensional spatial frequency, up to a maximum frequency related to the smallest structure which can be imaged, and therefore with the resolution of the telescope. Let us suppose now to observe the same source with an interferometer[4]; the instrument will directly observe the source in the Fourier domain, measuring the visibility function, but this measurement is not able to fill the entire Fourier plane, as discussed above, and in particular it will not map the inner region of this plane up to a spatial frequency corresponding to the shortest baseline. This “hole” is usually filled during the imaging process through some kind of interpolation, which, however, cannot provide reliable values for the missing visibility[5].

If the single-dish telescope diameter is greater than the shortest baseline of the interferometer, then there would be an annular region in the Fourier plane inside which we have both interferometric and single-dish data for the source (figure 4.7), which is to say that the single-dish and the interferometer are able to measure emission from common spatial frequency. The trick now is to use this overlapping region in the Fourier plane to cross-calibrate the data[6] and make them as coincident as possible in this region; this operation is known as “feathering”. After this calibration we can merge the two data sets to obtain a single visibility function sampled from the zero baseline to the longest interferometer baseline. An inverse transformation of the visibility obtained in this way results in an image with the same resolution of the original interferometric image, but also with well determined low spatial frequencies; from this image a total flux density recovery is possible.

In figure 4.8 an example of combination is reported. The bubble 3910 is very extended, more than $4'$ against a reasonable largest angular scale at 5 GHz of about $2'$, so it is very affected by flux density loss. In the first figure, the EVLA map for this object is represented, it is possible to notice how only the sharp emission at the borders of the bubble and the central object are imaged. Combining this image with the GBT one it is possible to obtain the figure below in which also the diffuse emission inside the outer shell is clearly visible.

---

[4] We are supposing that the two observations are carried out at the same wavelength.

[5] More precisely it must be treated as an extrapolation, hence the unreliability.

[6] Indeed, the data are supposed to be already best calibrated before any combination is attempted, anyway calibration errors are present and the two data sets may not (and they do not) coincide in the annular common region. However, the closer the data sets are in the common region the better results will be obtained by the algorithm.

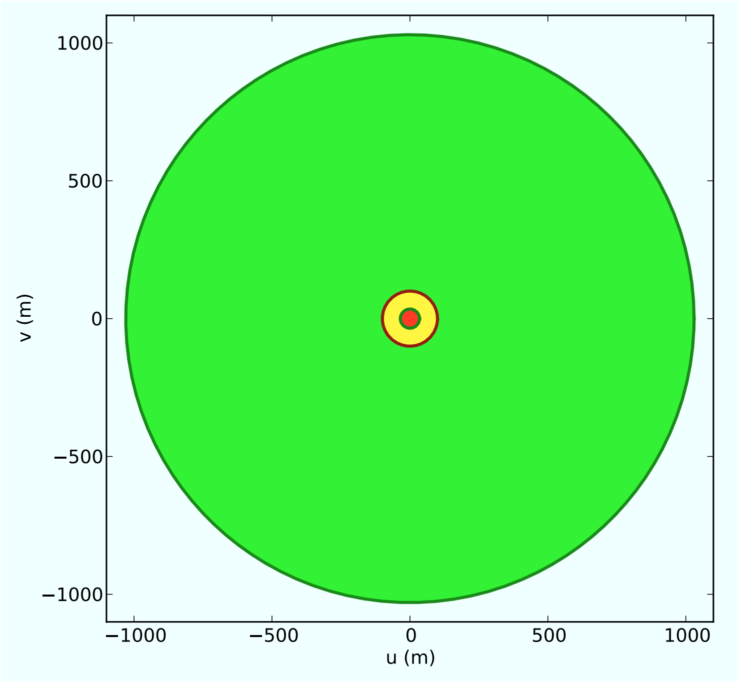

Figure 4.7: *uv* plane coverage for VLA (configuration D) and GBT. The VLA coverage area is delimited by the two green circumferences and it extends radially from 35 m to 1030 m. The GBT coverage area is delimited by the red circumference and it extends radially from 0 m to 100 m. The green region is therefore the *uv* plane area covered only by VLA data, the red region only by GBT data and the annular yellow region is covered by both the instruments.

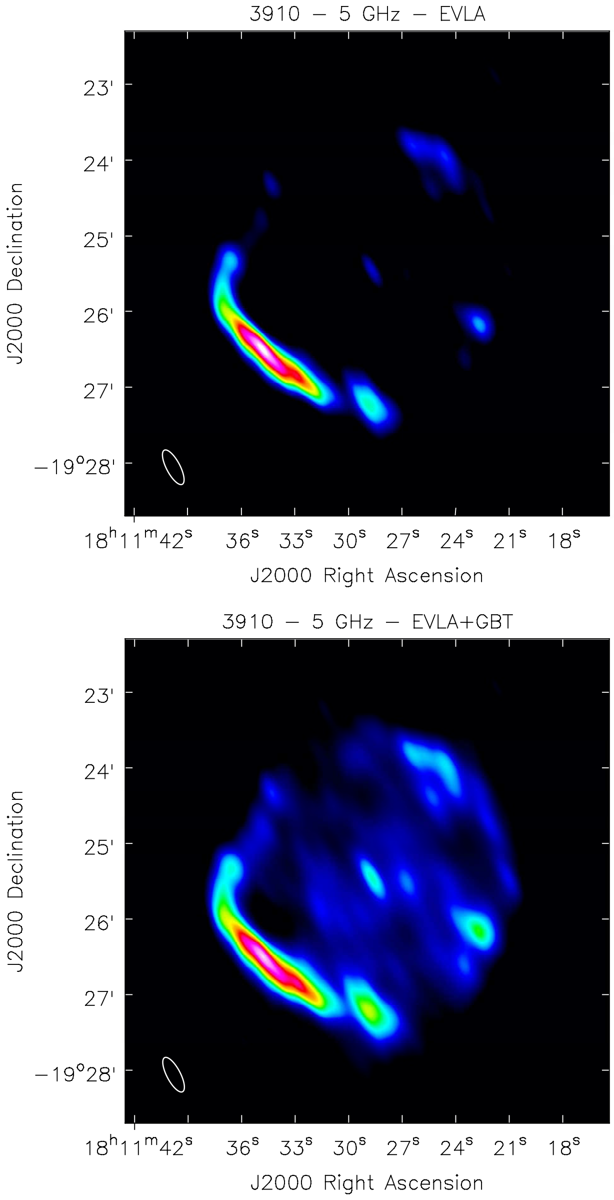

Figure 4.8: comparison between the interferometric image of the bubble 3910 (top) and its combination with GBT data (bottom).

Chapter 5

Searching for OH masers

It is known that in different classes of stars with circumstellar envelopes, conditions for a maser emission of different molecules may occur. In this chapter it will be discussed how we proposed and carry out different spectral-line observations with the Medicina Telescope and with the GBT in order to detect masers produced by the OH molecule. We will eventually show some interesting results.

5.1 Maser emitting sources

Our attention in the last three chapters has been focused on a subset of the MIPSGAL bubbles, that we called the "radio sample", characterized by continuum radio emission. This kind of emission arises from electrons undergoing free-free transitions, and so it can occur only in ionized media. But among the kinds of evolved star, it is possible to find objects which are not hot enough to ionize their circumstellar envelope; these stars, such as red giants, AGB or post-AGB, have therefore a neutral circumstellar envelope and they do not show any continuum radio emission. However, during the late stage of the stellar evolution, characterized by heavy mass loss, conditions for maser lines of different species are present in the circumstellar medium. Maser occurrences have been reported not only around AGB or post-AGB stars but also in the outer layers of some supernova remnants and in some star forming regions[1].
The RG, AGB and post-AGB stars (which represent the last stages of late-

---

[1] In these two cases also continuum radio emission is expected.

type stars life, and will be discussed in more detail in appendix section A.2) are characterized by an envelope composed of gas and dust. In fact, these stars lose mass from the extremely expanded outer layer of their atmosphere as soon as they get cool enough for dust grains to form. Absorbing stellar radiation, the warmed dust re-irradiates in the mid- and far-infrared giving rise to the shell that we observe as a bubble at those wavelengths [23]. In these envelopes masers of different molecules, mainly SiO, H_2O and OH, have been detected. The presence of the different maser lines in these stars is related to the evolutionary phase of the envelope and therefore they allow to reconstruct a complete chronological sequence of their evolution [24][25]. The first stage is characterized by the SiO masers which need a temperature of at least about 1700 K to form, and therefore they are usually located very close to the stellar atmosphere. Then H_2O masers (collisionally excited and at least at $T \sim 650\,\mathrm{K}$) arise from further regions located between about 10 AU and 700 AU away from the star. At the end also OH maser lines at 1612 MHz, at 1665 MHz and at 1667 MHz (the last two usually identified as the "main lines") appear, originating in the middle and in the external part of the circumstellar envelope from 500 AU up to 10^4 AU. After these stages, as the mass loss ends and the ionization begins, the main lines start to get weaker and weaker till they totally disappear, and so happens also to H_2O lines and finally to SiO lines, with the star entering the proto-PN phase. Subsequently the circumstellar envelope expands permitting the main lines to emerge again; finally all the OH lines strongly weaken as the star begins to enter the PN phase.

The OH line at 1720 MHz is instead peculiar to both star forming regions (also associated to main lines) and supernova remnants (alone) [26]. This maser line is produced by OH collisionally excited and, in the case of the SNRs, it is thought to originate from the interaction between the SNR ejecta and molecular clouds. It has been observed that at least 10% of galactic SNRs show this OH maser line.

In summary, the presence or absence of any of the OH maser lines and their intensity ratio can also help us to classify the bubbles, indicating that we are observing an AGB or post-AGB star (and in a well-determined evolutive stadium), or that we could be observing a supernova remnants or a star forming region (distinguishable through the continuum spectral index).

5.2 Observations at Medicina

As a pilot project, we proposed observations to search for OH maser at 1612, 1665 and 1667 MHz in a subsample of unidentified bubbles, not detected at radio wavelengths, with the Medicina radio telescope.
From the original MIPSGAL sample, which counts in 428 objects, we then selected only the sources visible from Medicina ($\delta > -30°$ to have an elevation of at least 10°) and without any identification in the Simbad database, getting 166 bubbles. In order to decrease the number of sources to be observed, we further selected the objects with galactic latitude $b > 0$. The final subsample included the 102 sources listed in table 5.1, with the "Telescope" column marked with "M"; all the bubbles observed at Medicina were observed again with the GBT.

ID	RA	DEC	Telescope
3148	18:07:05.2	−20° 15′ 16″	M+G
3157	18:08:11.6	−18° 01′ 01″	M+G
3173	18:14:17.1	−17° 02′ 16″	M+G
3176	18:13:32.5	−16° 44′ 36″	M+G
3179	18:15:58.6	−15° 02′ 36″	M+G
3188	18:19:45.1	−14° 48′ 02″	M+G
3190	18:17:15.4	−14° 53′ 10″	M+G
3192	18:18:42.2	−14° 54′ 09″	M+G
3193	18:18:51.7	−14° 45′ 10″	M+G
3194	18:19:29.9	−13° 17′ 56″	M+G
3198	18:22:20.6	−13° 14′ 08″	M+G
3223	18:26:22.1	−10° 01′ 15″	M+G
3232	18:28:41.5	−10° 27′ 06″	M+G
3233	18:25:41.6	−10° 15′ 46″	M+G
3234	18:32:17.3	−09° 16′ 13″	G
3257	18:29:09.4	−08° 46′ 01″	M+G
3259	18:33:43.3	−08° 23′ 35″	M+G
3282	18:39:32.2	−05° 44′ 20″	G
3309	18:39:37.4	−04° 32′ 56″	M+G
3310	18:41:19.9	−04° 56′ 06″	G
3312	18:42:06.3	−03° 48′ 23″	M+G
3313	18:42:08.2	−03° 51′ 03″	M+G
3333	18:41:16.0	−03° 24′ 11″	M+G

3337	18:42:44.6	−03° 03′ 15″	M+G
3346	18:43:49.7	−01° 42′ 07″	M+G
3347	18:45:12.0	−01° 30′ 32″	M+G
3348	18:44:56.9	00° 58′ 54″	M+G
3358	18:50:04.0	00° 44′ 32″	M+G
3362	18:50:18.3	00° 03′ 48″	M+G
3367	18:50:04.3	00° 18′ 45″	M+G
3384	18:53:56.8	01° 53′ 08″	M+G
3423	19:01:56.3	06° 08′ 46″	M+G
3424	19:00:19.2	06° 22′ 18″	M+G
3458	19:10:04.3	10° 43′ 28″	M+G
3488	19:22:30.4	15° 48′ 56″	M+G
3513	19:30:04.6	19° 36′ 31″	M+G
3573	19:44:43.0	23° 11′ 34″	G
3575	19:44:26.3	23° 10′ 06″	G
3604	19:27:06.7	15° 48′ 35″	G
3619	19:17:59.4	12° 13′ 55″	G
3626	19:18:12.7	11° 12′ 26″	G
3657	19:04:20.9	06° 00′ 00″	G
3662	19:04:33.4	04° 50′ 58″	G
3671	19:03:29.4	04° 07′ 20″	G
3681	18:57:33.1	02° 19′ 45″	G
3693	18:53:05.7	00° 11′ 36″	G
3698	18:54:09.1	−00° 21′ 13″	G
3700	18:52:55.4	−00° 50′ 37″	G
3701	18:51:00.3	−00° 32′ 30″	G
3704	18:51:02.1	−00° 58′ 21″	G
3707	18:49:27.3	−01° 04′ 20″	G
3724	18:46:35.9	−03° 20′ 43″	G
3779	18:37:02.9	−08° 53′ 14″	G
3809	18:31:58.8	−10° 27′ 43″	G
3820	18:31:57.1	−11° 32′ 46″	G
3857	18:23:34.1	−15° 25′ 07″	G
3882	18:17:48.5	−17° 48′ 12″	G
3899	18:13:31.1	−18° 56′ 42″	G
3910	18:11:28.9	−19° 25′ 29″	G
3915	18:11:30.8	−19° 59′ 41″	G
3922	18:10:13.7	−20° 35′ 33″	G

3925	18:07:10.1	−20° 47′ 28″	G
4407	17:56:36.2	−28° 57′ 18″	G
4410	17:59:20.1	−27° 55′ 14″	G
4416	18:01:36.1	−26° 55′ 40″	G
4417	18:03:02.8	−27° 50′ 17″	G
4423	18:09:02.7	−25° 32′ 52″	G
4426	18:09:13.3	−24° 47′ 36″	G
4427	18:10:32.9	−24° 00′ 27″	G
4428	18:11:22.5	−24° 26′ 24″	G
4443	17:48:46.6	−29° 53′ 34″	G
4446	17:50:10.3	−29° 21′ 42″	G
4451	17:55:44.8	−28° 32′ 59″	G
4454	17:53:53.5	−28° 32′ 05″	G
4455	17:52:37.3	−28° 27′ 53″	G
4463	17:54:34.4	−27° 42′ 51″	G
4464	17:54:46.3	−27° 37′ 56″	G
4465	17:57:03.9	−27° 51′ 30″	G
4466	17:53:39.5	−27° 52′ 04″	G
4468	17:58:16.7	−27° 01′ 56″	G
4472	18:01:06.2	−26° 39′ 21″	G
4474	18:09:01.3	−23° 23′ 08″	G
4475	18:05:14.8	−23° 47′ 09″	G
4477	18:06:32.4	−24° 05′ 14″	G
4478	18:10:50.0	−22° 30′ 21″	G
4483	18:09:20.7	−22° 05′ 50″	G
4505	17:46:13.7	−29° 41′ 09″	G
4506	17:47:47.6	−29° 32′ 33″	G
4507	17:48:01.8	−29° 35′ 11″	G
4508	17:48:23.2	−29° 44′ 23″	G
4509	17:47:56.1	−29° 44′ 08″	G
4511	17:51:00.6	−28° 48′ 10″	G
4514	17:54:28.2	−27° 27′ 15″	G
4515	17:51:54.6	−27° 36′ 11″	G
4520	17:58:48.0	−25° 44′ 41″	G
4522	17:55:43.1	−25° 55′ 51″	G
4523	17:56:38.7	−26° 08′ 15″	G
4525	17:57:14.3	−24° 29′ 05″	M+G
4526	18:02:33.7	−24° 02′ 13″	G

4527	18:02:22.3	−22° 38′ 00″	G
4530	18:00:35.2	−23° 16′ 18″	G
4567	17:39:17.0	−29° 28′ 59″	M+G
4572	17:39:01.0	−29° 45′ 00″	M+G
4573	17:45:44.7	−28° 27′ 04″	M+G
4574	17:43:40.7	−28° 11′ 06″	M+G
4581	17:45:50.4	−27° 28′ 44″	M+G
4583	17:49:32.1	−27° 07′ 32″	M+G
4584	17:49:04.9	−27° 24′ 47″	M+G
4586	17:48:43.4	−26° 17′ 04″	M+G
4589	17:56:13.4	−24° 13′ 13″	M+G
4590	17:53:26.0	−24° 26′ 49″	M+G
4591	17:59:43.8	−23° 19′ 36″	M+G
4595	18:01:06.4	−22° 56′ 05″	M+G
4599	18:00:29.3	−21° 46′ 23″	M+G
4600	17:59:47.8	−21° 33′ 13″	M+G
4607	18:04:36.3	−21° 05′ 26″	M+G
4639	17:36:59.4	−29° 44′ 07″	M+G
4640	17:35:43.6	−29° 38′ 22″	M+G
4642	17:36:50.8	−29° 57′ 53″	M+G
4649	17:37:52.7	−29° 13′ 13″	M+G
4650	17:36:32.4	−29° 02′ 42″	M+G
4651	17:35:36.5	−28° 47′ 42″	M+G
4654	17:40:01.6	−28° 33′ 32″	M+G
4656	17:40:48.6	−27° 00′ 27″	M+G
4657	17:42:28.1	−27° 13′ 34″	M+G
4660	17:39:32.3	−27° 18′ 11″	M+G
4661	17:41:25.2	−27° 34′ 40″	M+G
4662	17:43:13.7	−27° 39′ 56″	M+G
4663	17:43:32.1	−25° 53′ 33″	M+G
4668	17:49:20.8	−25° 34′ 10″	M+G
4670	17:48:39.3	−25° 15′ 06″	M+G
4671	17:46:42.8	−24° 59′ 15″	M+G
4672	17:46:08.1	−25° 11′ 17″	M+G
4673	17:46:31.0	−25° 26′ 53″	M+G
4678	17:50:37.4	−24° 50′ 34″	M+G
4680	17:50:30.6	−23° 38′ 24″	M+G
4681	17:49:54.9	−23° 54′ 35″	M+G

4682	17:52:01.8	−24° 13′ 21″	M+G
4684	17:53:20.6	−22° 24′ 10″	M+G
4687	17:54:25.7	−21° 51′ 16″	M+G
4690	17:56:42.9	−22° 31′ 42″	M+G
4691	17:59:51.1	−21° 20′ 39″	M+G
4701	17:32:01.0	−28° 52′ 04″	M+G
4702	17:29:44.7	−29° 06′ 57″	M+G
4703	17:31:07.9	−29° 34′ 10″	M+G
4705	17:34:45.8	−28° 20′ 22″	M+G
4706	17:32:26.3	−28° 38′ 15″	M+G
4707	17:32:55.9	−28° 42′ 50″	M+G
4708	17:32:24.1	−28° 48′ 02″	M+G
4714	17:37:37.7	−26° 35′ 01″	M+G
4716	17:39:05.1	−26° 52′ 39″	M+G
4717	17:39:13.9	−26° 53′ 39″	M+G
4718	17:36:14.2	−26° 42′ 52″	M+G
4719	17:36:38.4	−26° 51′ 39″	M+G
4720	17:43:00.1	−25° 35′ 49″	M+G
4721	17:42:07.5	−26° 02′ 12″	M+G
4722	17:42:20.6	−26° 04′ 38″	M+G
4723	17:41:23.5	−26° 14′ 50″	M+G
4726	17:43:18.5	−25° 11′ 57″	M+G
4727	17:46:03.2	−24° 07′ 04″	M+G
4728	17:46:18.9	−24° 15′ 30″	M+G
4729	17:44:20.1	−24° 17′ 00″	M+G
4732	17:50:28.1	−22° 39′ 57″	M+G
4733	17:49:04.3	−22° 29′ 50″	M+G
4735	17:54:53.7	−21° 19′ 41″	M+G
4737	17:54:55.1	−21° 13′ 41″	M+G
4739	17:56:48.7	−20° 11′ 34″	M+G
4740	17:49:32.8	−22° 25′ 53″	M+G
4741	17:44:11.0	−24° 22′ 35″	M+G

Table 5.1: bubbles observed for OH masers (“M” observed at Medicina, “G” observed with the GBT).

The observations were carried out on July 2011, for a total time of 56 h distributed in eight nights. As front-end we used the 1.6-GHz receiver placed in the primary focus; as back-end we chose the ARCOS spectrometer in single polarization.
We acquired two spectra simultaneously with a total bandwidth per each spectral window of 4 MHz with 512 channels. The first spectral window was centered at about 1612 MHz, while the second was centered at about 1666 MHz in order to observe both 1665 and 1667 MHz lines; the effective band center was automatically correct to take into account the approximated average radial velocity of the objects, estimated by ourselves through the galactic longitude of each source.
To reduce as much as possible the parasite effects due to atmospheric fluctuations, the observations were carried out using an on-off strategy in position-switching mode, that is each scan on source was followed by a scan off source, set 1.4° apart in right ascension and supposed to point to an empty sky region. The integration time we chose for each scan (both on and off) was 200 s and every source was observed at least three times.

5.3 First results

We knew that observations at 1.6 GHz could, very likely, suffer of interferences contamination at least in some portions of the spectrum; furthermore, the location of the Medicina telescope, close to several urban areas, increases this phenomenon and makes it impossible to limit it. For this reason we asked the Medicina staff about the feasibility of our project before the proposal submission. Their measurements *in situ* seemed to indicate that our spectral windows could be clean enough.
The data output format was the standard “toolbox” of the Max Planck Institut für Radioastronomie in Bonn. These raw data were subsequently converted to the CLASS format in order to be reduced and analyzed by means of GILDAS package maintained by the Institut de Radioastronomie Millimétrique in Grenoble.
Anyway, a preliminary view of the acquired spectra showed that they were heavily affected by RFI. In particular, around 1666 MHz there were so much interfereces that no useful information could have been extracted so far. At 1612 MHz the situation was almost the same but with a probable detection of an emission feature toward the bubble 4586.

Up to now, no useful spectra has yet been produced.

5.4 Observations at the GBT

The great corruption of the data acquired at Medicina, forces us to ask time for an other telescope. Since our greatest obstacle was the presence of RFI in our spectra, we turned our attention to GBT, which we knew to be sited in a radio-quiet zone. We then proposed to observe 169 bubbles, marked with "G" in table 5.1, with the GBT in spectral line mode. The sample included, by choice, all the bubbles previously observed in Medicina, with other 77 bubbles not observed, some of which showing also continuum emission (such as 3282 or 3333). Along with the bubbles, also sources with knwon maser emission have been observed, like VX Sagittarii, OH26.5 or W51M.

As front-end we chose the band-L receiver sited in the Gregorian focus, which covers a frequency range between 1.15 GHz and 1.73 GHz; as back-end we chose the GBT Spectrometer. In particular we observed in four spectral windows, centered at 1612.321 MHz, 1665.402 MHz, 1667.359 MHz and 1720.530 MHz. We selected a total bandwidth of 12.5 MHz and a dual circular polarization, with the spectrometer performing an autocorrelation (RR and LL). We chose to observe in frequency-switching mode with a separation between the two acquisition equals to 6.25 MHz (half bandwidth). The integration time was set to be 5 seconds with a scan time per source of 5 minutes.

The observations were carried out in remote on January, February and March 2012, for a total amount of 22 hours.

5.5 Preliminary analysis and data reduction

A preliminary analysis of the GBT spectra showed that some RFI were present, though much less than at Medicina. Anyway their presence prevented a data calibration from frequency-switched acquisition. Indeed, if an RFI affected the "off" spectrum, than it would affect also the calibrated one. The data reduction, therefore, was carried out using both pre-existing package and our routines.

The base package was GBTIDL maintained by the NRAO staff at GBT; it indeed does a basic calibration of the spectra but does not supply all the

necessary instruments to deal with RFI-affected data. However the first step is to load the raw data, which are in the usual format SDFITS. We set, as a preliminary operation, that the abscissa of the output spectra must be in LSR velocity (with relativistic frequency-to-velocity conversion).
Each scan is characterized by sixteen subset of data, given by the four spectral windows, the two polarization correlation (RR and LL) and by an "on-scan" and an "off-scan" as defined in the previous chapter. Given a spectral window, a polarization and a scan mode ("on" or "off"), for each source we have 60 different acquisitions, which we name "sub-scans". We subsequently take all the sub-scans (always for a given spectral window, polarization and scan mode) and we plot them stacked up one on another to form a bidimensional image. This image gives a comprehensive look of the data variation with time, allowing us to flag out corrupted acquisitions; in figure 5.1 an example of how these bidimensional images look like. At the end of this editing process, all the sub-scans are averaged. For each spectral window, the four edited spectra are averaged to obtain a single spectrum, with reduced time-located corruptions.
The spectra we obtain with this procedure need to be corrected for bandpass gain variations and need to be normalized by continuum subtraction. Since no reliable bandpass calibration was possible using the observed source, we performed both the operation subtracting from the spectrum a smooth appropriate curve. We tried to possible determination of this curve. A first solution was to fit a seventh-degree polynomial, selecting eight points of the line-free part of the spectrum; the second solution was to fit a twentieth-degree Chebyshev polynomial series[2] excluding only the few channels where lines were present, maybe resulting in a more robust fit. An example of fitting is shown in figure 5.2.
As an example, in figure 5.3 we report the four reduced spectra of the well-known maser source OH26.5.

5.6 Results with GBT

Following for all the observed source the procedure described in the previous section, we found that 13 sources (plus very likely other 9), over the 29

---

[2] Even if, in principle, this should not be different from a simple twentieth-degree polynomial fitting, using Chebyshev polynomials turned out to be more computationally stable, allowing to fit hundreds of points.

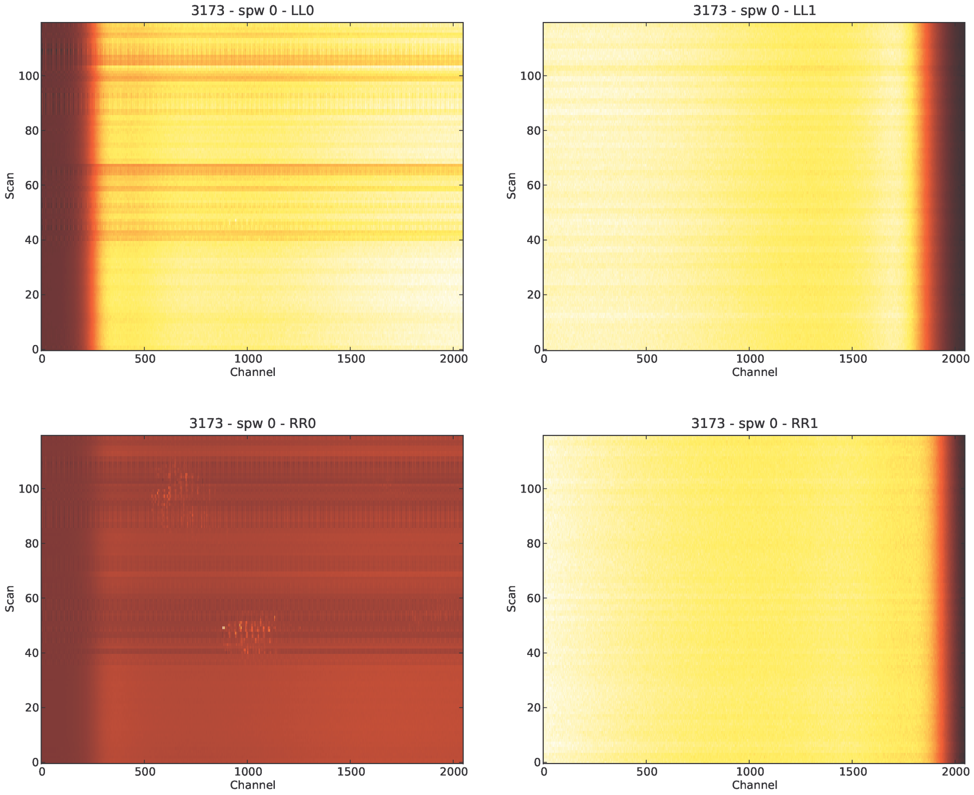

Figure 5.1: scans for bubble 3173 in the spectral window around 1612 MHz. The two spectra on the right are quite clean, while the two spectra on the left show different kinds of corruption. In particular, the top one show moderate interferences affecting all the channels, recognizable by regular vertical stripes that extend for few adjacent scans (time-located); the bottom one show also impressive interferences, visible as very brigth points (spikes).

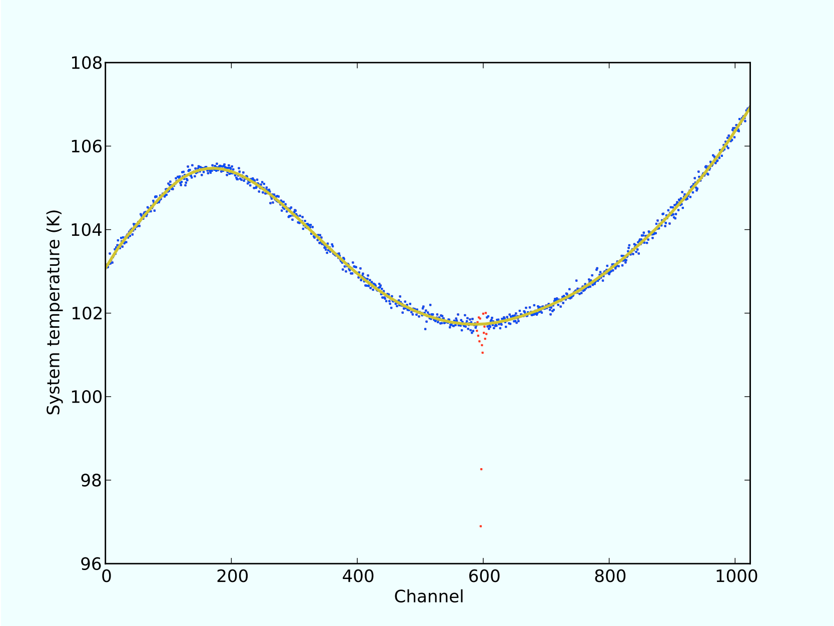

Figure 5.2: Example of baseline fitting, in a GBT spectrum, using a Chebyshev polynomial series up to the twentieth degree (yellow curve). The red points are the only excluded from the fit.

sources reduced so far, showed emission lines at least in one band, while the majority of the spectra shows prominent absorption lines. The profile features turned out to be greatly varying in the different sources, and this can be due both to an intrinsic complex structure of the source or to a multiple sources observations. At least two sources, 3179 and 3188, show a maser emission with a prominent U-shape, indicating its origin from an expanding shell.
In the following table a synthetic description of each spectrum is reported, "A" means prominent absorption lines, "M" clear masers from shells (U-shaped lines), "E" other emission features, "–" no clear lines detected, "?" means uncertain detections. Where multiple features were present, a multirow entry is listed with a progressive italic letter in the second column (if only one a "–" is written), increasing with increasing velocities.

ID	Feature	1612 MHz	1665 MHz	1667 MHz	1720 MHz

3148	–	E+A?	A	A	A?+E?
3157	–	–	–	–	–
3173	–	–	A	A	E?
3176	*A*	A	–	A?+E?	E?
3176	*B*	A	A	A	E?
3179	*A*	M	–	–	–
3179	*B*	A?	E?	–	–
3179	*C*	M	–	–	–
3188	*A*	M+A	–	E+A	–
3188	*B*	A	–	–	E
3190	*A*	M?	–	–	–
3190	*B*	–	–	–	E?
3309	–	E?	–	A?	–
3312	*A*	A?	A?	A?	A?+E?
3312	*B*	A	A	A	A?+E?
3337	*A*	–	A+E?	A+E?	E+A?
3337	*B*	E	–	–	–
3779	–	–	E	E	–
3882	–	–	E	E	–
4423	–	–	–	–	
4426	–	–	–	–	
4474	–	A?	A	–	–
4475	*A*	M?	–	–	–
4475	*B*	A?	E	–	–
4477	–	–	–	–	–
4478	–	A?	–	–	E
4483	–	M?+A?	E?+A	A	A
4705	–	–	–	–	
4706	–	–	–	–	

Table 5.2: spectral features.

In the following figures, we report some interesting spectra, with few others, presented along with a brief discussion on the relative bubble, in chapter 7; all the other reduced spectra are reported in appendix D. The dotted lines represent the 1σ level (red), the 3σ level (yellow) and the 5σ level (green).

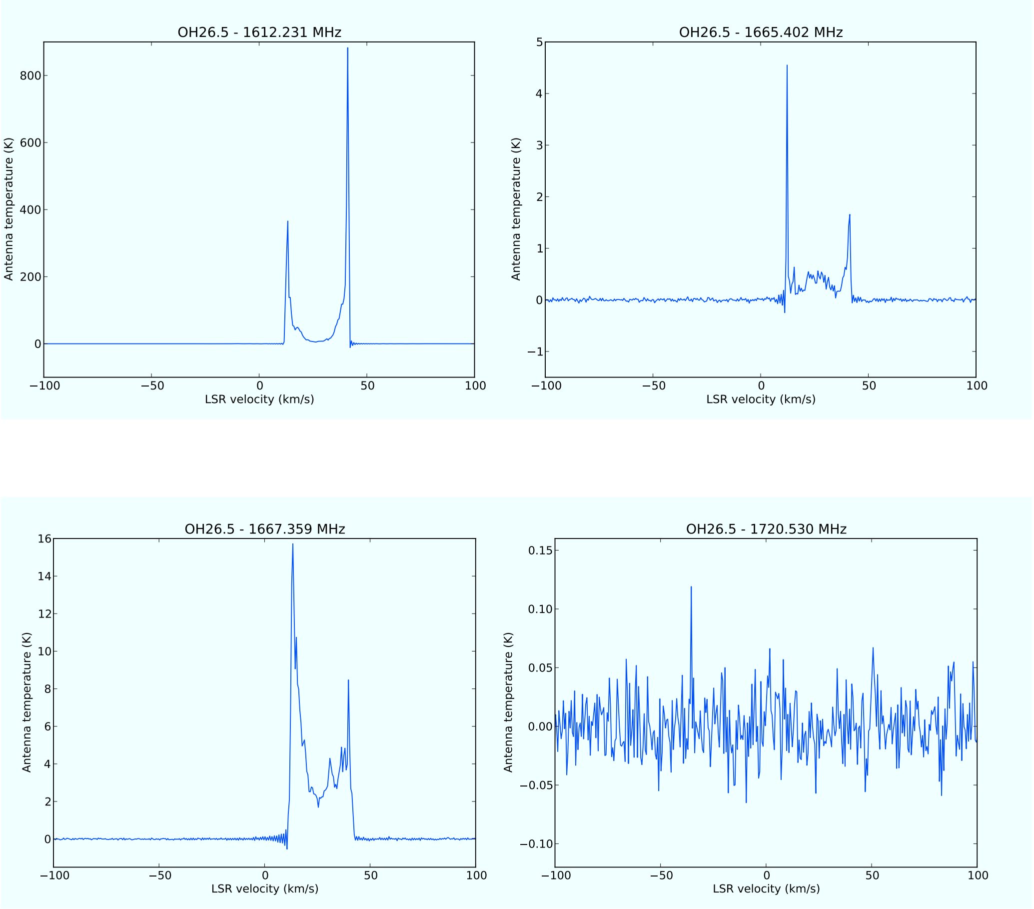

Figure 5.3: Complete spectrum of OH26.5.

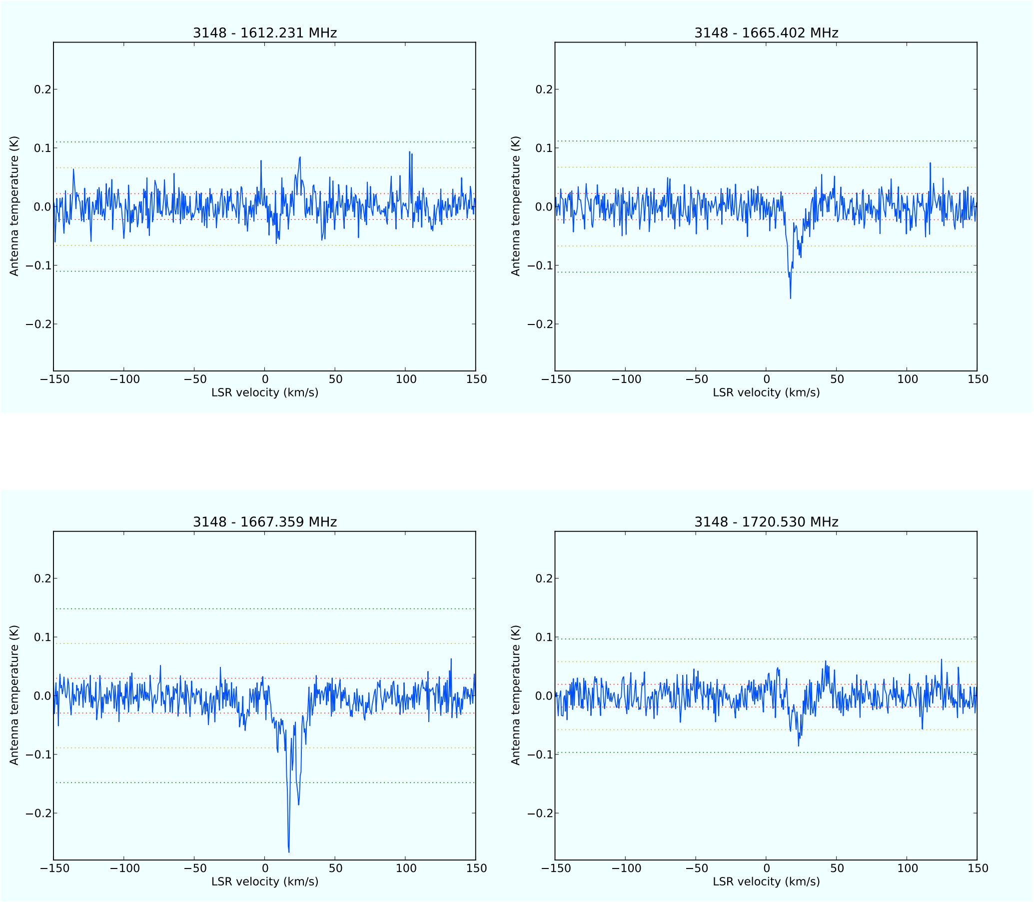

Figure 5.4: Complete spectrum of the bubble 3148.

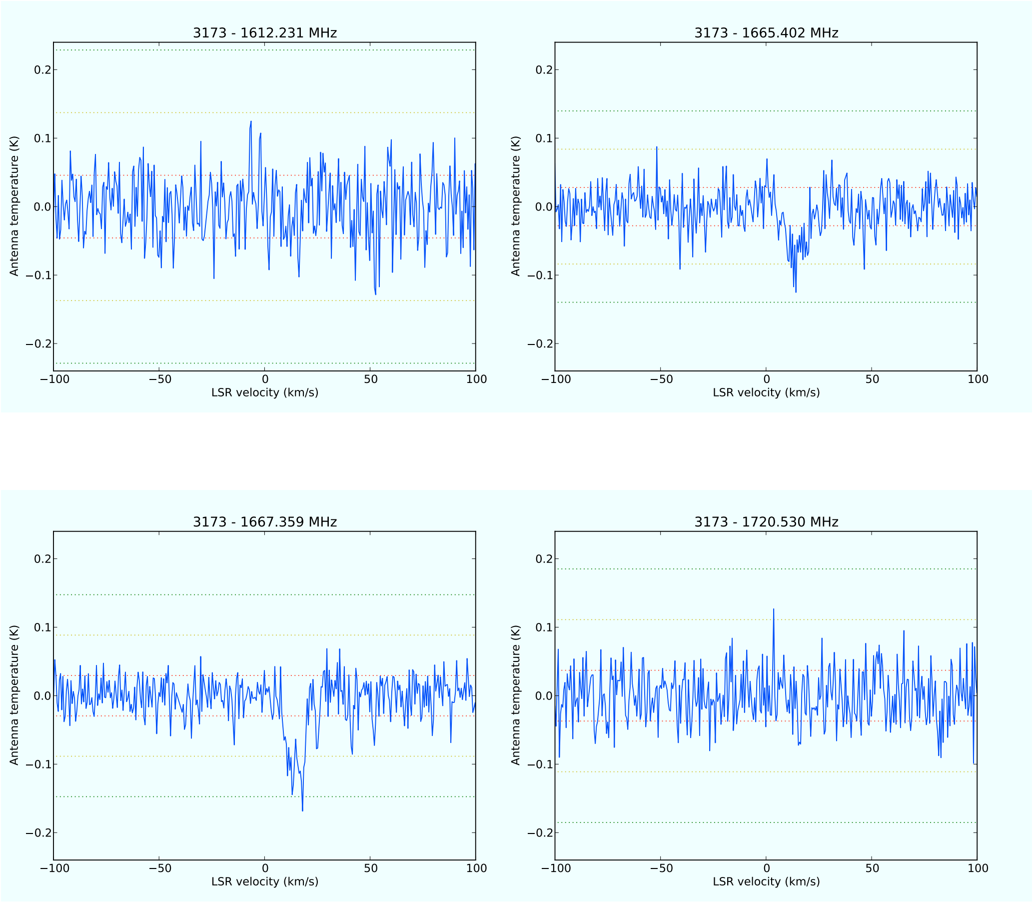

Figure 5.5: Complete spectrum of the bubble 3173.

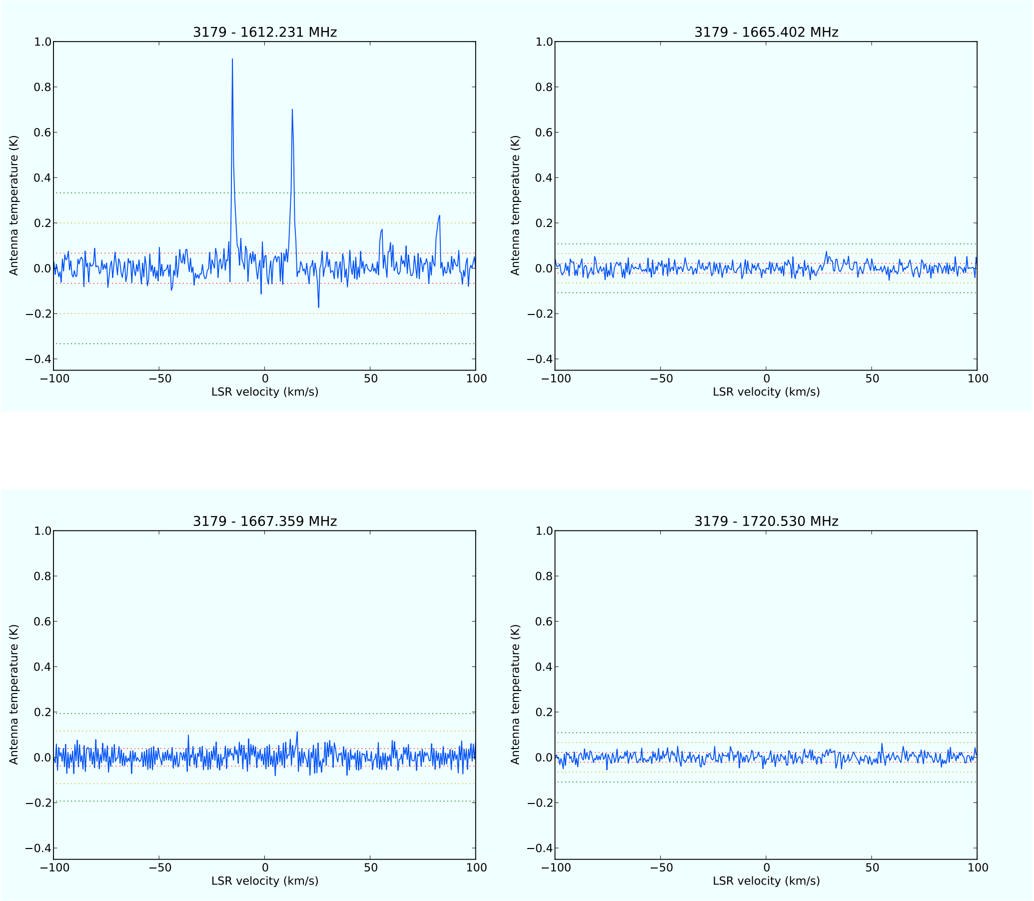

Figure 5.6: Complete spectrum of the bubble 3179. It is possible to notice a very impressive maser at 1612 MHz. The lack of the two main lines, and of any feature in the fourth band, suggests that this object is very likely a proto-PN [24].

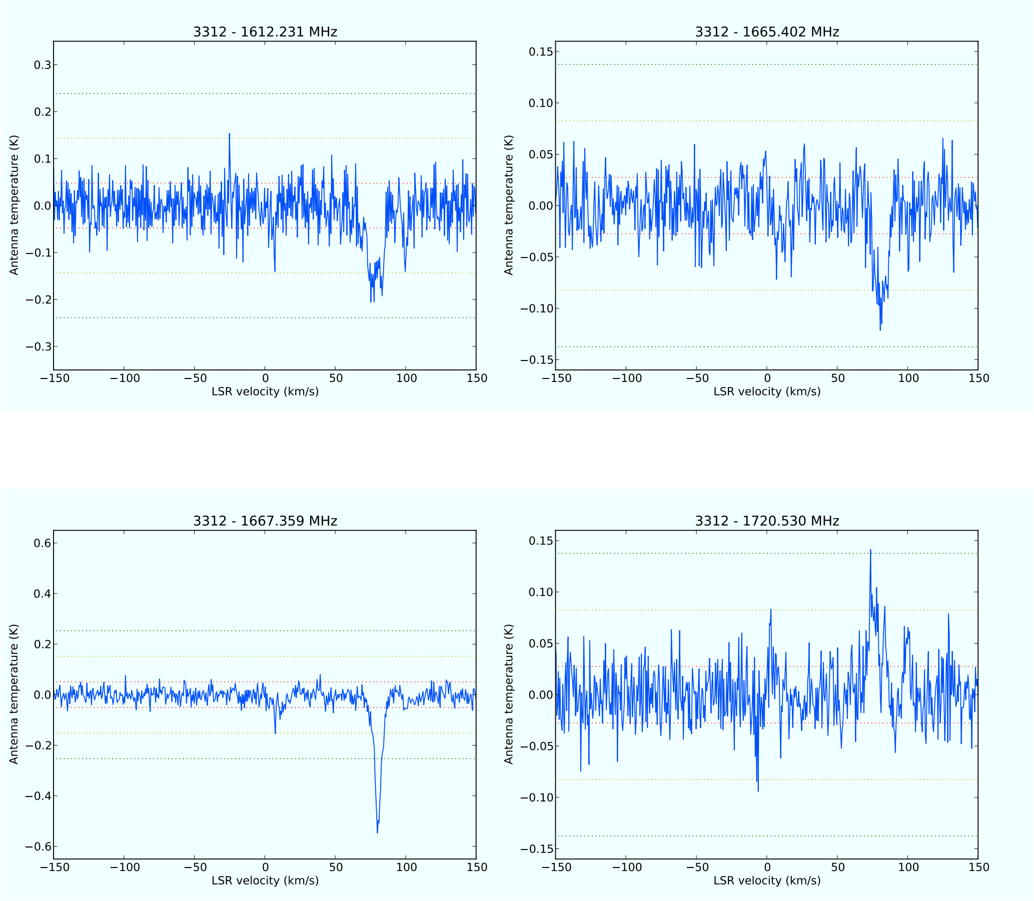

Figure 5.7: Complete spectrum of the bubble 3312.

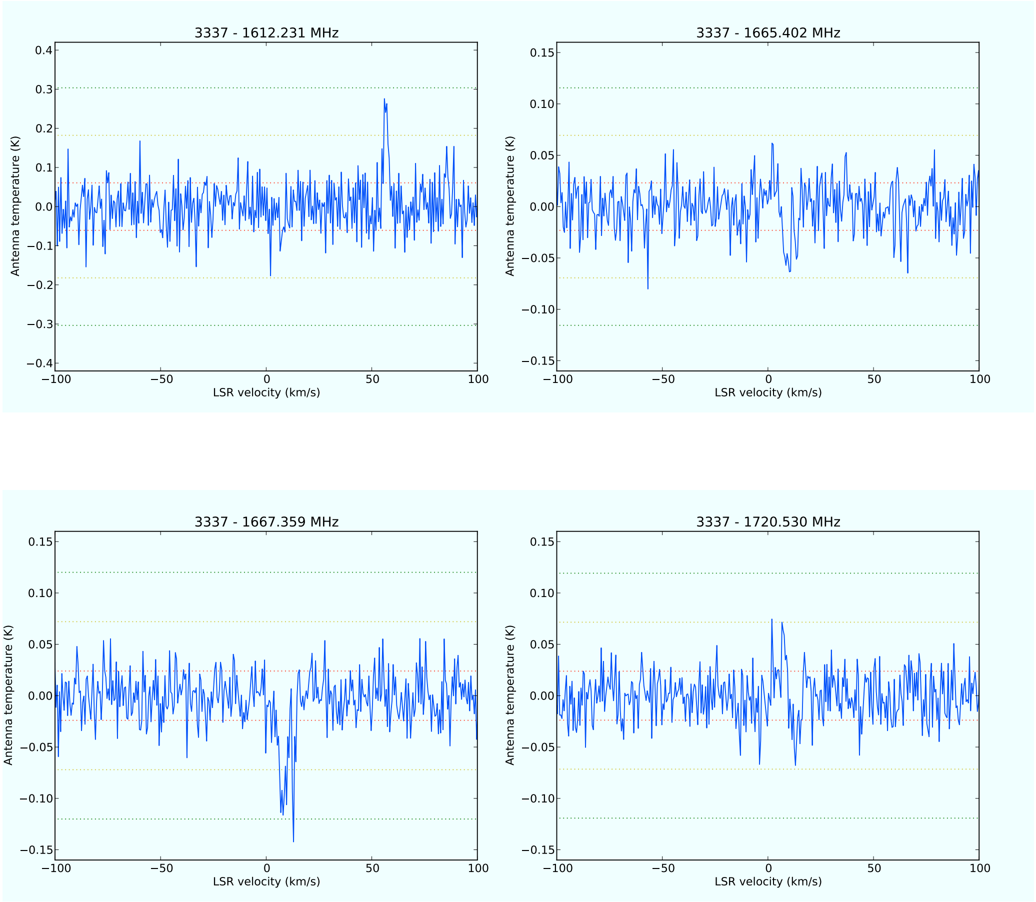

Figure 5.8: Complete spectrum of the bubble 3337.

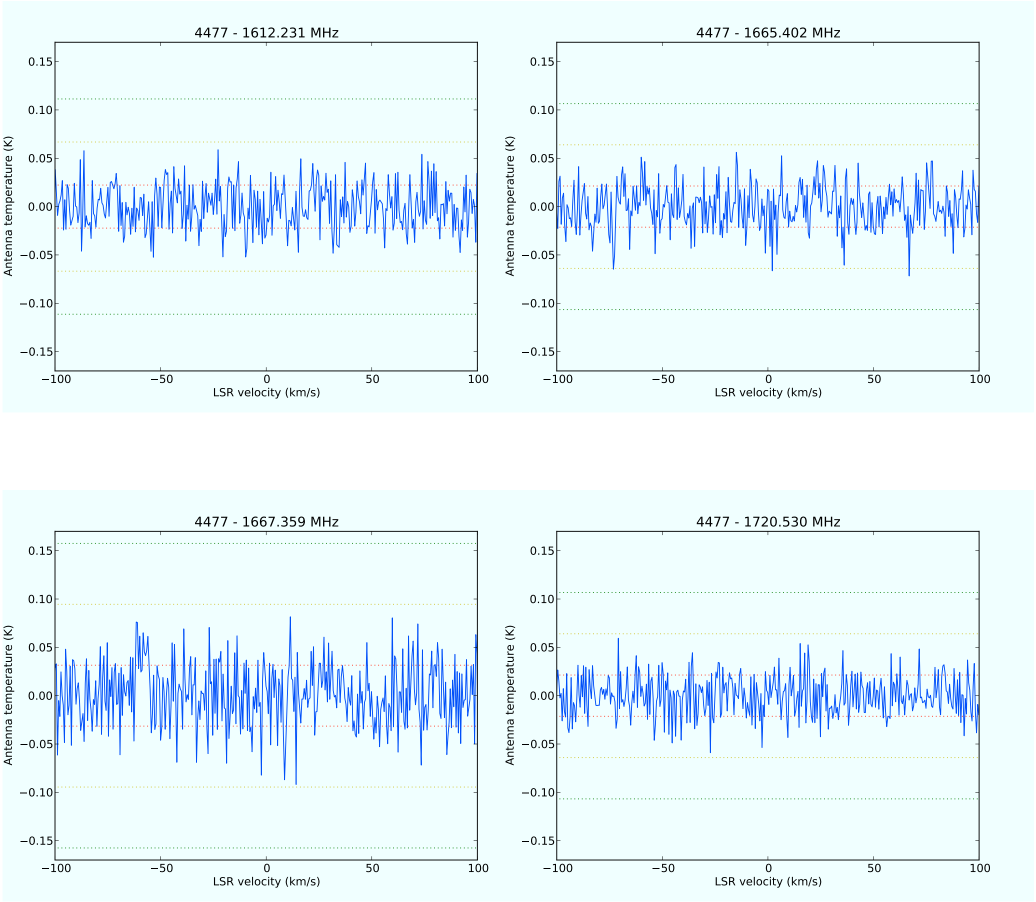

4477 - 1612.231 MHz

4477 - 1665.402 MHz

4477 - 1667.359 MHz

4477 - 1720.530 MHz

Figure 5.9: Complete spectrum of the bubble 4477.

Chapter 6

Archive search

In this chapter we will list all the multiwavelength archive data that have been used in the next two chapters. In particular, in each section (except for the first), we will brefely introduce an instrument or a survey, point out important characteristics such as the resolution and the sensitivity, and then we list the archive flux densities (and sometimes other quantities) of all the bubbles we detected both at 6 cm and at 20 m, and a few others.
If the source was clearly detected by an instrument or within a survey but no archive flux density is available then aperture photometry has been performed using the Aperture Photometry Tool [27].
In the last section we report the new Herschel observations of the entire bubble set; however no flux densities could be reported.

6.1 Radio archive observations

As discussed in section 2.1, the preliminary selection of the bubbles to observe with the EVLA was made searching for their detection evidences in the two catalogs NVSS and MAGPIS.
The NRAO VLA Sky Survey (NVSS) covers the sky north of $\delta > -40^\circ$ at 1.4 GHz, by means of observations with VLA in D and DnC configurations between 1993 September and 1996 October. The principal data products are a set of 2326 $4' \times 4'$ continuum images and a catalog of almost 2×10^6 discrete sources stronger than 2.5 mJy. The images all have a $45''$ FWHM resolution and nearly uniform sensitivity of about 0.45 mJy/beam (Stokes I rms) [28].
The Multi-Array Galactic Plane Imaging Survey (MAGPIS) is a collection of

bits and pieces of the Galactic sky that have been imaged at high resolution. Currently this web site includes the 6 and 20-cm VLA radio images and catalogs described in White, Becker and Helfand (2005) [29], as well as the main MAGPIS database of high-dynamic range, high-sensitivity VLA images for the region $5° < l < 48.5°$, $|b| < 0.8°$ [16]. Much of this latter area is being imaged with XMM-Newton at hard-X-ray wavelengths and by the GLIMPSE Spitzer legacy project at 3.6, 4.5, 5.8 and 8 µm, and all of it has been mapped at mid-infrared wavelengths by MSX. Mosaics of both the GLIMPSE and MSX infrared data, gridded onto the same coordinate system as the radio images, are included at this site, as will be the X-ray data as they become available. The sensitivity of the radio images at 20 cm is usually around 1 mJy/beam.

These archive data were used as a pathfinder for our observations. Their sensitiviy limit and the fact that they were acquired in different epochs forced us to ask for new observational time.

Another source of radio data is the VLA archive. However it turned out that, because of the usual extreme faintness of our sources and that for many of them it was a fist detection, only very few past observation revealed useful, as, for example, the observations concering bubble 3282 (see appendix B).

6.2 IRAS

The Infrared Astronomical Satellite (IRAS) was the first-ever space-based observatory to perform a survey of the entire sky at infrared wavelengths. Launched on January 25, 1983, its mission lasted ten months. The telescope was a joint project of the United States (NASA), the Netherlands (NIVR), and the United Kingdom (SERC).

With a primary mirror of 57 cm, IRAS was the first observatory to perform an all-sky survey at infrared wavelengths. It mapped 96% of the sky four times, at 12 µm, 25 µm, 60 µm and 100 µm wavelengths, with resolutions ranging from $30''$ at 12 µm to $2'$ at 100 µm. It discovered about 350 000 sources, many of which are still awaiting an identification.

The IRAS maximum sensitivity, for a point source, was supposed to be about 0.5 Jy at the first three bands, and about 1 Jy at 100 µm, but it was indeed usually much worse. With this sensitivity, many of our bubbles are below the detection limit; anyway for those which have been observed, the IRAS values could be very important to trace the dust SED, helping us to discriminate between different kinds of source.

In table 6.1 we report the flux densities of those bubbles detected at least in one band; when available, upper limits for non-detections are listed in red. As it is possible to notice no one of the bubbles considered was detected at 100 µm. Moreover for no considered bubbles flux densities were available in more than two band. As we will discuss in section 8.3, this has prevented the possibility of study the IRAS color of these sources, and only thanks to their integration with our radio data it has been possible to obtain interesting results.

ID	$F(12\,\mu\mathrm{m})$ (Jy)	$F(25\,\mu\mathrm{m})$ (Jy)	$F(60\,\mu\mathrm{m})$ (Jy)	$F(100\,\mu\mathrm{m})$ (Jy)
3222	< 4.43	8.52 ± 0.77	< 19.9	< 240
3354	1.59 ± 0.19	< 6.45	28.7 ± 3.16	< 324
3438	0.99 ± 0.15	3.86 ± 0.39	< 17.9	< 29.3
3448	< 2.47	1.71 ± 0.27	7.99 ± 0.88	< 29.0
4436	< 4.53	0.94 ± 0.10	4.83 ± 0.53	< 378
4473	< 3.72	2.56 ± 0.41	< 24.3	< 466
4602	< 4.79	3.11 ± 0.40	7.90 ± 0.95	< 50.0

Table 6.1: IRAS photometry.

6.3 MIPS observations

The Multiband Imaging Photometer for Spitzer (MIPS), was one of the three instruments on board of the Spitzer Space Telescope. It produced imaging and photometry in three broad spectral bands, centered nominally at 24 µm, 70 µm, and 160 µm, and low-resolution spectroscopy between 55 µm and 95 µm. The instrument contained three separate detector arrays each of which resolves the telescope Airy disk with pixels of size near the diffraction limit. All three arrays viewed the sky simultaneously; multiband imaging at a given point was provided via telescope motions. The 24 µm camera has roughly a $5'$ square field of view. The 70 µm camera was designed to have a $5'$ square field of view, but a cabling problem compromised the outputs of half the array; the remaining side provided a field of view that was roughly $2.5' \times 5'$. The 160 µm array projected to the equivalent of a $0.5' \times 5'$ field of view and filled in a $2' \times 5'$ image by multiple exposures.
Among its other utilizations, MIPS was used to conduct the MIPSGAL survey, which discovered most of the objects studied in these work. In the table 6.2 we list the photometry of our bubbles, along with it mean diameter, as reported in the MIPSGAL catalog at 24 µm. For the other bands, the MIPS archive products appear too contaminated by artifact that any flux density determination through aperture photometry is prevented; anyway a column in the table 6.2 indicates whether the source is detected or not at 70 µm as extended emission ("?" indicates a possible detection, "–" indicates no data available).

ID	$F(24\,\mu\mathrm{m})$ (Jy)	Dimensions	$70\,\mu$m?
3188	0.05 ± 0.02	$16''$	no
3192	0.18 ± 0.09	$18''$	?
3193	0.31 ± 0.04	$18''$	?
3214	0.29 ± 0.01	$18''$	yes
3222	9.30 ± 0.09	$26''$	yes
3309	0.07 ± 0.02	$15''$	no
3333	0.25 ± 0.03	$23''$	?
3347	0.15 ± 0.02	$18''$	no
3354	1.20 ± 0.10	$44''$	yes
3367	0.60 ± 0.02	$16''$	?
3384	0.27 ± 0.03	$21''$	no
3438	3.40 ± 0.03	$21''$	yes
3448	1.10 ± 0.01	$33''$	yes
3654	1.10 ± 0.04	$27''$	yes
3706	1.40 ± 0.10	$25''$	?
3736	11.00 ± 0.22	$37''$	yes
3866	0.30 ± 0.11	$18''$	?
4409	1.40 ± 0.03	$28''$	yes
4422	6.00 ± 0.12	$30''$	–
4436	0.60 ± 0.02	$18''$	yes
4452	0.03 ± 0.01	$15''$	no
4465	0.26 ± 0.03	$18''$	?
4473	2.30 ± 0.09	$20''$	yes
4479	1.60 ± 0.03	$20''$	–
4486	0.37 ± 0.03	$18''$	yes
4497	0.72 ± 0.03	$15''$	–
4552	0.44 ± 0.08	$25''$	?
4580	0.20 ± 0.01	$18''$	?
4584	0.08 ± 0.01	$18''$	–
4589	1.10 ± 0.02	$16''$	–
4602	2.50 ± 0.05	$28''$	yes
4607	0.49 ± 0.02	$18''$	?

Table 6.2: MIPS photometry.

6.4 IRAC observations

The Infrared Array Camera (IRAC) is one of three focal plane instruments on the Spitzer Space Telescope. IRAC is a four-channel camera that obtains simultaneous broadband images at 3.6, 4.5, 5.8, and 8.0 µm. Two nearly adjacent $5' \times 5'$ fields of view in the focal plane are viewed by the four channels in pairs (3.6 and 5.8 µm; 4.5 and 8 µm). All four detector arrays in the camera are 256×256 pixels in size, with the two shorter wavelength channels using InSb and the two longer wavelength channels using Si:As IBC detectors. IRAC is a powerful survey instrument because of its high sensitivity, large field of view, and four-color imaging [30].

IRAC sensitivity for a point source is about 0.1 mJy for a one-second long observation. It could achieve a resolution of about $1''$. With this characteristic, unfortunately only few bubbles (intended as extended sources, with some of them that could just not emit at all in these bands) can be detected by IRAC, mostly at 8 µm. However, IRAC allowed us to see the central source present in some bubbles (usually seen at shorter wavelengths).

All the data, listed in tables 6.3 and 6.4, and the images in the next chapter are from the GLIMPSE survey or, in some cases[1], have been derived by aperture photometry. It was a Spitzer Legacy Science Program, that mapped 2/3 of the inner Galactic disk with a pixel resolution of about $1.2''$. The survey covered Galactic latitudes $|b| \leq 1°$ and longitudes $|l|$ from 10° to 65° (both sides of the Galactic center). The survey area contained the outer ends of the Galactic bar, the Galactic molecular ring, and the inner spiral arms [31].

As it is possible to see few data are indeed availble. In particular for only five bubbles it has been possible to detect a diffuse emission and calculate a flux density in at least one band (at 8 µm).

---

[1] Whenever no archive data were available, specially for extended sources.

ID	$F(3.6\,\mu\text{m})$ (mJy)	$F(4.5\,\mu\text{m})$ (mJy)	$F(5.8\,\mu\text{m})$ (mJy)	$F(8.0\,\mu\text{m})$ (mJy)
3222	105.3 ± 4.1	127.8 ± 7.3	134.2 ± 3.8	56.6 ± 7.8
3367	4.6 ± 0.4	3.6 ± 1.2	3.0 ± 0.2	–
3438	1339.5 ± 51.8	1213.8 ± 71.6	1052.3 ± 22.3	772.4 ± 14.9
3448	1.5 ± 0.1	2.1 ± 0.3	1.0 ± 0.2	–
4552	11.7 ± 1.7	14.1 ± 0.9	11.3 ± 0.6	6.5 ± 0.3

Table 6.3: IRAC central object photometry (from GLIMPSE).

ID	$F(3.6\,\mu\text{m})$ (mJy)	$F(4.5\,\mu\text{m})$ (mJy)	$F(5.8\,\mu\text{m})$ (mJy)	$F(8.0\,\mu\text{m})$ (mJy)
3354	–	–	149.6 ± 2.9	320.0 ± 5.8
3367	–	–	–	11.5 ± 0.5
3448	–	–	–	25.0 ± 1.3
4473	–	28.3 ± 2.7	48.2 ± 2.0	158.7 ± 1.9
4602	9.1 ± 1.4	19.7 ± 1.1	12.8 ± 1.0	32.2 ± 0.9

Table 6.4: IRAC nebula photometry (from GLIMPSE).

6.5 The Two Micron All Sky Survey

The Two Micron All Sky Survey (2MASS) was a survey conducted between June 1997 and February 2001, thanks to two highly-automated 1.3-m telescopes, one at Mt. Hopkins, AZ, and one at CTIO, Chile [32]. Each telescope was equipped with a three-channel camera, each channel consisting of a 256×256 array of HgCdTe detectors, capable of observing the sky simultaneously at three bands: J (centered at 1.25 µm), H (1.65 µm), and K_s (2.17 µm). To achieve these goals, 2MASS has uniformly scanned the entire sky to detect and characterize point sources brighter than about 1 mJy in each band, with signal-to-noise ratio greater than 10, using a pixel size of $2.0''$.

The survey has produced a catalog containing positional and photometric information for 470 992 970 point sources and 1 647 599 extended sources. From this catalog we were able to extract photometric informations about our bubbles. Many of them were not detected in some or all of 2MASS bands; for

the other we usually detected a point source at the center of the nebula. In table 6.5 the photometry of some bubbles is reported; for some of them only upper limits were obtainable (omitted in table). If no values are reported then that bubble was not detected in any 2MASS band.
The flux densities reported in the table are referred only to the central sources.

ID	$F(J)$ (mJy)	$F(H)$ (mJy)	$F(K_s)$ (mJy)
3222	–	2.13 ± 0.07	14.20 ± 0.33
3367	–	1.99 ± 0.16	4.67 ± 0.24
3438	218.82 ± 4.43	692.3 ± 18.5	1211.0 ± 17.9
3448	0.92 ± 0.07	1.17 ± 0.11	1.86 ± 0.15
4552	–	–	6.74 ± 0.33

Table 6.5: 2MASS central object photometry.

6.6 MSX

The Midcourse Space Experiment (MSX) was a Ballistic Missile Defense Organization satellite experiment to map bright infrared sources in space. Operational from 1996–1997, MSX mapped the galactic plane and areas either missed or identified as particularly bright by the Infrared Astronomical Satellite (IRAS) at wavelengths of 4.29 µm, 4.35 µm, 8.28 µm, 12.13 µm, 14.65 µm, and 21.34 µm. It carried the 33-cm SPIRIT III infrared telescope with solid hydrogen-cooled five line-scanned infrared focal plane arrays.

Calibration of MSX posed a challenge for designers of the experiment, as baselines did not exist for the bands it would be observing under. Engineers solved the problem by having MSX fire projectiles of known composition in front of the detector, and calibrating the instruments to the known blackbody curves of the objects. The MSX calibration served as the basis for other satellites working in the same wavelength range, like AKARI and the Spitzer Space Telescope.

MSX data is currently available in the Infrared Science Archive (IRSA) provided by NASA's Infrared Processing and Analysis Center (IPAC) [33]. The resolution achieved by MSX was 18″ [34], and a sensitivity for a point source of order of 100 mJy. MSX data have been very important for this study since they cover the portion of spectrum between IRAC and MIPS. Furthermore, there exists study of object classification by their MSX colors [35].

ID	λ_0
A	8.28 µm
B_1	4.29 µm
B_2	4.35 µm
C	12.13 µm
D	14.65 µm
E	21.34 µm

Table 6.6: MSX bands.

ID	$F(A)$ (mJy)	$F(C)$ (mJy)	$F(D)$ (mJy)	$F(E)$ (mJy)
3222	110.4 ± 8.7	663 ± 72	1526 ± 104	6268 ± 389
3438	948.7 ± 39.8	1161 ± 86	865 ± 69	2312 ± 162
4602	61.2 ± 7.2	–	931 ± 70	1334 ± 108

Table 6.7: MSX nebula photometry.

6.7 WISE

The Wide-field Infrared Survey Explorer (WISE) was a NASA infrared-wavelength astronomical space telescope with a diameter of 40 cm, launched on December 14, 2009, and hibernated on February 17, 2011. The telescope performed an all-sky astronomical survey with images in four mid-infrared bands listed in table 6.8 [36].

For the analysis conducted in this work, the first two band are useful to complement the IRAC data while the other two band fill in the gap between IRAC and MIPS. Though the WISE sensitivity is comparable to the Spitzer sensitivity, its resolution is about twice as worse. In fact, the spatial resolutions in the four bands are $6.1''$, $6.4''$, $6.5''$, and $12''$ and the sensitivities are 0.08 mJy, 0.11 mJy, 1 mJy, and 6 mJy, respectively.. In table 6.9 the photometry of our bubble (when detected) is reported; for the first two bands it usually refers to the central object while for the other two to the entire nebula.

ID	λ_0
$W1$	3.4 µm
$W2$	4.6 µm
$W3$	11.6 µm
$W4$	22.1 µm

Table 6.8: WISE bands.

ID	$F(W1)$ (mJy)	$F(W2)$ (mJy)	$F(W3)$ (mJy)	$F(W4)$ (mJy)
3222	46.6 ± 1.2	79.1 ± 1.6	575.3 ± 11.1	9035.7 ± 141.5
3367	6.0 ± 0.3	5.4 ± 0.3	82.6 ± 2.5	407.7 ± 11.3
3438	1516.1 ± 68.4	1735.3 ± 56.0	646.1 ± 8.9	5355.0 ± 64.1
3448	2.9 ± 0.3	3.9 ± 0.2	165.3 ± 2.1	1195.5 ± 15.4
4436	–	–	95.7 ± 1.6	571.7 ± 11.1
4465	–	–	6.0 ± 0.6	192.6 ± 4.4
4473	–	18.5 ± 0.6	304.2 ± 4.2	2062.3 ± 38.0
4486	–	–	55.4 ± 2.1	202.1 ± 6.0
4497	–	–	62.0 ± 2.1	485.2 ± 12.5
4552	9.3 ± 0.9	11.6 ± 0.7	17.5 ± 1.4	330.5 ± 8.5
4589	–	–	91.2 ± 1.5	981.7 ± 14.5
4602	5.6 ± 0.6	11.1 ± 0.5	261.3 ± 3.4	1996.9 ± 22.1
4607	–	–	44.5 ± 3.0	307.3 ± 11.0

Table 6.9: WISE photometry.

6.8 HRDS

The Green Bank Telescope (GBT) H II Region Discovery Survey (HRDS), was a survey conducted with the GBT at 8.665 GHz and aimed to find H II regions in the Galactic zone $343° \leq l \leq 67°$ with $|b| \leq 1°$. The survey detected 603 discrete hydrogen radio recombination line components at 9 GHz from 448 targets. The derived survey completeness limit, 180 mJy at 9 GHz, is sufficient to detect all H II regions ionized by single O-stars to a distance of 12 kpc.

ID	F (mJy)	Δv (km/s)	v (km/s)	T_L (mK)
3354	18 ± 7	22.0 ± 0.7	-39.2 ± 0.7	2.4 ± 0.7
3866	132 ± 56	16.7 ± 0.3	52.6 ± 0.3	6.6 ± 0.3

Table 6.10: HRDS data.

6.9 AKARI

AKARI (previously known as ASTRO-F or IRIS - InfraRed Imaging Surveyor) was the second space mission for infrared astronomy in Japan. AKARI has been developed by members of JAXA/ISAS and collaborators an was an ambitious plan to make an all-sky survey with much better sensitivity, spatial resolution and wider wavelength coverage than IRAS. AKARI had a 68.5-cm telescope cooled down to 6 K, and observed in the wavelength range from 1.7 µm to 180 µm. AKARI was successfully launched into space by a M-V rocket and placed in a sun-synchronous polar orbit of about 700 km. That operation of AKARI was completed on the November 24, 2011.
AKARI was equipped with two kinds of instruments; the FIS (Far-Infrared Surveyor) for far-infrared observations and the IRC (InfraRed Camera) for near and mid-infrared observations. The FIS was intended to make an all-sky survey at far-infrared wavelengths. Two detectors of the FIS were photoconductors which used semiconductor crystal Ge:Ga. Stressed Ge:Ga chips are sensitive to far-infrared light of longer wavelength than normal ones. Each detector was used with filters. Therefore the FIS has effectively four observation bands, approximately centered at 65 µm, 90 µm, 140 µm and 160 µm. In the first two bands, a resolution (as pixel size) of about 27″ could be achieved, while with the last two the maximum resolution was about 44″.
The IRC was composed of three independent camera systems. The NIR camera was assigned to near-infrared wavelengths in the range from 1.7 µm to 5.5 µm (maximum resolution about 1.5″). The MIR-S camera was assigned to shorter mid-infrared wavelengths over the range from 5.8 µm to 14.1 µm (with a reference wavelength of 9 µm) and the MIR-L camera was assigned to longer mid-infrared wavelengths between 12.4 µm and 26.5 µm (with a reference wavelength of 18 µm); both MIR instruments achieved a resolution of 2.5″ [37].
The flux densities reported in tables 6.11 and 6.12 are retrived from the “AKARI/IRC mid-IR all-sky Survey” [38] and from the “AKARI/FIS All-Sky Survey Point Source Catalogues” [39].

ID	$F(9\,\mu\mathrm{m})$ (mJy)	$F(18\,\mu\mathrm{m})$ (mJy)
3367	–	368.5 ± 45.5
3438	696.8 ± 64.2	2319.0 ± 46.1
3448	–	872.7 ± 44.1
4436	–	510.2 ± 15.6
4473	–	1406.0 ± 74.9
4589	–	692.6 ± 20.6
4602	–	1029.0 ± 127.0

Table 6.11: IRC photometry.

ID	$F(65\,\mu\mathrm{m})$ (Jy)	$F(90\,\mu\mathrm{m})$ (Jy)	$F(140\,\mu\mathrm{m})$ (Jy)	$F(160\,\mu\mathrm{m})$ (Jy)
3354	30.38 ± 3.81	–	38.03 ± 2.77	47.92 ± 3.74
4602	–	6.58 ± 1.07	22.45 ± 4.92	–

Table 6.12: FIS photometry.

6.10 Guide Star Catalog II

The GSC II (currently GSC 2.2) is a catalog of 435 457 355 stars measured from Schmidt plates at the Space Telescope Science Institute. It is magnitude limited to 18.5 in photographic F or 19.5 in photographic J, with bright objects filled in from the Tycho 2 Catalog.

ID	$F(R)$ (mJy)
3438	0.40 ± 0.16

Table 6.13: GSC II photometry.

6.11 USNO-B1.0

USNO-B1.0 is an all-sky catalog that presents positions, proper motions, magnitudes in various optical passbands, and star/galaxy estimators for 1 042 618 261 objects derived from 3 643 201 733 separate observations. The data were obtained from scans of 7435 Schmidt plates taken for the various sky surveys during the last 50 years. USNO-B1.0 is believed to provide all-sky coverage, completeness down to $V = 21$, $0.2''$ astrometric accuracy at J2000, 0.3 magnitude photometric accuracy in up to five colors, and 85% accuracy for distinguishing stars from non-stellar objects.

ID	$F_1(R)$ (mJy)	$F_2(R)$ (mJy)	$F(I)$ (mJy)
3438	0.21	0.56	3.31
3448	0.10	0.31	–

Table 6.14: USNO-B1.0 photometry.

6.12 UKIDSS

UKIDSS is a near-infrared sky survey, the successor to 2MASS. UKIDSS began in May 2005 and will survey 7500 square degrees of the Northern sky,

extending over both high and low Galactic latitudes, in JHK to $K = 18.3$. This depth is three magnitudes deeper than 2MASS. UKIDSS will be the true near-infrared counterpart to the Sloan survey, and will produce as well a panoramic clear atlas of the Galactic plane. In fact UKIDSS is made up of five surveys and includes two deep extra-Galactic elements, one covering 35 square degrees to $K = 21$, and the other reaching $K = 23$ over 0.77 square degrees.
The survey instrument is WFCAM on the UK Infrared Telescope (UKIRT) in Hawaii. WFCAM has four 2048×2048 Rockwell devices, at 94% spacing. The pixel scale of $0.4''$ gives an exposed solid angle of 0.21 square degrees [40].

ID	$F(J)$ (mJy)	$F(H)$ (mJy)	$F(K)$ (mJy)
3448	0.91 ± 0.01	1.14 ± 0.01	1.50 ± 0.01

Table 6.15: UKIDSS photometry.

6.13 MGPS

The second epoch of the Molonglo Galactic Plane Survey (MGPS-2) was carried out with the Molonglo Observatory Synthesis Telescope at a frequency of 843 MHz and with a restoring beam of about $45'' \times 45''$, making it the highest resolution large-scale radio survey of the southern Galactic plane. It covers the range $|b| < 10°$ and $245° < l < 365°$.

ID	$F(843\,\mathrm{MHz})$ (mJy)
4486	28.8 ± 3.5
4497	25.4 ± 2.6
4552	17.8 ± 3.0

Table 6.16: MGPS photometry.

6.14 Herschel

The Herschel Space Observatory is an ESA space telescope launched on May 2009 and it is still operating in the Sun–Earth Lagrangian point L_2. On board of Herschel there are three instruments: the Photoconductor Array Camera and Spectrometer (PACS) is both a photometer (observing in three bands at 70 µm, 100 µm and 160 µm) and an integral field spectrometer (observing from 55 µm to 210 µm); the Heterodyne Instrument for the Far Infrared (HIFI) is an heterodyne spectrometer (observing from 157 µm to 625 µm); finally the Spectral and Photometric Imaging REceiver (SPIRE) is both a photometer (observing in three bands at 250 µm, 350 µm and 500 µm) and a Fourier transform spectrometer (observing from 190 µm to 672 µm).
One of the Herschel open time key-project is Hi-GAL. This survey is mapping the galactic plane (with $|b| < 1$) in five bands, namely the first and third band of PACS and all the three bands of SPIRE, covering therefore a wavelength range between 60 µm and 600 µm.
In the table 6.17 all the bubbles observed in the Hi-GAL survey are reported. If a bubble has been clearly detected then the column is marked with a "y", if a bubble has not been clearly detected then the column is marked with a "n", if the detection of a bubble is uncertain then the column is marked with a "?", finally, if a bubble has not been observed in that specific band then the column is marked with a "–". The bubbles which have not been observed in any of these five bands are not reported at all. Data analysis is still in progress and so no more informations can be given in this moment.

ID	70 µm?	160 µm?	250 µm?	350 µm?	500 µm?
3148	y	n	n	n	n
3149	y	y	y	?	n
3153	y	n	n	n	n
3157	n	n	–	–	–
3173	y	n	n	n	n
3176	y	y	y	y	?
3177	y	n	n	n	n
3179	y	n	n	n	n
3188	n	n	n	n	n
3190	n	n	n	n	n
3192	n	n	n	n	n
3193	?	n	n	n	n

3194	?	n	n	n	n
3198	n	n	n	n	n
3214	y	n	n	n	n
3222	y	y	n	n	n
3223	n	n	n	n	n
3232	y	n	n	n	n
3233	n	n	n	n	n
3234	n	n	n	n	n
3257	n	n	n	n	n
3259	y	n	n	n	n
3269	y	?	?	?	n
3280	y	y	?	n	n
3282	y	?	?	?	?
3293	n	n	n	n	n
3309	n	n	n	n	n
3310	y	?	?	?	n
3312	y	?	?	?	?
3313	y	n	n	n	n
3328	y	y	n	n	n
3332	?	n	n	n	n
3333	y	?	n	n	n
3337	y	n	n	n	n
3346	y	n	n	n	n
3347	y	n	n	n	n
3348	y	n	n	n	n
3354	y	y	y	y	y
3358	n	n	n	n	n
3360	y	n	n	n	n
3362	y	?	?	n	n
3367	y	?	n	n	n
3381	y	?	n	n	n
3384	y	n	n	n	n
3423	?	n	n	n	n
3424	?	n	n	n	n
3429	?	y	y	?	?
3438	y	n	n	n	n
3448	y	y	?	?	?
3458	n	n	n	n	n

3488	?	?	n	n	n
3513	y	y	y	?	n
3537	n	n	n	n	n
3538	n	n	n	n	n
3558	y	?	n	n	n
3573	n	n	n	n	n
3575	n	n	n	n	n
3604	y	?	n	n	n
3611	n	n	n	n	n
3619	n	n	n	n	n
3626	n	n	n	n	n
3631	y	n	n	n	n
3634	n	n	n	n	n
3643	n	n	n	n	n
3653	y	n	n	n	n
3654	y	y	n	n	n
3657	n	n	n	n	n
3662	n	n	n	n	n
3670	y	n	n	n	n
3671	n	n	n	n	n
3681	y	y	y	y	?
3693	y	n	n	n	n
3698	n	n	n	n	n
3700	?	n	n	n	n
3701	y	n	n	n	n
3704	y	n	n	n	n
3706	y	?	?	n	n
3707	y	?	?	n	n
3719	y	n	n	n	n
3724	?	n	n	n	n
3736	y	y	n	n	n
3739	y	y	n	n	n
3773	n	n	n	n	n
3779	y	n	n	n	n
3809	y	n	n	n	n
3820	n	n	n	n	n
3834	y	n	n	n	n
3857	n	n	n	n	n

3866	y	n	n	n	n
3882	y	n	n	n	n
3883	y	n	n	n	n
3899	y	n	n	n	n
3910	y	?	?	?	?
3915	y	n	n	n	n
3922	n	n	n	n	n
3925	n	n	n	n	n
3940	–	–	n	n	n
3944	n	n	n	n	n
3947	n	n	n	n	n
3952	?	n	n	n	n
3955	n	n	n	n	n
3957	?	n	n	n	n
3987	y	n	n	n	n
3994	y	y	?	n	n
3997	y	y	y	?	?
4001	y	n	n	n	n
4006	y	n	n	n	n
4017	?	n	n	n	n
4020	y	y	?	?	n
4021	y	n	n	n	n
4022	n	n	n	n	n
4048	y	y	y	?	?
4052	n	n	n	n	n
4053	y	n	n	n	n
4054	y	n	n	n	n
4057	n	n	n	n	n
4066	y	n	n	n	n
4072	y	?	n	n	n
4076	n	n	n	n	n
4079	y	n	n	n	n
4083	y	y	y	n	n
4095	y	y	y	y	?
4107	n	n	n	n	n
4110	y	n	n	n	n
4111	y	y	?	n	n
4121	y	?	n	n	n

4124	y	y	?	?	?
4126	y	n	n	n	n
4134	y	y	?	?	n
4136	n	n	n	n	n
4137	y	?	n	n	n
4144	y	n	n	n	n
4162	?	n	n	n	n
4167	y	n	n	n	n
4185	y	n	n	n	n
4191	y	n	n	n	n
4204	y	y	y	y	y
4206	y	y	y	?	n
4218	y	y	n	n	n
4222	y	?	n	n	n
4230	n	n	n	n	n
4231	y	y	n	n	n
4236	y	n	n	n	n
4239	y	?	n	n	n
4260	n	n	n	n	n
4261	y	?	?	?	?
4262	y	?	?	?	?
4267	y	y	y	y	?
4274	n	?	?	?	n
4292	y	n	n	n	n
4298	y	y	y	y	y
4299	y	y	y	y	n
4344	y	y	y	y	?
4353	y	y	y	y	?
4356	n	n	n	n	n
4357	?	?	?	n	n
4364	n	n	n	n	n
4373	n	n	n	n	n
4376	n	n	n	n	n
4384	y	y	y	?	?
4390	y	–	–	–	–
4428	–	–	n	n	n
4431	n	n	–	–	–
4433	n	n	–	–	–

4437	n	n	n	n	n
4438	n	n	–	–	–
4443	n	n	–	–	–
4445	n	n	–	–	–
4446	y	?	n	n	n
4447	n	n	–	–	–
4450	n	n	–	–	–
4455	n	n	–	–	–
4456	n	n	–	–	–
4457	y	?	–	–	–
4458	y	?	–	–	–
4463	y	n	n	n	n
4464	y	n	n	n	n
4466	y	n	n	n	n
4467	–	–	n	n	n
4468	n	n	–	–	–
4471	–	–	n	n	n
4473	–	–	n	n	n
4475	–	–	n	n	n
4479	y	y	y	?	?
4483	–	–	n	n	n
4485	y	y	y	y	y
4486	y	?	n	n	n
4487	–	–	n	n	n
4489	n	n	n	n	n
4490	y	y	y	?	n
4491	?	n	n	n	n
4492	?	n	n	n	n
4493	y	?	n	n	n
4494	?	n	n	n	n
4495	y	n	n	n	n
4496	y	n	n	n	n
4497	y	y	y	?	n
4498	y	n	n	n	n
4499	y	n	n	n	n
4500	y	?	n	n	n
4501	y	n	n	n	n
4502	n	n	n	n	n

4503	y	n	n	n	n
4504	?	n	n	n	n
4505	?	n	n	n	n
4506	y	n	n	n	n
4507	y	n	n	n	n
4508	?	?	n	n	n
4509	?	n	n	n	n
4510	y	?	?	?	?
4511	n	n	n	n	n
4514	y	n	n	n	n
4515	y	n	n	n	n
4520	?	n	n	n	n
4521	y	y	?	n	n
4522	n	n	n	n	n
4523	n	n	n	n	n
4524	y	y	?	?	n
4525	n	n	n	n	n
4526	n	n	n	n	n
4527	y	n	n	n	n
4528	n	n	n	n	n
4530	n	n	n	n	n
4531	y	?	n	n	n
4533	n	n	n	n	n
4534	y	y	y	y	y
4535	?	n	n	n	n
4538	n	n	n	n	n
4541	n	n	n	n	n
4542	?	n	n	n	n
4545	n	n	n	n	n
4546	y	y	n	n	n
4547	y	y	y	?	n
4549	y	n	n	n	n
4550	y	n	n	n	n
4551	?	n	n	n	n
4552	y	?	n	n	n
4555	?	n	n	n	n
4559	n	n	n	n	n
4560	y	?	?	?	n

4561	y	n	n	n	n
4562	y	y	?	n	n
4563	y	n	n	n	n
4564	y	?	?	n	n
4565	y	n	n	n	n
4567	y	?	n	n	n
4568	y	?	n	n	n
4569	y	n	n	n	n
4571	?	n	n	n	n
4572	y	?	?	?	n
4573	?	n	n	n	n
4574	n	n	n	n	n
4575	y	n	n	n	n
4576	n	n	n	n	n
4580	y	?	n	n	n
4581	y	?	n	n	n
4583	n	n	n	n	n
4584	n	n	n	n	n
4586	y	?	n	n	n
4587	n	n	n	n	n
4589	y	?	n	n	n
4590	n	n	n	n	n
4591	y	n	n	n	n
4595	y	n	n	n	n
4599	y	n	n	n	n
4600	y	?	?	n	n
4602	y	y	y	?	n
4607	y	?	n	n	n
4609	y	n	–	–	–
4619	–	n	n	n	n
4623	n	n	n	n	n
4624	n	n	?	?	?
4627	–	–	n	n	n
4629	n	n	n	n	n
4639	n	n	n	n	n
4640	–	–	n	n	n
4642	n	n	n	n	n
4644	–	–	n	n	n

4645	–	–	n	n	n
4646	–	–	n	n	n
4648	–	–	n	n	n
4649	–	–	n	n	n
4654	–	–	n	n	n
4658	–	–	n	n	n
4662	–	–	n	n	n
4665	–	–	n	n	n
4668	n	n	n	n	n
4670	y	n	–	–	–
4678	?	n	n	n	n
4682	y	n	–	–	–
4685	y	y	y	?	n
4690	n	n	–	–	–
4691	n	n	n	n	n

Table 6.17: Herschel detections.

Chapter 7

Discussion on individual sources

This chapter is dedicated to the analysis of the data gathered throughout the observations reported in the previous chapters. We will discuss individually some interesting sources, integrating the archive data with ours. We will also discuss possible classification found in literature and whether our data supports or not those hypotheses.

7.1 Detected sources

From the analysis of tables 2.3 and 3.5, it can be see that the majority of the bubbles observed were detected in both bands, as we could expect; in particular for band C we detected 44 bubbles over 55 observed with also 3 uncertain detections and 8 non-detections, for band L we detected 23 bubbles over 40 observed with 3 uncertain detections and 14 non-detections. Many unclassified sources detected both in band L and C were not resolved, in particular only 9 sources were clearly resolved at 1.4 GHz and only 18 at 5 GHz (see tables 2.3 and 3.5). This could be an indication that they are, indeed, very compact radio sources and, therefore, we can expect that many of them are not optically thin at least in band L. A few others are resolved in one or in both bands; the images that we are going to present show that, in these cases, the radio nebula is usually as extended as the mid-infrared one. However the relatively poor resolution of our images does not allow to make deeper morphological comparisons.

In the table 7.1 flux densities and estimated spectral indices are presented for all those bubbles clearly detected in both bands. The procedures used to calculate the flux densities were discussed in sections 2.4 and 3.4. For these sources the spectral index was estimated as

$$\alpha = \frac{\ln \dfrac{F_L}{F_C}}{\ln \dfrac{\nu_L}{\nu_C}},$$

where F_L and F_C are the flux densities relative to the frequencies ν_L and ν_C; the error associable to the spectral index, computed by propagation, is given by

$$\Delta\alpha = \frac{\sqrt{\left(\dfrac{\Delta F_L}{F_L}\right)^2 + \left(\dfrac{\Delta F_C}{F_C}\right)^2}}{\ln \dfrac{\nu_C}{\nu_L}},$$

where we used

$$\left|\ln \frac{\nu_L}{\nu_C}\right| = \ln \frac{\nu_C}{\nu_L},$$

and we neglected the error on frequencies. An histogram of the spectral index statistical distribution will be presented in figure 8.1.

All the sources listed in the table 7.1 and a few others will be treated individually from the section 7.3 on. For each one of them a brief summary of all the available observations (archive and our data) will be presented, along with: infrared rgb images (that we obtained from GLIMPSE and MIPSGAL archive FITS using ds9), radio images obtained from our data (as contour maps), the complete SED of both the nebula and the central source (if present), the GBT spectrum we obtained (if observed)[1] and if necessary and available other peculiar plots.

Moreover for each one of them we will plot the two radio measurements along with three dotted lines. The red one is conducted through the point at 1.4 GHz and represents the emission of a source with $\alpha = 2$; this is what we would expect from an optically thick nebula with a free-free emission[2].

---

[1] Recalling what we said in section 5.6, the dotted lines in these plots represent the 1σ level (red), the 3σ level (yellow) and the 5σ level (green).

[2] We are ruling out the possibility that a positive spectral index could be, as well, indicative of an optically thick synchrotron emission. Even if, in principle, this could be

The green one is conducted through the point at 5 GHz and represents the emission of a source with $\alpha = -0.1$; this is what we would expect from an optically thin nebula with a free-free emission. Finally, the blue line is conducted through the point at 5 GHz and represents the emission of a source with $\alpha = -0.75$; this is what we would expect from an optically thin nebula with a synchrotron emission[3]. This three-line scheme should give an immediate comprehension of the emission mechanism: in the case of an optically thick free-free emission the 5 GHz point should lie close to the red line, in the case of an optically thin free-free emission the 1.4 GHz point should lie close to and below the green line, in the case of an optically thin synchrotron emission the 1.4 GHz point should lie close to the blue line and well above the green one.

---

possible, it is easy to show that such a source should be characterized by an unexpectedly high magnetic field.

[3] To be more precise, we would expect a spectral index roughly between -0.5 and -1.

ID	$F(L)$ (mJy)	$F(C)$ (mJy)	Sp. index
3222	21.5 ± 3.1	22.9 ± 1.5	0.05 ± 0.13
3333	4.0 ± 0.2	6.4 ± 0.3	0.39 ± 0.26
3354	12.0 ± 1.1	12.3 ± 0.1	0.02 ± 0.08
3367	6.8 ± 0.9	4.7 ± 0.9	-0.30 ± 0.19
3438	10.2 ± 0.8	10.5 ± 0.1	0.02 ± 0.07
3448	12.8 ± 1.1	12.7 ± 0.4	-0.01 ± 0.08
3654	64.1 ± 0.8	59.7 ± 0.5	-0.06 ± 0.01
3706	10.8 ± 3.7	19.6 ± 0.8	0.49 ± 0.28
3866	9.7 ± 3.5	10.3 ± 0.6	0.05 ± 0.30
4436	6.6 ± 0.4	5.8 ± 0.1	-0.11 ± 0.05
4465	1.0 ± 0.6	1.6 ± 0.1	0.39 ± 0.48
4473	34.7 ± 3.9	38.1 ± 0.8	0.08 ± 0.09
4486	20.1 ± 1.1	15.5 ± 0.9	-0.25 ± 0.06
4497	15.0 ± 0.9	15.1 ± 0.4	0.01 ± 0.06
4552	15.9 ± 1.1	15.0 ± 0.7	-0.04 ± 0.07
4589	8.9 ± 0.6	9.0 ± 0.2	0.01 ± 0.06
4602	14.7 ± 1.7	17.7 ± 0.7	0.15 ± 0.10
4607	5.9 ± 0.6	8.2 ± 0.4	0.27 ± 0.09

Table 7.1: Spectral index for some sources.

7.2 Non-detected sources at 20 cm

Another important evidence, emerging from tables 2.3 and 3.5, is that some sources, successfully detected in band C, were not detected in band L observations. Indeed, these non-detections can easily be understood supposing that these source are optically thick at 1.4 GHz. Under this hypothesis, it is possible that these sources are below the noise level of band L maps.
It is however possible to estimate a minimum spectral index for each non-detected bubble assuming that the sources flux densities are not greater than the rms of the corresponding maps; we find that these minimum spectral indices are usually compatible with an optically thick emission regime. Assuming pure black-body emission ($\alpha = 2$) a minimum flux density for $\nu = 1.4675$ GHz has been computed for each bubble. The results are listed in table 7.2. It is important to notice that almost all these non-detections pose important constraints to the emission mechanism, and it is possible to assert that all the bubbles with a positive lower limit for the spectral index are very likely thermal emitters.

ID	$F(C)$ (mJy)	rms(L) (mJy/beam)	α	BB(L) (mJy)
3188	1.0 ± 0.2	1.5	$\gtrsim -0.3$	0.1
3192	1.2 ± 0.6	0.7	$\gtrsim 0.4$	0.1
3193	1.4 ± 0.6	0.7	$\gtrsim 0.6$	0.1
3309	3.4 ± 0.4	0.9	$\gtrsim 1.1$	0.3
3313	5.1 ± 0.7	1.0	$\gtrsim 1.3$	0.4
3347	1.5 ± 0.3	1.9?	$\gtrsim -0.2$	0.1
3362	12.1 ± 2.5	1.9	$\gtrsim 1.5$	1.1
3724	3.2 ± 0.4	1.5	$\gtrsim 0.6$	0.3
3736	18.1 ± 0.5	0.6?	$\gtrsim 2.8?$	1.6
4409	7.3 ± 0.1	0.5	$\gtrsim 2.2?$	0.6
4452	2.1 ± 0.4	0.6	$\gtrsim 1.0$	0.2
4580	2.0 ± 0.4	1.0	$\gtrsim 0.6$	0.2
4584	2.1 ± 0.5	1.2	$\gtrsim 0.5$	0.2

Table 7.2: Bubbles detected only in band C.

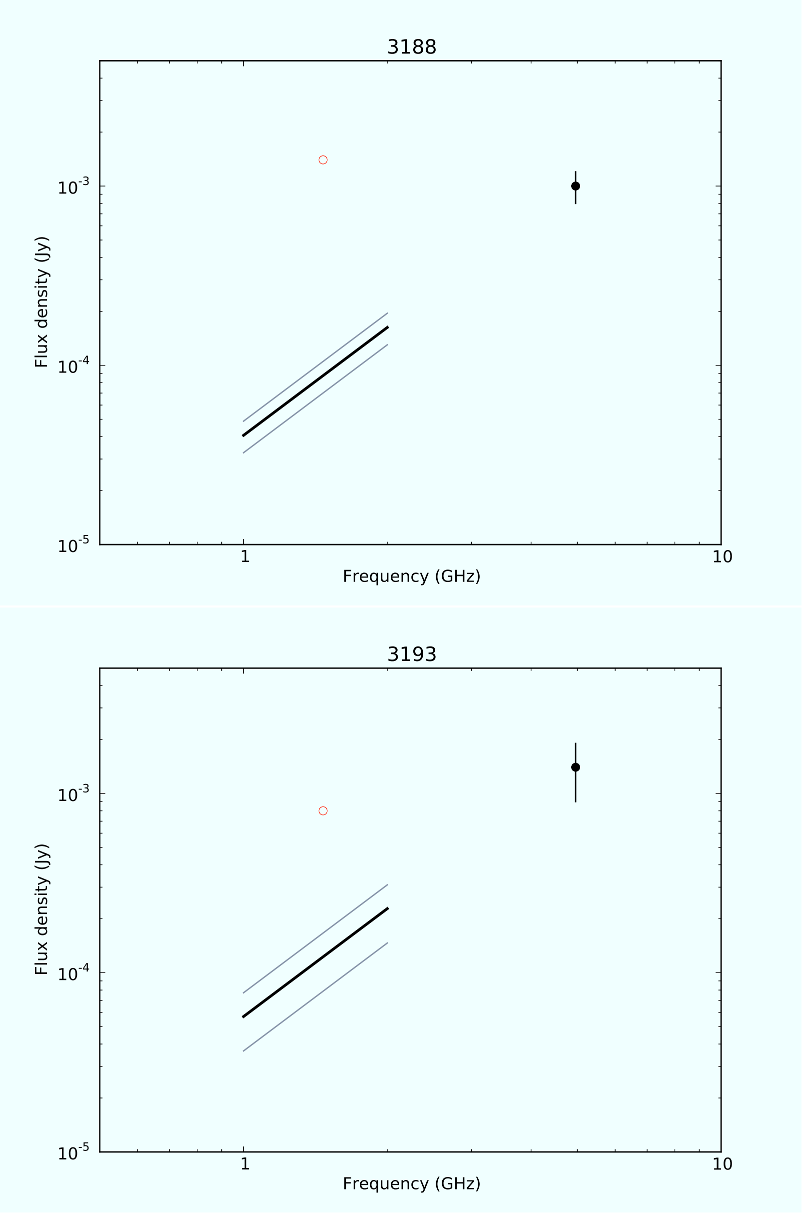

Figure 7.1: examples of sources detected only in band C. The flux density is extrapolated towards lower frequencies assuming a pure black-body emission (black line and gray lines for errors). The red circle represents the sensitivity limit of the respective map in band L.

7.3 Bubble 3188

The bubble 3188 was first discovered by MIPSGAL at 24 µm. The GLIMPSE survey failed to detect either a point source or a diffuse emission associated with the 24-µm nebula at any of the four IRAC bands. No sources were also detected by 2MASS in the near infrared or even MSX and WISE at any bands. No radio information were available for this bubble that bubble is not listed in any other catalog. From the VLA archive no useful past observations were available.

We were able to succesfully detect this bubble at 6 cm as a point source, and this would be the first radio detection for this source. Its flux density however is very low since it is estimated as 1.0 ± 0.3 mJy. Its radio faintness could explain why we failed to detect this source at 20 cm, where we could expect an even lower flux density and we have a poorer sensitivity. Indeed, as explained in section 7.2, the sensitivity of the 20-cm map we obtained for this bubble is around 1.5 mJy/beam, intended as rms. With this sensitivity it is not possible to exclude any possibility about the radio emission mechanism as the lower limit for the radio spectral index is found to be -0.3.

Also at 24 µm the source appears very faint, with its shape being a ring with a diameter of $16''$, as reported in the MIPSGAL catalog. The background at this wavelength appears very confused and bright.

We also observed the source searching for OH masers with GBT. We found evidence of a prominent OH maser at 1612 MHz, with a well-defined "U" shape at a mean LSR velocity value of about 20 km/s. A probable absorption feature around 35 km/s partially overlap the maser emission. Also at 1667 MHz there appears some kind of emission roughly at a velocity around the left peak of the previous maser but with an absorption feature around the other peak. At the other two bands no features are visible at that velocity. A high velocity line is visibile around 120 km/s at 1612 MHz (absorption) and at 1720 MHz (emission) (see figure 7.4).

The nature of the bubble 3188 is presently unknown. Despite the fact that no useful informations can be derived by radio continuum or mid-infrared image, the presence of a maser line only at 1612 MHz coming from a shell would suggest a classification as a very evolved OH/IR star entering the proto-PN phase or a pure proto-PN. Being, however, this bubble in a very crowded field, it is possible that this maser emission is from a nearby object, indeed. In figure 7.2 an infrared view of the bubble is shown; our radio map at 5 GHz are instead shown in figure 7.3.

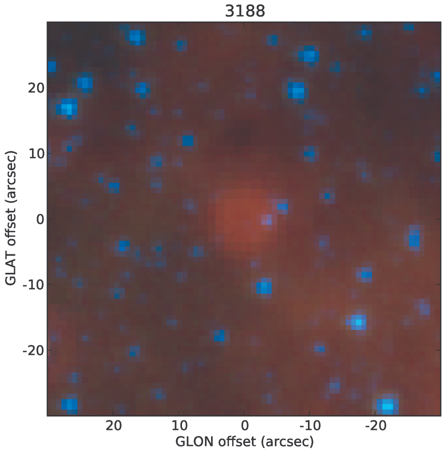

Figure 7.2: rgb image of the bubble 3188 at 24 µm (red), 8 µm (green) and 3.6 µm (blue). It is possible to notice the bubble is detected only at 24 µm and that there is no evidence of a central source.

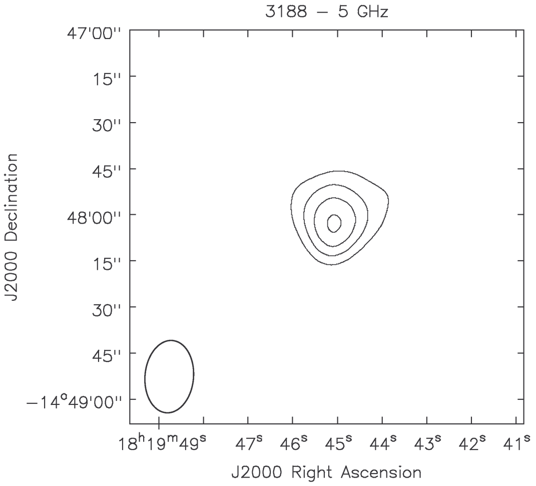

Figure 7.3: radio contour image of the bubble 3188 from our data at 5 GHz. Contours are 0.3, 0.6, 0.9 and 1.2 mJy/beam.

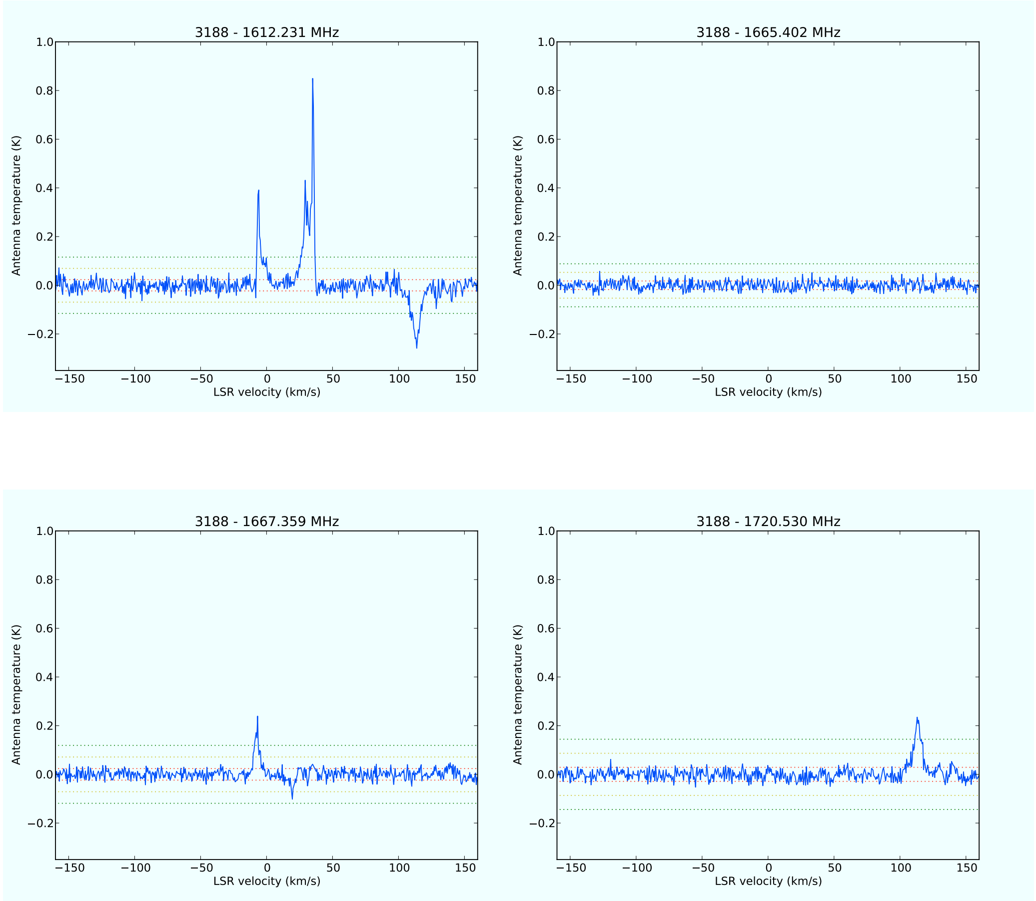

Figure 7.4: Complete spectrum of the bubble 3188. It is possible to notice a very impressive maser at 1612 MHz, maybe present also at 1667 MHz. An high velocity line (∼120 km/s LSR) is visible in absorption in the first band and in emission in the last one. Around 1665 MHz no feature are visible. The maser emission is clearly from a shell; if it will be confirmed to originate from our bubble than this could be classified as a very evolved OH/IR star entering the proto-planetary nebula phase or a pure PPN [24].

7.4 Bubble 3222

The bubble 3222 (whose main ID is 2MASS J18455526–0225089) was first discovered by IRAS at 25 µm and listed in the IRAS catalog in 1986. It was observed as point source by 2MASS in bands H and K_s but not in band J [41]. It was also observed by MSX in bands A, C, D and E [42], by GLIMPSE in all bands and by WISE in all bands [43]. The bubble was observed as a radio source, both at 1.4 GHz and at 5 GHz, by the New GPS survey [29] as a compact source and listed in the MAGPIS catalog [16]. The bubble was also successfully observed with the J.C. Maxwell Telescope [44] in order to detect ^{13}CO $J = 2-1$ line emission (figure 7.8). From the VLA archive no useful past observations were available.

From our data the sources appears unresolved in both bands, so the flux density has been calculated using the CASA task `imfit`. For this source we obtained a spectral index of 0.05 ± 0.13, suggesting that the source is still optically thick at 1.4 GHz, though near to turn-over (figure 7.7).

At 24 µm the source appears as a bright spherical nebula with a diameter of $26''$, as reported in the MIPSGAL catalog. Just outside the nebula, it is possible to see a faint shell with a diameter of about $50''$, but this feature is an image artifact due to PSF lobes.

The nature of the bubble 3222 is presently unknown though it has been classified as PN candidate [45] in an unclear way. It is anyway possible to find that a classification as PN would be compatible with the MSX color as shown in figure 8.12 as well as classification as compact H II region.

In figure 7.5 an infrared view of the bubble is shown; our radio maps at 1.4 GHz and 5 GHz are instead shown in figure 7.6.

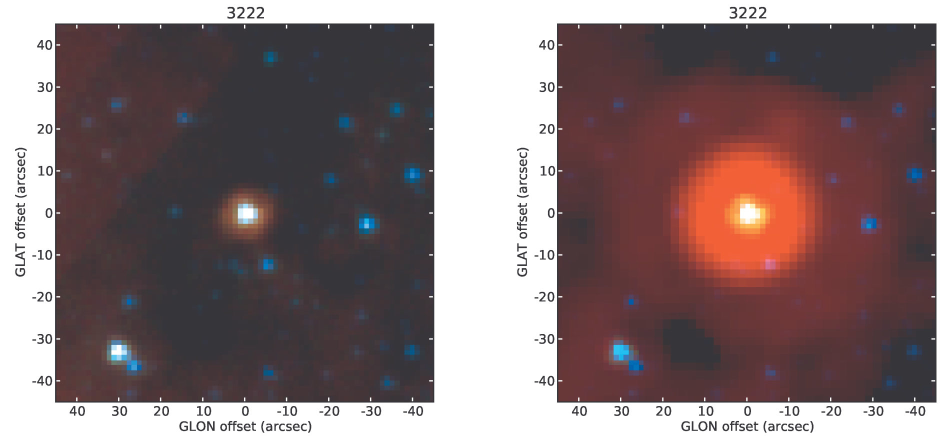

Figure 7.5: rgb images of the bubble 3222: left at 8 μm (red), 5.8 μm (green) and 3.6 μm (blue); right at 24 μm (red), 8 μm (green) and 3.6 μm (blue). In the left image it is possible to see that the emission at 5.8 μm and at 8 μm is slightly more extended than the emission at 3.6 μm; in the right image the bubble seems to show a second outer shell, but it is an artifact (PSF sidelobe).

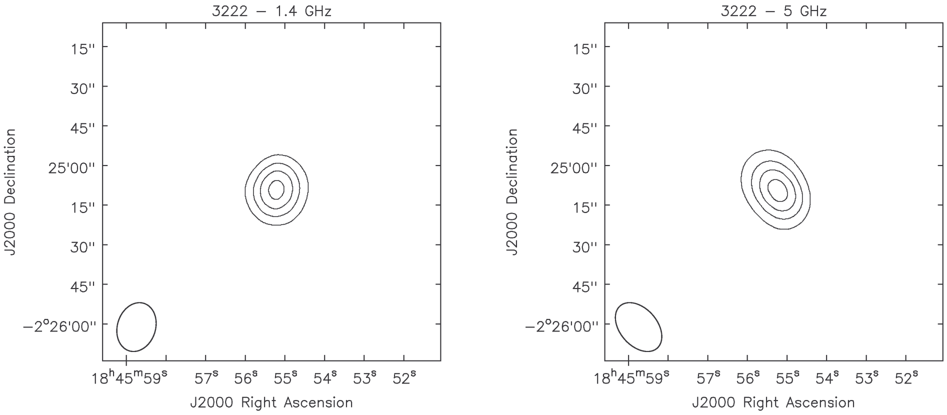

Figure 7.6: radio contour images of the bubble 3222 from our data. Contours are 10, 15, 20 and 25 mJy/beam (left) and 5, 10, 15, and 20 mJy/beam (right).

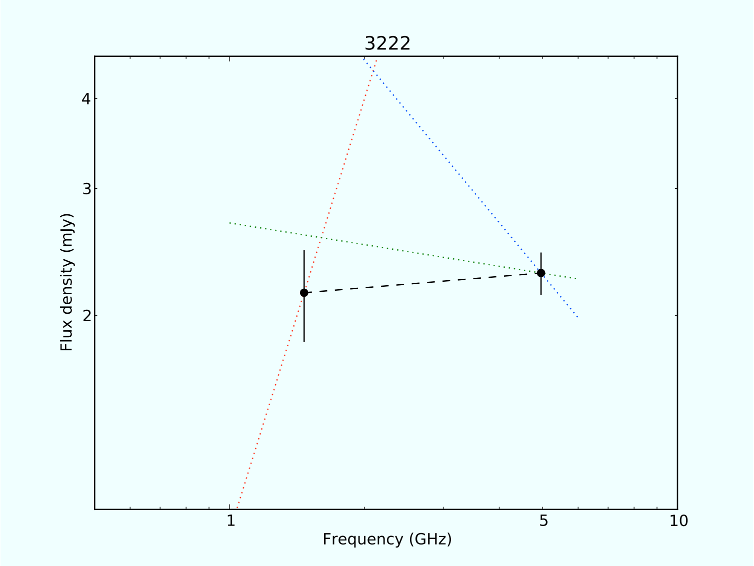

Figure 7.7: radio continuum spectrum of the bubble 3222.

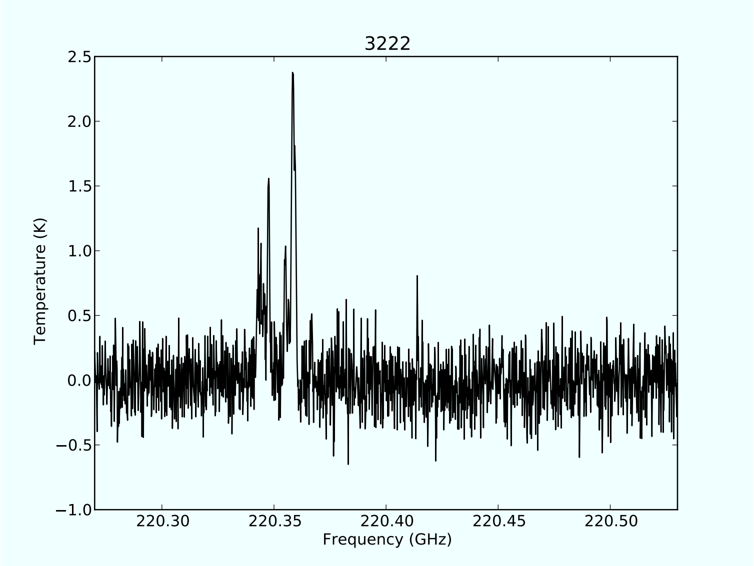

Figure 7.8: detection of ^{13}CO $J = 2-1$ emission toward the bubble 3222 with the JCMT.

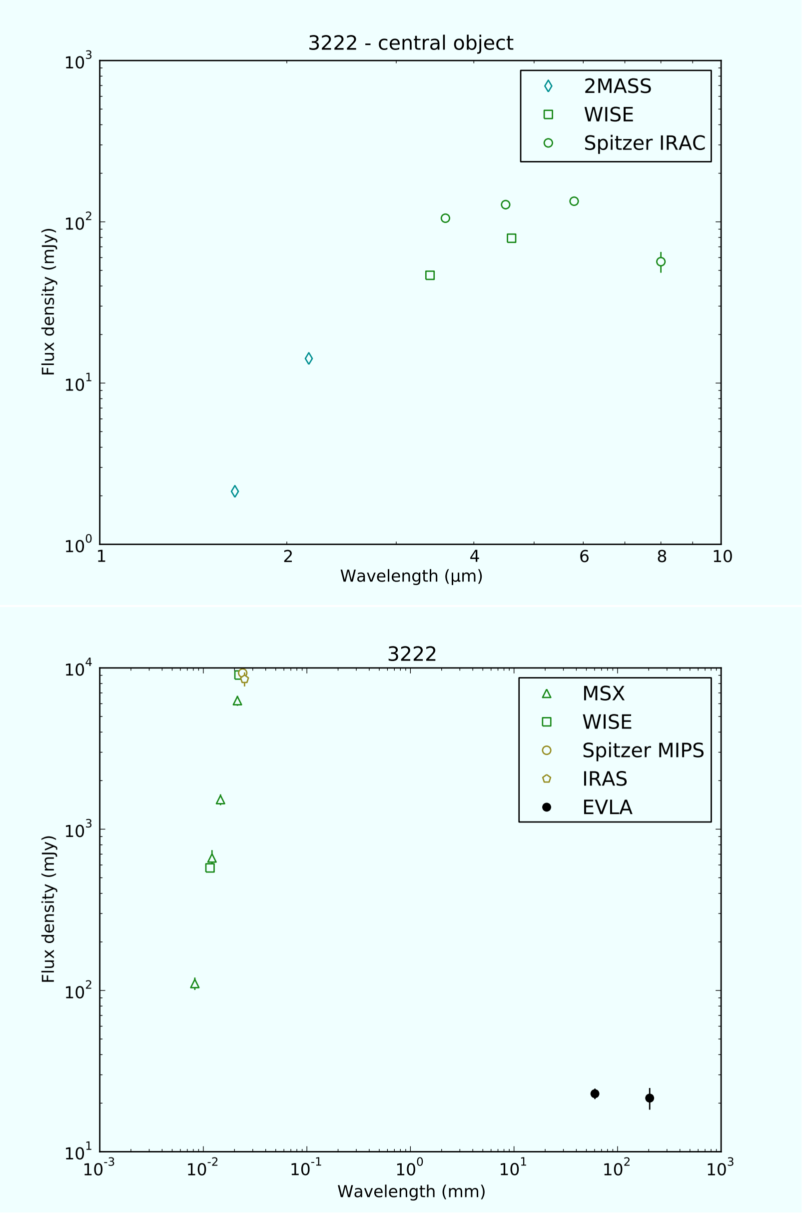

Figure 7.9: complete SED of the bubble 3222.

7.5 Bubble 3333

The bubble 3333 was first discovered by MIPSGAL. The GLIMPSE survey failed to detect either a point source or a diffuse emission associated with the 24-µm nebula at any of the four IRAC bands. No sources were also detected by 2MASS in the near infrared or even MSX and WISE at any bands. In the NVSS catalog it is possible to find a source with a position roughly compatible with the bubble (15 ± 13 arcseconds away), but since it is near the sensitivity low limit of the survey ($\sim 2.5\,\mathrm{mJy}$) the uncertainties on flux density and position are great. The bubble is not listed in any other catalog. From the New GPS survey at 20 cm cut-outs nothing can be said since the source appears resolved out and confused with the background (it is not listed as detected source at all). From the VLA archive no useful past observations were available.

From our data the sources appears resolved in both bands, though its emission at 1.4 GHz is weaker and the respective map presents a much higher noise level.

The flux density has been calculated convolving first the band-L map to have the same beam of the other map and then integrating over the same area, given by the 1σ level of the band-L image obtained after the convolution. For this source we obtained a spectral index of 0.39 ± 0.26, suggesting that the source is still optically thick at 1.4 GHz, though near to turn-over.

The source dimensions at 5 GHz are about $53'' \times 48''$ at 5σ level, larger than the dimensions of the 24 µm source ($23''$ according to MIPSGAL catalog). At 24 µm the source appears as a broad shell while in radio, even if it is resolved, due to the poor resolution it appears as simply globular.

We also observed the source searching for OH masers with GBT. We found some evidences of absorption lines around 1665 MHz and 1667 MHz, while the two other spectral windows were too much corrupted by RFI that no useful data could be extracted. The two spectra are reported in figure 7.14.

The nature of the bubble 3333 is presently unknown; the lack of a counterpart in the GLIMPSE tiles and in others mid-infrared catalogs makes it possible that the nebula emission at 24 µm is mainly due to the [O IV] line, rather than to a dust thermal continuum, though it may also be not detected because of its low brightness. The presence of a gas environment is compatible with our radio detection of a likely thermal free-free emission.

In figure 7.10 an infrared view of the bubble is shown; our radio maps at 1.4 GHz and 5 GHz are instead shown in figure 7.11.

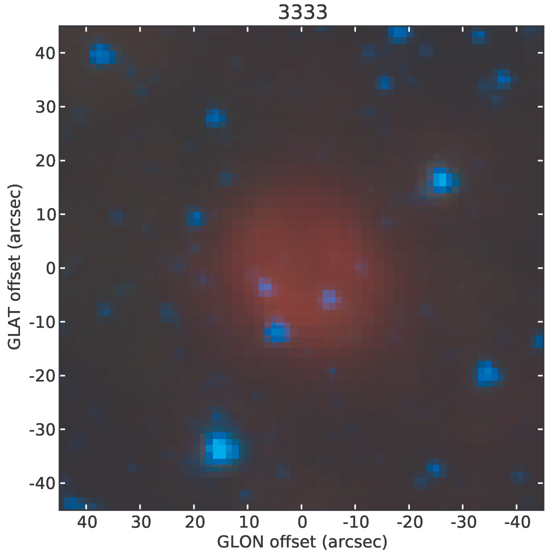

Figure 7.10: rgb image of the bubble 3333 at 24 µm (red), 8 µm (green) and 3.6 µm (blue). It is possible to notice the bubble is detected only at 24 µm and that there is no evidence of a central source.

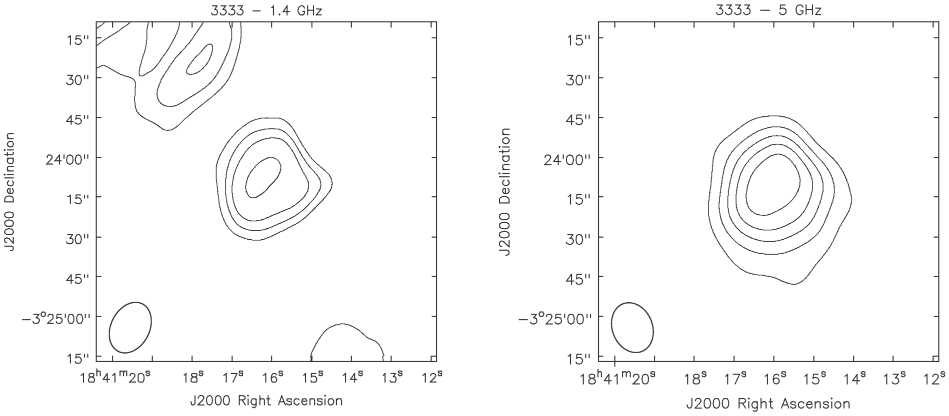

Figure 7.11: radio contour images of the bubble 3333 from our data. Contours are 0.35, 0.70, 1.05 and 1.75 mJy/beam (left) and 0.5, 1.0, 1.5, 2.0 and 2.5 mJy/beam (right).

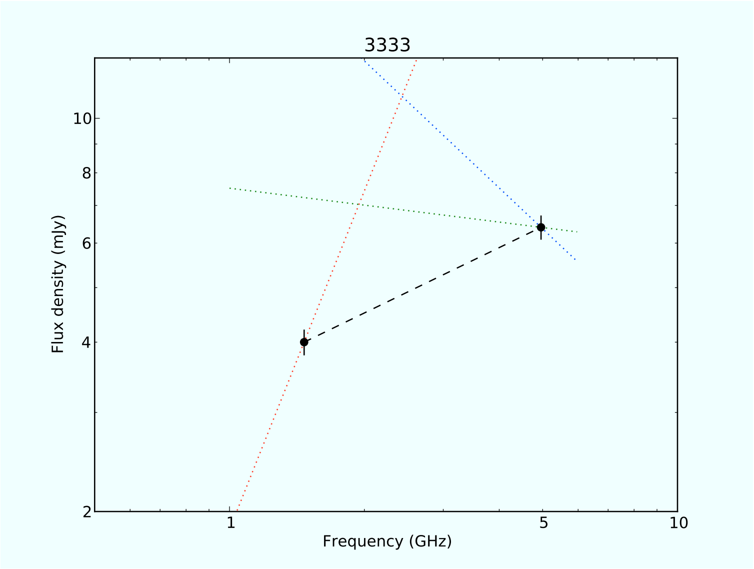

Figure 7.12: radio continuum spectrum of the bubble 3333.

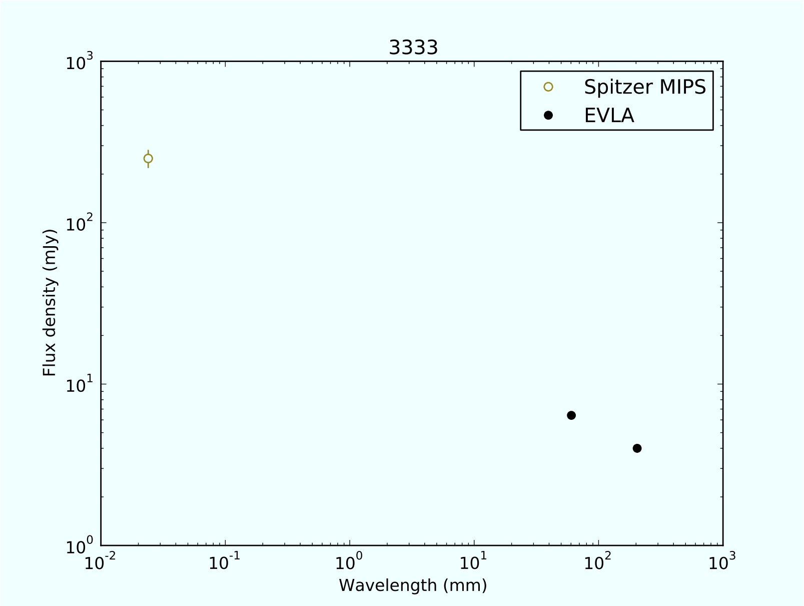

Figure 7.13: SED of the bubble 3333 nebula.

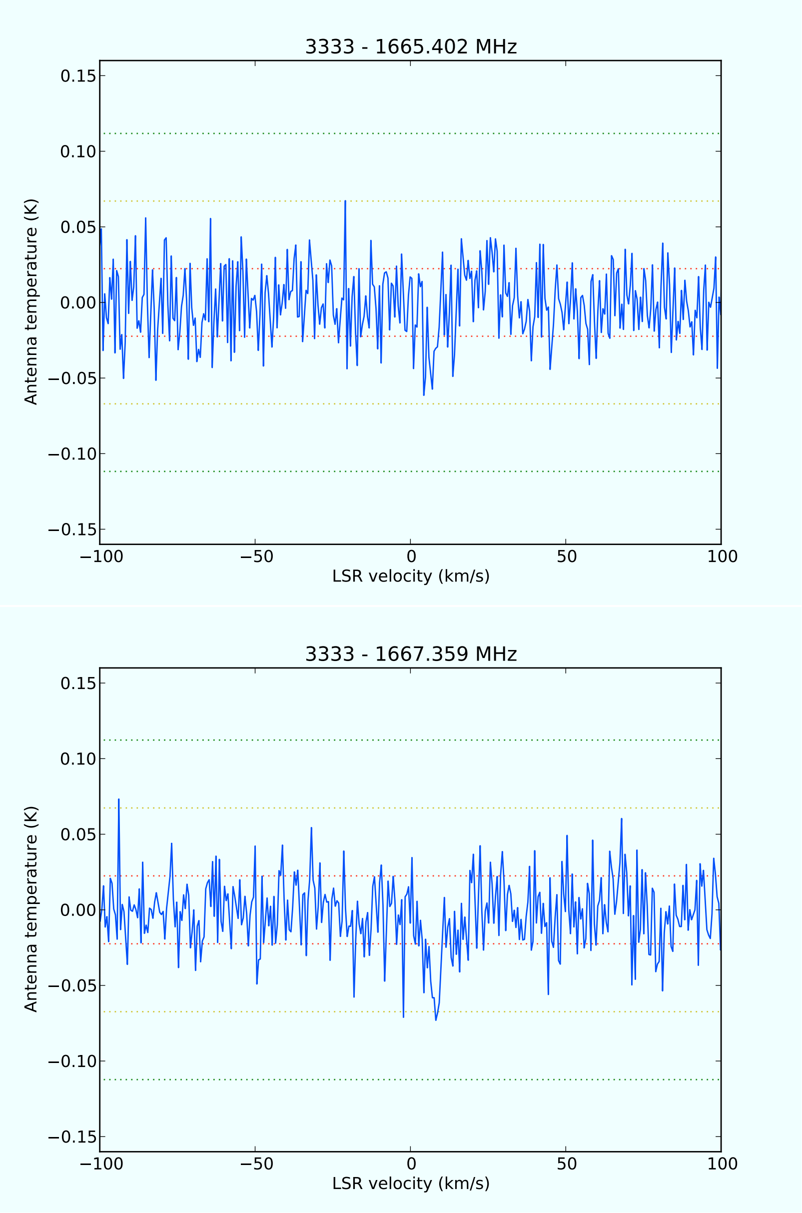

Figure 7.14: GBT spectra of the bubble 3333.

7.6 Bubble 3354

The bubble 3354 (whose main ID is IRAS 18441-0048) was first discovered by IRAS only at 60 µm. The MIPSGAL survey was able to detect a shell nebula with a bright spot near its edge at 24 µm. In the GLIMPSE tiles, the bubble appears as a very faint shell at 5.8 µm and at 8 µm, while it is almost invisible in the other two bands. There are no compact sources clearly associated to the nebular emission but two of them deserve attention. The first one is detected in all IRAC bands and identified by GLIMPSE survey as G031.7293+00.6980; this object, most likely a star, is located in the inner part of the nebula and, on the contrary with respect to other nearby stars, shows an unusal red color; it is not detected in any band by 2MASS while WISE detects a point source slightly more than $2''$ away [43]. The second compact source is the bright spot detected at 24 µm, it is possible that it is not a real compact source since it is not detected by IRAC, which instead observes a faint diffuse emission. WISE succeeded to observe the bubble in the bands $W3$ and $W4$, but not in the other two bands, and not reliable flux densities can be extracted. At the radio wavelengths, the bubble has been detected by NVSS [28], by MAGPIS [16] and also by the HRDS survey [46] with the GBT.

From our data, the source appears resolved in both bands, with a roundish morphology. The flux density has been calculated convolving first the band-L map to have the same beam of the other map and then integrating over the same area, given by the 2σ level of the band-L image obtained after the convolution. For this source we obtained a spectral index of 0.02 ± 0.08, resulting then in a quite flat spectrum. Since no photometry was available for GLIMPSE nebula, it has been computed using aperture photometry.

The source diameter at 1.4 GHz is about $39''$ at 2σ level. As already said, the 24 µm source (extended for $44''$) appears as an irregular ring with a bright spot on the edge; it is noteworthy that the radio source seems centered on this bright spot rather then on the bubble itself. The HRDS found that the nebula shows narrow RRLs with a $\Delta v \simeq 22$ km/s and a velocity of -39.2 km/s, which would place the source in the outer Galactic disk [46]. These parameters along with the presence of a well detected shell in the IRAC bands should rule out the possibility that this bubble is a planetary nebula; a more consistent conclusion is that this source could be an H II region, compatible also with a SED peak beyond 100 µm.

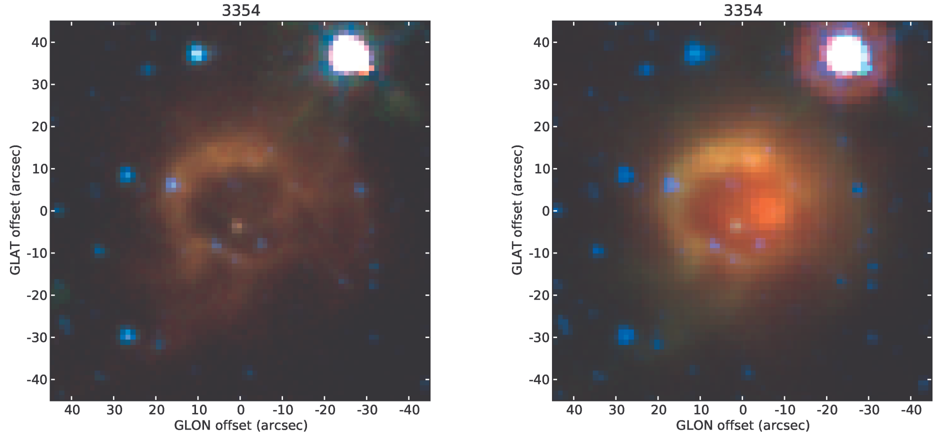

Figure 7.15: rgb images of the bubble 3354: left at 8 µm (red), 5.8 µm (green) and 3.6 µm (blue); right at 24 µm (red), 8 µm (green) and 3.6 µm (blue). A shell is well detected at 5.8 µm and at 8 µm, but also at 24 µm, where also a bright spot is visible. In the left image it is possible to notice a very red star in the middle of the shell.

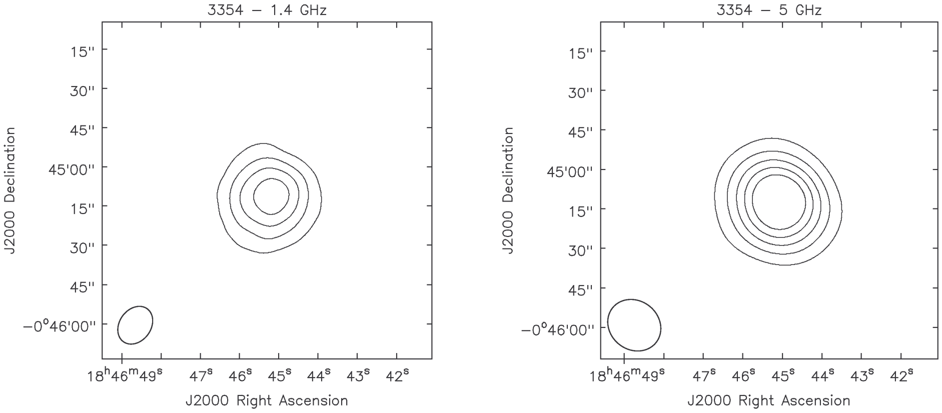

Figure 7.16: radio contour images of the bubble 3354 from our data. Contours are 1, 2, 3 and 4 mJy/beam (left) and 1, 2, 3, 4 and 5 mJy/beam (right).

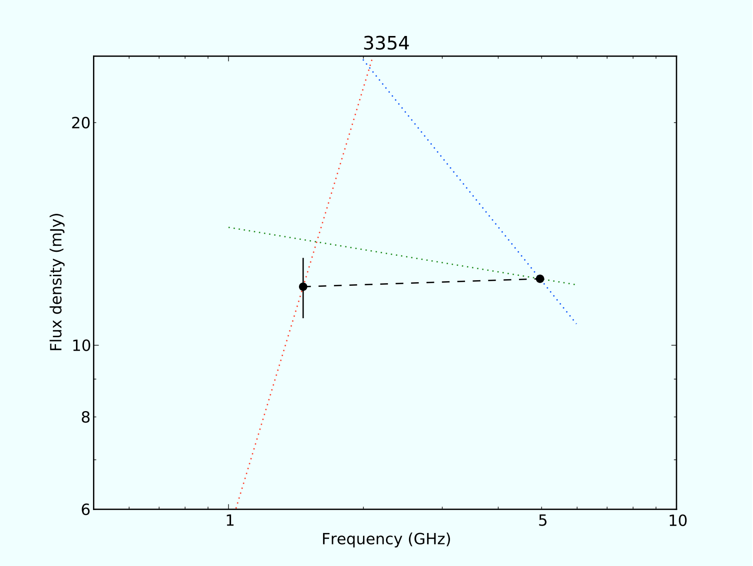

Figure 7.17: radio continuum spectrum of the bubble 3354.

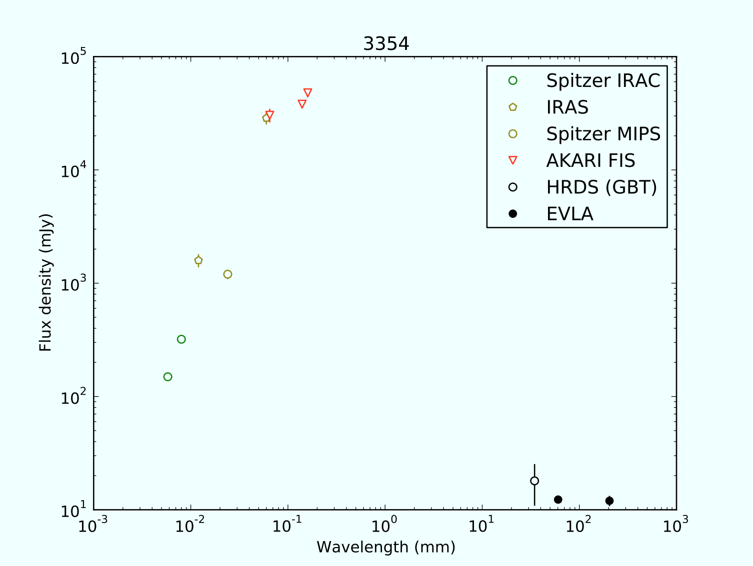

Figure 7.18: SED of the bubble 3354 nebula. For IRAC points the photometry has been calculated from the FITS file, since no archive photometry was available.

7.7 Bubble 3367

The bubble 3367 was first discovered by MIPSGAL survey, that was able to detect a disk nebula at 24 µm. From the GLIMPSE tiles, a point source is detected in the three low bands in the middle of the nebula while at 8 µm a small nebula surround this compact object. It was observed as point source by 2MASS in bands *H* and K_s but not in band *J* [41]. It was also observed by WISE in all bands [43] and by AKARI at 18 µm with IRC. The bubble was observed as a radio source, at 5 GHz, by the New GPS survey [29] as a compact source. From the VLA archive no useful past observations were available.

From our data the sources appears unresolved in both bands, so the flux density has been calculated using the CASA task `imfit`. For this source we obtained an enigmatic spectral index of -0.30 ± 0.19, too steep to be compatible with a free-free emission, even if the large error does not allow to rule out this hypothesis.

The morphology in the infrared resembles closely to that of the bubble 3222, classified as a PN candidate, even if the radio spectral index would not be compatible.

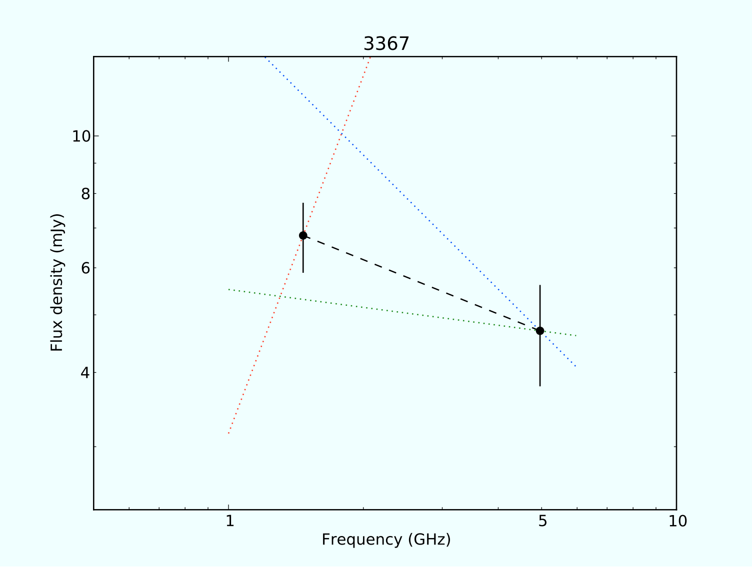

Figure 7.19: radio continuum spectrum of the bubble 3367.

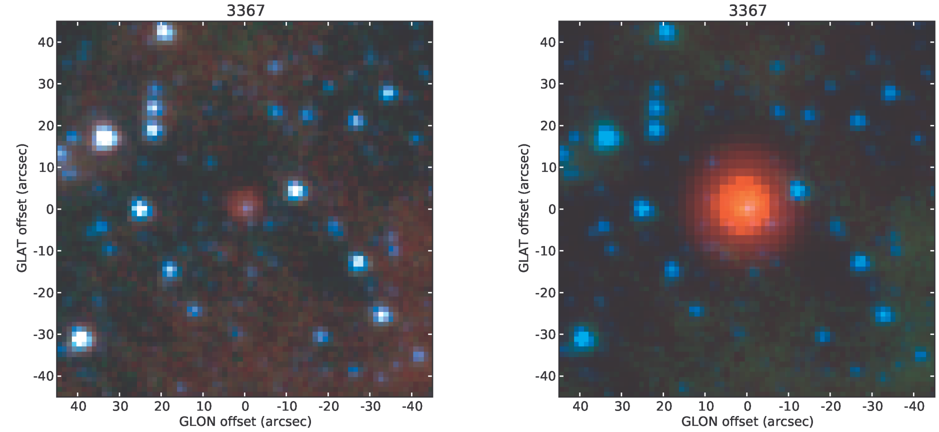

Figure 7.20: rgb images of the bubble 3367: left at 8 µm (red), 5.8 µm (green) and 3.6 µm (blue); right at 24 µm (red), 8 µm (green) and 3.6 µm (blue). The extended nebula is detected only at 24 µm, while a more compact one is visible at 8 µm.

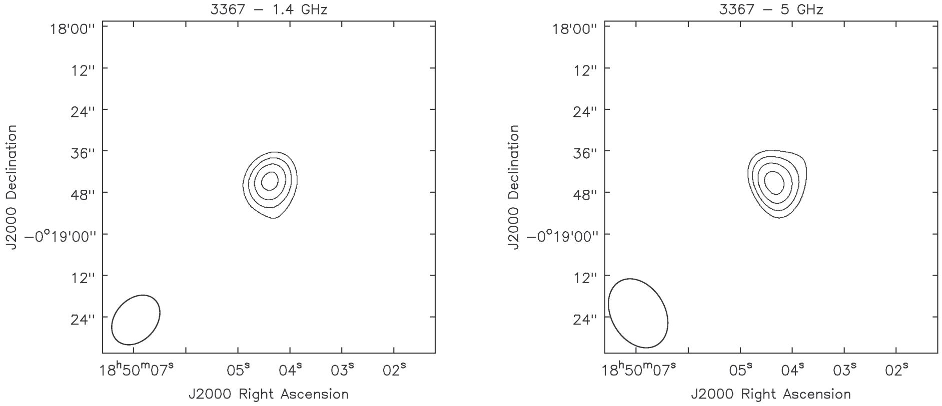

Figure 7.21: radio contour images of the bubble 3367 from our data. Contours are 3, 5, 7 and 9 mJy/beam (left) and 2.5, 3.5, 4.5 and 5.5 mJy/beam (right).

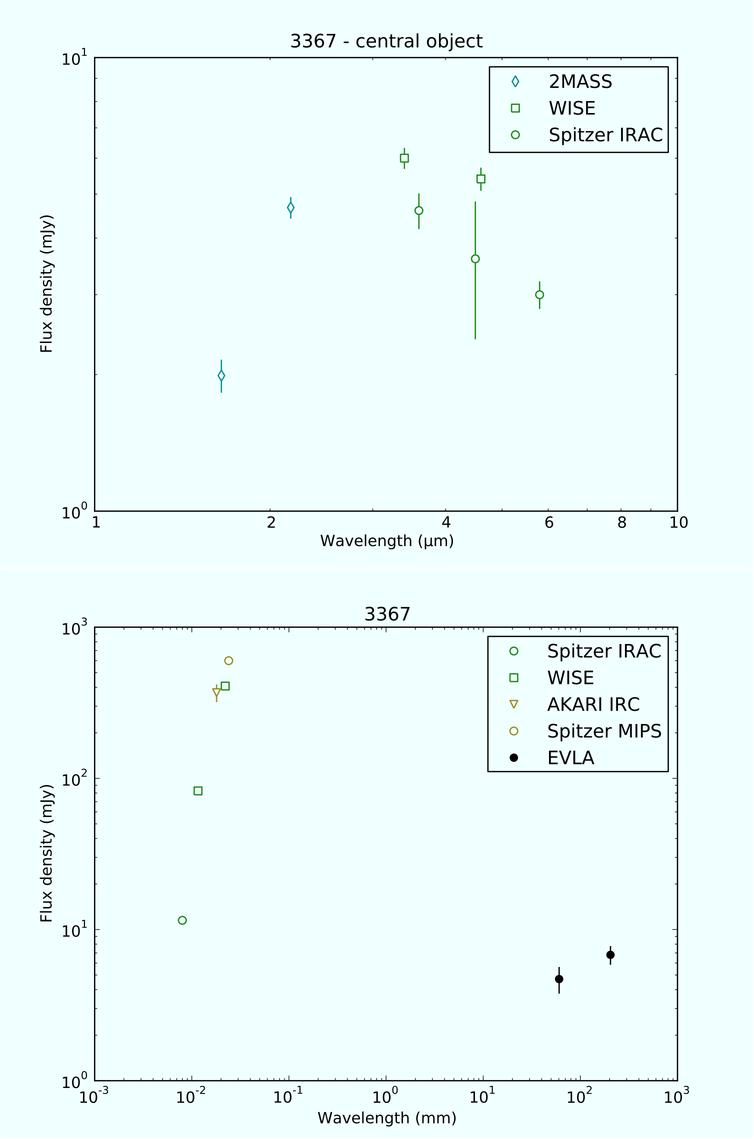

Figure 7.22: complete SED of the bubble 3367.

7.8 Bubble 3384

The bubble 3384 was first discovered by MIPSGAL. The GLIMPSE survey did not detect either a point source or a diffuse emission associated with the 24-μm nebula at any of the four IRAC bands. No sources were also detected by 2MASS in the near infrared or even MSX and WISE at any bands. In the NVSS catalog it is possible to find a source with a position roughly compatible with the bubble (7 ± 12 arcseconds away), but since it is near the sensitivity low limit of the survey the uncertainties on flux density and position are great. The bubble is not listed in any other catalog. From the VLA archive no useful past observations were available.

Initial band-C map of bubble 3384 appeared corrupted by artifacts and quite noisy, with an rms of about 0.39 mJy/beam. The source appeared slightly resolved with a peak intensity of 5.0 mJy; a cautious 3-cycle self-calibration process has then been performed, leading to a reduction of the artifact and to a lower noise level (rms $\sim$ 0.16 mJy/beam). The peak intensity of the self-calibrated map rose to 10.9 mJy, giving a total integrated flux of 17.8 ± 0.4 mJy at 5σ level.

At 1.4 GHz the source appears much weaker; indeed it appears as a point source with a peak intensity of 2.1 mJy. Since the rms of the band-L image is as high as 0.82 mJy/beam, it is reasonable to suppose that the extended emission at this frequency is below the noise level, and we observe therefore only the brightest region.

Considering only the peak intensity we would obtain a spectral index of 1.4 ± 0.3, still compatible with an optically thick free-free source. The source dimensions at 5 GHz are about $52'' \times 42''$, about twice bigger than the 24 μm source. Anyway the 24 μm image show a slightly bipolar structure for the bubble 3384, oriented approximately in the same direction of 5 GHz emission major axis.

Due to the significant lack of data nothing can be said now about the nature of this bubble.

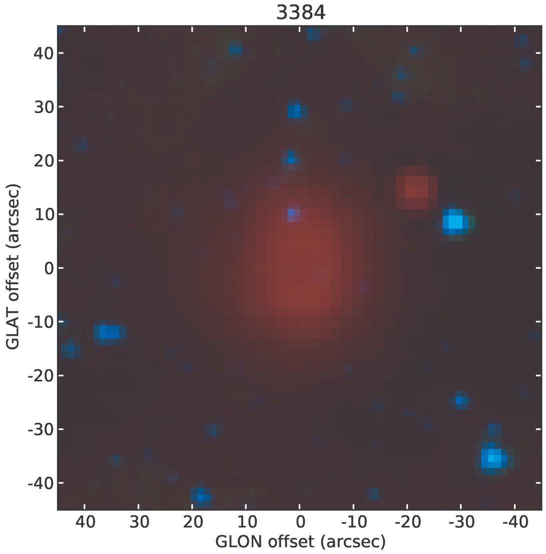

Figure 7.23: rgb image of the bubble 3384 at 24 µm (red), 8 µm (green) and 3.6 µm (blue). It is possible to notice the bubble is detected only at 24 µm and that there is no evidence of a central source.

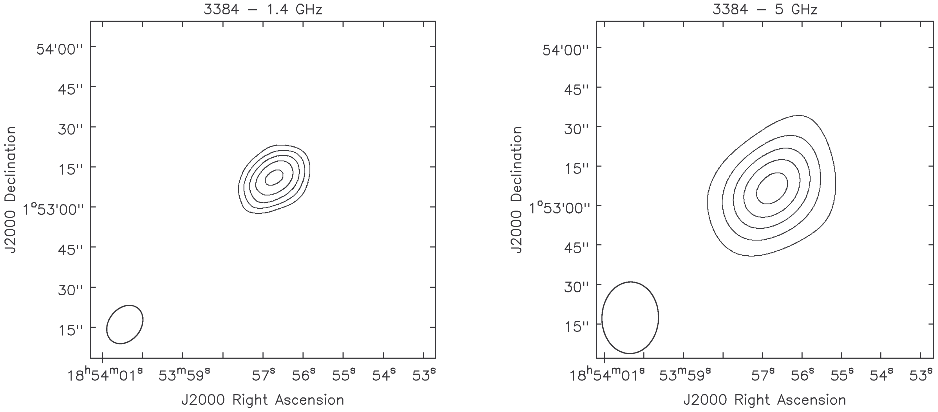

Figure 7.24: radio contour images of the bubble 3384 from our data. Contours are 0.4, 0.8, 1.2, 1.6 and 2 mJy/beam (left) and 2, 4, 6, 8 and 10 mJy/beam (right).

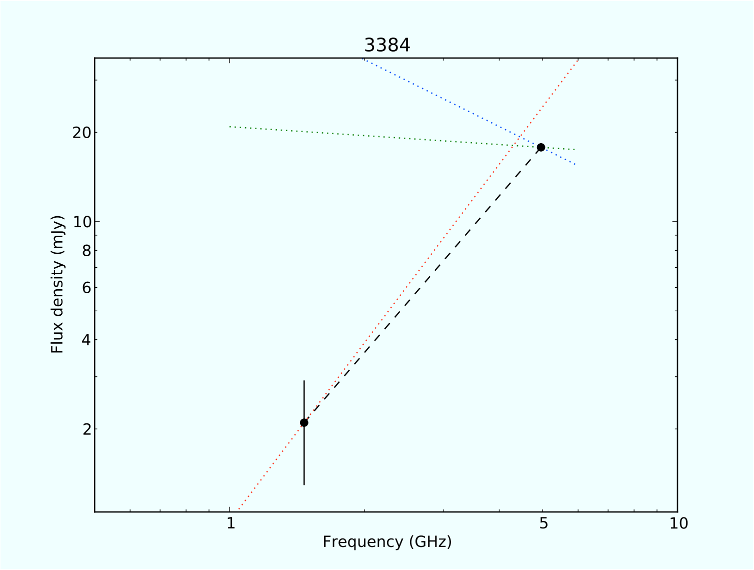

Figure 7.25: radio continuum spectrum of the bubble 3384.

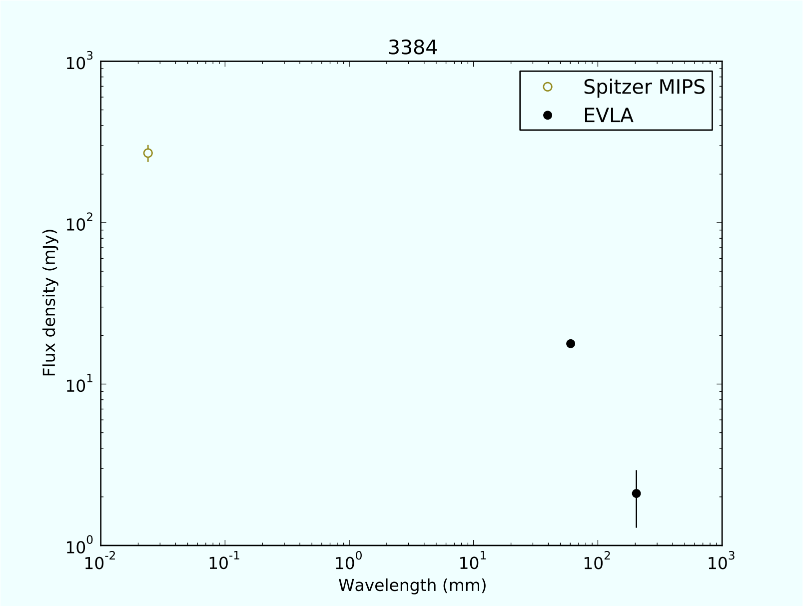

Figure 7.26: SED of the bubble 3384 nebula.

7.9 Bubble 3438

The bubble 3438 (whose main ID is IRAS 19040+0817) was first discovered by IRAS at 12 µm and at 25 µm and listed in the IRAS catalog in 1986. In the MIPSGAL tiles at 24 µm it appears as a ring nebula with a very bright central object. The central object, but not the nebula, is clearly detected in all IRAC bands and in all 2MASS bands [41]. It was also observed by MSX in bands A, C, D and E [42] and by WISE in all bands [43]. The central object is so bright that it was observed in band R and band I by GSC II and by USNO-B1.0 [47]. The bubble was observed as a radio source at 5 GHz by the RMS survey [45]. From the VLA archive no useful past observations were available.

The source appears maybe resolved in band L, with a roundish morphology, but it is clearly not resolved in band C. The flux density for the band-L map ha been calculated integrating over an area given by the 2σ level. For this source we obtained a spectral index of 0.02 ± 0.07, resulting then in a quite flat spectrum.

The source dimensions at 1.4 GHz are about $25'' \times 22''$ at 5σ level. The 24 µm source appears ring-like with a bright at its center; the radio source cover approximately the same area of the mid-IR image. It is not clear whether the source is really resolved or not at 1.4 GHz, also because an high resolution image at 5 GHz from the RMS survey show a point source with a beam of $1.4'' \times 1.3''$. A concatenation of this dataset with ours shows that the source is really point-like at 5 GHz with a beam of $1.6'' \times 1.5''$ and with a calculated flux density of 8.2 ± 0.2 mJy, which would give a spectral index of -0.18 ± 0.07. Since the archive data were taken in 2003 it is not to be excluded that the slight flux density difference could be a real luminosity variation of the source.

The 2MASS+MSX color classification [35] of the central star is compatible either with a young Herbig Ae/Be star or with an evolved OH/IR star, while it seems not compatible with a PN or a compact H II region. So, despite of the relative abundance of observations, the nature of this bubble is still unclear.

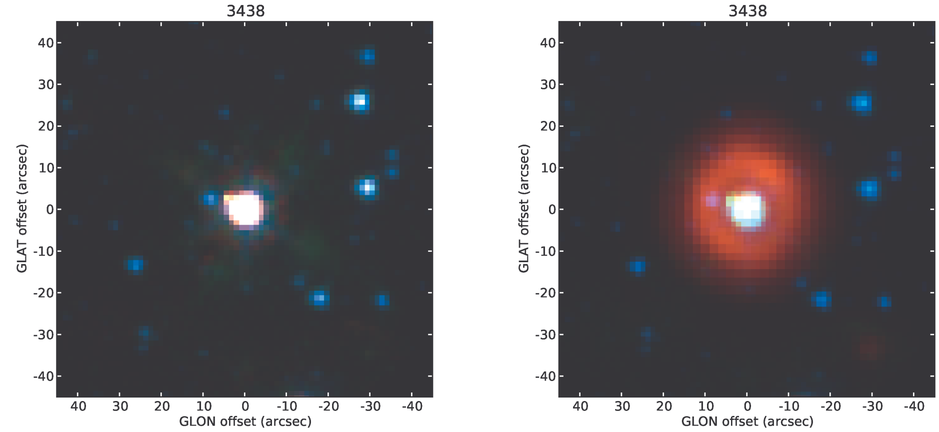

Figure 7.27: rgb images of the bubble 3438: left at 8 µm (red), 5.8 µm (green) and 3.6 µm (blue); right at 24 µm (red), 8 µm (green) and 3.6 µm (blue). The source is characterized by a very bright central source, but the nebula is detected only at 24 µm.

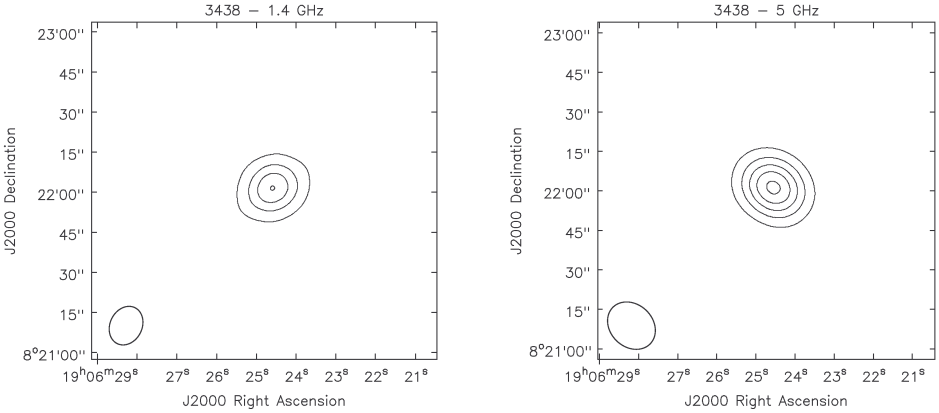

Figure 7.28: radio contour images of the bubble 3438 from our data. Contours are 1.5, 3, 4.5 and 6 mJy/beam (left) and 2, 4, 6, 8 and 10 mJy/beam (right).

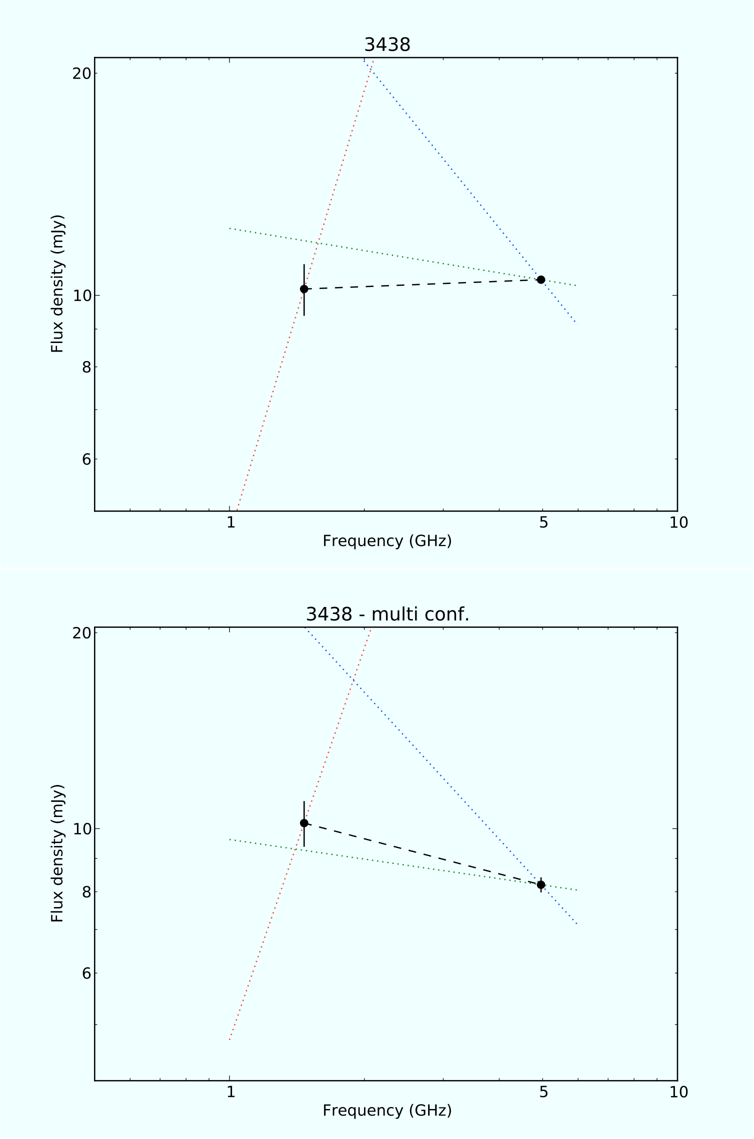

Figure 7.29: radio continuum spectrum of the bubble 3438.

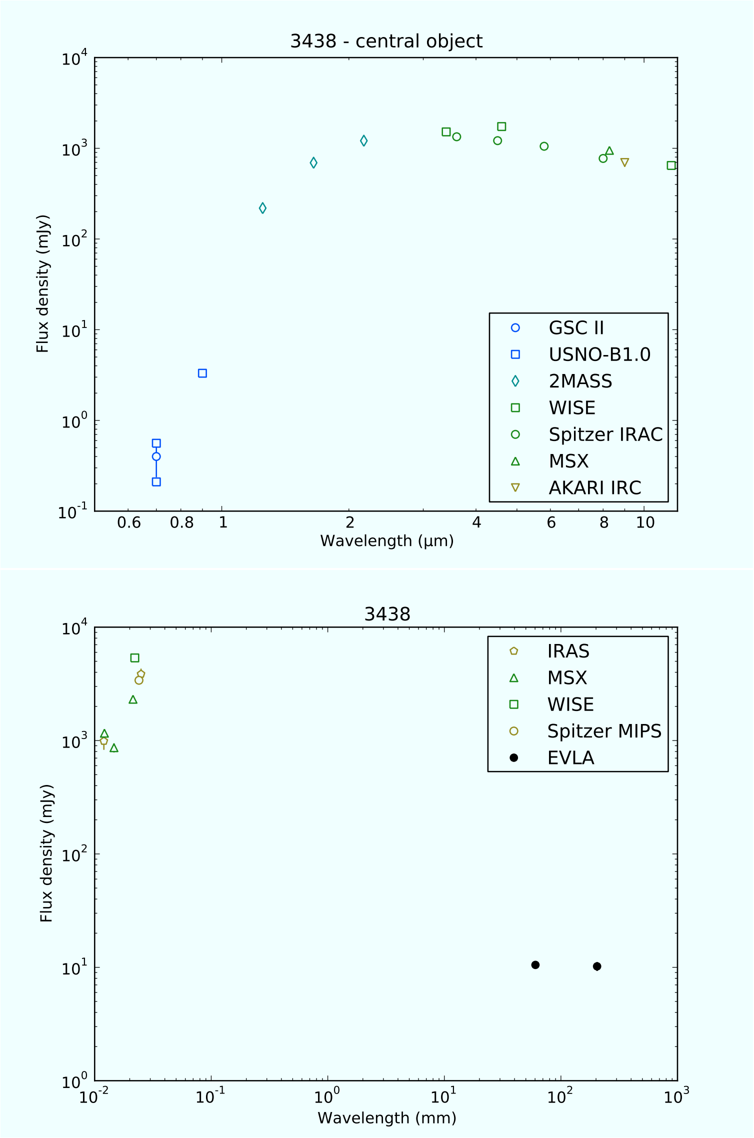

Figure 7.30: complete SED of the bubble 3438.

7.10 Bubble 3448

The bubble 3448 (whose main ID is IRAS 19041+0902) was first discovered by IRAS at 25 µm and at 60 µm and listed in the IRAS catalog in 1986. In the MIPSGAL tiles at 24 µm it appears as a bipolar nebula whose diameter is 33″; at 8 µm, and only in this band, the GLIMPSE survey shows the same bipolar nebula though fainter. A central object is clearly detected in all IRAC bands and in all 2MASS bands [41]. It was also observed by WISE in all bands [43] and in band *R* by USNO-B1.0 [47]. The bubble was observed as a radio source at 20 cm by the NVSS survey [28].

Also this source appears slightly resolved in band *L*, with a roundish morphology, but not resolved in band *C*. The flux density for the band-*L* map has been calculated integrating over an area given by the 3σ level. For this source we obtained a spectral index of -0.01 ± 0.08, resulting then in a quite flat spectrum. From the VLA archive no useful past observations were available.

The source dimensions at 1.4 GHz are about $28'' \times 23''$ at 3σ level. The 24 µm source covers approximately the same area of the radio emission.

The nature of this bubble is presently unclear. Gvaramadze et al. (2010) found that the spectrum of the central star is WR-like, and the bubble could be a PN with a [WC] central star [8][48]. This classification would be compatible with our radio spectral index.

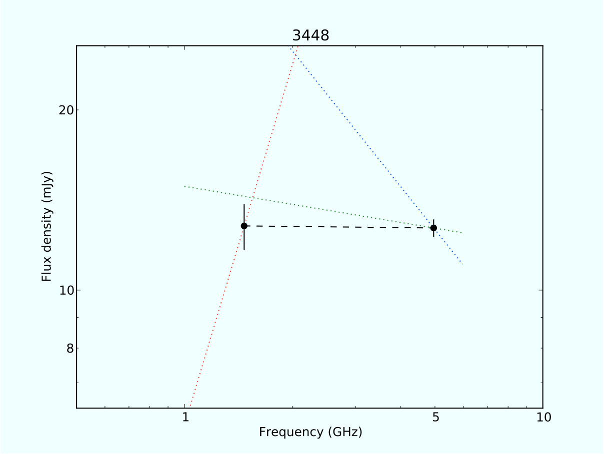

Figure 7.31: radio continuum spectrum of the bubble 3448.

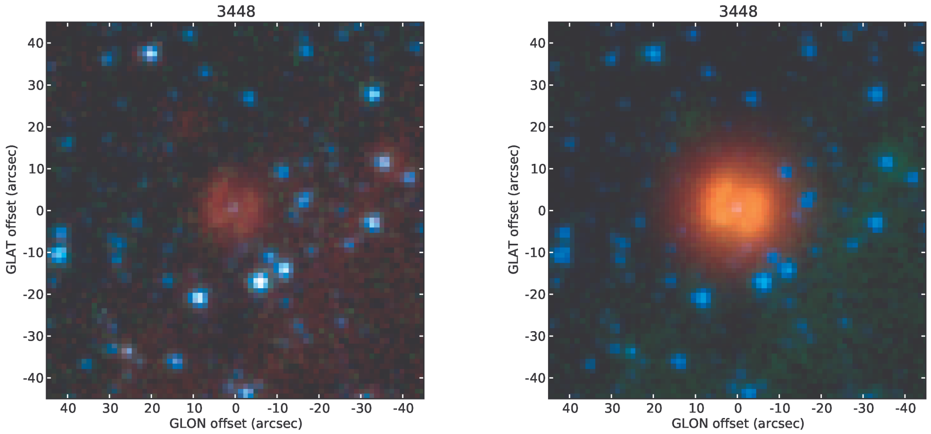

Figure 7.32: rgb images of the bubble 3448: left at 8 µm (red), 5.8 µm (green) and 3.6 µm (blue); right at 24 µm (red), 8 µm (green) and 3.6 µm (blue). The bipolar nebula is clearly detected both at 24 µm and at 8 µm, while at shorter wavelengths only the central object is visible.

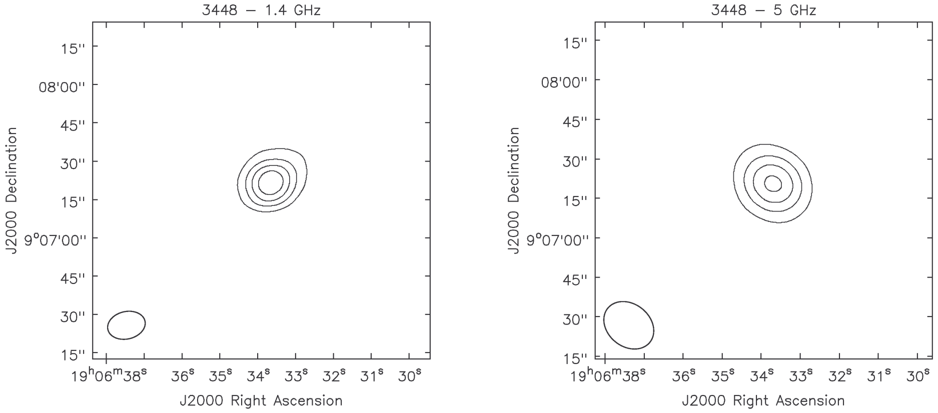

Figure 7.33: radio contour images of the bubble 3448 from our data. Contours are 2, 4, 6 and 8 mJy/beam (left) and 3, 6, 9 and 12 mJy/beam (right).

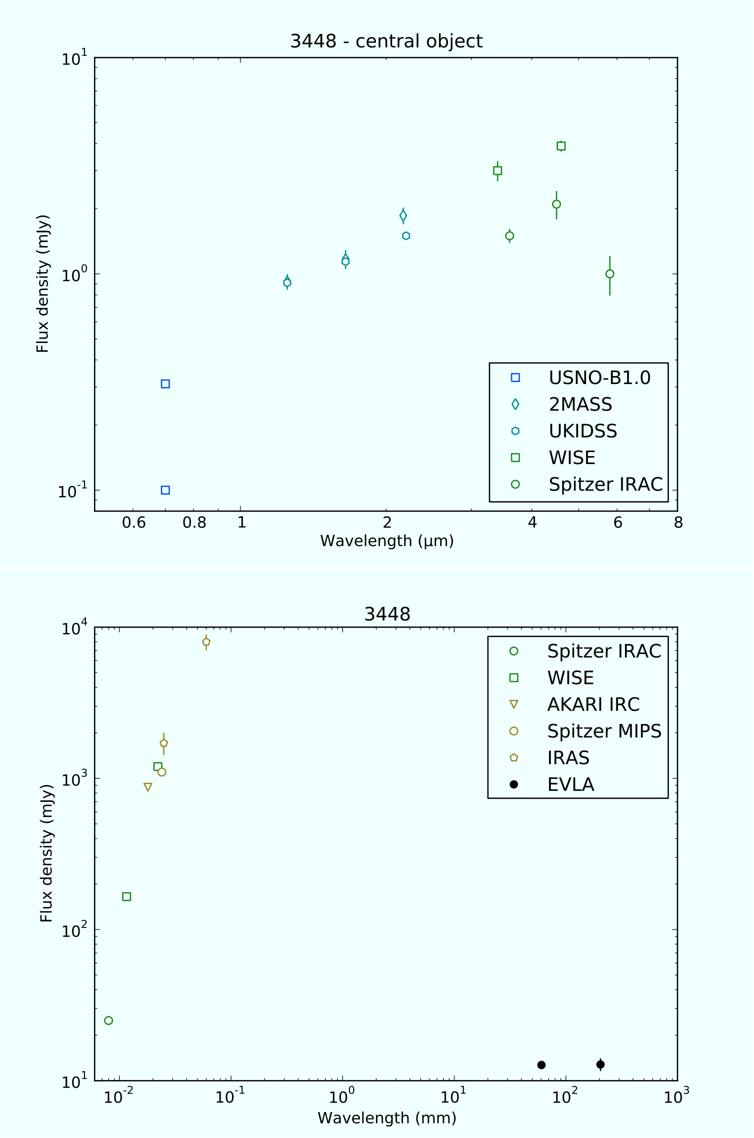

Figure 7.34: complete SED of the bubble 3448.

7.11 Bubble 3866

The bubble 3866 was first discovered by MIPSGAL. The GLIMPSE survey failed to detect either a point source or a diffuse emission associated with the 24-µm nebula at any of the four IRAC bands, even if images with very high contrasts reveal the possible existence of a very faint point source. No sources were also detected by 2MASS in the near infrared or even MSX and WISE at any bands. Associated to this bubble, however, a well known radio source (GPSR5 16.228–0.369), is detected both at 6 cm [49][29] and at 20 cm [16]. It has been also observed with the GBT in the HRDS survey at 8.665 GHz [46]. From the VLA archive no useful past observations were available.

From our data, the source appears not resolved in both bands. For this source we obtained a spectral index of 0.05 ± 0.30, resulting in a quite flat spectrum, but with important uncertainties. The 24 µm source appears as a ring with a bipolar morphology.

The nature of this bubble is presently unclear. Anderson et al. (2011) suggest that the source could be a PN candidate due to absence of a nebula at 8 µm. However it shows RRL widths of about 17 km/s, a low value for a PN, even if Anderson et al. pointed out that other PN candidates also show narrow RRLs [46].

It is interesting to notice that the flux density reported by the HRDS survey (that is 132 ± 56 mJy, see table 6.10), though affected by a great error, is remarkably higher than our estimations our other values reported by other EVLA survey, all around 10 mJy. Even if the HRDS data are referred to an higher frequency, nothing, not even a strong stellar wind, could justify a so great flux density increment.

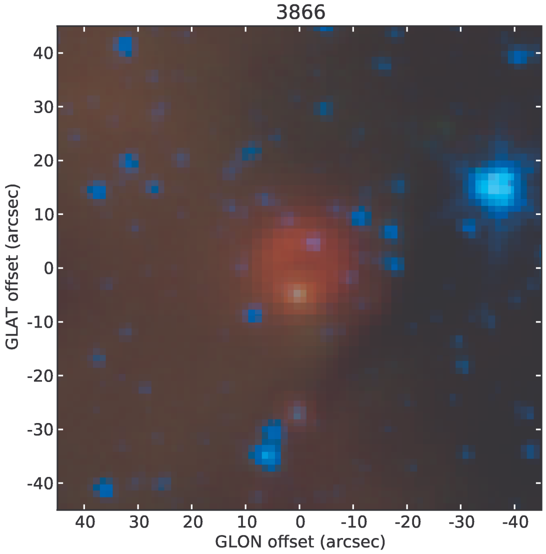

Figure 7.35: rgb image of the bubble 3866 at 24 µm (red), 8 µm (green) and 3.6 µm (blue). It is possible to notice the bubble is detected only at 24 µm and that there is no evidence of a central source.

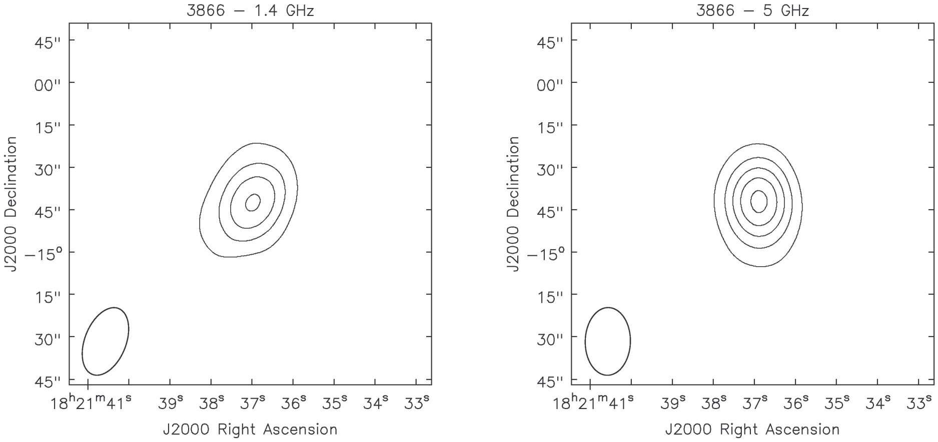

Figure 7.36: radio contour images of the bubble 3866 from our data. Contours are 3, 6, 9 and 12 mJy/beam (left) and 2, 4, 6, 8 and 10 mJy/beam (right).

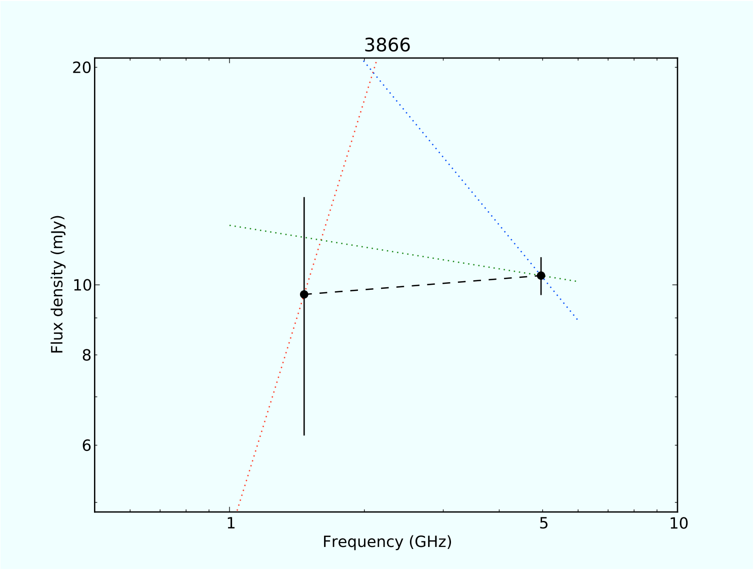

Figure 7.37: radio continuum spectrum of the bubble 3866.

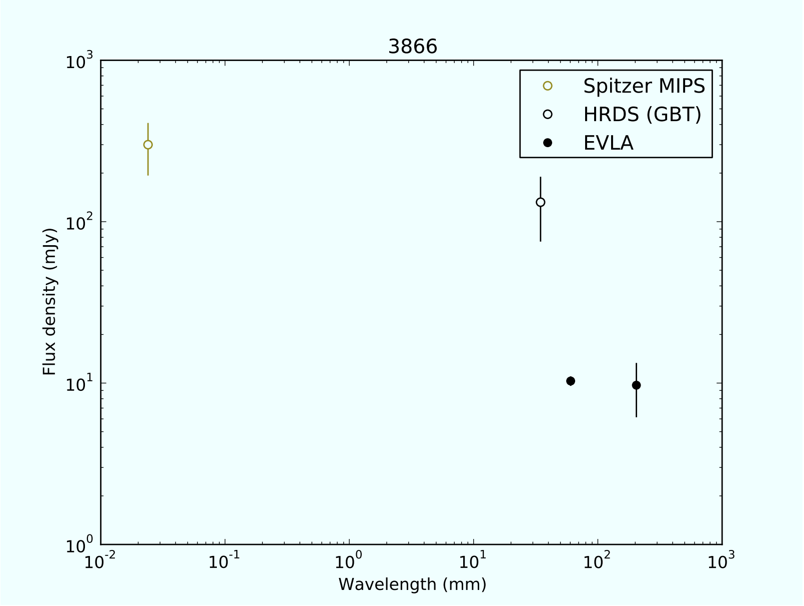

Figure 7.38: SED of the bubble 3866 nebula.

7.12 Bubble 4436

The bubble 4436 (whose main ID is IRAS 17412–3236) was first discovered by IRAS at 25 µm and at 60 µm and listed in the IRAS catalog in 1986. In the MIPSGAL tiles at 24 µm it appears as an irregular disk nebula, with a slight bipolar structure, whose diameter is 18″. The GLIMPSE survey failed to detect either a point source or a diffuse emission associated with the 24-µm nebula at any of the four IRAC bands. No sources were also detected by 2MASS in the near infrared and by MSX. WISE detected the nebula in the bands $W3$ and $W4$, as well as AKARI that detected the source at 18 µm. The source was also observed at 20 cm by the NVSS survey. From the VLA archive no useful past observations were available.

From our data, the source appears not resolved in both bands. For this source we obtained a spectral index of -0.11 ± 0.05, perfectly compatible with a free-free emission.

The nature of this bubble is presently unknown. In the section 8.3 we will show how, using our radio data and IRAS archive data, this bubble can be considered a planetary nebula candidate.

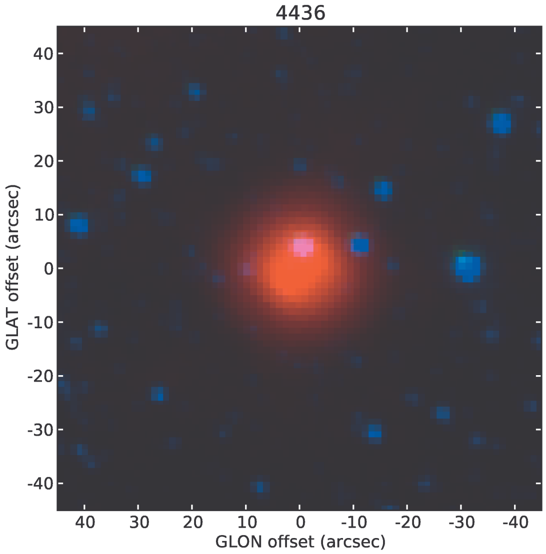

Figure 7.39: rgb image of the bubble 4436 at 24 µm (red), 8 µm (green) and 3.6 µm (blue). It is possible to notice the bubble is detected only at 24 µm and that there is no evidence of a central source.

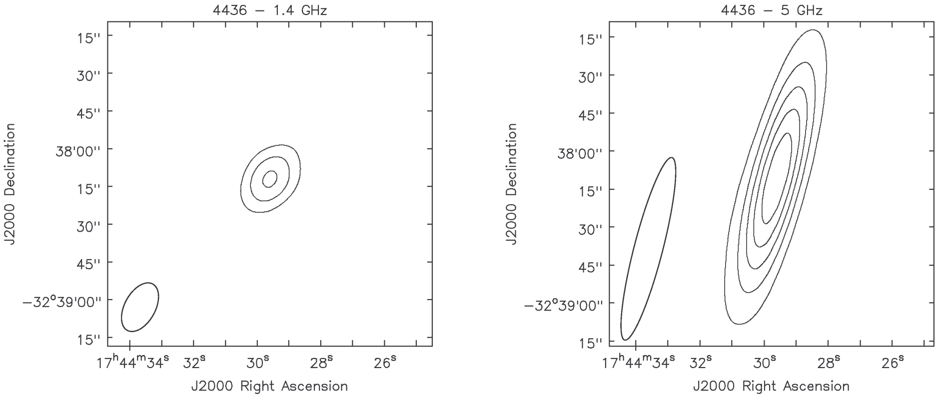

Figure 7.40: radio contour images of the bubble 4436 from our data. Contours are 2, 4 and 6 mJy/beam (left) and 1, 2, 3, 4 and 5 mJy/beam (right).

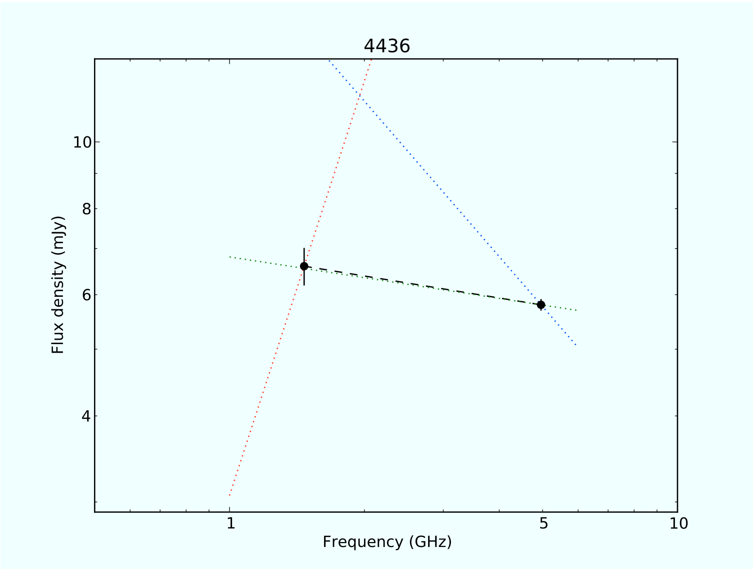

Figure 7.41: radio continuum spectrum of the bubble 4436.

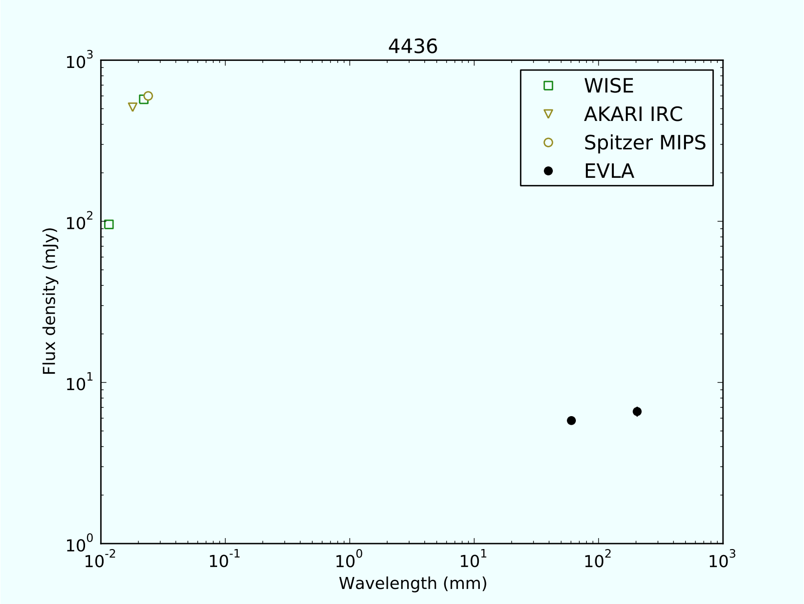

Figure 7.42: SED of the bubble 4436 nebula.

7.13 Bubble 4465

The bubble 4465 was first discovered by MIPSGAL at 24 µm. It appears as a ring nebula with a diameter of 18″. The GLIMPSE survey failed to detect either a point source or a diffuse emission associated with the 24-µm nebula at any of the four IRAC bands. No sources were also detected by 2MASS in the near infrared and by MSX, while WISE detected the nebula in the bands $W3$ and $W4$. The source was also observed at 20 cm by the NVSS survey. From the VLA archive no useful past observations were available.

From our data, the source appears not resolved in both bands. For this source we obtained a spectral index of 0.39 ± 0.48, compatible with a optically thick free-free emission, but with great uncertainties.

The nature of this bubble is presently unknown.

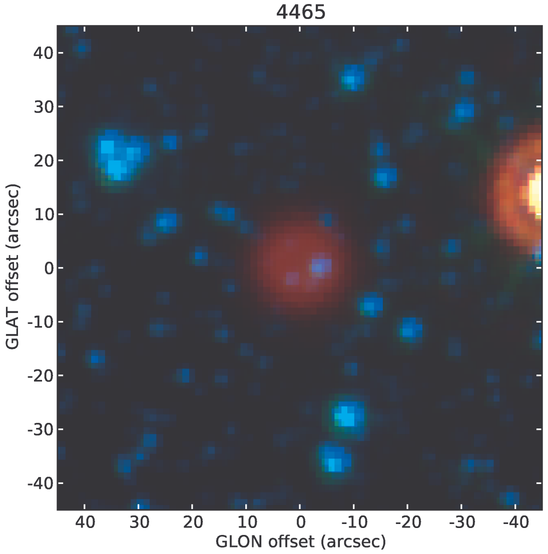

Figure 7.43: rgb image of the bubble 4465 at 24 µm (red), 8 µm (green) and 3.6 µm (blue). It is possible to notice the bubble is detected only at 24 µm and that there is no evidence of a central source.

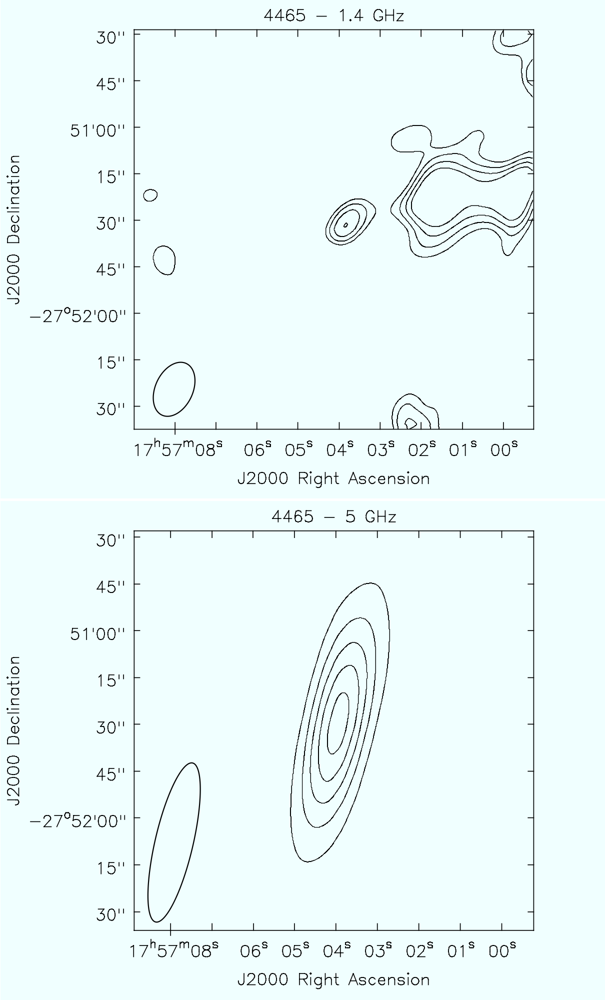

Figure 7.44: radio contour images of the bubble 4465 from our data. Contours are 0.7, 0.8, 0.9 and 1 mJy/beam (top) and 0.3, 0.6, 0.9, 1.2 and 1.5 mJy/beam (bottom).

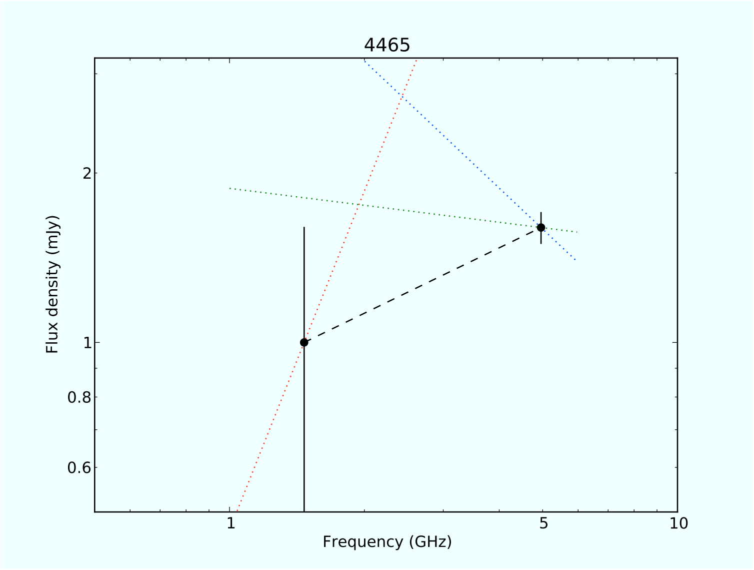

Figure 7.45: radio continuum spectrum of the bubble 4465.

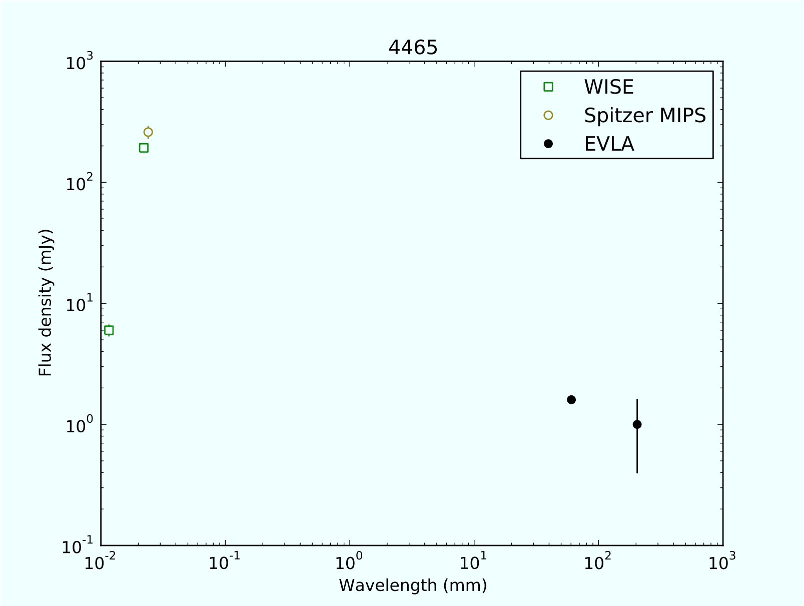

Figure 7.46: SED of the bubble 4465 nebula.

7.14 Bubble 4473

The bubble 4473 (whose main ID is IRAS 17597–2441) was first discovered by IRAS at 25 µm and listed in the IRAS catalog in 1986. In the MIPSGAL tiles at 24 µm it appears as a ring nebula whose diameter is $20''$. The nebula was clearly detected by GLIMPSE at 4.5 µm, 5.8 µm and 8 µm, showing exactly the same shape and the same dimension as at 24 µm; at 3.6 µm the nebula is, very likely, detected too, but its very faint and confused with the background. The nebula was also detected by WISE in bands $W2$, $W3$ and $W4$ and by AKARI at 18 µm. There is no evidence of a central source in any band. The bubble was also observed as a radio source at 20 cm by the NVSS survey [28]. From the VLA archive no useful past observations were available.

From our data, this bubble could be slightly resolved in band L, but it is not resolved in band C. For this source we obtained a spectral index of 0.08 ± 0.09, resulting then in a quite flat spectrum. Since no archive flux density values were found for the IRAC nebula, aperture photometry has been performed.

The nature of this bubble is still unknown. In sections 8.4 and 8.5 we will see that our data combined with archive data from IRAC and WISE suggest a classification as a possible planetary nebula candidate.

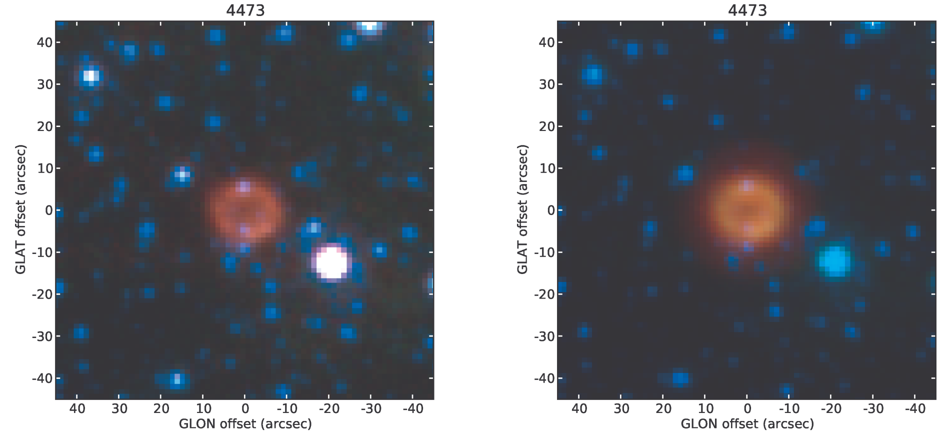

Figure 7.47: rgb images of the bubble 4473: left at 8 μm (red), 5.8 μm (green) and 3.6 μm (blue); right at 24 μm (red), 8 μm (green) and 3.6 μm (blue). The ring nebula is clearly detected both at 24 μm, at 8 μm and at 5.8 μm; there is no evidence of a central source.

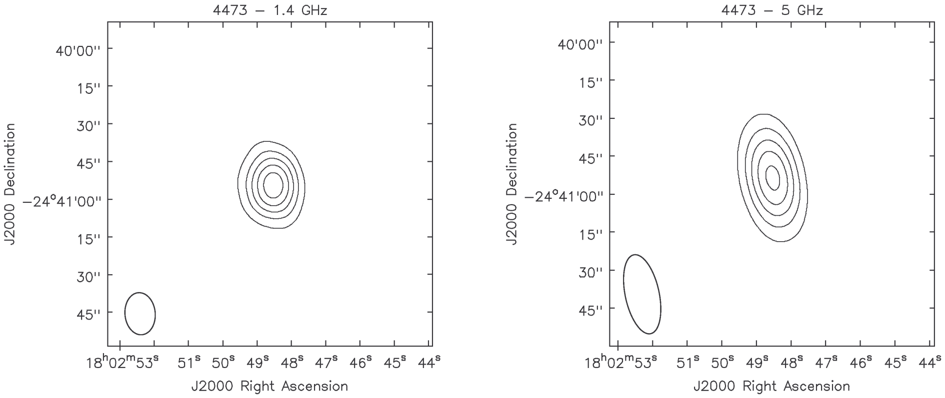

Figure 7.48: radio contour images of the bubble 4473 from our data. Contours are 6, 12, 18, 24 and 30 mJy/beam (left) and 7, 14, 21, 28 and 35 mJy/beam (right).

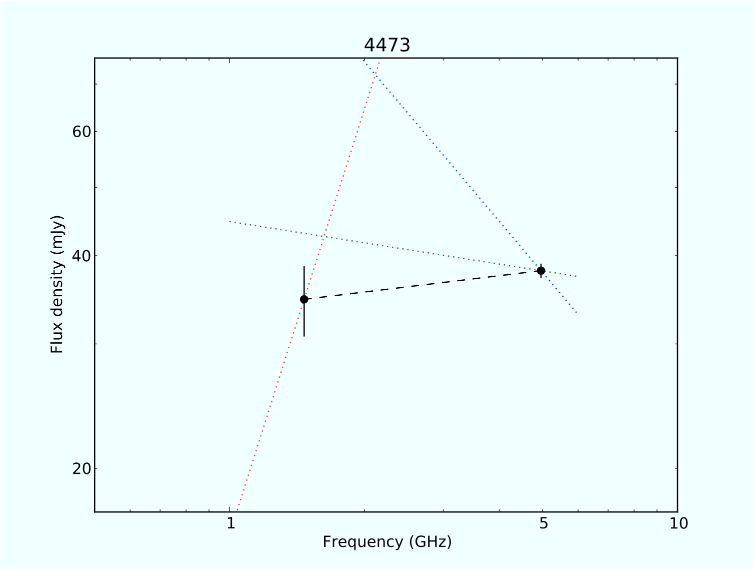

Figure 7.49: radio continuum spectrum of the bubble 4473.

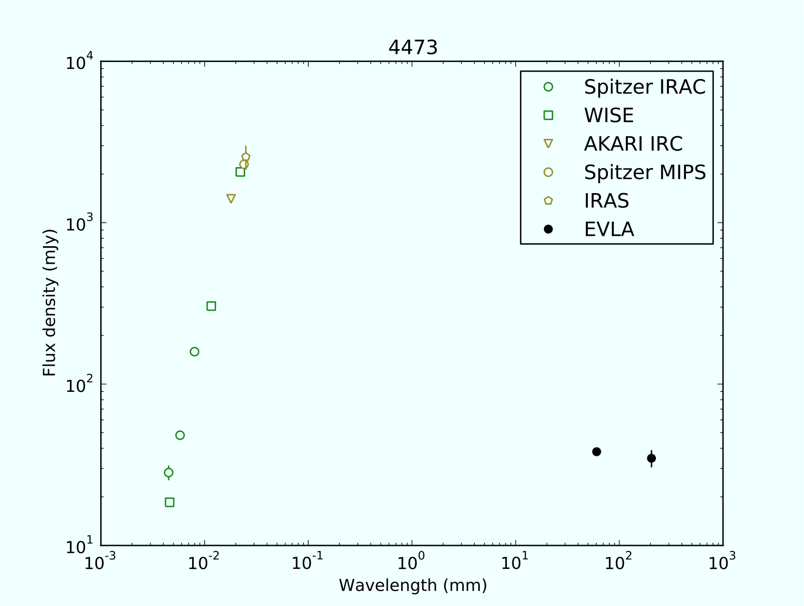

Figure 7.50: SED of the bubble 4473 nebula.

7.15 Bubble 4486

The bubble 4486 was first discovered by MIPSGAL. The GLIMPSE survey did not detect either a point source or a diffuse emission associated with the 24-μm nebula at any of the four IRAC bands. No sources were also detected by 2MASS and MSX. WISE detected the nebula in bands $W3$ and $W4$. In the NVSS catalog it is possible to find a source with a position compatible with the bubble (3.6 ± 1.9 arcseconds away), and it might also be detected by the Molonglo Galactic Plane Survey (MGPS-2) [50] at 843 MHz. The bubble is not listed in any other catalog. From the VLA archive no useful past observations were available.

Even this source appears resolved in band L, with a slightly elongated morphology, and it is not resolved in band C. The flux density for the band-L map has been calculated integrating over an area given by the 3σ level. For this source we obtained a spectral index of -0.25 ± 0.06, similar to what we obtained for bubble 3367.

The source dimensions at 1.4 GHz are about $28'' \times 20''$ at 10σ level. The 24 μm source appears roundish but less extended than the radio emission region.

The nature of this bubble is still unclear. From our data and from the archive data from MGPS, it is possible to suppose that this bubble is not a thermal emitter.

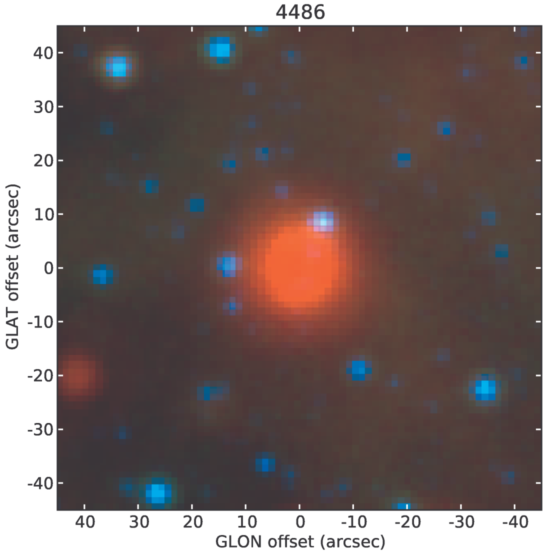

Figure 7.51: rgb image of the bubble 4486 at 24 µm (red), 8 µm (green) and 3.6 µm (blue). It is possible to notice the bubble is detected only at 24 µm and that there is no evidence of a central source.

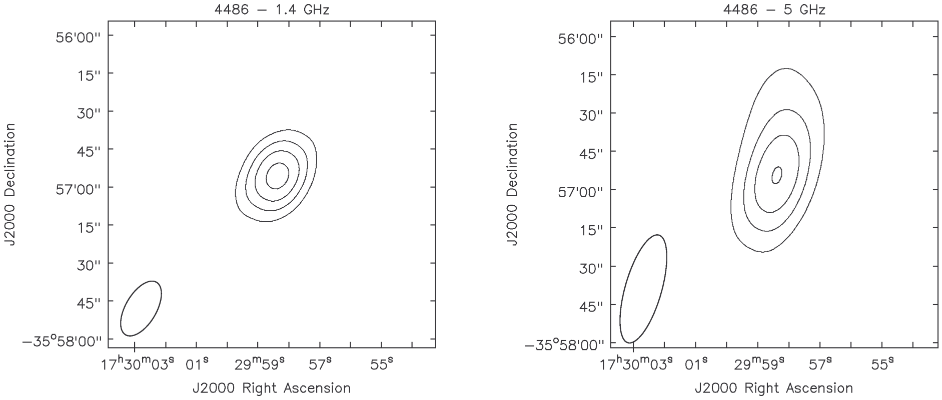

Figure 7.52: radio contour images of the bubble 4486 from our data. Contours are 3, 6, 9 and 12 mJy/beam (left) and 4, 8, 12 and 16 mJy/beam (right).

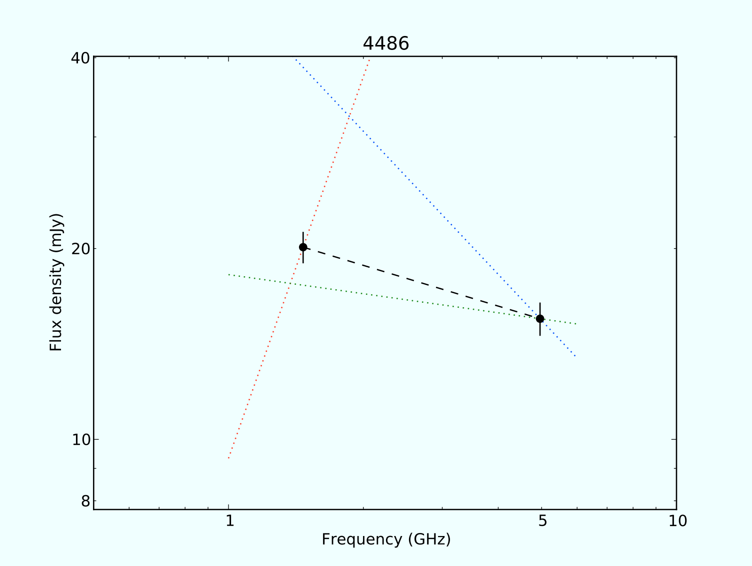

Figure 7.53: radio continuum spectrum of the bubble 4486.

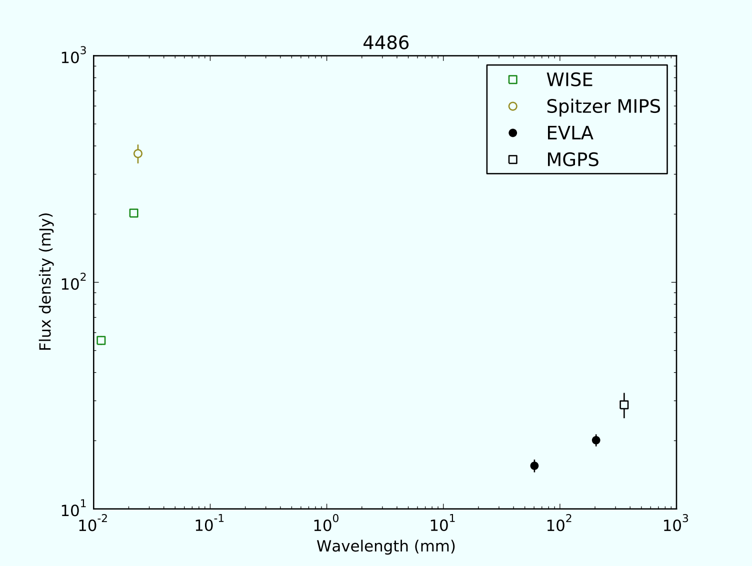

Figure 7.54: SED of the bubble 4486 nebula.

7.16 Bubble 4497

The bubble 4497 was first discovered by MIPSGAL as a peaked disk nebula. The GLIMPSE survey did not detect either a point source or a diffuse emission associated with the 24-µm nebula at any of the four IRAC bands. No sources were also detected by 2MASS and MSX. WISE detected the nebula in bands $W3$ and $W4$. The bubble is associated to a well known radio source, first detected in 1994 at 6 cm [49], and listed as GPS5 356.816–0.385. It was observed at 20 cm and listed in the NVSS catalog, and it might also be detected by the Molonglo Galactic Plane Survey (MGPS-2) [50] at 843 MHz. The bubble was also re-observed with the EVLA at 6 cm in 2005 [29]. From the VLA archive no useful past observations were available.
From our observations, the bubble appears point-like in both bands. For this source we obtained a spectral index of 0.01 ± 0.06, resulting then in a quite flat spectrum.
The nature of this bubble is presently unknown.

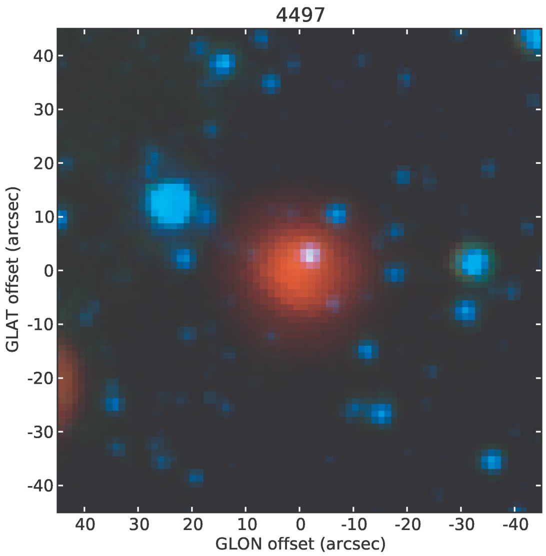

Figure 7.55: rgb image of the bubble 4497 at 24 µm (red), 8 µm (green) and 3.6 µm (blue). It is possible to notice the bubble is detected only at 24 µm and that there is no evidence of a central source.

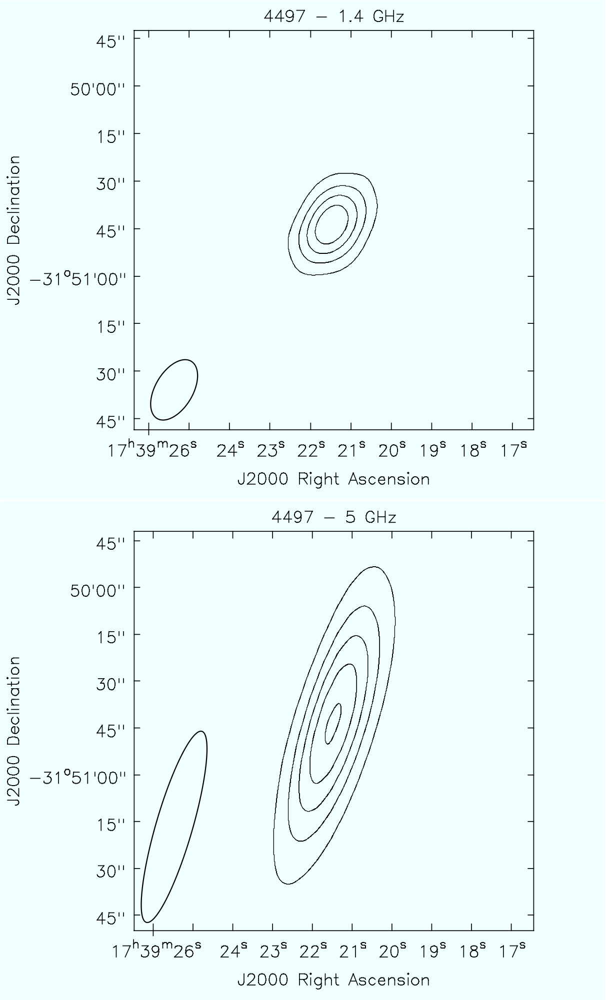

Figure 7.56: radio contour images of the bubble 4497 from our data. Contours are 3, 6, 9 and 12 mJy/beam (top) and 3, 6, 9, 12 and 15 mJy/beam (bottom).

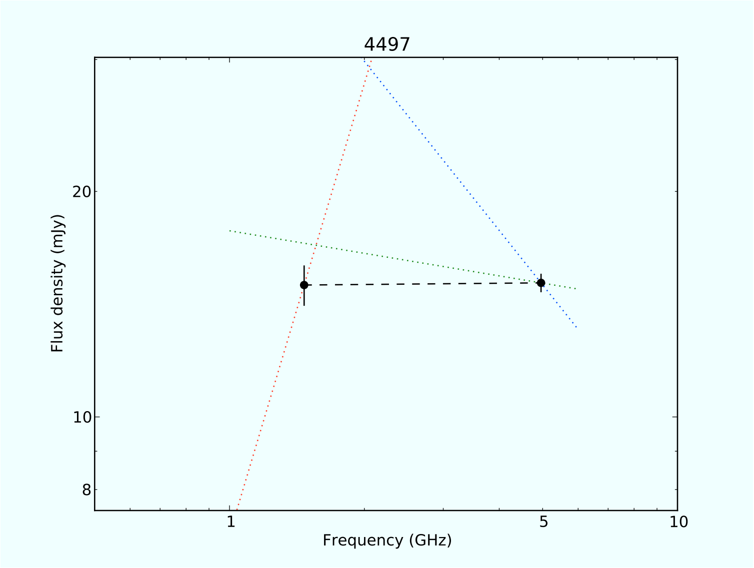

Figure 7.57: radio continuum spectrum of the bubble 4497.

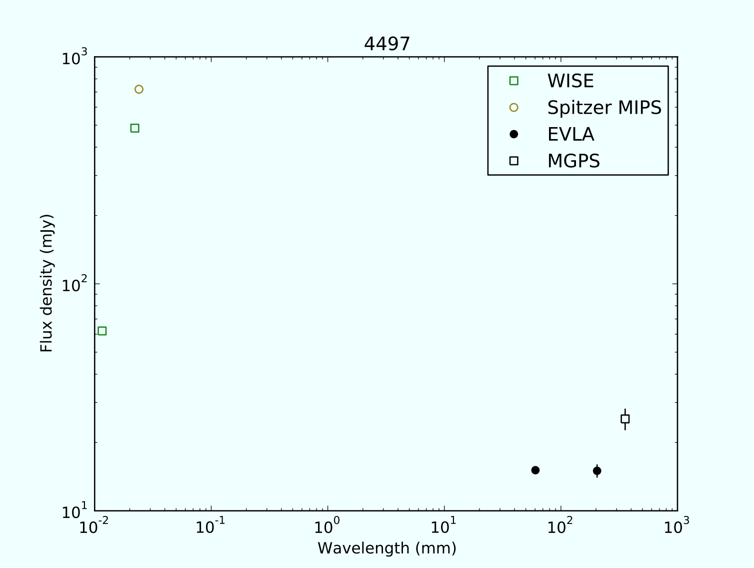

Figure 7.58: SED of the bubble 4497 nebula.

7.17 Bubble 4552

The bubble 4552 is associated with the radio source GPSR5 356.144+0.053. In the MIPSGAL tiles at 24 μm it appears as an irregular ring nebula whose diameter is 25″; the GLIMPSE survey shows a central object is clearly detected in all IRAC bands. It was also observed by 2MASS bands in band K_s only [41] and by WISE in all bands [43]. In the radio wavelengths, the bubble was observed as a radio source at 6 cm by the GPSR survey [49], at 20 cm by the NVSS survey [28] and at 843 MHz by the Molonglo Galactic Plane Survey (MGPS-2) [50]. From the VLA archive no useful past observations were available.

The source is not resolved in band C and initial band-L map appeared corrupted by artefacts. Since the peak intensity of the source in band L were about 10 mJy a self-calibration process has been performed, leading to a reduction of the artefacts and to a lower noise level. The source appears D-shaped, but this morphology maybe affected by imaging error. The flux density for the band-L map has been calculated integrating over an area given by the 3σ level. For this source we obtained a spectral index of -0.04 ± 0.07, resulting then in a quite flat spectrum compatible with optically thin free-free emission.

The source dimensions at 1.4 GHz are about $22'' \times 18''$ at 10σ level. The 24 μm source appears roundish but bipolar and less extended than the radio emission region.

It is important to notice that the central object, though located almost exactly at the center of the nebula, shows a very blue color. It is therefore possible that it is, simply, perspectively aligned with the nebula.

The nature of the source is presently unknown.

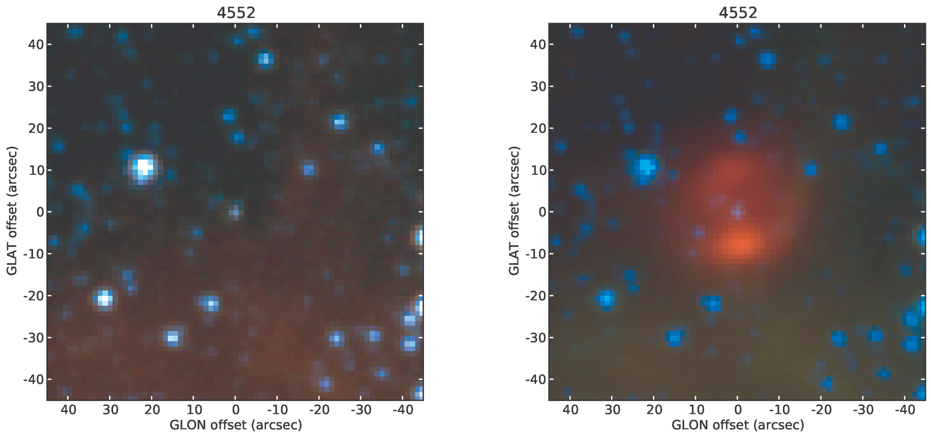

Figure 7.59: rgb images of the bubble 3448: left at 8 µm (red), 5.8 µm (green) and 3.6 µm (blue); right at 24 µm (red), 8 µm (green) and 3.6 µm (blue). The ring nebula is detected only at 24 µm, while at shorter wavelengths only the central object is visible.

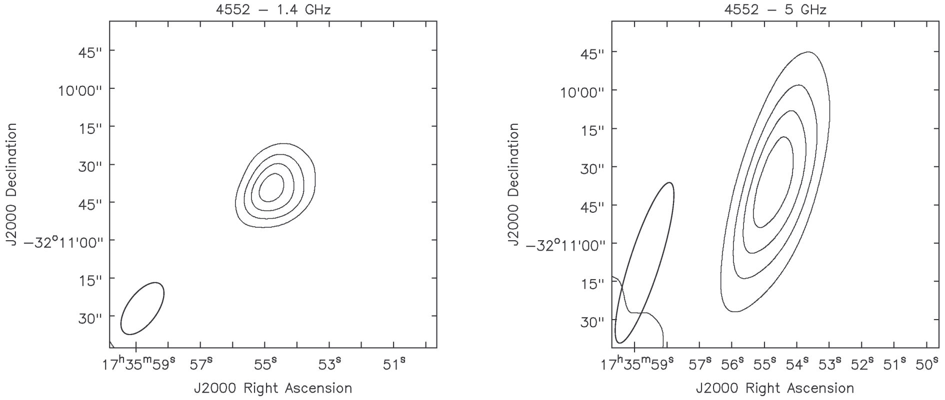

Figure 7.60: radio contour images of the bubble 4552 from our data. Contours are 2.5, 5, 7.5 and 10 mJy/beam (left) and 3, 6, 9 and 12 mJy/beam (right).

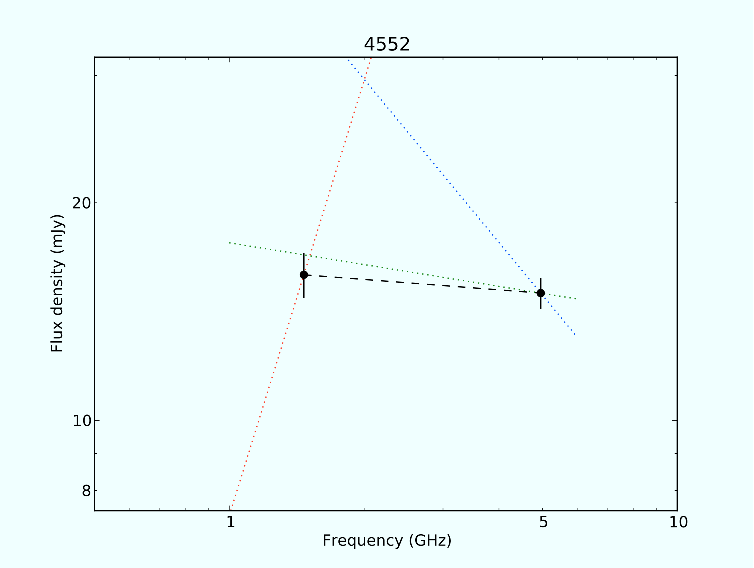

Figure 7.61: radio continuum spectrum of the bubble 4552.

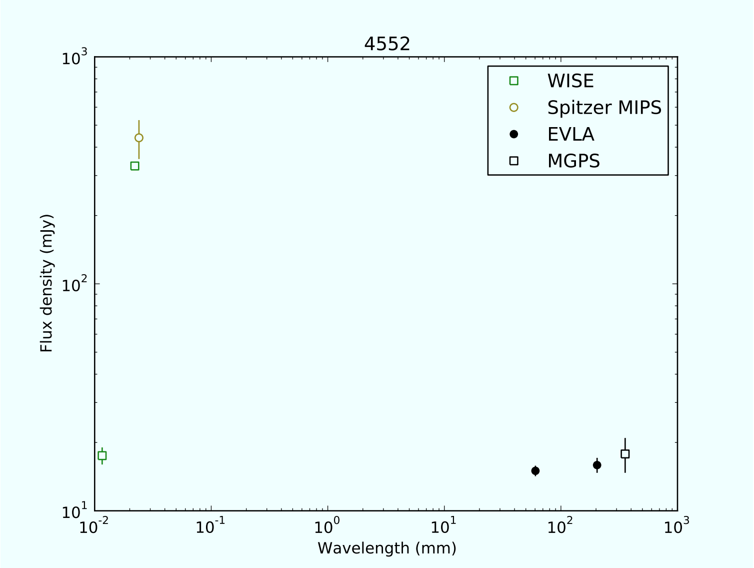

Figure 7.62: complete SED of the bubble 4552.

7.18 Bubble 4589

The bubble 4589 was first discovered by MIPSGAL, where, at 24 µm, it appears as a disk nebula whose diameter is 16″. It is very difficult to say if the nebula is detected in GLIMPSE; at 8 µm there appears a faint emission in the bottom-right part of 24 µm nebula, but it is not clear if that source is the same nebula or not. The nebula was also detected by WISE in bands $W3$ and $W4$ and by AKARI at 18 µm. There is no evidence of a central source in any band. The bubble was also observed as a radio source at 20 cm by the NVSS and MAGPIS surveys [28][16] and at 6 cm [29]. From the VLA archive no useful past observations were available.

From our observations, the bubble appears point-like in both bands. For this source we obtained a spectral index of 0.01 ± 0.06, resulting then in a quite flat spectrum.

We also observed the source searching for OH masers with GBT. We found some evidences of OH lines in all four band around a LSR velocity of about 50 km/s. For the first three spectral windows we observe an absorption line while in the last band the line is in emission; it is possible that this emission is the evidence of a shock, though the line height barely reach the 3σ level. In the first spectral window also a secondary emission line is visible slighty below 200 km/s LSR. The four spectra are reported in figure 7.67.

The nature of this bubble is presently unknown.

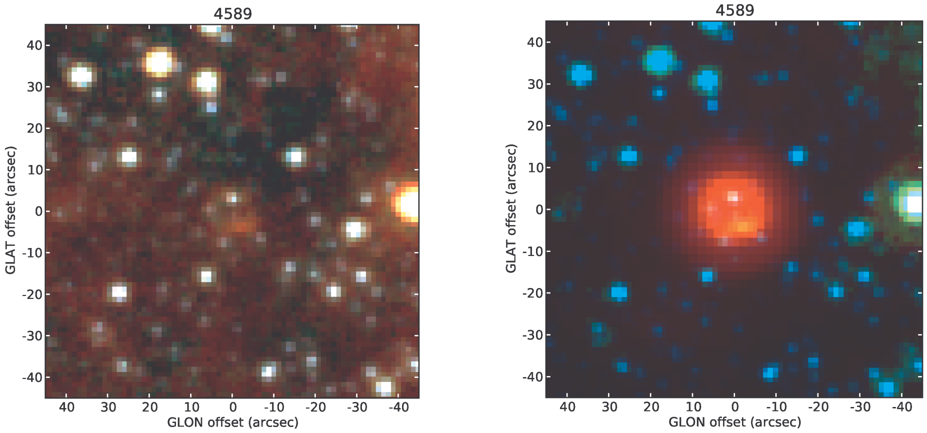

Figure 7.63: rgb images of the bubble 4589: left at 8 µm (red), 5.8 µm (green) and 3.6 µm (blue); right at 24 µm (red), 8 µm (green) and 3.6 µm (blue). The disk nebula is detected at 24 µm and, possibly, also at 8 µm and at 5.8 µm; there is no evidence of a central source.

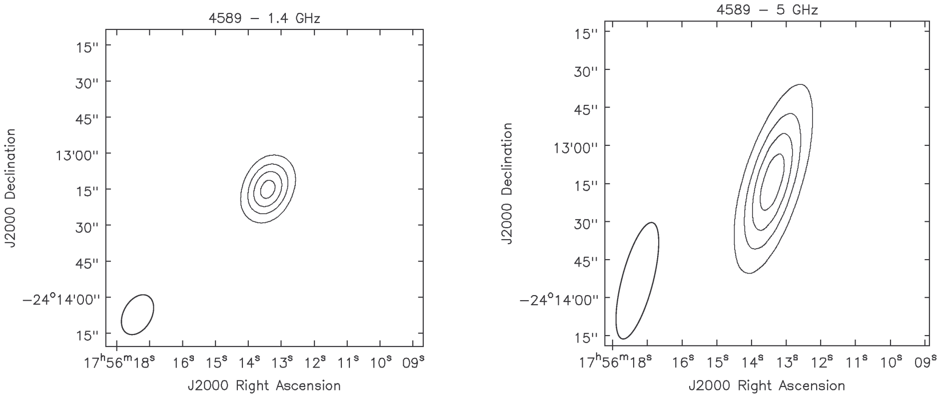

Figure 7.64: radio contour images of the bubble 4589 from our data. Contours are 2, 4, 6 and 8 mJy/beam (left) and 2, 4, 6 and 8 mJy/beam (right).

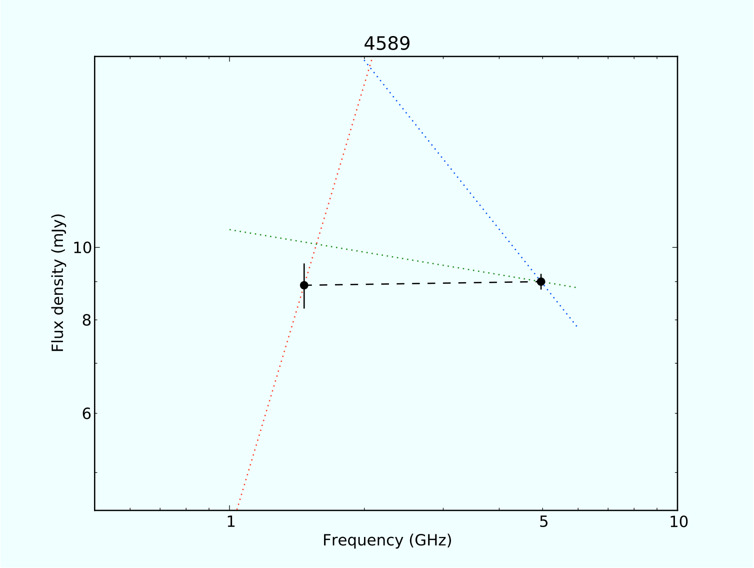

Figure 7.65: radio continuum spectrum of the bubble 4589.

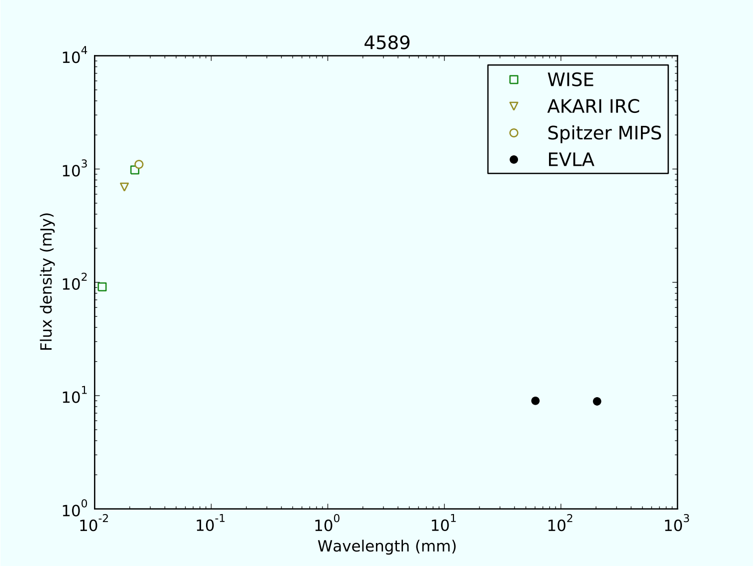

Figure 7.66: SED of the bubble 4589 nebula.

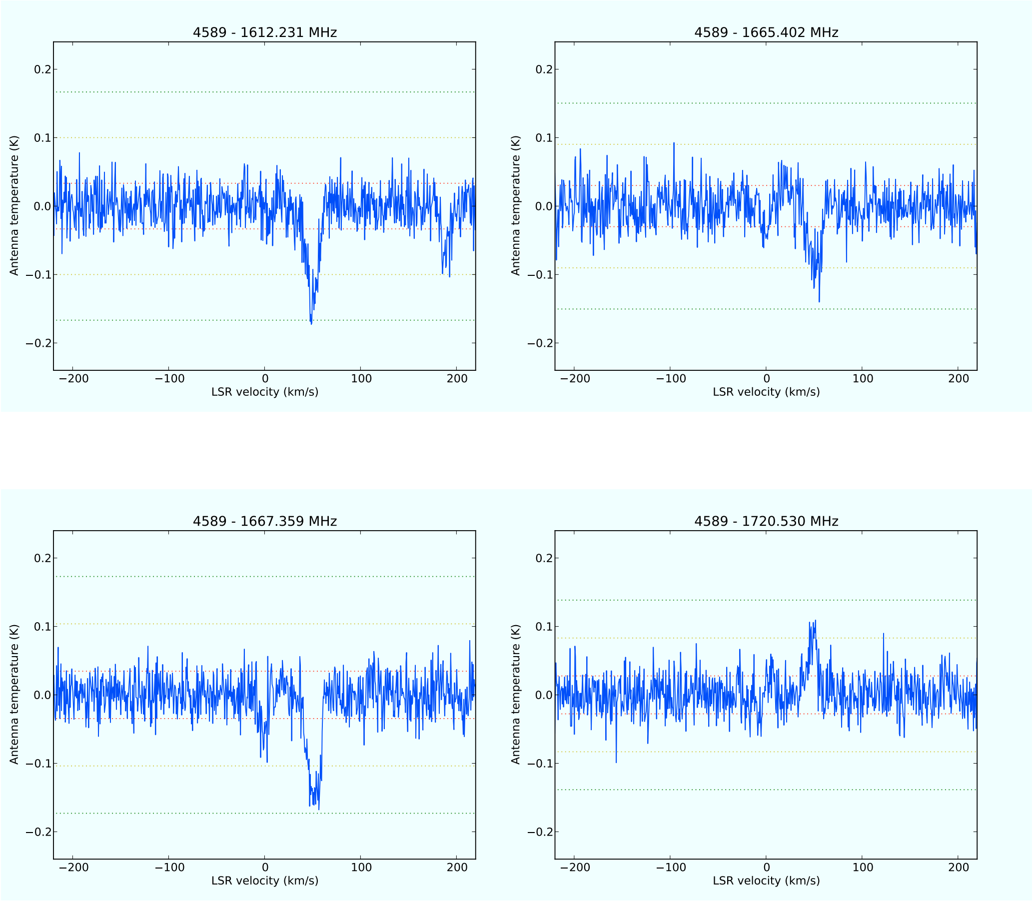

Figure 7.67: GBT spectra of the bubble 4589. The emission features in the last spectrum may be the evidence of shock. However the line height barely reach the 3σ level (yellow dotted line).

7.19 Bubble 4602

The bubble 4602 (whose main ID are IRAS 18016-2037 and PN PBOZ 33) was first discovered by IRAS at 25 µm and 60 µm and listed in the IRAS point source catalog in 1986. In the MIPSGAL tiles at 24 µm it appears as a disk nebula whose diameter is 28″. The nebula was clearly detected by GLIMPSE at 4.5 µm, 5.8 µm and 8 µm, showing a ring shape; at 3.6 µm the nebula is, very likely, detected too, but its very faint and confused with the background. The nebula was also detected by MSX in bands A, D and E, by WISE in all bands and by AKARI at 18 µm, 90 µm and 140 µm. It is clearly visible in Hα with the same morpholgy of the infrared emission, as it is possible to see in the SuperCOSMOS H-alpha Survey[4] tiles [51]. There is no evidence of a central source in any band. The bubble was also observed as a radio source at 20 cm by the NVSS and MAGPIS surveys [28][16]. From the VLA archive no useful past observations were available.

From our data, this bubble appears as a point source in both bands. For this source we obtained a spectral index of 0.15 ± 0.10, compatible with a free-free emission. Since no archive flux density values were found for the IRAC nebula, aperture photometry has been performed. The nebula observable in GLIMPSE tiles appears as a ring nebula, while at 24 µm it appears as a disk; this is very likely due to the poorer resolution at 24 µm.

The source was classified as a PN candidate by Pottasch et al. (1988) [13], based on its IRAS color. This classification was confirmed in the "Strasbourg-ESO Catalogue of Galactic Planetary Nebulae" [52], where spectroscopic observations failed to classify undoubtly the object as PN (it remained classified as a possible PN). The infrared nebula was then associated to the NVSS source 180438-203726 [53]. Finally it was listed in the "Version 2000 of the Catalogue of Galactic Planetary Nebulae" where the object is considered in a possible transition phase between OH/IR and PN [54].

---

[4] SuperCOSMOS is an archive of digitised data derived from scans of survey films of the Southern Galactic Plane taken for the AAO/UKST H-alpha survey.

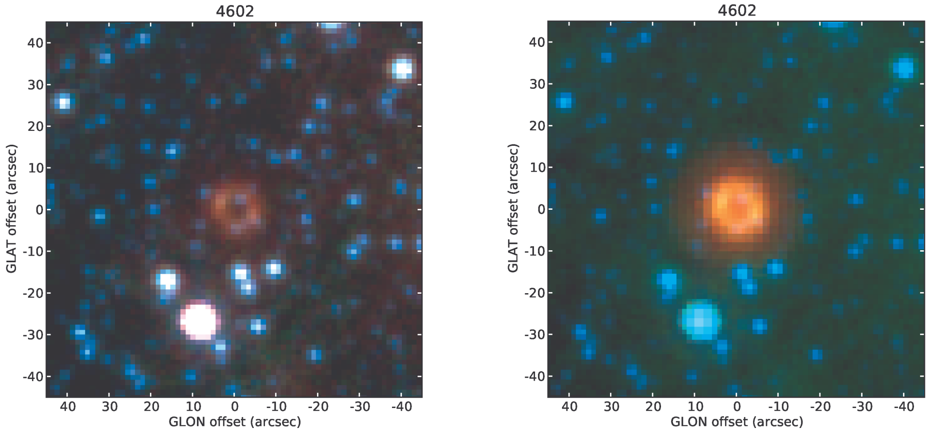

Figure 7.68: rgb images of the bubble 4602: left at 8 µm (red), 5.8 µm (green) and 3.6 µm (blue); right at 24 µm (red), 8 µm (green) and 3.6 µm (blue). The nebula is well detected at 24 µm, at 8 µm, at 5.8 µm and possibly also at 3.6 µm; there is no evidence of a central source.

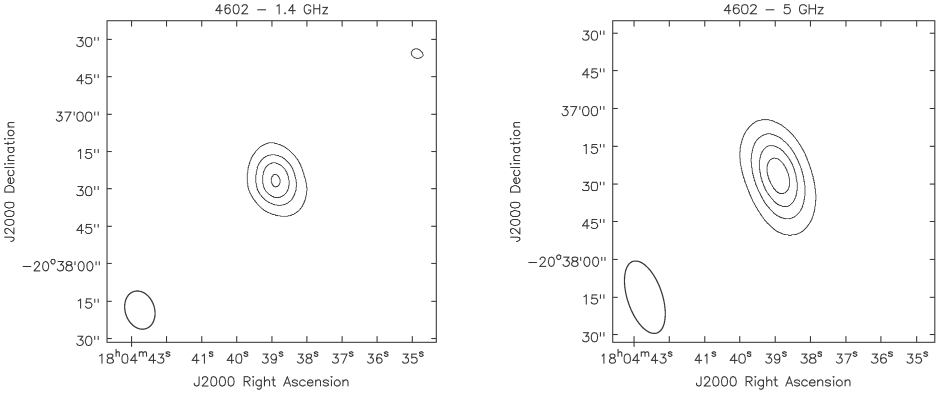

Figure 7.69: radio contour images of the bubble 4602 from our data. Contours are 4, 8, 12 and 16 mJy/beam (left) and 4, 8, 12 and 16 mJy/beam (right).

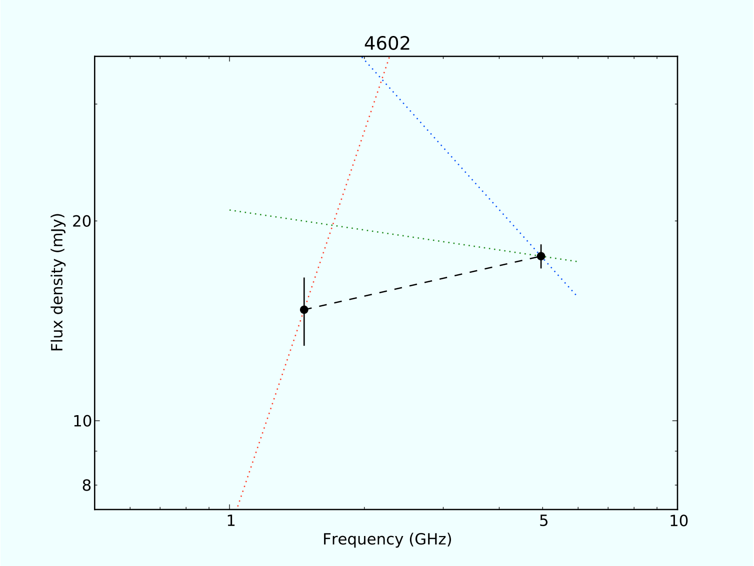

Figure 7.70: radio continuum spectrum of the bubble 4602.

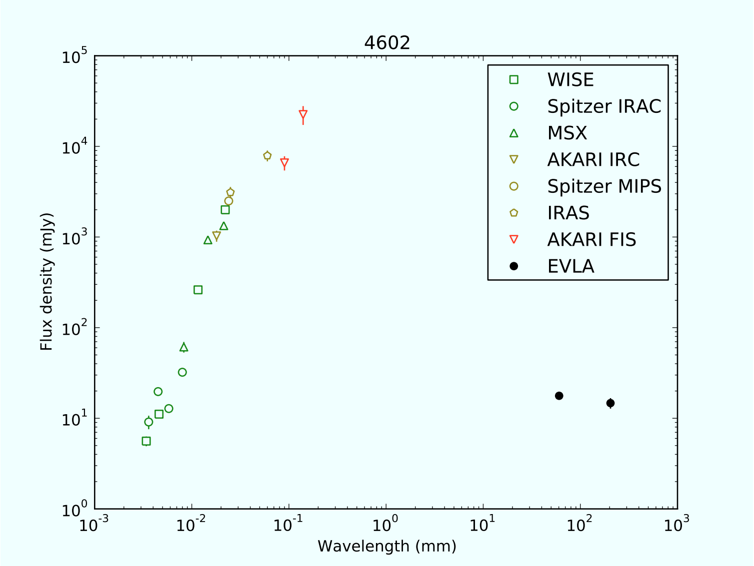

Figure 7.71: SED of the bubble 4602 nebula.

7.20 Bubble 4607

The bubble 4607 was first discovered by MIPSGAL, where, at 24 µm, it appears as a disk nebula whose diameter is 18″. In the GLIMPSE tile at 8 µm there appears a faint emission in a compatible position with the 24 µm nebula, but it is not clear if that source is the same nebula or just noise due to nearby brigth source; the bubble is, in fact, located in a very crowded zone also with a very complex background. The nebula was also detected by WISE in bands $W3$ and $W4$. There is no evidence of a central source in any band. The bubble was observed as a radio source at 20 cm by the MAGPIS survey [16]. From the VLA archive no useful past observations were available.
Initial band-C map of bubble 4607 appeared corrupted by artifacts. Therefore a self-calibration process has then been performed, leading to a reduction of the artifact and to a lower noise level (rms ~ 0.26 mJy/beam). The self-calibration process led to no appreciable peak flux density variation. The source appears unresolved in both bands. For this source we obtain a spectral index of 0.27 ± 0.09, compatible with an optically thick free-free source. We also observed this bubble searching for OH masers with GBT. We found some evidences of OH lines in all four band around a velocity of about 30 km/s with respect to LSR. For the first three spectral windows we observe an absorption line while in the last band the line is in emission. In the fourth spectral window also an absorption line is visible at about 175 km/s with respect to LSR. The two main lines seem to show a double peak structure compatible with a shell. The four spectra are reported in figure 7.76.
The nature of this bubble is still unclear.

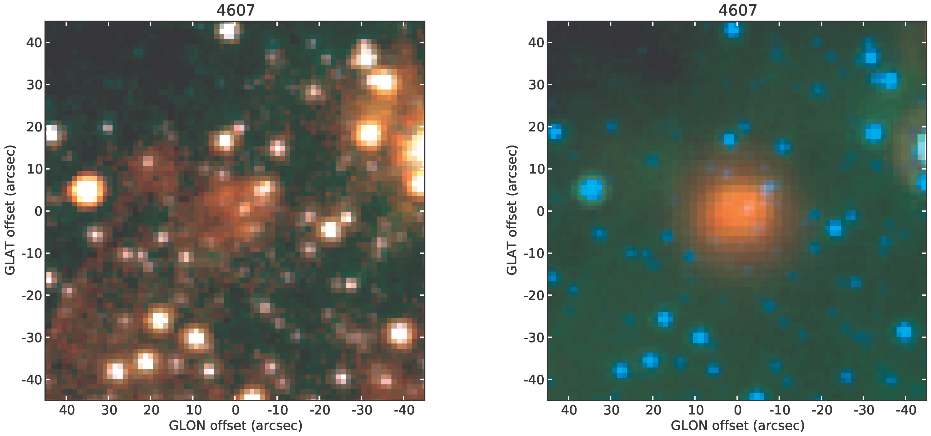

Figure 7.72: rgb images of the bubble 4607: left at 8 µm (red), 5.8 µm (green) and 3.6 µm (blue), the red channel (8 µm) has been dramatically color-enanched in order to show the possible faint nebula; right at 24 µm (red), 8 µm (green) and 3.6 µm (blue). The nebula is well detected only at 24 µm and there is no a clear evidence of a central source.

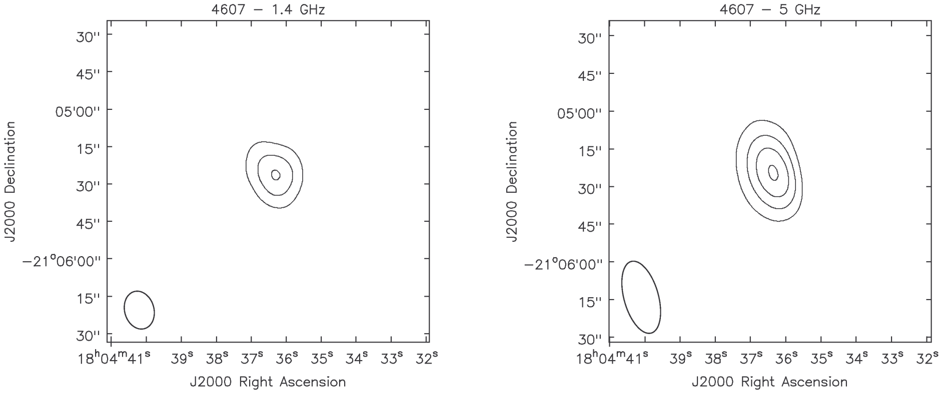

Figure 7.73: radio contour images of the bubble 4607 from our data. Contours are 2, 4 and 6 mJy/beam (left) and 4, 6, 8 and 10 mJy/beam (right).

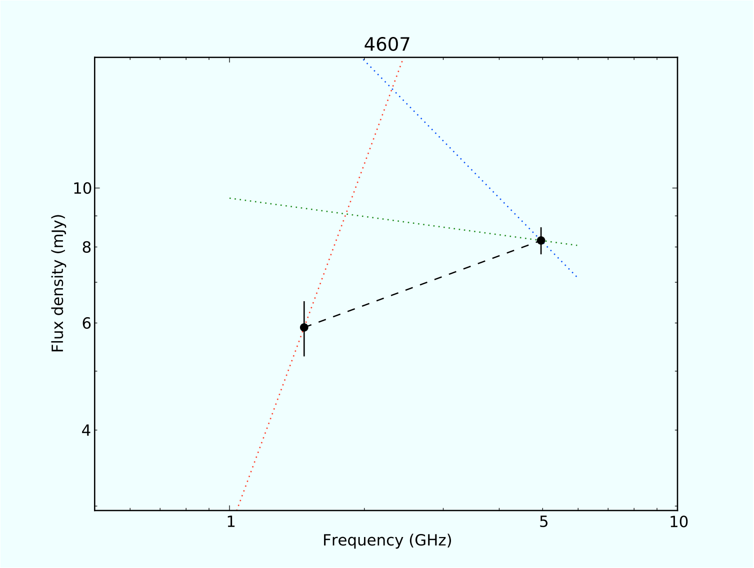

Figure 7.74: radio continuum spectrum of the bubble 4607.

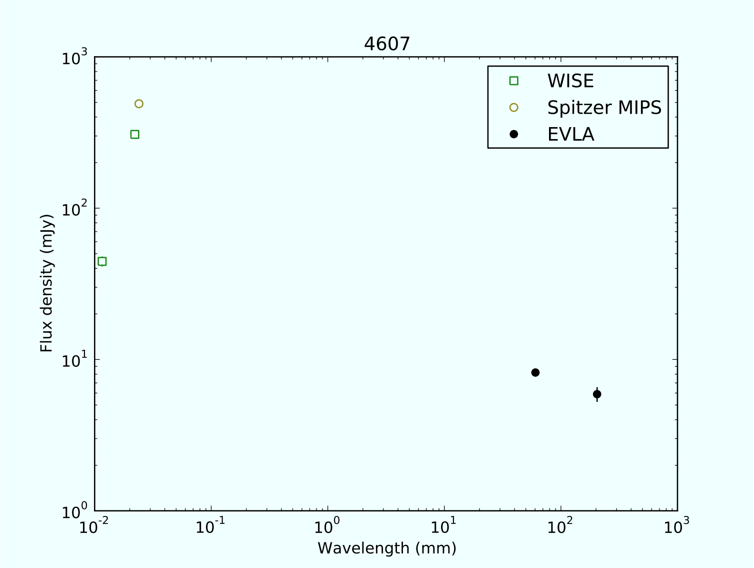

Figure 7.75: SED of the bubble 4607 nebula.

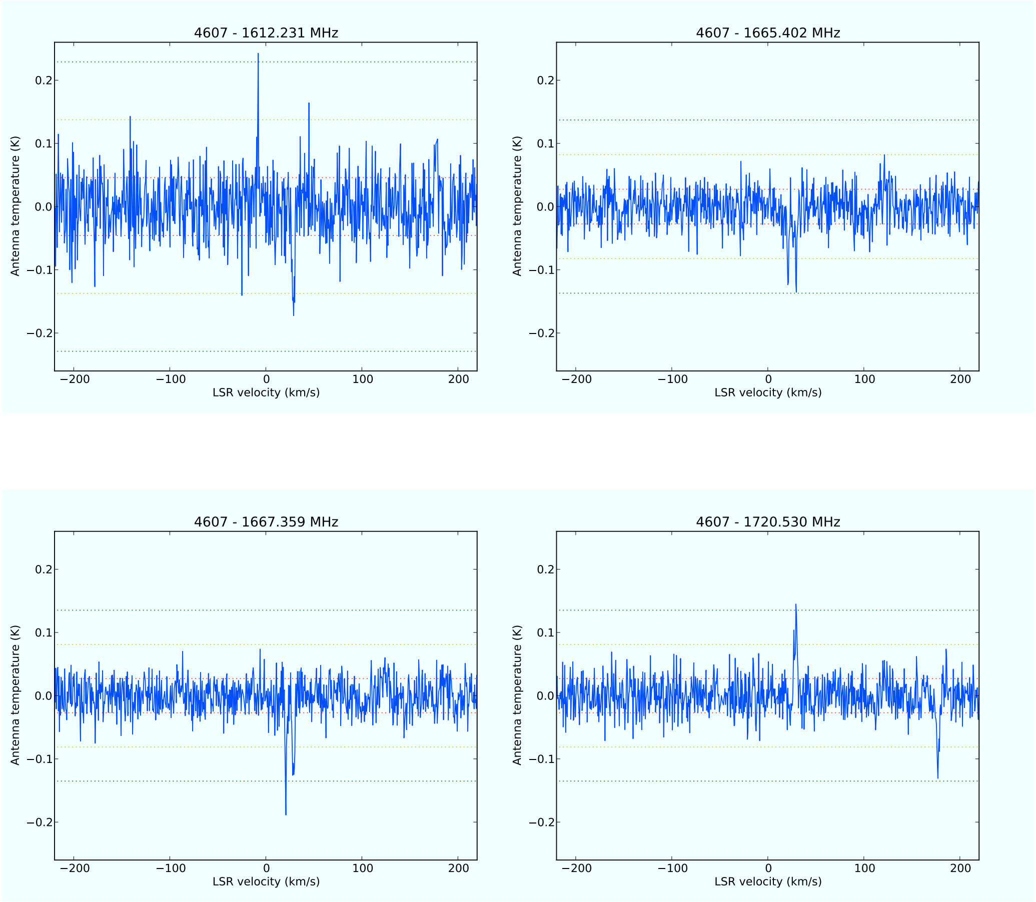

Figure 7.76: GBT spectra of the bubble 4607.

Chapter 8

Classification of the bubbles

In this chapter we will examine different classification schemes and we will try to make inferences on the nature of unclassified bubbles.

8.1 Radio emission characterization

In the section 7.1 we have talked about the determination of the radio spectral index between 1.4 GHz and 5 GHz for all those bubbles whose flux densities were well-determined. What we have obtained was that most of the bubbles presented a positive or slightly negative spectral index, indicating that we are very likely observing thermal free-free emission usually in optically thick regime.

In figure 8.1 we report a histogram where the statistical distribution of the calculated spectral indices is shown. Despite of the fact that different bins could lead to different apparent shapes, it is possible to notice how the distribution is strongly peaked around a spectral index value equal to 0. This result was quite expected, indeed. It has been said, in fact, that the majority of the already classified bubbles are planetary nebulae; furthermore also other kinds of evolved stars (such as LBV or WR) are characterized by a radio free-free emission, with only SNR showing clear non-thermal features. An improved depiction of the spectral index distribution could be found in figure 8.2. In this plot it is possible to see that almost all spectral index values are located close to green line, representing the locus where the spectral index is equal to -0.1 (pure optically-thick free-free emission).

In the last chapter we have reported how some bubbles have been studied by

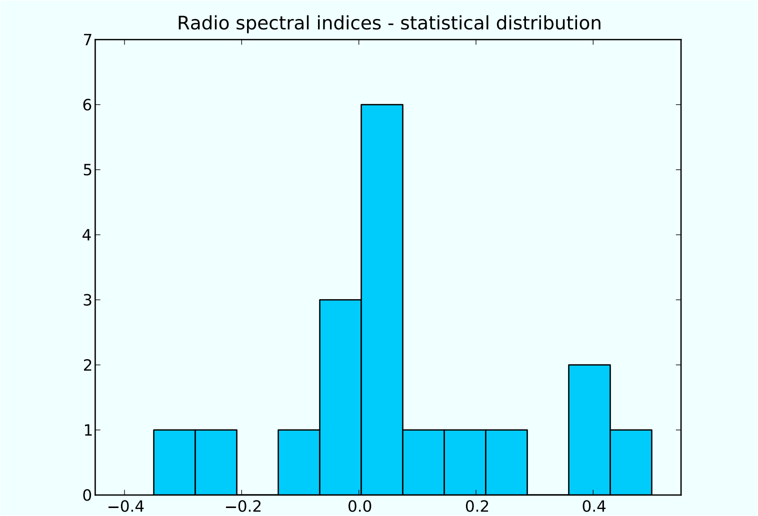

Figure 8.1: statistical distribution of the bubble radio spectral indices. It is appreciable how the distribution is peaked around $\alpha = 0$; different, but reasonable, choices of the histogram bin do not change the distribution shape significantly.

different authors in literature. For five of them a possible classification has been given, being four planetary nebula candidates (magenta mark in figure 8.2) and one H II region candidate (green mark in figure 8.2). As previously explained and as graphically evident, the spectral indices we found for these five sources is compatible with their classification hypothesis.

Four sources show a spectral index value quite negative to deserve a discussion, the bubbles 3367 e 4486. Their spectral indices were estimated as -0.30 and -0.25 respectively, values usually to much negative to be considered as pure free-free emission. However it is evident that the errors associated with these two measures are great (in the latter case because of the source faintness) and so, in principle, a thermal emission cannot ruled out for these bubbles. These strange values, anyway, make important to further investigate on these two objects.

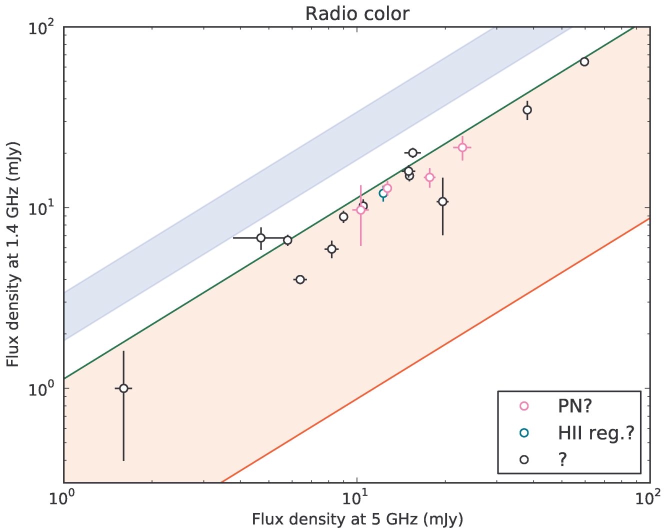

Figure 8.2: flux densities comparison at 1.4 GHz and at 5 GHz. The red area represents all the possible expected values for a free-free emission, with the red line representing a pure black-body emission ($\alpha = 2$) and the green a pure optically thin free-free emission ($\alpha = -0.1$); the blue area represents spectral indices between -0.5 and -1, typical of an optically thin synchrotron emission. It is noticeable how the points usually lie close to the green line.

8.2 Relation between radio and MIPSGAL

The only determination of the radio spectral indices cannot be sufficient for a satisfactory classification scheme for the bubbles. In this section we will see if it is possible to correlate radio data with the MIPSGAL data at 24 µm to obtain further informations.
In principle the emission at 24 µm and the emission at 6 cm have a different origin. In fact, the emission at 24 µm originates both from warm dust, as thermal emission, and from some gas forbidden lines, as the [O IV] line at 25.89 µm and others (see section 1.1); the radio emission at 6 cm, instead, originates from the ionized gas, usually as thermal free-free emission or also as synchrotron emission in case of strong magnetic fields. However it has been shown from several authors that a strong correlation between mid- and far-infrared and radio exists [55][56].

In figure 8.3 the flux density at 24 µm from the MIPSGAL catalog (table 6.2) is plotted against the flux density at 6 cm from our observations (table 2.3), for all the bubble with measured 6-cm flux density with the only exception of the bubble 3313 (see below). Visually, the correlation appears very clear with the $\log(F_{\mathrm{ir}}/F_{\mathrm{ra}})$ between 1 and 3 for all the object. In particular, if we suppose that there is a linear correlation between the flux density sets and we define for each bubble the quantity

$$q = \log \frac{F_{\mathrm{ir}}}{F_{\mathrm{ra}}}$$

we find that $\overline{q} = 1.9 \pm 0.4$, with the error being its standard deviation. The hypothesis of a linear correlation could be corroborated by a linear fit of the logarithmic values of the two data-sets, in fact we obtain

$$\log F_{\mathrm{ir}} = 0.9 \log F_{\mathrm{ra}} + 2.0$$

where, despite of the small size of our sample, it is possible to see that the relation is almost perfectly linear (0.9 instead of 1) and that, as a consequence, the simple mean value of the ratios, $\overline{q}$ is a good estimation (1.9 instead of 2.0 from the fit) for their constant of proportionality.

The bubble 3313 apparently as a much higher $F_{\mathrm{ir}}/F_{\mathrm{ra}}$ value, about 4000. At 24 µm this bubble appears very extended (about 80″) and maybe interacting with the bubble 3312. Spectroscopical near-infrared studies of the central sources of these two bubbles reveal that both can be classified as Wolf–Rayet stars of the same spectral type WN8–9h [57]. Our radio observations at 6 cm show a very faint irregular nebula around the central star of the bubble 3313 (figure 2.10), less extended than the 24-µm nebula, with no emission around the other bubble or in any other region where the 24-µm is present. No emission is visible from our maps at 20 cm. Indeed it is possible that there could be radio extended emission with a too low brightness (specially at 20 cm) or that has been resolved out (specially at 6 cm). For these reason the flux density computation has not be considered reliable enough and the bubble has not been included.

In conclusion we can say that the emission at 24 µm is well-correlated to the emission at 6 cm, but from our data we cannot use the flux density ratios to discriminate between sources. For example, if we compute $\overline{q}$ only for the eight "certain" planetary nebulae we find a value of 1.7 ± 0.4, that is in the same range of the total mean value.

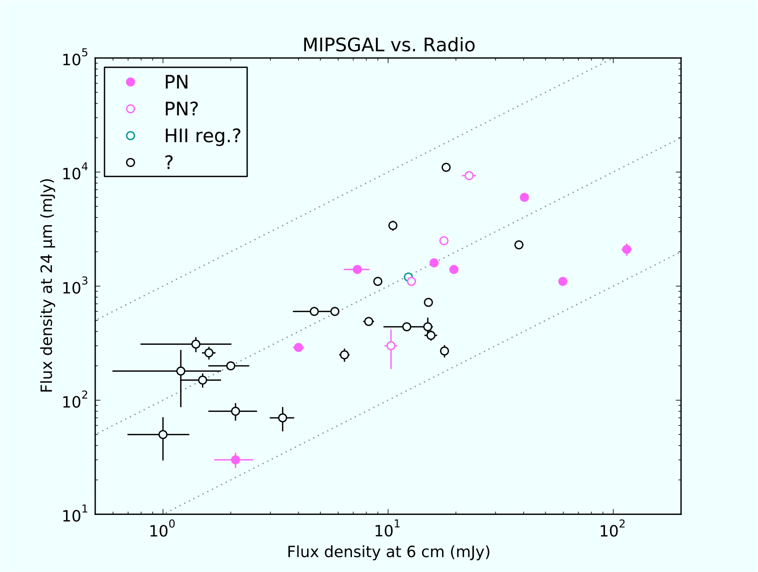

Figure 8.3: correlation between MIPSGAL flux densities at 24 µm and radio data at 6 cm from our EVLA observations. The grey dotted lines represent flux density ratios of 10, 100 and 1000.

8.3 Relation between radio and IRAS

In this section a classification scheme for planetary nebulae is discussed moving from our radio data and IRAS archive data (see section 6.2). Though IRAS had a so poor resolution that, in general, planetary nebulae could not be resolved, its sensitivity was high enough to allow planetary nebulae detections at least at the distance of the galactic center [13].

Unfortunately, only few bubbles studied here have archive IRAS flux density values, with no one of them having flux density determinations in more than two bands[1]. Using, however, IRAS point source catalog values for known planetary nebulae and H II regions and, for each one of these object, searching for historic VLA observations at 6 cm [49], it was possible to draw different color plots useful for our classification purposes.

As a first step, it is important to notice that, as we could expect from the previous section, the IRAS flux densities at 25 µm are well-correlated with

---

[1] With no records at all at 100 µm.

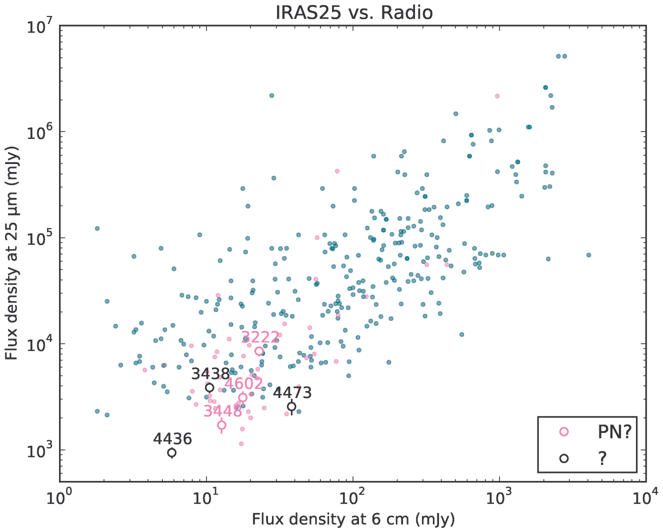

Figure 8.4: correlation between IRAS flux densities at 25 μm and radio data at 6 cm. Small points are archive planetary nebulae (magenta) and H II regions (green); larger points represent our bubbles with IRAS archive values and our radio data. It is possible to notice that the two flux densities are well-correlated and that the planetary nebulae are usually characterized by lower flux density values.

the radio flux densities at 6 cm (figure 8.4). In this plot we can see that the planetary nebulae occupy the lower-left region of the figure, meaning that they are usually fainter than other H II regions. All our six bubbles, for which both flux density values are available, are also located in the lower-left region of the plot; however, the only conclusion that could be given is that they are all compatible with a planetary nebula, nothing more.

A more interesting result can be obtained by plotting the IRAS flux density values at 60 μm against the radio flux densities at 6 cm (figure 8.5). In this plot it is still evident how infrared and radio flux density values correlate but it is also possible to notice how planetary nebulae represent a population clearly separated from other H II regions (with exceptions, indeed). This behavior can be easily explained assuming that the typical infrared spectral energy distribution for planetary nebulae is usually peaked towards shorter wavelengths with respect to the other H II regions (see section A.3). From

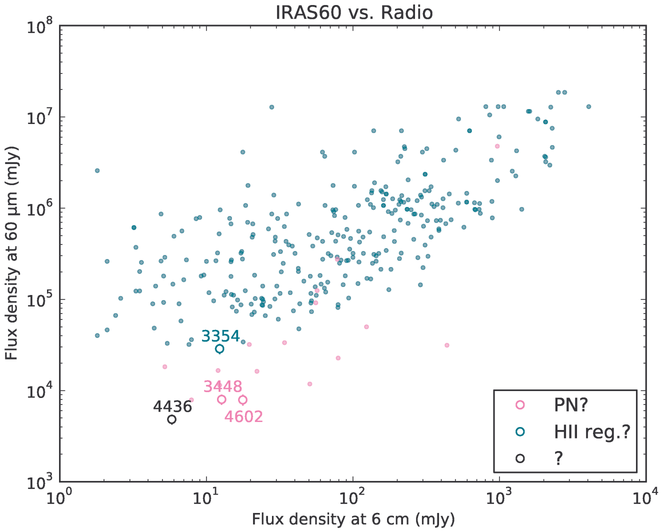

Figure 8.5: correlation between IRAS flux densities at 60 µm and radio data at 6 cm. Small points are archive planetary nebulae (magenta) and H II regions (green); larger points represent our bubbles with IRAS archive values and our radio data. It is possible to notice that the planetary nebula population is characterized by a lower value of the two flux density ratio and is well-separated from the H II regions.

this plot, the bubble 4436 could be considered as a planetary nebula candidate. This hypothesis cannot be greatly corroborated by a pure IRAS flux-flux plot, as shown in figure 8.6. Here we can also see how planetary nebulae take place in a well-defined region of the plot, separated by other H II regions. Furthermore, in this plot it is possible to appreciate how the bubbles studied in this work are characterized by a significant lower flux density with respect to already known and classified sources. Indeed, their faintness is the reason why they were hardly detected by IRAS. In particular for the bubble 4436 it is difficult to say which classification is more appropriate since it appears very "far" from the known sources.

Despite the fact that only few data are available, we can also construct color-color diagrams. The first one is shown in figure 8.7 and correlated the ratios between IRAS values at 25 µm and 60 µm (ordinate) and IRAS 25 µm with our radio data at 6 cm (abscissa). This plot summarizes, indeed, the plots in

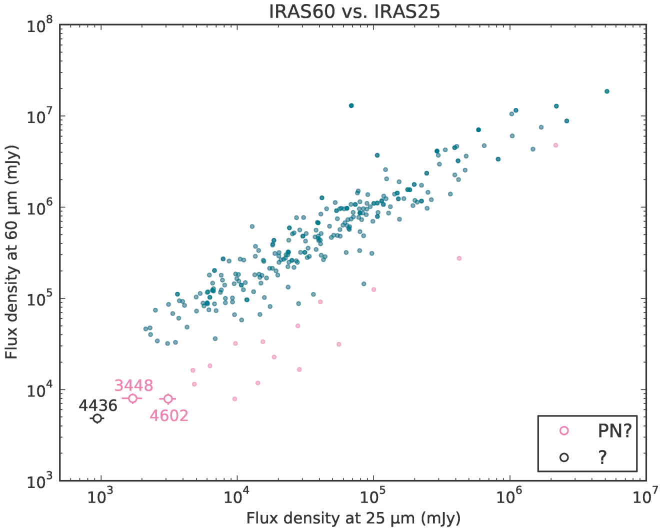

Figure 8.6: correlation between IRAS flux densities at 60 µm and at 25 µm. Small points are archive planetary nebulae (magenta) and H II regions (green); larger points represent our bubbles with IRAS archive values. Also in this plot it is possible to notice that the planetary nebula population is characterized by a lower value of the two flux density ratio and is well-separated from the H II regions.

figures 8.4 and 8.5, since only three bands are given. The planetary nebulae are well-separated from the other H II regions and occupy the lower part of the plot. Also in this plot, the bubble 4436 appears in an ambiguous position. Using, eventually, the IRAS data at 12 µm other two color-color plots may be constructed. We report them in figures 8.8 and 8.9, but it turns out that no one of them is very useful. In the first one IRAS flux densities at 12 µm and 60 µm are correlated with radio values. As for the previous plots, the planetary nebulae are located separately from the other H II. Unfortunately only one bubble is detected at 12 µm and 60 µm; this bubble, namely 3354, was classified as an H II region candidate (section 7.6). In our plot it is found just in the boundary zone between planetary nebulae and H II region, therefore doubts remain. In the second plot IRAS flux densities at 12 µm and 25 µm are correlated with radio values. Here we can see that there is not any separation between planetary nebulae and other H II region. This

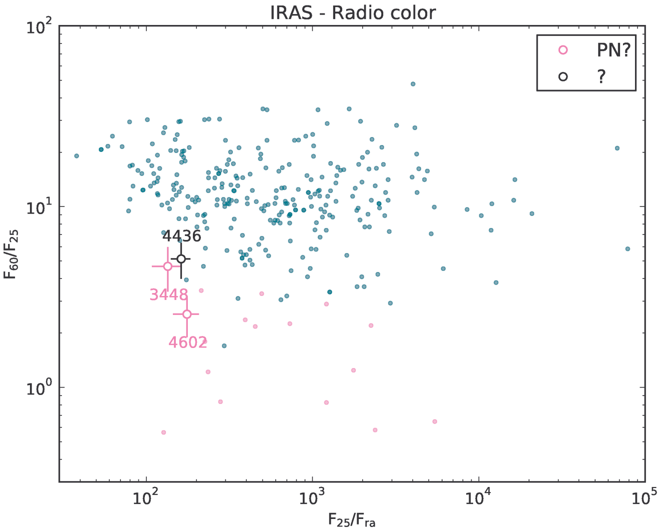

Figure 8.7: IRAS and radio color-color plot. Small points are archive planetary nebulae (magenta) and H II regions (green); larger points represent our bubbles with IRAS archive values at 25 µm and 60 µm and our radio data.

plot, therefore, cannot say anything about the bubble 3438, the only one detected both at 12 µm and at 25 µm. This is a consequence of the strong correlation between the flux densities at this two IRAS bands. It can be easily explained assuming that the emission in this two bands is due to the thermal dust whose emission peaks at wavelengths longer than 25 µm; in this case, the slope of the spectral energy distribution between 12 µm and 25 µm is the same for all the kinds of source considered here.

8.4 The importance of GLIMPSE data

As we discussed in the introduction, one of the characteristic of the bubbles is that they are mostly detected only at 24 µm. The GLIMPSE survey, in fact, failed to detect an extended emission for the majority of the bubbles, despite of the great sensitivity of IRAC. However, as we reported in section 6.4, for some bubbles we were able to extract the central source photometry from the on-line point-source catalog (table 6.3) and we were also able

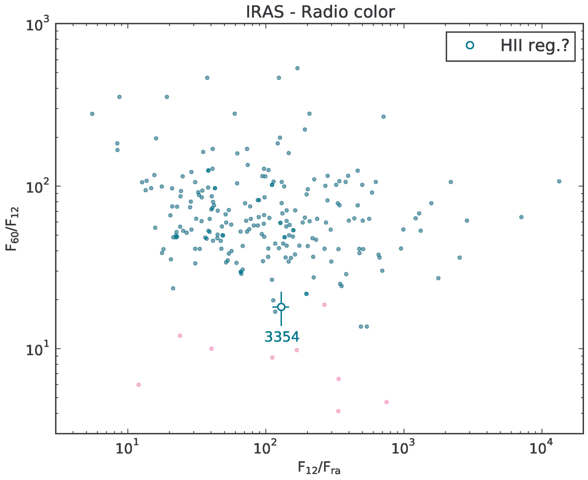

Figure 8.8: IRAS and radio color-color plot. Small points are archive planetary nebulae (magenta) and H II regions (green); larger points represent our bubbles with IRAS archive values at 12 µm and 60 µm and our radio data.

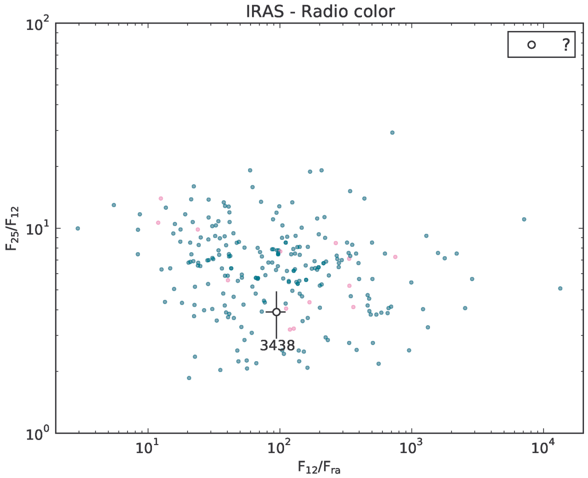

Figure 8.9: IRAS and radio color-color plot. Small points are archive planetary nebulae (magenta) and H II regions (green); larger points represent our bubbles with IRAS archive values at 12 µm and 25 µm and our radio data.

to perform aperture photometry of the very few nebulae clearly visible also at these wavelengths (table 6.4). The results obtained represent a little aid in the classification process, in particular they are important for planetary nebulae classification; in this section we will discuss our bubbles detected in GLIMPSE, starting from the results by Cohen et al. (2007 and 2011) [58][59]. It is worthy of being said that preliminary informations on the nature of a source detected in all the IRAC bands[2] could come directly from their rgb image superposition of monochromatic maps at 8 µm, at 5.8 µm and one among the other two bands [60]. In these three-color images the planetary nebulae usually appear red, while H ii regions appear yellow or white. This is due, for H ii regions, to PAH emission (yellow) or broad-band thermal emission by dust (white) [59]. Looking at GLIMPSE rgb images in the previous chapter we can see that the bubbles 3367, 3448, 4473 and 4602 (figures 7.20a, 7.32a, 7.47a and 7.68a) all show a clear red color; of these four bubbles, two, namely 3448 and 4602 are found in literature as planetary nebula candidates [8][54], while nothing is found about the nature of the other two. From what emerges from this discussion and follows in the next section, it can be concluded that bubbles 3367 and 4473 could also be considered planetary nebula candidates. It impressing, in particular, how the bubble 4473 morphologically resembles bubble 4602 in the GLIMPSE images. On the other hand, the bubble 3354, classified as H ii region in literature [46], shows the expected yellow appearance (figure 7.15a).

All the five bubbles for which the emission at IRAC bands has been considered are detected at 8 µm, while only one is detected in all four bands. It has been shown that the ratio between the flux density at 8 µm and at 20 cm ranging in a well-determined interval and that different kinds of planetary nebulae are characterized by different values of this ratio. In figure 8.10 we plot the GLIMPSE flux densities (from point-source catalog) against the radio values from our data. It is possible to notice how the bubble 3354 clearly does not satisfy the selection criterion, in agreement with a classification as an H ii region and not a planetary nebula. The other four bubbles all lie inside the area where planetary nebulae should be found. In particular both the unclassified bubble 4473 is very close to the median ratio value of 4.7, with a calculated ratio of 4.5. These four bubbles can be divided in two groups, according to their ratio value: the first group comprises bubbles

---

[2] Indeed it is necessary to have the images at 8 µm, at 5.8 µm and at least at one of the other two bands.

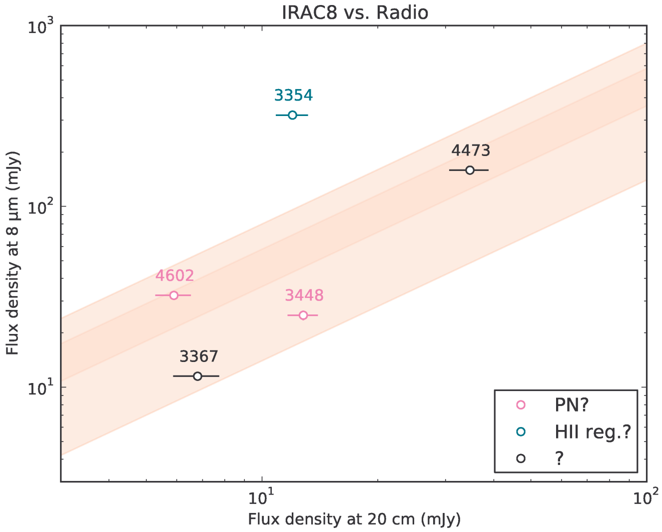

Figure 8.10: GLIMPSE flux densities at 8 μm according to point-source catalog against radio flux densities at 20 cm derived from our observations. The colored area represents the ratio interval where planetary nebulae are usually located according to Cohen et al. (2011) [59], with a confidence level of 1σ (darker area) and 3σ (lighter area).

4473 and 4602 and the second group bubbles 3367 and 3448. We have already talked about the morphological similarities of bubbles 4473 and 4602: the result found here may suggest that these two objects could share many of their physical characteristics. The other two bubbles appear different from the first two; indeed, for bubble 3367 no morphological consideration can be done, while bubble 3448 seems to have bipolar structure. If all these bubbles will be confirmed to be planetary nebulae their morphological and physical differences may be due to intrinsic properties or their evolutionary stage.

8.5 IRAC and WISE correlation

In this section we will discuss a possible classification scheme based on the nebular photometry with IRAC and WISE. In particular we will consider the flux density values at 8 μm (IRAC channel 4), at 12 μm (WISE band $W3$)

and at 22 µm (WISE band $W4$). This section takes advantage from the work of Anderson et al. (2012) [11].

It has been demonstrated that the flux density calculated at 22 µm by WISE is well-correlated with the MIPS photometry at 24 µm, indicating a good reliability of these data. The basic idea is that the planetary nebulae has a different mid-infrared spectral energy distribution with respect to H II regions surrounding massive stars. Therefore mid-infrared color determination can be a useful method to discriminate between planetary nebulae and other H II regions when a simply visual inspection is not sufficient[3].

Indeed, it has been shown that better discriminating color indices can be constructed using far-infrared data from the Herschel survey Hi-GAL (see section 6.14). However these data, though scheduled to be public, are not yet publicly available. Therefore we are restricting to the three bands mentioned above; with these data we are going to consider the two ratios between each one of the WISE band and the IRAC one.

The WISE band at 12 µm traces similar dust emission components as that of the IRAC band at 8.0 µm. However the WISE band is significantly broader and, within it, PAH features at 11.2 µm, 12.7 µm, and 16.4 µm are present [61]. The PAH features at 7.7 µm and 8.6 µm also fall within the bandpass although at diminished sensitivity. In this band, there are also nebular emission lines that may be strong in evolved planetary nebulae. The IRAC band at 8 µm contains also the PAH features at 7.7 µm and 8.6 µm, but in a full sensitivity range. Since PAH molecules fluoresce when excited by far-ultraviolet photons, they emit very strongly in H II regions [62][63]. PAH emission is also moderately strong for carbon-rich planetary nebulae but is weak or absent for oxygen-rich ones [64]. Finally, the WISE band at 22 µm (as for the MIPS band at 24 µm) traces mainly the warm dust. For H II regions, this emission is detected both from the PDR and also in the inner regions spatially coincident with the ionized gas; the first one is probably a combination of emission from very small grains and from a larger grain population whose temperature is closer to 25 K, while the second one likely comes from very small grains out of thermal equilibrium. For planetary, the emission at 22 µm also likely contains contributions from dust at a range of temperatures, but there may also be nebular emission lines that contribute to the emission in this band.

---

[3] Radio spectral energy distribution is not sufficient to discriminate planetary nebulae from H II regions since they all emit via thermal free-free (see section 8.1).

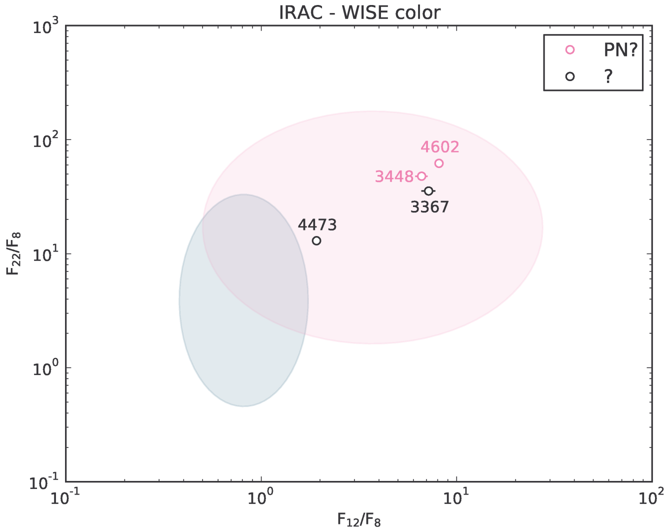

Figure 8.11: color plot using flux density value at 8, 12 and 22 μm. The colored area represents the most probable location of planetary nebulae (magenta) and H II region (green) in such a plot at 3σ level [11]. It is possible to notice that the two PN candidates (3448 and 4602) lie well in the PN area as well as the bubble 3367; the bubble 4473, though in the PN area is very close to the H II area.

Since the emission mechanism of planetary nebulae is slightly different with respect to other H II regions, the color indices we have discussed above allow to perform a basic discrimination. In particular, taken into account the distribution for planetary nebulae and H II region found by Anderson et al. (2012), the figure 8.11 show the areas (up to 3σ) of the color-color plot where, most likely, each kind of object is found. Superimposed to these areas, we report the four bubbles for which all the three flux density values are known. As reported also in previous sections, the bubbles 3448 and 4602, already indicated as planetary nebula candidates, clearly satisfy this color selection too. Also the bubble 3367 seems to well satisfy this criterion being located very close to both 3448 and 4602. The bubble 4473 is located further, but it is still contained in the "planetary nebula" area.
In conclusion, also this test corroborates the hypothesis that the bubbles 3367 and 4473 can be treated as planetary nebula candidates.

8.6 MSX color

The last method for bubble classification discussed in this work employs the MSX flux densities reported in table 6.7. This section makes use of the result in MSX color classification by Lumsden et al. (2002) [35].

Unfortunately only three of bubbles the bubbles studied here had at least three MSX archive flux densities (namely 3222, 3438 and 4602), with values in four bands (all except bands B_1 and B_2) for two of them (3222 and 3438). Of these three bubbles two (3222 and 4602) were proposed as planetary nebula candidates in literature. In the figures 8.12 and 8.13 we report two color-color plot using four and three MSX bands respectively. The choice of these color was determined by the MSX color studies in literature.

In the first plot we use all MSX bands except B_1 and B_2, for which no data are available. We plot the ratio between bands D and C, at about 14 μm and 12 μm, against the ratio between bands E and A, at about 21 μm and 8 μm (for a more accurate reference wavelength for these bands see table 6.6). In this plot, as in the following, the green area representing H II regions is intended to encompass only compact H II regions surrounding young stars; it is possible to notice that this area is, unfortunately, almost coincident with the planetary nebula area (magenta). Worse, our two bubbles lie in two ambiguous positions[4]. The planetary nebula candidate 4602 lies on the boundary of planetary nebulae area but inside the young H II region area; from the consideration done on this bubbles, we may cautiously reject this hypothesis. The other bubble, 3438, is situated on the boundary between planetary nebulae and OH/IR stars; its morphology and the presence of a central source very bright not only at 24 μm but also in the near-infrared and in optical do not agree with a planetary nebula classification, while the clear presence of a strong radio emission, both at 6 cm and at 20 cm, is not much compatible with an OH/IR star.

Also in the second plot the green area representing compact H II regions is almost coincident with the planetary nebula area (magenta). Even in this plot, however, all the three bubbles lie in ambiguous positions. The two planetary nebula candidates, 3222 and 4602, lie on the boundary of planetary

---

[4] Unlike all the previous plots in this chapter, where values for the confidence area for the different kinds of sources were available, in this chapter the confidence areas have been drawn "by hand" trying to encompass all the sources of the same type presented by Lumsden et al. (2002) in their color-color plots. Visually pathological sources were discarded.

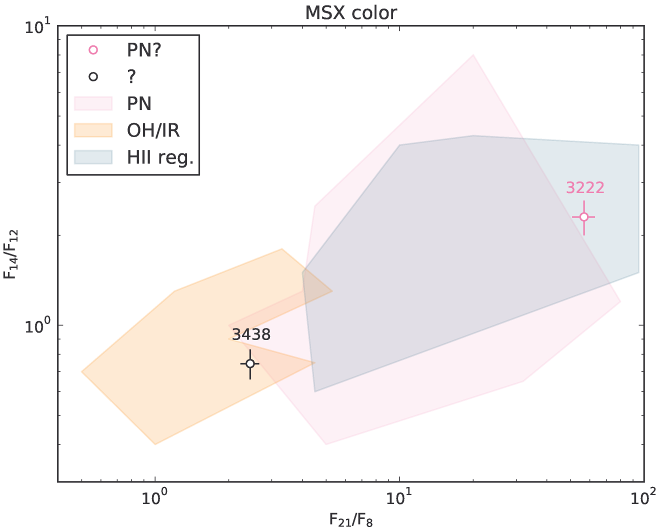

Figure 8.12: MSX color using bands A, C, D and E. Colored areas represent the approximate distribution of known sources [35], being magenta for planetary nebulae, orange for OH/IR stars and green for compact H II regions surrounding young stars.

nebulae area near the H II region area. The other bubble, 3438, is situated, also in this plot, on the boundary between planetary nebulae and OH/IR stars; from the previous considerations no hypothesis on its nature can be ruled out, neither the possibility for this bubble to be a massive object (WR or LBV).

8.7 Possible classification

The broad discussion made in chapter 7 and the considerations carried on in this chapter have allowed to draw a first, partial, picture of the nature of the bubbles.

Our radio observations, when both frequencies have been available, have clarified that almost all of the previous unclassified bubbles are thermal emitters. Even if this statement cannot say exactly what kind of object we are looking at, it allows to ruled out the hypothesis that those thermally emitting bub-

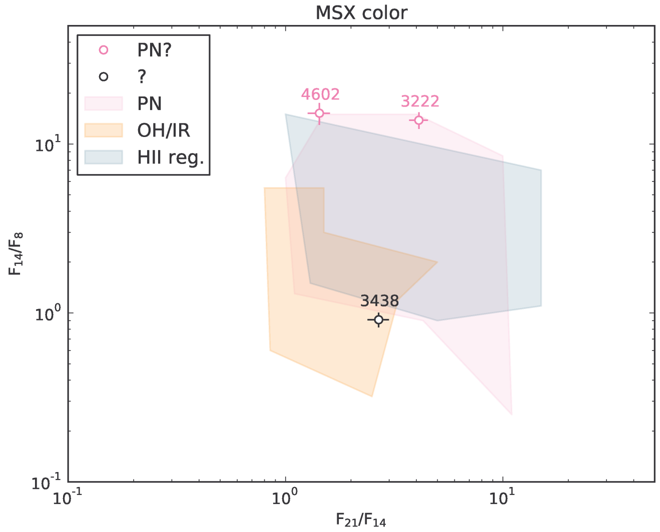

Figure 8.13: MSX color using bands *A*, *D* and *E*. Colored areas represent the approximate distribution of known sources [35], being magenta for planetary nebulae, orange for OH/IR stars and green for compact H II regions surrounding young stars.

bles are supernova remnants. The very presence of a radio emission towards a bubble, anyway, tells us that source is hot enough to ionize its circumstellar medium, ruling out the hypothesis of a red giant, an AGB or a post-AGB star.

In this chapter we have seen how comparing our radio data with archive infrared data from the Spitzer surveys MIPSGAL and GLIMPSE, as well as with data from telescopes such as IRAS and WISE, proved a very helpful method to tentatively classify our bubbles. Both simple correlation and color-color plots have allowed to hypothesize that three, previously totally unclassified, bubbles, namely 3367, 4436 and 4473, could be treated as planetary nebula candidates. Unfortunately less multiwavelength studies for massive objects exists with respect to low mass sources, as planetary nebulae. This is mostly due to a comparatively greater rarity of these objects. Indeed, most Wolf–Rayet stars, for example have been tentatively classified by their infrared morphology, appearing usually more extended than low mass objects and presenting a more complex shape and a well-detected central star;

spectroscopy of their central star could give precious hints, even if ambiguity may still remain (see sections 9.2, 9.3 and A.3).
An extremely powerful allied proved to be the spectroscopical analysis with GBT data searching for OH masers. The preliminary results exposed in chapter 5 and in appendix D have shown that, thanks to the very good data quality, a lot of OH masers have been detected. Even if the GBT field of view is too wide to blindly assert that these masers truly come from the bubbles, and not from field objects, many of them present the characteristic U-shape, clue of emission from an expanding shell.
Finally, a synoptic table on classification hypotheses is report below for some of the bubble treated in this work. In the column "Type" the possible classification is reported, in particular "PN" stands for planetary nebula, "LBV" for luminous blue variable, "WR" for Wolf–Rayet star, "HIIReg" for H II region, PPN for protoplanetary nebula, "SNR" for supernova remnant. If the classification is unclear and the object is a candidate of a certain type then a "?" follows the type; if only a "?" is present then the nature of that object is completely unknown. If the bubble has been observed to be a radio thermal emitter and no more is known about its nature then a "*RadTh*" is reported; if it uncertain if this radio emission is thermal or not also a "?" is reported. In the "Note" column a reference on the sections in which that bubble has been significantly studied is reported; if no hints on its nature were found in literature then "*This work*" is reported, otherwise references to consulted articles are indicated.

ID	Type	Notes
3179	PPN?	*This work, see section 5.6.*
3188	PPN?	*This work, see section 7.3.*
3192	*RadTh*	*This work, see section 7.2.*
3193	*RadTh*	*This work, see section 7.2.*
3214	PN	[1] *see section 2.4.*
3222	PN?	[45] *see section 7.4.*
3282	LBV?	[65] *see appendix B.*
3309	*RadTh*	*This work, see section 7.2.*
3310	SNR	[1] *see section 2.4.*
3312	WR?	[57] *see section 8.2.*
3313	WR?	[57] *see sections 7.2 and 8.2.*
3328	PN	[1] *see section 2.4.*
3333	*RadTh*	*This work, see section 7.5.*

3354	HiiReg?	[46] *see section 7.6.*
3362	*RadTh*	*This work, see section 7.2.*
3367	PN?	*This work, see sections 8.4 and 8.5.*
3384	*RadTh*	*This work, see section 7.8.*
3438	*RadTh*	*This work, see sections 7.9 and 8.6.*
3448	PN?	[8] *see sections 7.10 and 8.3.*
3558	PN	[1] *see section 2.4.*
3654	PN	[1] *see section 2.4.*
3706	PN	[1] *see section 2.4.*
3724	*RadTh*	*This work, see section 7.2.*
3866	PN?	[46] *see section 7.11.*
3910	SNR	[1] *see section 2.4.*
4409	PN	[1] *see sections 2.4 and 7.2.*
4422	PN	[1] *see section 2.4.*
4436	PN?	*This work, see section 8.3.*
4452	PN	[1] *see sections 2.4 and 7.2.*
4465	*RadTh*	*This work, see section 7.13.*
4473	PN?	*This work, see sections 8.4 and 8.5.*
4479	PN	[1] *see section 2.4.*
4486	*RadTh*?	*This work, see section 7.15.*
4497	*RadTh*	*This work, see section 7.16.*
4552	*RadTh*	*This work, see section 7.17.*
4580	*RadTh*	*This work, see section 7.2.*
4584	*RadTh*	*This work, see section 7.2.*
4589	*RadTh*	*This work, see section 7.18.*
4602	PN?	[54] *see sections 7.19 and 8.3.*
4607	*RadTh*	*This work, see section 7.20.*

Table 8.1: classification of the bubbles.

Chapter 9

Conclusions

In this last chapter we will review the entire work, discussing what results have been achieved thanks to this analysis. We will point out which problems and difficulties have emerged, sometimes unexpectedly, from the long, and still on-going, data reduction and analysis process; in particular we will focus on what proved too complicated to be satisfactorily resolved within this work, such as the combination of single-dish and interferometric data. At the end, we will briefly get a glimpse on this work legacy and on the future studies that should be undertaken.

9.1 Comments on the data reduction process

One of the main purposes of this work was to show how radio data can be a powerful weapon to solve open questions in galactic astrophysics. In particular the extraordinary sensitivity of instruments like VLA and GBT had allowed to conduct observations of unprecedented depth, getting, for example, to the clear detection of faint radio sources with flux densities of order of 1 mJy.

These new great capabilities, however, translate in an increased difficulty in the data reduction. The situation is much different between VLA and GBT. For the first one a good and comprehensive reduction package, CASA, already exists, though it presently does not seem to be perfectly adequate to the new huge datasets produced after the expansion of the VLA. For the GBT the situation is worse, since only a basic package exists for spectral line data and no general software exists for continuum observations.

The greatest difficulty in VLA data reduction with CASA is, certainly, represented by the editing process. In fact, though the data at 5 GHz appeared with no significant corruption, the data at 1.4 GHz were so heavily affected by interferences that the editing process took at least 90% of the entire time dedicated to this frequency data reduction. The extremely large new bandwidth of VLA in band L has both increased the number of affecting interferences but also the way they can be filtered out. Indeed, the philosophy under interferences flagging is to individuate "normally behaving" portion of the data and use them as template for the remaining part. In fact, if some interferences are so evident that a quick look is sufficient to find them out, many other are well-hidden beneath the data; furthermore a perfect individuation of an interference allows to flag all the corrupted data and only them, without deleting good data. In 2011 Urvashi developed the CASA task `testautoflag` for an automatic flagging process. The basic idea under this, still experimental, task is the same explained in section 3.4 and re-prised here; after having calculated a bandpass template, it looks for data deviating more than a user-defined threshold away from the template and repeats this procedure for every time, baseline and frequency chunk and mixing up this variables [66]. The work carried out in section 3.4 could help to improve this task significantly, since, as we have seen, many kind of different interferences occurred and therefore subtler algorithm could be implemented.

The automation of the flagging process is not only desirable but necessary to avoid that larger and larger dataset take significant amount of time to be edited. It has been shown, in fact, how calibration automation has reduces the total amount of time required for this operation; the goal would be to get to a similar process also for editing, bearing however in mind the incomparable intrinsic difficulty.

The second huge problem, connected to data reduction, has emerged in chapter 4, when we discussed continuum observations with GBT and their subsequently concatenation with interferometric data. In this context the total lack of general procedures has dramatically emerged. The raw output data of GBT can be stored as standard SDFITS files; these files can be, reductively, described as tables[1] where in each entry a single datum (proportional to the sky brightness toward the pointed direction) is recorded along with telescope

---

[1] These files are indeed standard FITS files with primary HDU with no data (but with a header) and one or more binary expansion tables, characterized by single-dish standardized keyword.

and time dependent parameters as the current azimuth and elevation or the current system temperature. The construction of the map from this set of pointing involves non-trivial operations since they do not lie on a regular grid because of pointing errors. Therefore to obtain the map, bidimensional regridding and interpolation are needed.

Another important problem with single-dish continuum data emerged in section 4.3. In fact, the map showed the so-called “stripe effect”, consisting on prominent stripes, along the whole image, in the direction of the scan, because of systematic errors introduced by instrumental noise shift and instability. In section 4.6 the algorithm used in this work for destriping has been presented has a proper procedure (listed in section C.3) since no other routines were found with the required characteristics. The algorithm returned very good results for the pure appearance of the maps, even if a flux density study on them has not yet been extensively conducted. The procedure is generalizable with little efforts and could, almost as it is and with a proper interface, be integrated in CASA.

The very great issue concerning the single-dish continuum data is however their combination with interferometric data. In section 4.7 we have reported that one of the best solution was to use the CASA task `feather`, specifically designed for this purpose. The basic algorithm under this task was to Fourier transform the single-dish data and to create a fictitious *uv* dataset that was feathered with the interferometric data using a common *uv* region for cross-calibration. Problems arise since the user is not able to control and check most of the parameters and the intermediate results of this operation. In particular it is not possible to act directly on the matched visibilities. This prevent to fine tune to the few user-controllable parameters before that an image has been produced, without a way to reliably determine the quality of the combination.

The problem of the combination of single-dish data and interferometric ones is not, obviously, limited to VLA, since the flux-loss problem is an intrinsic issue of all interferometer. When interferometer like ALMA or SKA will be full operative this question will be very pressing; in particular for ALMA that, even when totally complete, will have a very small largest angular scale and single-dishes for total power observation are therefore needed and already embedded in the project.

The last considerations about the data reduction concern the GBT spectral line observations. These data are available in SDFITS format and can be basically reduced using the package GBTIDL maintained by the GBT staff.

Unfortunately, also this software is not fully adequate to a fine data reduction, as we have discussed in section 5.5. In fact, one of the most important lack of this software is the impossibility to perform an accurate data editing in order to individuate and remove interferences. Also the calibration process does not seem to be perfect and a "manual" calibration has therefore been performed.

9.2 The (un)veiled nature of the bubbles

As it could be evinced reading throughout this work, the classification of the bubbles is a very complicated matter and a definitive answer is far from being given. Specially in the last two chapter, it has clearly emerged that the multiwavelength and multi-method approach is the only way to reach a satisfactory classification, that is with as less ambiguous as possible.

It is possible to state that our purpose to characterize the radio emission, both as continuum and as masers, has given good results. For at least 14 bubbles, previously unclassified, the spectral index analysis suggests their nature as thermal free-free emitters. This statement has, for some bubbles, corroborated some unconfirmed hypothesis about their classification and has, for others, given a first indication about their nature. Of course, in this latter case, nothing more has been possible to say on specific sources since many radio emitters share a thermal free-free spectrum; however it has served as exclusion rule for synchrotron emitters like supernova remnants.

Extremely useful proved to be the GBT observations searching for OH masers. As explained, some OH lines are strictly characteristic of evolved stars such as AGB and post-AGB. These stars are not radio emitters, so our search for OH masers has been focused to undetected sources[2]. The presence of some OH maser lines can be therefore seen as a precious indicator of the nature of the observed bubble. It is important to notice that the GBT beam, at the frequency we observed, is about $9'$ wide; this does not preclude the possibility that the maser emission originates from other field sources. However some maser detections show a very clear "U" shape, a clue that the maser emission is associated to an expanding shell, as expected for our bubbles.

Important results have been obtained when our radio data have been combined with archive data from infrared observation with Spitzer, IRAS, WISE

---

[2] Clearly it is possible that objects expected to show a radio continuum emission are not detected simply because they are too faint.

and MSX. It has been shown, in the previous chapter, that correlation and color-color plot can be very useful to discriminate between sources. This can be easily understood given data each kind of source has its peculiar spectral energy distribution and these plots can be see as a powerful method to look at these peculiarities.

A brief discussion on achievements in bubble classifications will be now presented (a comprehensive list has been reported in table 8.1).

The bubbles 3222, 3448, 3866 and 4602 have been reported in literature as planetary nebula candidates. For all these four bubbles we have found a radio spectral index compatible with a free-free emission, corroborating their classification. For bubbles 3448 and 4602 confirmations come also from the correlation between our radio data with IRAS and IRAC data and with IRAC–WISE color.

The bubbles 3312 and 3313 have both been classified in literature as Wolf–Rayet stars. Their proximity in the sky may be due to a real proximity in reality and their respective shells could be interacting. Interesting, while we detected radio emission from 3313 at 5 GHz we failed to detect 3312. Their classification as Wolf–Rayet stars has been driven firstly by morphological consideration since both present a very extended and filamentary shell with a well-detected central source. Spectroscopic follow-up on these central sources seems to have confirmed this hypothesis but doubts still remains.

Also the bubble 3354 has been classified starting from pure morphological consideration but as an H II region. Our radio data appear to support this hypothesis having given a free-free spectral index. By a combination of our radio data with IRAC data at 8 µm it has been possible to exclude that this bubble is a planetary nebula.

For the nature of the bubbles 3179 and 3188 no hypothesis in literature were found. Our GBT spectra, however, show that towards these bubbles an OH maser emission at 1612 MHz from an expanding shell is present. Since no radio continuum or other prominent OH masers have been detected, it has been possible to argue that this bubbles are in a transitional phase between AGB and planetary nebula and can be considered as protoplanetary nebula candidates.

The bubble 3282 was already note as an luminous blue variable candidate. This bubble was deeply studied and the results are extensively presented in appendix B. Though it is not formally possible to declare that this object is certainly an LBV, since no flux density history is available, our study seems to support this hypothesis.

The bubbles 3367 and 4473 have not previously been classified in literature. Our radio spectral index analysis has shown that both these bubbles are thermal free-free emitters. Furthermore, it has been shown in sections 8.4 and 8.5 that both the correlation between our data at 20 cm and flux densities at 8 μm as well as the IRAC–WISE color suggest that these two objects could be considered planetary nebula candidates. It is remarkable, moreover, how the morphology of the bubble 4473 in the IRAC bands strictly resembles the morphology of the planetary nebula candidate 4602.

Also the bubbles 4436 has not previously been classified in literature and our radio spectral index analysis suggest that it is thermal free-free emitters. For this bubble, however, only IRAS data exists for further considerations. Considering that this bubble appears very faint both in radio and in the infrared it is very difficult to use the correlations between our data and archive IRAS data. Anyway in section 8.3 it has been shown that also 4436 emission is compatible with a planetary nebula and therefore it should be considered at least as a planetary nebula candidate.

For some bubbles we detected in radio the archive data were insufficient to proceed even to a tentative classification. However for bubbles 3192, 3193, 3309, 3333, 3362, 3384, 3438, 3724, 4465, 4497, 4552, 4580, 4584, 4589 and 4607, no one of them previously discussed in literature, our radio spectral index analysis has revealed that they all are thermal free-free emitters.

In synthesis we have shown how important radio data can be but also that a multiwavelength approach is usually fundamental to get to a classification scheme. In particular we have shown how radio and 24 μm flux densities, though strictly correlated, alone are not capable of reliable classification.

We have sometimes discussed about the morphology of the bubbles at different wavelengths, considering a peculiar shape as indicative of some kind of circumstellar envelope. It is important to say, however, that these considerations are applicable only to few sources. Indeed, many bubbles are barely resolved and their lack of significant feature may be both an intrinsic property or an instrumental limit.

9.3 Future studies

From what we have discussed in the previous section it appears clear that a lot of work is still to do. In particular two different directions shall be pursued at the same time. The first one is concerning new data collection and the second one is concerning the completion of the analysis of the present data.

A great portion of the electromagnetic spectrum ranging from mid-infrared to radio is still uncovered by useful observations. This range of wavelengths is just the one covered by ALMA, and it is the only instrument in this interval to reach such high resolution and sensitivity. ALMA observations could be an important way to characterize the dust of these objects, building accurate sub-millimeter SEDs, and also to characterize their chemistry by means of spectral line observations.

Another important observation program would use the SINFONI spectrometer at VLT to obtain near-infrared spectra of the central source. In fact we have seen that this kind of characterization can lead to important results, specially in the classification of Wolf–Rayet stars.

Our recent observations with the GBT of the presence of OH maser lines in, at least, 70 bubbles is pushing us towards obtain higher-resolution images. In fact, the resolution of the GBT at 1.6 GHz does not allow to exclude that the maser emission could come from other sources. Therefore, observations with the EVLA will be proposed to confirm the association of masers with bubble; subsequently, it will be possible to propose VLBI observations to map the OH emission.

Since most of bubbles appear unresolved in our EVLA observations, a proposal for more extended EVLA configurations is planned for the next deadline (February 2013); these data would be concatenated with the present data in configurations C and D, obtaining both very high resolution and very high reliability in flux density recover (no additional flux loss would occur). New higher-resolution maps would be of unprecedented sensitivity and would allow to make morphological comparison between radio and mid-infrared, highlighting systematic analogies and differences.

Many of the bubbles are not visible from the northern hemisphere. For these bubbles also an ATCA proposal is planned for the next deadline, in such a way to obtain image comparable to those of the northern hemisphere with EVLA.

Despite of the possibility to obtain observation time, the study of the MIPSGAL bubbles is just at its beginning and the complete analysis of the radio data now available would take many months or years. Their reduction has been rising concerns on huge dataset management. For example, I found out extremely useful to write a CASA calibration pipeline to automate the calibration process (still with some degree of user control); this pipeline allowed to quickly calibrate dataset previously split in spectral windows. An analog automation of data flagging proved much harder, but experience with 20-cm data (with a lot of RFI) would suggest that different ways could be investigated.

Other important clues from the available data could rise from polarimetric analysis (which has not been conducted yet); a detection of highly linear polarized emission, for example, could support the hypothesis of synchrotron processes even for those objects observed only at one frequency.

Beside the radio continuum data, different observations were also carried out with Herschel. The analysis of these data has just begun, but it is possible to say that many bubbles, detected with EVLA, are detected at 70 µm and few of them also at longer wavelengths up to 350 µm.

Parallel to continuum studies, a deep analysis is deserved by the GBT spectra. From the preliminary analysis it is possible to infer that for many bubbles the spectra can unveil important informations as the dynamics of each shell or an estimate of their distances from galactic rotation models. From further studies of the strength of each OH maser line, it is possible to understand, in case of an AGB star, in which evolutionary stage that evolved star is observed [24][25].

The purpose for the next future is then to understand the nature of each bubble, getting to an exhaustive picture of these objects by means of already present data and possibly future ones; in particular continuing the multi-wavelength study spreading from radio to near-infrared, where each single contribution could carry important informations, but also by extracting as many informations as possible from spectral data.

Appendix A

Physical properties of some galactic sources

In this appendix chapter we will discuss some physical properties of the galactic objects encounterd in the previous chapters. The following sections are not to be intended as an exhaustive review of their topics, but as brief summaries that point out how physical differences reflect on what we observe, in order to help to unveil the nature of unclassified objects.

A.1 Ultra-compact H II regions

The ultra-compact H II regions are clouds of gas (mainly hydrogen) ionized by the radiation field of a massive young stellar object.
These objects are immersed in the interstellar medium, composed of molecular cloud and dust, which absorb entirely the intense radiation of the proto-star, from the ultraviolet to the near infrared. If the forming star is massive enough, the Lyman continuum photon flux is able to ionize, almost completely, a wide region (up to about 0.1 pc with $n_e \geq 10^4\,\mathrm{cm}^{-3}$) of hydrogen around the proto-star. Furthermore, ultraviolet and optical photons heat the dust which re-emit in the infrared.
Therefore, in the near infrared the emission is dominated by the gas free-free emission, the thermal emission from the very hot dust and the non-thermal equilibrium emission from very small dust grains. Moving toward the mid-infrared it is possible to detect the PAH emission; this emission usually comes from a region of neutral gas (called photon dissociation region, PDR) just

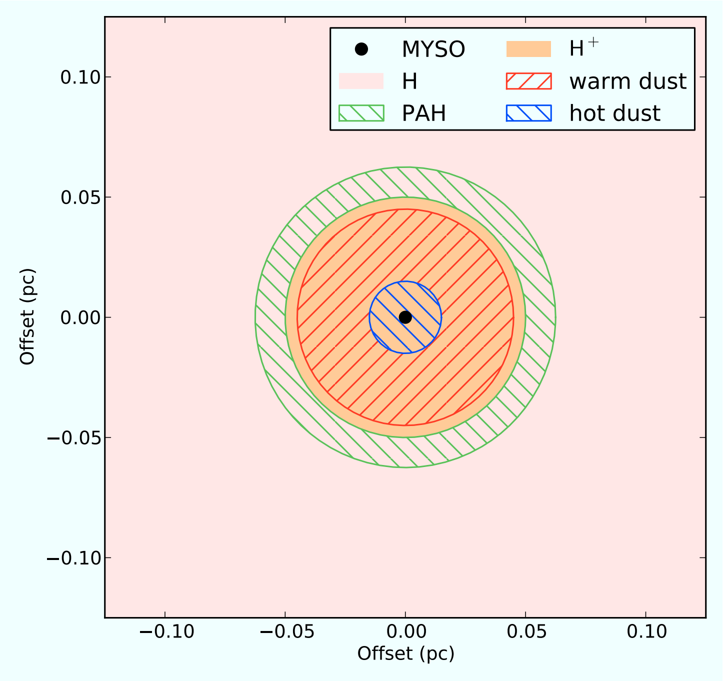

Figure A.1: a schematic model of a photon-bounded ultra-compact H II region. The extension of warm dust region may vary with respect to the H$^+$ zone. Dimensions are indicative and the ISM is not represented.

outside the ionized front, because the PAH are destroyed by the ultraviolet photons. In the mid-infrared the emission comes, almost exclusively, from the thermal warm dust, covering a region of about the same extesions as the ionized zone. At the radio wavelength the emission is due to the thermal free-free transitions and the morphology of the source is usually well represented by one of the following five shapes: spherical, cometary, core-halo, shell and irregular. In figure A.1 a model of a photon-bounded ultra-compact H II region is illustrated.

In some regions, also an extended radio emission has been found, associated with the compact emission thanks to radio recombination lines velocities equal for both the regions. In those regions where the extended emission is missing, it has been possible to detect CH_3OH maser emission; these are thought to be very young ultra-compact H II regions.

As previously said, the ultra-compact H II regions are located inside large molecular clouds, places of intense star formation. The composition of this environment can be studied by means of millimetric and sub-millimetric spectroscopy. In the inner part of the region it has been possible to observe emission lines, for example, of CO, CS, HCO^+ and NH_3, and also absorption lines from H_2CO and NH_3. Also carbon radio recombination lines have been observed from the PDR. These spectroscopic studies also allowed to shed light on the dynamics and the evolution of these nebulae.

The presence of a young OB star ionizing the nebula would also give us the opportunity to study its stellar wind. However, the strong extinction prevents us to observe the central object at least at ultraviolet and optical wavelenghts; even if the extinction decreases in the near-infrared, at these wavelength the emission of the nebula becomes important and covers the star emission. Therefore, in order to study the stellar wind in the near-infrared, very high resolution is needed so that it is possible to separate the star from the nebula. It has also been reported the detection of hard X-ray emission toward the central object; this emission is thought to arise from shocks within a radiatively driven stellar wind.

A.2 Evolved late-type stars

In this section we will briefly summarize the post-main sequence evolution of stars with ZAMS mass between 0.5 and $10 M_\odot$ (we refer to them as late-type stars[1]), all characterize by a roughly common evolutionary path leading to the formation of a planetary nebula (outer stellar layers) and a white dwarf (inner core).

When hydrogen fusion in the stellar core is over, the star moves away from the main sequence, migrating toward the red giant branch. In this stage the stellar helium core collapses, beacuse its internal pressure is not sufficient to balance gravity; however, the gravitational collapse releases energy, heating a shell outside the core where hydrogen fusion continues. The core continues to collapse until the electron degeneracy pressure is high enough to support the star gravity. Hydrogen fusion in a shell causes the star outer layers to expand so much that the effective temperature decreases (making the star redder).

The shell hydrogen fusion causes further contraction of the stellar core until

---

[1] Stars much below $0.5 M_\odot$ in the ZAMS are believed to evolve differently, and they will not considered here.

the temperature and pressure become sufficient to ignite helium fusion (as a helium flash for stars under about $1.4M_{\odot}$). The energy released by helium fusion causes the core expansion and an inhibition of the shell hydrogen fusion. The star, therefore, contracts and increasing its surface temperature (Horizontal Branch an Red Clump phases).

When all the helium in the core is completely fused in carbon and oxygen, fusion reaction can continue in outer shells. The star than migrates toward the asymptotic giant branch (AGB) phase, passing through an instability period, which increases the mass loss through powerful stellar winds and violent pulsations (such as OH/IR stars). The expelled gas, relatively rich in heavy elements created within the star, builds up in an expanding shell (circumstellar envelope) cooling as it moves away from the star. Under this conditions, dust particles and molecules can form and, thanks to the central star radiation maser emission may occur (see section 5.1).

After the AGB phase the star evolves in a protoplanetary nebula. This stage is entered as the hydrogen envelope has been reduced to about $10^{-3}M_{\odot}$, when it is believed that no further significant mass loss occur, and the effective temperature of the star is reduced to about 5 000 K. Though the central star is too cool to ionize the slow-moving circumstellar shell ejected during the AGB phase, there is evidence of collimated high-velocity winds which shock and shape this shell [67].

We do not expect to observe continuum radio emission from AGB stars, since their effective temperature is too low to ionize the circumstellar medium. However, as explained in section 5.1, these object may be characterized by maser emission from different molecules, such as OH.

A.3 Planetary nebulae

As explained in the previous section, the last stages of a late-type star life are characterized by a high degree of instability. Eventually pulsations are large enough to eject the outer layer of the star into space. As the star lose more and more outer layer, deeper and deeper layers are exposed. The deeper the layer is located the higher its temperature is; when the exposed surface reaches a temperature of about 30 000 K, the ultraviolet photons flux is able to ionize the ejected layers, forming a planetary nebula.

The central star undergoes a two stage evolution, first becoming hotter as it continues to contract and hydrogen shell fusion reactions occur and then slowly cooling when the hydrogen shell is exhausted. In the second phase, it radiates away its energy and fusion reactions cease, as the central star is not heavy enough to start the carbon and oxygen fusion. During the first phase the central star maintains constant luminosity while reaching effective temperatures around $10^5\,\mathrm{K}$; in this stage the central stars show an optical and near-infrared spectrum similar to a Wolf–Rayet star and therefore are usually identified as [WC] or [WN] (see section A.4). In the second phase, it eventually cools down so much that the ultraviolet radiation is no more able to ionize the circumstellar gas, ending the planetary nebula phase while the star becomes a white dwarf. The mean life duration of a planetary nebula, starting from the CSE ionization to its recombination, lasts around 10^4 years. The typical dimensions of a planetary nebula are around one light year, with a typicial density ranging from 10^2 to $10^4\,\mathrm{cm}^{-3}$, that could be, indeed, as high as $10^6\,\mathrm{cm}^{-3}$ for very young planetary nebaulae. The total mass of the ionized gas is usually between 0.1 and $1M_\odot$, while its electron temperature is usually around $10^4\,\mathrm{K}$.

From a morphological point of view, planetary nebaulae show a great variety of shapes, with high-resolution images unveiling extremely complex structures. Though projection effects are present, the reason for the huge variety of physical shapes is not fully understood. Gravitational interaction with companion stars or planets has been proposed as one possible reason, along with the interaction of the nebula with the stellar magnetic field.

A.4 Early-type evolved stars

The post-MS evolution of early-type star is more complicated with respect to late-type stars; in this section we will limit to describe the evolution of very massive star, which are expected to undergo a LBV phase and, subsequentely, to become a Wolf–Rayet star.

The luminous blue variables consitutes a small group of bright stars showing brightness and temperature variation of various entity and that can give rise to occasional strong mass-loss episodes [68]). They are supposed to represent a brief stage (about 40 000 years) of very massive star life.

Typical LBV spectra show emission lines from H I, He I, Fe II and [Fe II], usually with a P Cygni profile. For these stars it is possible to define a “quiet phase”, during which the star appear of spectral type O or B, and an “active phase”, during which the spectral type moves to A or F. However it is believed that the bolometric luminosity does not vary greatly between this two phases and that the effective temperature variation is due to a variation of outer layer opacity.

The typical LBV luminosity varies between $10^5 L_\odot$ and $10^6 L_\odot$, undergoing important oscillations. There are three kinds of luminosity variation: the first kind, said "microvariation", is charachterized by period of few days and luminosity variations of order of 0.1 magnitudes; the second one, said "normal" or S Doradus like, is charachterized by period of few years and luminosity variations as great as 2 magnitudes, with a mass-loss rate around $10^{-4} M_\odot\,\mathrm{y}^{-1}$; finally, the third one, said "Plinian" or η Carinae like, are characterized by great eruption with a great mass-loss (up to $10 M_\odot$ in 10 years) and has a period of order of centuries.

The LBVs originate from stars with a ZAMS mass of at least $40 M_\odot$. When these massive stars move away from the main sequence they encounter the Humphreys–Davidson limit, which causes their instability. During this period the stars move back and forth horizontally through the HR diagram, with great variations of their effective temperature without an appreciable luminosity change. In this stage the LBVs lose a great portion of their mass and finally evolve toward a WR star or a type II supernova.

Wolf–Rayet stars are characterized by strong, broad emission lines of helium and nitrogen (WN) or helium, carbon, and oxygen (WC and WO). The characteristic emission lines are formed in the extended and dense high-velocity wind region enveloping the very hot stellar photosphere. This ejection process uncovers in succession, first the nitrogen-rich products of CNO cycle burning of hydrogen (WN stars), and later the carbon-rich layer due to He burning (WC and WO stars). Most of these stars are believed finally to progress to become supernovae of Type Ib or Type Ic.

Both luminous blue variable and Wolf–Rayet stars are expected to show a continuum free-free radio emission.

A.5 Supernova remnants

A supernova remnant is the structure resulting from the explosion of a star in a supernova. The supernova remnant is bounded by an expanding shock wave, and consists of ejected material expanding from the explosion, and the interstellar material it sweeps up and shocks along the way.

The shock is responsible for the charge particle acceleration; multiple accelerations due to turbulent motion causes the circumstellar envelope to reach kinematic temperatures of order of 10^6 K and the charged particle to become relativistic, showing a power-law energy spectrum like

$$N \propto E^{-\delta}$$

with $\delta \simeq 2$. Since these charge particles are relativistic and there is the presence of a magnetic field, the typical emission of a supernova remant is the synchrotron.

A.6 Characteristic comparison

	UCHII	AGB	PN	LBV	WR	SNR
D (pc)	≤ 0.1	~ 0.1	~ 0.3	~ 1	> 1	> 1
n_e (cm^{-3})	$\geq 10^4$	$10^2 - 10^4$	$10^2 - 10^4$	$\sim 10^3$	$\sim 10^3$	
EM (pc/cm^6)	$\geq 10^7$	$\sim 10^6$	$\sim 10^6$	$\sim 10^6$	$\sim 10^6$	
Neb. mass ($M_\odot$)	–	$0.1 - 1$	$0.1 - 1$	~ 10	~ 10	~ 10
Maser	CH_3OH	OH/SiO	no	no	no	OH
Radio cont.?	yes	no	yes	yes	yes	yes
Thermal radio?	yes	–	yes	yes	yes	no
RRL Δv (km/s)	$30 - 40$	–	$40 - 50$	–	–	–
CO peak (K)	> 1	–	< 1	–	–	–
FIR peak (μm)	~ 100	–	$25 - 60$	–	–	–
PAH?	yes	yes	no	maybe	no	no
NIR nebula?	maybe	maybe	no	no	no	no
NIR cen. obj.?	maybe	yes	maybe	yes	yes	no
Cen. obj. sp.	–	K–M	[Wx]	O–F	Wx	–
Optical neb.?	no	no	yes	yes	yes	yes
X-ray?	yes	no	no	no	no	yes

Appendix B

More on G26.47+0.02

Among the radio sample, the bubble 3282 was already known as a LBV candidate. This source is usually identified as G26.47+0.02 but, hereafter, we will refer to it simply as G26. The bubble was the subject of further and deeper multiwavelength studies, that allowed us to speculate that G26 could be a type-IIn supernova progenitor [65], and this chapter partially summarize these results. This appendix chapter is aimed to demonstrate what kind of study could be done on a single bubble and which physical informations could be extracted if enough data were available.

B.1 The observations of the LBV candidate G26 within the bubble project

As part of the bubble project, the source was observed at 6 cm with the EVLA on March 14th 2010, with an integration time of 10 minutes. The observation was carried out in configuration D and with a total bandwidth of 256 MHz. The theoretical thermal noise, for a 10-min long observation, was expected to be about 60 μJy/beam. Alongside with G26, and other sources, bandpass, flux and phase calibrators have been observed.

The data reduction process has been performed with the CASA package. It was not necessary a deep data flagging since they did not appear to be corrupted.

The bandpass calibration has been done using 3C286 as calibrator; it was observed about every 55 minutes for 150 s. Since its phase fluctuations with time were not neglectable and much greater than fluctuations with frequency,

Project	Year	Conf.	Band	Beam	Notes
AH707	2001	B	L	$6.9'' \times 5.2''$	
AH707	2001	C	L	$22.6'' \times 18.6''$	
AH707	2000	D	L	$111.6'' \times 62.4''$	
AH707		multi	L	$12.2'' \times 10.8''$	*B, C, D concatenation*
AR539	2004	C	C	$6.6'' \times 4.4''$	
AU129	2010	D	C	$19.9'' \times 15.5''$	*This work*
AR539		multi	C	$10.5'' \times 8.9''$	*C, D concatenation*
AL647	2005	B	X	$1.0'' \times 1.0''$	*Central object only*
AR539	2004	C	U	$2.2'' \times 1.5''$	*Central object only*

Table B.1: VLA archive data of G26.

a preliminary correction of the phase variations with time has been done. The phase solution found was applied on the fly while determining the bandpass solutions. The gain calibration has been done using the standard calibrator J1822–0938. For the details of these data calibration, see section 2.3.
The imaging has been done using the Clark algorithm; the restored beam was $19.9'' \times 15.5''$.

B.2 G26 VLA archive observations

In order to overcome the present lack of radio data, a VLA archive search was also performed, retrieving data only for projects where, even if G26 was not the main target, the array was pointed at a position less than $15'/\nu(\mathrm{GHz})$ away from the phase center, that is within 1/3 of the primary beam. Data were found and retrieved at 1.4 GHz, in configuration B, C and D (project AH707), at 5 GHz, configuration C (project AR539), at 8.4 GHz, in configuration B (project AL647) and at 15 GHz, in configuration C (project AR539). Dataset in configuration A proved unusable due to low sensitivity. Details of the archive dataset are summarized in table B.1, where the project code, the year when the observations took place, the array configuration, the observing frequency and the correspondent synthetic beam are also reported. Both new data as well as archive data were processed within CASA, version 3.0.2, following the standard procedures.
As it is possible to notice from table B.1, in the bands L and C data obtained

in more than one configuration were available. Therefore, at each frequency, data from each configuration were firstly independently calibrated (in the usual way) and then combined into a single *uv* data set, in order to obtain multi-configuration maps both at 1.4 GHz and at 5 GHz.
For this bubbles, the imaging process was performed by setting the Briggs robust parameter equal to 0, a compromise between uniform weighting of the baseline for highest angular resolution and to natural weighting for highest sensitivity, resulting in a synthetic beam of $12.2'' \times 10.8''$ with a rms noise of 0.5 mJy/beam, at 1.4 GHz, and in a synthetic beam of $10.5'' \times 8.9''$ with a rms noise of 0.18 mJy/beam, at 5 GHz. Primary beam correction has been applied for all the archive datasets.
As previously said, the source was also detected at 8.4 GHz (band X) and at 15 GHz (band U). In both these two cases, however, due to the high angular resolution and the notably reduced largest angular scale, only the central object could be properly mapped, with the most of the nebular emission resolved out.
No useful archive observations were found in other bands.

B.3 Discussion on radio data

The flux density calculation for the radio nebula has been performed with CASA. For bands L and C the source appeared resolved and, therefore, in order to calculate the total flux density the emitting region has been encompassed with a polygonal within the task `viewer`; selecting an empty region of the image, also a noise estimation has been done. The results are summarized in the table B.2.

Band	Flux density (mJy)
L	175.0 ± 2.1
C	157.8 ± 0.1

Table B.2: radio flux densities.

In the bands X and U the source appears point-like, since, essentially, only the central object was seen, as explained above. The central object flux density were therefore calculated using the task `imfit`; the values are listed in table B.3. Using this task we were also able to perform an accurate astrometry of the central source, as reported in table B.4.

Band	Flux density (mJy)
X	43.50 ± 0.14
U	67.13 ± 0.38

Table B.3: radio flux densities of the central object (second values with IMFIT).

Band	RA	DEC
X	18:39:32.24261 ± 0.00010 s	$-05^\circ\,44'\,20.12852'' \pm 0.00155$ arcsec
U	18:39:32.24116 ± 0.00030 s	$-05^\circ\,44'\,20.16950'' \pm 0.00608$ arcsec

Table B.4: coordinates of the central source (with `imfit`).

In figure B.1 all the radio flux densities calculated are plotted, with the open circles representing the entire flux density values while the solid ones representing only the central source contributions.

We used radio flux density values at 6 cm (our data) and at 20 cm (archive data) in order to have a spectral energy distribution of G26 and obtain a spectral index. The spectral index value we obtained is

$$\alpha(20,6) = -0.082 \pm 0.011,$$

where the error has been estimated, by the error propagation formula, as

$$\Delta\alpha = \frac{\sqrt{\left(\frac{\Delta F_L}{F_L}\right)^2 + \left(\frac{\Delta F_C}{F_C}\right)^2}}{\ln\frac{\nu_C}{\nu_L}},$$

where F_L, F_C, ν_L and ν_C are the flux densities and the central frequencies calculated for band 20 cm and 6 cm images; the errors on the central frequencies are neglectable.

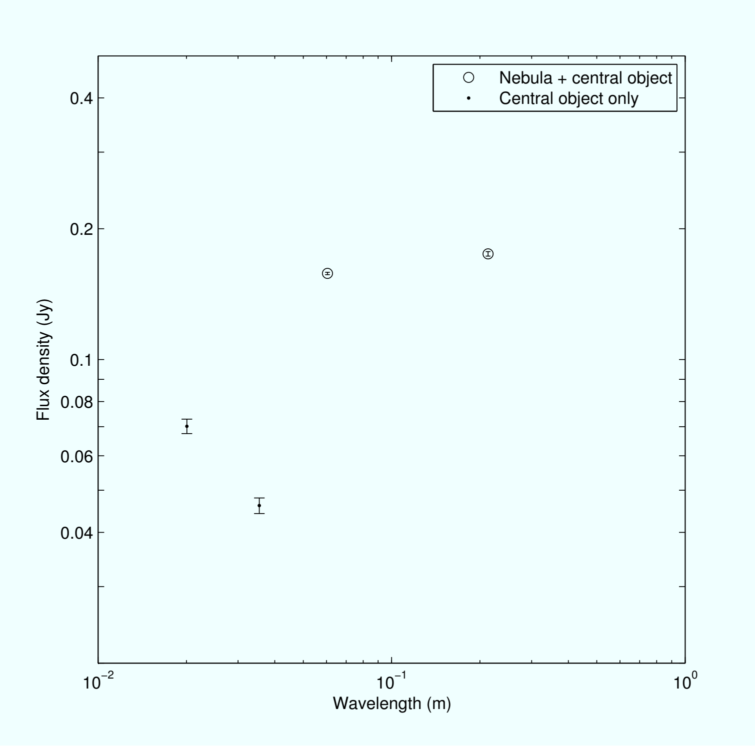

Figure B.1: G26 flux densities.

A spectral index was also calculated for central object flux densities, in particular we obtain

$$\alpha(3.6, 2) = 0.739 \pm 0.099.$$

The spectral index calculated for the radio nebula suggests that the emission mechanism is very likely thermal free-free; the radio source region traces then the ionized gas around the central star. A morphological comparison with the mid-infrared images shows that the gas occupies the inner region of the nebula while the dust is located further from the central region. However both radio and mid-infrared seem to share the same (scaled though) morphology, showing clearly bipolar features.

The spectral index of the central object is compatible with the presence a stellar wind. If we consider also near-infrared data (table B.5), we can plot how the flux density of the central source varies with the wavelength. As the plot suggests, all the data can be well fitted by a power law function, with

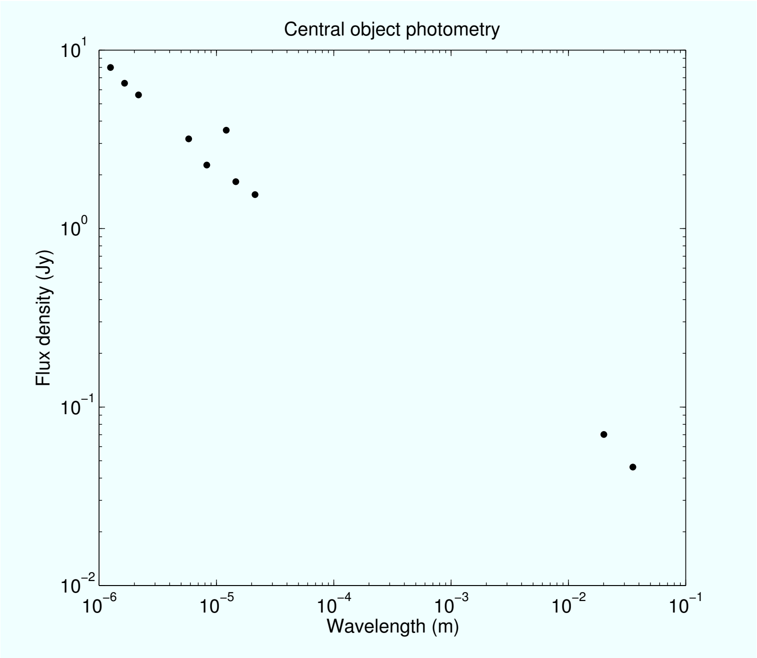

Figure B.2: G26 central object photometry.

the only exception of the 12 μm point. In particular, choosing as function template the relationship

$$F \propto \nu^k$$

we found for k the value (with 95% confidence bound)

$$k = 0.6093 \pm 0.0390$$

or, if we exclude also radio data

$$k = 0.6096 \pm 0.0494,$$

which are totally consistent with each other.
In figure B.3, B.4, B.5 and B.6, we show the VLA maps of G26 in the four radio bands.

Wavelength	Res.	Survey (Tel.)	Notes
70	4.5″	Hi-GAL	
24	6.0″	MIPSGAL	
21.3	?	MSX	*No image, flux only*
14.6	?	MSX	*No image, flux only*
12.1	?	MSX	*No image, flux only*
8.3	?	MSX	*No image, flux only*
8.0	1.2″	GLIMPSE	
5.8	1.2″	GLIMPSE	*Central object only*
4.5	1.2″	GLIMPSE	*Central object only*
3.6	1.2″	GLIMPSE	*Central object only*
2.17	?	2MASS	*No image, flux only*
1.65	?	2MASS	*No image, flux only*
1.25	?	2MASS	*No image, flux only*
0.7	1″	SERC-I (UK Schmidt)	*Central object only*
0.6	1″	SERC-I (UK Schmidt)	*Central object only*

Table B.5: other data, wavelength in microns.

B.4 The presence of a dusty nebula

The detection of the nebula around the central source of G26 in the mid-infrared suggests that, associated with circumstellar gas, a significant amount of dust surrounds the star.

In particular, the central source and the associated nebula have been detected by Spitzer (both IRAC and MIPS), by WISE and by Herschel. The central object is detected in all the IRAC bands, while hints for the presence of a compact, very faint nebula surrounding the central source are evident at 8 μm. In particular, a small component, extending for about 15″ and oriented in the south-west direction is present. The dusty nebula is well visible in the WISE and MIPS maps (see figure B.7 for the MIPSGAL image at 24 μm).

In the Herschel maps, the dusty nebula is well detected only by PACS at 70 μm, but it is not possible to exclude the detection in the other Herschel channels, as the lower angular resolution and the increasing contribution of Galactic background at wavelengths longer than 70 μm prevent us to clearly isolated the nebula.

The morphology of mid-IR nebula associated to G26 consists of a overall

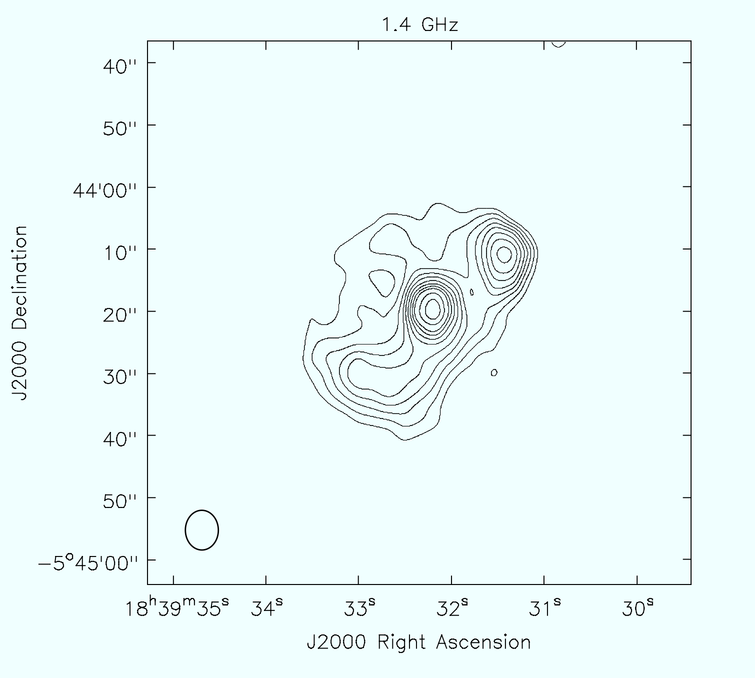

Figure B.3: G26 at 1.4 GHz image; contour levels are 1.2 + 0.5×(2, 4, 6, 8, 10, 12.5, 15, 17.5, 20, 25, 30) mJy/beam.

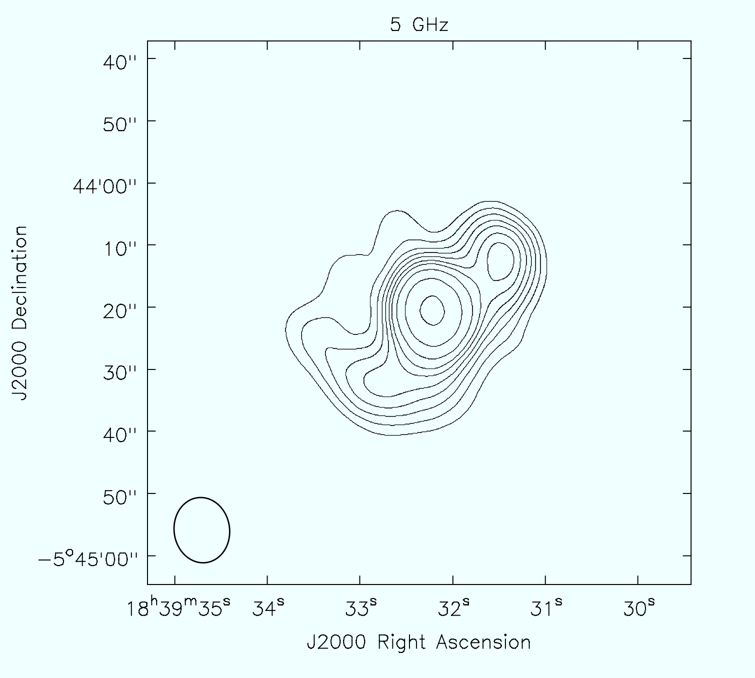

Figure B.4: G26 at 5 GHz image; contour levels are $3.5 + 1.2\times$(2, 4, 6, 8, 10, 12.5, 15, 20, 30, 50) mJy/beam.

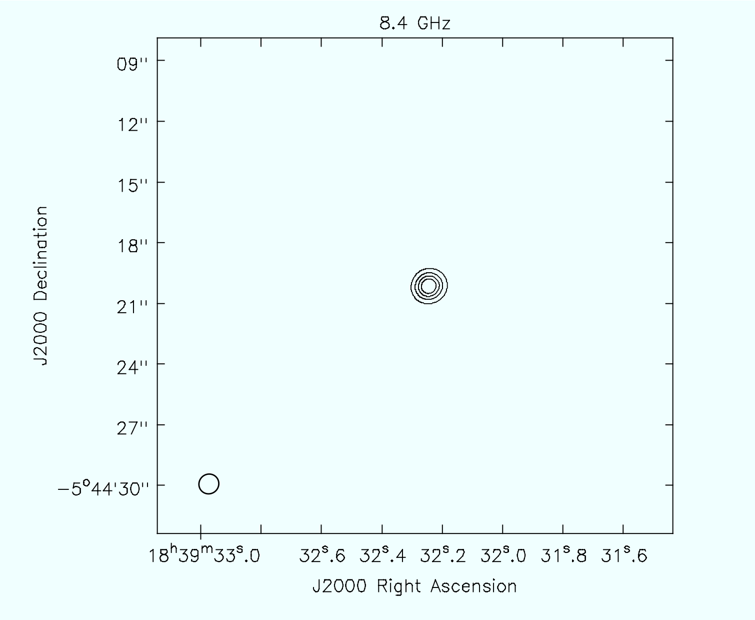

Figure B.5: G26 at 8.4 GHz image; contour levels are 6, 12, 18 and 24 mJy/beam.

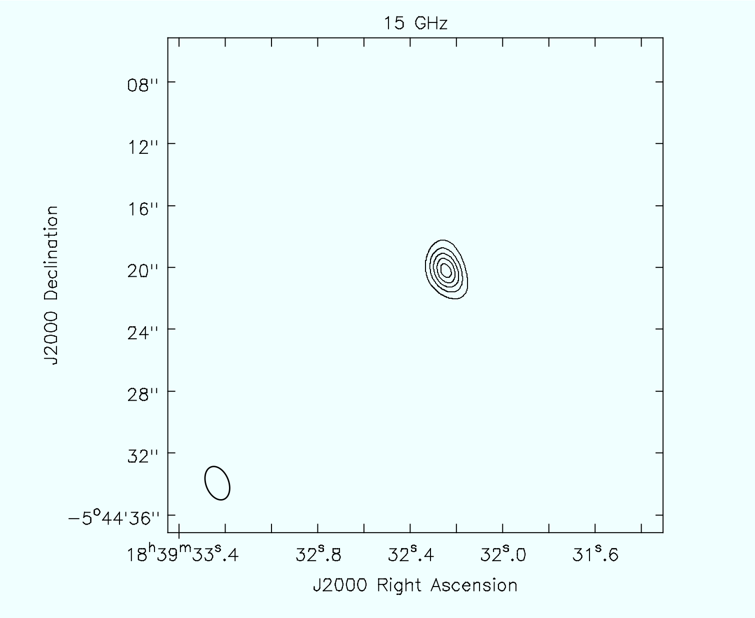

Figure B.6: G26 at 15 GHz image; contour levels are 10, 20, 30, 40 and 50 mJy/beam.

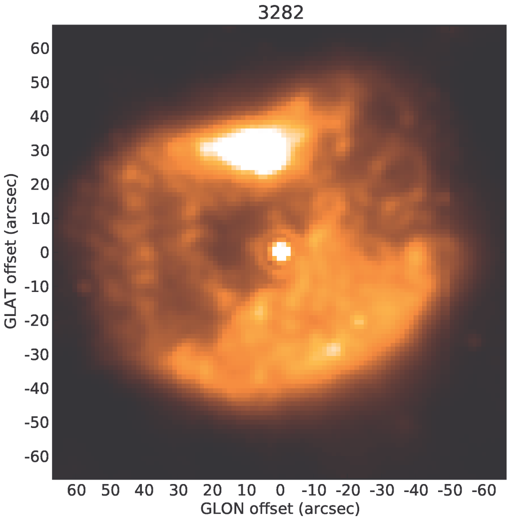

Figure B.7: G26 MIPSGAL image at 24 μm.

spherical structure, elongated in the north-east and south-west direction, with an average radius of about 80″ (that is about 2.5 pc at the supposed distance of 6.5 kpc [69]), centered on the LBV candidate [69]. The WISE, MIPS and PACS maps share a very similar morphology, indicating that they are tracing the same dusty component. However, the image at 24 μm from MIPS and the image at 70 μm with PACS maps, both with an angular resolution of about 6″, point out finer details of the nebula morphology, indicating that the dust distribution inside the nebula is not homogeneous, with two main regions with higher brightness, the first, more extended, in the south-east part and the second, the brightest one, in the north-west part of the nebula. This bright component is already present in the IRAC map at 8 μm. The detailed dust distribution seems to suggest a wrapping of the extended nebula towards the center.

At 24 μm a structure of a partial double ring is also visible in the north-east, with a partial inner ring at ∼30″ and the second partial ring at ∼50″ from the central source. Both rings appear to have an extent of about 10″ and are barely visible also at 70 μm.

Aperture photometry has been performed at 24 μm and at 70 μm, obtaining, respectively, a total flux density of 82.7 ± 2.7 Jy and 94 ± 23 Jy. In the hypothesis of an optically thin dusty nebula, and with assumption on the dust composition, the average dust temperature has been evaluated as 71 K in case of silicates and as 92 K in case of graphite, in agreement with precedent results [69]. From these estimations it was also possible to calculate the total dust mass; assuming the usual distance of 6.5 kpc, we obtained $3.2 \cdot 10^{-2} M_{\odot}$ in case of silicate and $1.2 \cdot 10^{-2} M_{\odot}$ in case of graphite, both comparable to literature values.

B.5 Characteristic of the gas nebula

As previously exposed, also the gas nebula shows a complex structure. It consists of a compact component, related to the central star, a more extended (about $40''$) bipolar structure, centered on the compact component, and a more diffuse radio emission with a very irregular shape extending up to about $100''$. This morphology is shared by both 1.4-GHz and 5-GHz maps; at 8.4 GHz, besides the central object, evidence of a partially resolved out nebula is also visible. As observed in other Galactic LBVs [70][71], the ionized part of the nebula, traced by the radio emission, is unbalanced, indicating, perhaps, a period of aspherical mass-loss from the central object or aspherical ionization of the nebula.

As pointed out in section B.3, the radio flux densities at 8.4 GHz and 15 GHz of the central source suggest that we are observing a stellar wind. It is now possible to estimate the current mass-loss of the central star [72]; assuming a temperature of the plasma of the wind of 104 K, value of about 200 km/s for the stellar velocity and a distance of 6.5 kpc [69], we derive a mass loss rate of $1.9 \cdot 10^{-4} M_{\odot}\,\mathrm{yr}^{-1}$. This value confirms that G26 has one of the highest current mass-loss rate of any known Galactic LBV.

In the hypothesis of optically thin nebula the radio flux density can be used to evaluated the total ionized mass, although, because of its irregular shape, the application of the standard formulas [73], may lead to wrong estimations. Assuming that the geometrical depth of the inner component is equal to the transversal size of the nebula, a total ionized mass of $7.6 M_{\odot}$ at 6.5 kpc, for the inner nebula has been calculated. If now the more extended component of the nebula is taken into account, a total ionized mass of $9.7 M_{\odot}$ is derived. These two values are very similar and it could be concluded that mass-loss occurs episodically but providing almost the same quantity of material each time.

A morphological comparison between the radio and the infrared nebula allows to unveil the distribution and the interaction of gas and dust. The inner torus is close to the central object and its material is ionized and visible via its radio free-free emission. Such radio nebula is well confined inside the dusty part of the stellar ejecta. The outermost torus of material is far from the star, where condition are favorable to dust to condense, and is visible via thermal dust emission. In between these two main structures there is also diffuse radio emission which is extending towards the south-east and the north-west part of the nebula and, in particular, a low brightness component appears to be the radio counterpart of the most luminous dusty structure. The overall structure of the nebula surrounding G26 is very similar to that observed around the LBV candidate HDE316285 [74], also characterized by the presence of a stellar wind with extreme proprieties [75].

From the estimated dimension of the ionized nebula and its electron density, from the number of ionizing photons, it has been possible to infer that the central star should be a B0.5–B1 supergiant, with a effective temperature between 20 400 and 23 600 K [76], hotter than previous estimation [69]. However this result has been obtained with the caveat that the supergiants considered in Panagia (1973) [76] are less luminous than G26 and this must be taken into account when determining the temperature of the ionizing source. Moreover, the presence of low excitation features, such as Fe II, Mg II and Na I, seem to indicate for the central object a lower temperature than that inferred on the basis of the number of ionizing photons required to excite the nebula. On the other hand, there are some other factors sustaining a more powerful ionizing source, in fact there is more radio emission behind the compact torus, as indicated by the outermost radio nebula, and a still more intense ultraviolet radiation is necessary to justify it and there is a significant quantity of dust in the nebula competing with the gas in absorbing the ultraviolet photons.

B.6 G26 as a type IIn supernova progenitor

Even if there are no firm evidences for G26 to be variable, it is possible to assume that it has gone though an hotter phase during which the outermost nebula has been ionized. It is, indeed, possible to calculate an age of the nebula around 4000 years; the presence of a outermost ionized nebula would also be consistent with a previous hotter phase of the central object.

There are growing evidences for a close connection between core-collapse supernovae and LBVs. Several authors have reported observations that point out SN explosions that had occurred in stars in the LBV phase as well as immediately after the LBV phase [77]. A peculiar type of core-collapse supernovae, the Type IIn, is characterized by optical spectra indicating strong interaction with the circumstellar environment. Although they constitute a small fraction of core-collapse supernovae, they are characterized by an extreme luminosity, that can be modeled as a strong interaction of the SNe shock with the circumstellar environment, whose characteristic in mass, and thus in mass-loss rate, can be ascribable to enhanced mass-loss episodes as observed in the LBV phase. Moreover, mir-IR detections indicate that the infrared emission is very likely related to a pre-existing dust shell, whose mass content is consistent with LBV progenitors [78]. For example, SN 2010jl was a very bright SN IIn, showing a significant infrared excess, that could be modeled in some details [79]. In particular the model was consistent with a IR-echo of a pre-existing dust, located around SN2010jl, heated by the initial SN flash. The physical parameters of the circumstellar envelope of the progenitor resulted to be arranged in a torus-like configuration, with a dust mass between 0.03 and $0.35M_{\odot}$, depending on the chemical composition of the dust and on the inclination of the dusty torus with respect to the plane of the sky. Assuming a gas-to-dust ratio of 100, this translates into a total mass of circumstellar envelope between 3 and $35M_{\odot}$.

In conclusion, the extreme characteristic of the circumstellar envelope associated to G26, in particular, its peculiar aspherical morphology, fit quite well the requirement for the SN2010jl progenitor according to the Andrews et al. (2011) modeling [79]. This may indicate that G26 could be a precursor of a Galactic, very bright Type-IIn supernova, that will explode with the same characteristics as SN2010jl.

Appendix C

Scripts

C.1 EVLA calibration pipeline

The script reported below summarize the calibration pipeline written to help to reduce the huge quantity of our EVLA data. In the future, this procedure could be incorporated in CASA as a third part task, once undergone some style improvements. For synthesis purpose, all unnecessary comments and all commands which simply influence the text color have been removed.

```
################################
# General calibration pipeline #
# Adriano Ingalllinera - 2010  #
################################

print("General calibration pipeline for EVLA continuum data")
print("Adriano Ingallinera - 2010\n")

visMS=raw_input("Insert the Measurement Set: ")

cPh=raw_input("Insert the gain calibrator ID: ")
cFl=raw_input("Insert the flux calibrator ID
               (-1 if not present): ")
cBp=raw_input("Insert the bandpass calibrator
               ID (-1 if not present): ")
objs=raw_input("Insert objects ID: ")
```

```
if cFl=='-1':
  cFl=cPh

if cBp=='-1':
  cBp=cFl


################
### Flux setting
################
print("Executing setjy...")
setjy(vis=visMS,field=cFl)
print("Done")


########################
### Bandpass calibration
########################
print("Check of the bandpass calibrator")
print("Executing plotms in background")
plotms(vis=visMS,field=cBp,xaxis='channel',yaxis='phase',
       correlation='RR',avgtime='1e8',spw='0')
print("Please check (than press ENTER):")
raw_input("1. Select an antenna and check if it behaves
           properly")
raw_input("2. Check phase versus time")

bpgflag=raw_input("Gain calibration needed on bandpass
                   calibrator (suggested)? [Y/n]: ")
refAnt=raw_input("Inserirt the reference antenna: ")

if bpgflag in ['','y','Y']:
  print("\nCalculating time gain for bandpass calibrator")
  print("Executing gaincal...")
  gaincal(vis=visMS,caltable='bpphase.gcal',field=cBp,spw='',
        refant=refAnt,calmode='p',solint='int',minsnr=2.0)
  print("Calibration table 'bpphase.gcal' created")
  print("Done")
```

```
  print("Calibration solution check")
  print("Executing plotcal in background")
  plotcal(caltable='bpphase.gcal',xaxis='time',
          yaxis='phase',iteration='antenna',subplot=331,
          plotrange=[-1,-1,-180,180])
  raw_input("Check if it behaves properly (then press ENTER)")

print("\nCalculating bandpass solution")
print("Executing bandpass...")
bandpass(vis=visMS,caltable='bandpass.bcal',field=cBp,
         refant=refAnt,solint='inf',solnorm=T,
         gaintable='bpphase.gcal')
print("Calibration table 'bandpass.bcal' created")
print("Done")
print("Check bandpass solutions amplitude and phase")
print("Executing plotcal in background")
plotcal(caltable='bandpass.bcal',xaxis='chan',yaxis='amp',
        iteration='antenna',subplot=331)
raw_input("Press ENTER to check the phase")
print("Executing plotcal in background")
plotcal(caltable='bandpass.bcal',xaxis='chan',yaxis='phase',
        iteration='antenna',subplot=331,
        plotrange=[-1,-1,-180,180])
raw_input("\nSolutions will be now applied to bandpass
           calibrator,\npress ENTER to continue")
print("Executing applycal...")
applycal(vis=visMS,field=cBp,gaintable='bandpass.bcal',
         gainfield=cBp,calwt=F)
print("Done")
raw_input("Check with plotms if data behave properly"))


####################
### Gain calibration
####################
fld=cPh+","+cBp+","+cFl
print("\nPhase calibration of all calibrator integrated
      over 10 s")
```

```
print("Executing gaincal...")
gaincal(vis=visMS,caltable='intphase.gcal',field=fld,spw='',
        refant=refAnt,calmode='p',solint='int',minsnr=2.0,
        gaintable='bandpass.bcal')
print("Calibration table 'intphase.gcal' created")
print("Done")

print("Phase gain solutions check")
print("Executing plotcal in background")
plotcal(caltable='intphase.gcal',xaxis='time',yaxis='phase',
        iteration='antenna',subplot=331,
        plotrange=[-1,-1,-180,180])
raw_input("Press ENTER to continue")

print("\nPhase calibration of all calibrators integrated
       over a scan")
print("Executing gaincal...")
gaincal(vis=visMS,caltable='scanphase.gcal',field=fld,spw='',
        refant=refAnt,calmode='p',solint='inf',minsnr=2.0,
        gaintable='bandpass.bcal')
print("Calibration table 'scanphase.gcal' created")
print("Done")

print("Phase gain solutions check")
print("Executing plotcal in background")
plotcal(caltable='scanphase.gcal',xaxis='time',yaxis='phase',
        iteration='antenna',subplot=331,
        plotrange=[-1,-1,-180,180])
raw_input("Press ENTER to continue")

print("\nAmplitude and phase calibration for all calibrators")
print("Executing gaincal...")
gaincal(vis=visMS,caltable='amp.gcal',field=fld,spw='',
        refant=refAnt,calmode='ap',solint='inf',minsnr=2.0,
        gaintable=['bandpass.bcal','intphase.gcal'])
print("Calibration table 'amp.gcal' created")
print("Done")
```

```
print("Amplitude and phase gain solutions check")
print("Executing plotcal in background")
plotcal(caltable='amp.gcal',xaxis='time',yaxis='amp',
        iteration='antenna',subplot=331)
raw_input("Press ENTER to check the phase")
print("Executing plotcal in background")
plotcal(caltable='amp.gcal',xaxis='time',yaxis='phase',
        iteration='antenna',subplot=331,
        plotrange=[-1,-1,-1,-1])
raw_input("Press ENTER to continue")

raw_input("\nFlux bootstrap will be now executed,
           \npress ENTER to continue")
print("Executing fluxscale...")
fluxscale(vis=visMS,caltable='amp.gcal',fluxtable='flux.cal',
          reference=cFl)
print("Calibration table 'flux.cal' created")
print("Done")

print("New gain solution amplitude check")
print("Executing plotcal in background")
plotcal(caltable='flux.cal',xaxis='time',yaxis='amp',
        iteration='antenna',subplot=331)


######################
### Applying solutions
######################
raw_input("\nCalibration solutions will now be applied to
          all the sources")

print("\nSolution application to gain calibrator")
print("Executing applycal...")
applycal(vis=visMS,field=cPh,gaintable=['bandpass.bcal',
         'intphase.gcal','flux.cal'],gainfield=[cBp,cPh,cPh],
         calwt=F)
print("Done")
```

```
print("\nSolution application to bandpass calibrator")
print("Executing applycal...")
applycal(vis=visMS,field=cBp,gaintable=['bandpass.bcal',
         'intphase.gcal','flux.cal'],gainfield=[cBp,cBp,cBp],
         calwt=F)
print("Done")

print("\nSolution application to flux calibrator")
print("Executing applycal...")
applycal(vis=visMS,field=cFl,gaintable=['bandpass.bcal',
         'intphase.gcal','flux.cal'],gainfield=[cBp,cFl,cFl],
         calwt=F)
print("Done")

print("\nSolution application to target objects")
print("Executing applycal...")
applycal(vis=visMS,field=objs,gaintable=['bandpass.bcal',
         'scanphase.gcal','flux.cal'],gainfield=[cBp,cPh,cPh],
         calwt=F)
print("Done")

print("Check corrected data")
print("Executing plotms in background")
plotms(vis=visMS,field=cPh,ydatacolumn='corrected',
       xaxis='time',yaxis='phase',correlation='RR,LL',
       avgchannel='64',spw='',antenna='')


raw_input("Calibration complete, press ENTER to exit")
```

C.2 GBT continuum observation

The script listed below is an example of a real script used during our continuum observations at Green Bank Telescope.

```
#L-band mapping


Catalog("/home/astro-util/astridcats/fluxcal.cat")
```

```
Catalog(pointing)

cata = Catalog("""
coordmode=J2000
3282 18:39:32.2 -05:44:20
3310 18:41:19.9 -04:56:06
3328 18:42:46.8 -03:13:17
3558 19:55:02.4 +29:17:20
3736 18:42:22.5 -05:04:29
3910 18:11:28.9 -19:25:29
4485 17:23:04.4 -36:18:20
4595 18:01:06.4 -22:56:05
G79 20:31:42.1 +40:22:01
3310_3736 18:41:51.2 -05:00:18
""")

Lcont = """
receiver  = 'Rcvr1_2'
beam      = 'B1'
obstype   = 'Continuum'
backend   = 'DCR'
nwin      = 1
restfreq  = 1475
deltafreq = 0
bandwidth = 20
swmode    = "tp"
swtype    = "none"
swper     = 0.025
swfreq    = 0,0
tint      = 0.1
vlow      = 0.0
vhigh     = 0.0
vframe    = "topo"
vdef      = "Radio"
noisecal  =  "lo"
pol       = "Circular"
"""
```

```
Configure(Lcont)
Balance()

AutoPeak()

#RA mapping parameters
rasizeR = Offset("J2000",2.52,0.0,cosv=True)
decsizeR  = Offset("J2000",0.0,1.26,cosv=True)
deldec  = Offset("J2000",0.0,0.042,cosv=True)
duration = 6.0

#DEC mapping parameters
rasizeD = Offset("J2000",1.26,0.0,cosv=True)
decsizeD  = Offset("J2000",0.0,2.52,cosv=True)
delra  = Offset("J2000",0.042,0.0,cosv=True)


# PRIMO GRUPPO

#13:30 LST
mysource="3310_3736"
RALongMap(mysource,rasizeR,decsizeR,deldec,duration)
DecLatMap(mysource,rasizeD,decsizeD,delra,duration)

#14:00 LST
mysource="3910"
RALongMap(mysource,rasizeR,decsizeR,deldec,duration)
DecLatMap(mysource,rasizeD,decsizeD,delra,duration)

#14:30 LST
mysource="4595"
RALongMap(mysource,rasizeR,decsizeR,deldec,duration)
DecLatMap(mysource,rasizeD,decsizeD,delra,duration)

#15:00 LST
mysource="4485"
RALongMap(mysource,rasizeR,decsizeR,deldec,duration)
```

```
DecLatMap(mysource,rasizeD,decsizeD,delra,duration)


# SECONDO GRUPPO

# 21:30 LST
mysource="3282"
RALongMap(mysource,rasizeR,decsizeR,deldec,duration)
DecLatMap(mysource,rasizeD,decsizeD,delra,duration)

# 22:00 LST
mysource="3328"
RALongMap(mysource,rasizeR,decsizeR,deldec,duration)
DecLatMap(mysource,rasizeD,decsizeD,delra,duration)

# 22:30 LST
mysource="3558"
RALongMap(mysource,rasizeR,decsizeR,deldec,duration)
DecLatMap(mysource,rasizeD,decsizeD,delra,duration)

# 23:00 LST
mysource="G79"
RALongMap(mysource,rasizeR,decsizeR,deldec,duration)
DecLatMap(mysource,rasizeD,decsizeD,delra,duration)
```

The script first loads from file two catalogs containing standard calibrators, then another catalog, containing our sources, is given. The variable `Lcont` is inizialized to contain instruments settings. A full explanation of the other functions is given in section 4.4. The mapping parameters are then set and each source is scanned in both directions.

C.3 Destriping procedure

In this section the complete script for the destriping procedure, described in section 4.6, is listed; the main function is `destipe`, while other functions allow intermediate data checking.

```
import numpy as np
```

```
import matplotlib.pyplot as plt
import pyfits as pf
from numpy.fft import fft2,fftshift


def uvplot(pdata,phead):
naxis1=phead['NAXIS1']
naxis2=phead['NAXIS2']
crpix1=phead['CRPIX1']
crpix2=phead['CRPIX2']
print naxis1,crpix1
uvx=zeros(naxis1*naxis2)
uvy=zeros(naxis1*naxis2)
ran1=np.arange(0,naxis1)
ran2=np.arange(0,naxis2)
for i in ran2:
for j in ran1:
uvx[naxis2*i+j]=sqrt((i-crpix2+1)**2+(j-crpix1+1)**2)
uvy[naxis2*i+j]=pdata[i,j]
return [uvx,uvy]


def from_FITS(file_in,cut=True):
pfits=pf.open(file_in)
pdata=pfits[0].data
phead=pfits[0].header
if cut:
pdata=pdata[:,1:phead['NAXIS1']]
phead.update('NAXIS1',phead['NAXIS1']-1,'')
phead.update('CRPIX1',phead['CRPIX1']-0.5,'')
pfits.close()
return pdata,phead



def hmask(n,a=1,s=0.1):
m=ones((n,n))
c=np.floor(n/2.)
```

```
for i in range(n):
m[i,:]=1-a*np.exp(-(i-c)**4/s)
return m



def vmask(n,a=1,s=0.1):
m=ones((n,n))
c=np.floor(n/2.)
for i in range(n):
m[:,i]=1-a*np.exp(-(i-c)**4/s)
return m



def app_mask(fftima,d,n,s):
if d=='R':
return fftima*vmask(n,s=s)
else:
return fftima*hmask(n,s=s)



def differenze():
oggetto='3310_3736'

scan='_L_R11'
imaR,head=from_FITS(oggetto+scan+'.fits')
fftimaR=fft2(imaR)
wfimaR=app_mask(fftimaR,'R',head['NAXIS1'],100)

scan='_L_D11'
imaD,head=from_FITS(oggetto+scan+'.fits')
fftimaD=fft2(imaD)
wfimaD=app_mask(fftimaD,'R',head['NAXIS1'],100)

wfima=(wfimaR+wfimaD)/2.
```

```
desima=abs(ifft2(wfima))

for i in [-1,0,1]:
aux=fftimaR[0,0]
fftimaR[:,i]=fftimaD[:,i]
fftimaR[0,0]=aux

aux=fftimaD[0,0]
fftimaD[i,:]=fftimaR[i,:]
fftimaD[0,0]=aux

plt.figure()
imshow(fftshift(abs(fftimaR)-abs(fftimaD)),
       interpolation='nearest')
plt.title('|R|-|D|')
plt.figure()
imshow(fftshift(abs(fftimaR)),interpolation='nearest')
plt.title('|R|')
plt.figure()
imshow(fftshift(abs(fftimaD)),interpolation='nearest')
plt.title('|D|')

plt.figure()
imshow(fftshift(angle(fftimaR)-angle(fftimaD)),
       interpolation='nearest')
plt.title('arg(R)-arg(D)')
plt.figure()
imshow(fftshift(angle(fftimaR)),interpolation='nearest')
plt.title('arg(R)')
plt.figure()
imshow(fftshift(angle(fftimaD)),interpolation='nearest')
plt.title('arg(D)')

plt.figure()
imshow(fftshift(real(fftimaR)-real(fftimaD)),
       interpolation='nearest')
plt.title('Re(R)-Re(D)')
plt.figure()
```

```
imshow(fftshift(real(fftimaR)),interpolation='nearest')
plt.title('Re(R)')
plt.figure()
imshow(fftshift(real(fftimaD)),interpolation='nearest')
plt.title('Re(D)')

plt.figure()
imshow(fftshift(imag(fftimaR)-imag(fftimaD)),
       interpolation='nearest')
plt.title('Im(R)-Im(D)')
plt.figure()
imshow(fftshift(imag(fftimaR)),interpolation='nearest')
plt.title('Im(R)')
plt.figure()
imshow(fftshift(imag(fftimaD)),interpolation='nearest')
plt.title('Im(D)')



def analisi(riga):
oggetto='3310_3736'
scan='_L_R11'
imaR,head=from_FITS(oggetto+scan+'.fits')
fftimaR=fft2(imaR)

for i in range(14):
mask=zeros((27,27))
mask[i,riga]=1
mask[i,-riga]=1
if i:
mask[-i,riga]=1
mask[-i,-riga]=1
plt.figure()
mf=fftimaR*mask
subplot(121)
imshow(fftshift(abs(mf)),interpolation='nearest',cmap='gray')
subplot(122)
imshow(abs(ifft2(mf)),interpolation='nearest',cmap='gray')
```

```
def destripe(source,band,session,num=1,mode=0,writeFITS=True):
"""Destripes a pair of orthogonal scans."""

scan='_'+band+'_R'+str(session)+str(num)
ima,head=from_FITS(source+scan+'.fits')
fftimaR=fft2(ima)

scan='_'+band+'_D'+str(session)+str(num)
ima,head=from_FITS(source+scan+'.fits')
fftimaD=fft2(ima)

fftimaD=fftimaD*fftimaR[0,0]/fftimaD[0,0]

aux=fftimaR[0,0]
fftimaR[:,0]=fftimaD[:,0]
fftimaR[0,0]=aux

aux=fftimaD[0,0]
fftimaD[0,:]=fftimaR[0,:]
fftimaD[0,0]=aux

if mode:
for i in np.arange(2,26):
fftimaR[i,1]=fftimaD[i,1]
fftimaR[i,-1]=fftimaD[i,-1]
fftimaD[1,i]=fftimaR[1,i]
fftimaD[-1,i]=fftimaR[-1,i]

fftimaM=(fftimaD+fftimaR)/2.
desima=abs(ifft2(fftimaM))
imshow(desima)

if writeFITS:
file_out=source+'_'+band+'_des'+str(session)+str(num)+'.fits'
pf.writeto(file_out,desima,head)
```

```
return desima,head


def flagdec(a,b,s):
m=np.zeros((127,127))
for i in range(127):
for j in range(127):
m[i,j]=a*np.sin(s*(j-63)*cos(b)-s*(i-63)*sin(b))
fm=fft2(m)
plt.figure()
imshow(m)
plt.figure()
imshow(fftshift(abs(fm)),interpolation='nearest')
plt.figure()
imshow(fftshift(np.angle(fm)),interpolation='nearest')
plt.figure()
imshow(abs(fft2(fm)),interpolation='nearest')
```

Appendix D

Other GBT spectra

In the following pages several other GBT spectra will be shown. Some of them present few corruption due to RFI that could not be filtered out. Many other spectra are totally featureless or show some absorption in one ore more bands. For the strangest spectra few comments are written.

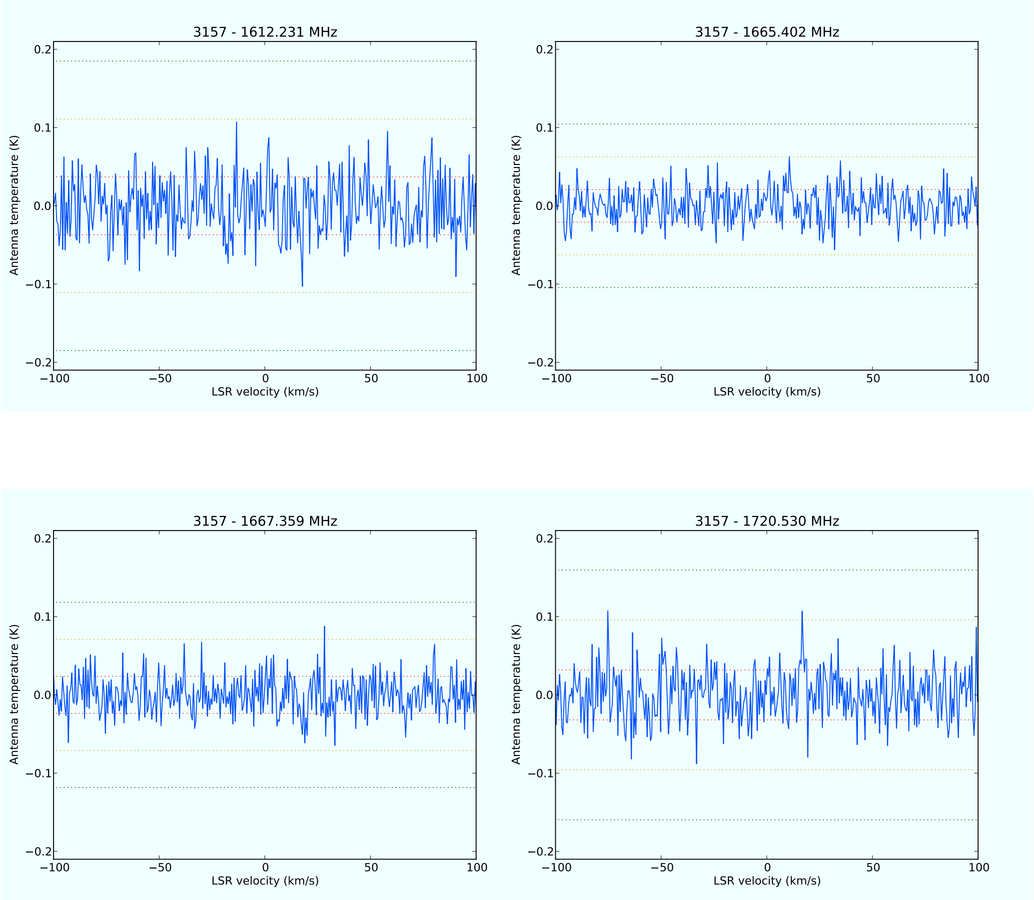

Figure D.1: Complete spectrum of the bubble 3157. The features in the fourth spectrum are like to be interferences. No prominent lines are visible; maybe an emission line is present in the fourth band at about 15 km/s with respect to LSR.

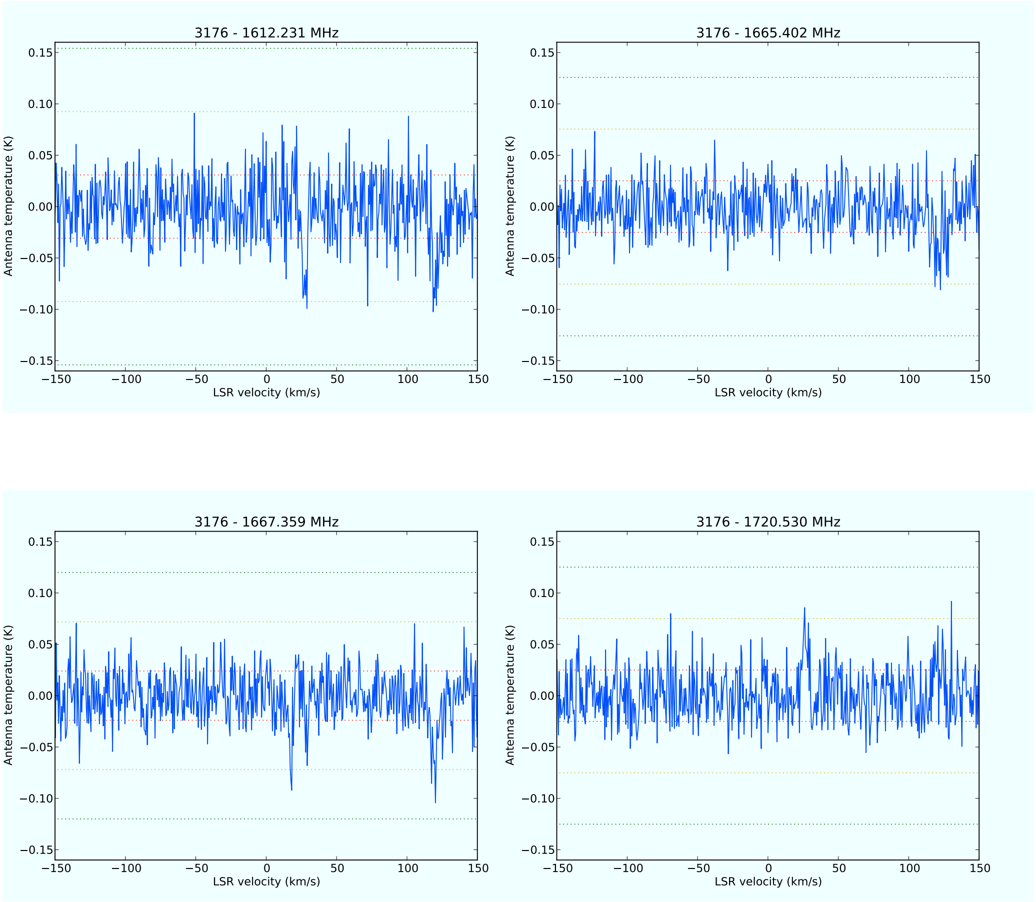

Figure D.2: Complete spectrum of the bubble 3176.

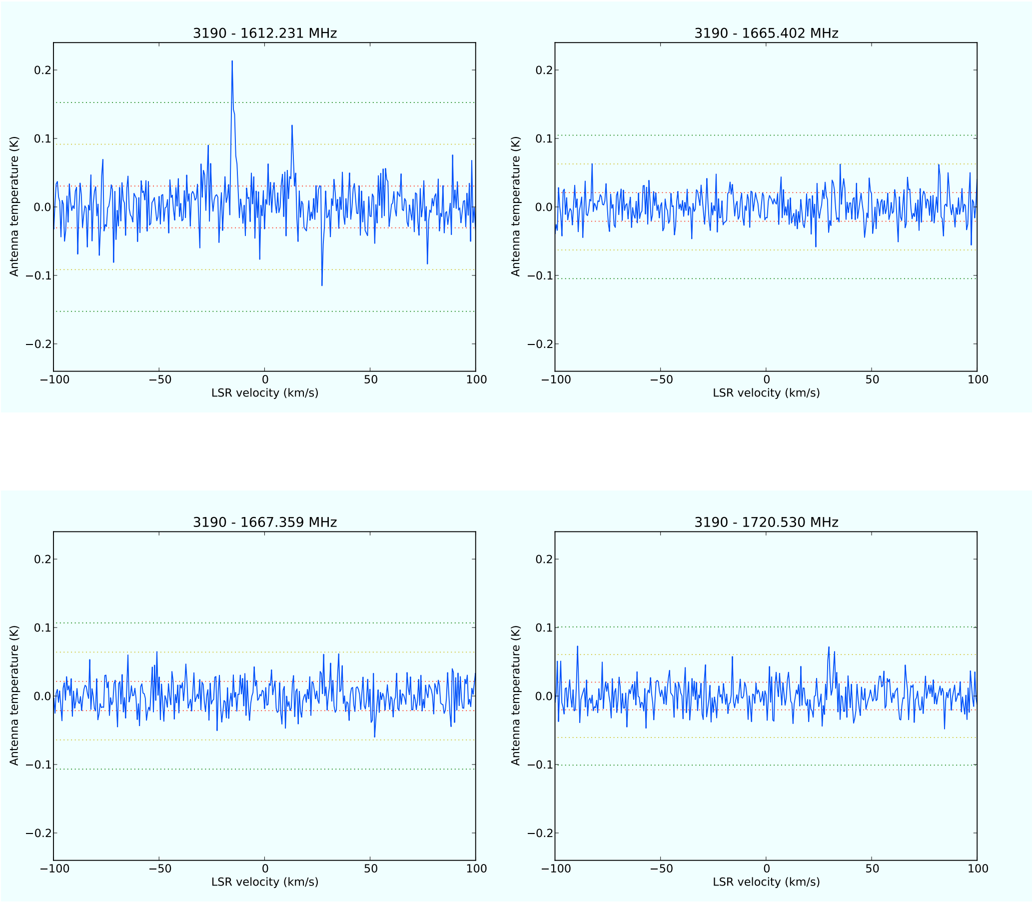

Figure D.3: Complete spectrum of the bubble 3190. A possible maser is visible in the first band.

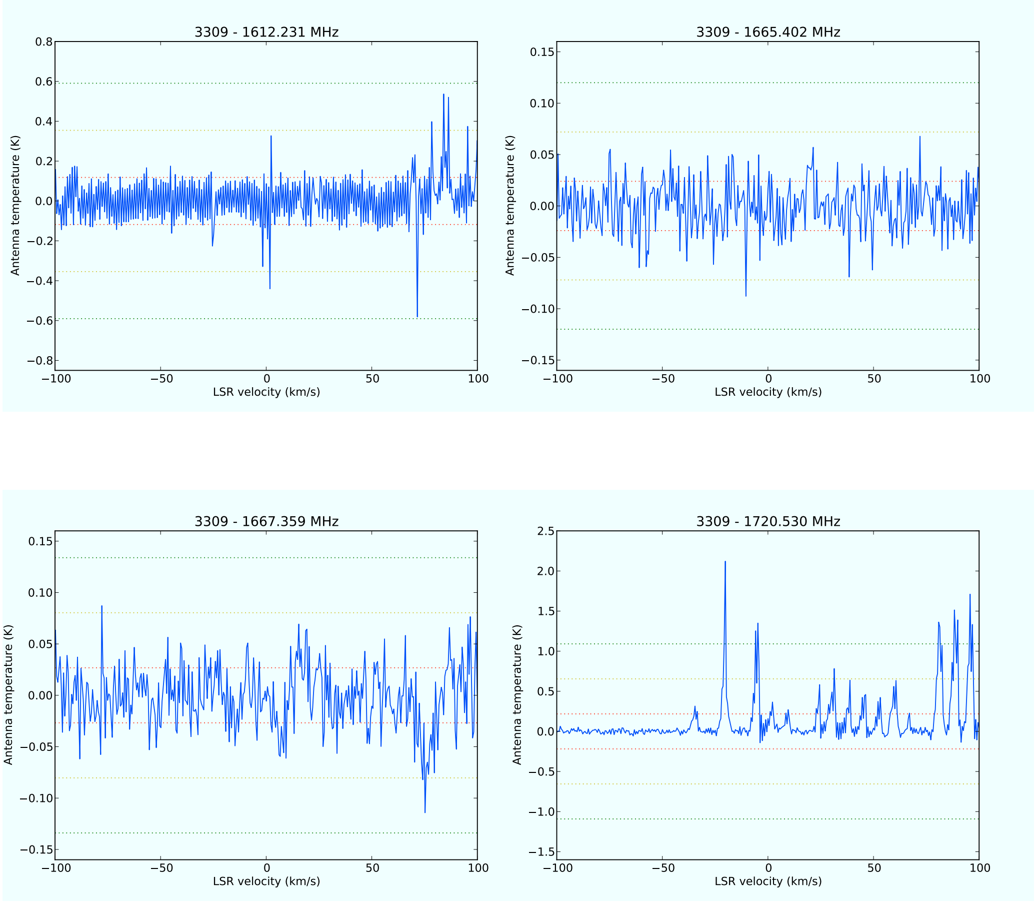

Figure D.4: Complete spectrum of the bubble 3309. The features in the fourth spectrum are like to be interferences.

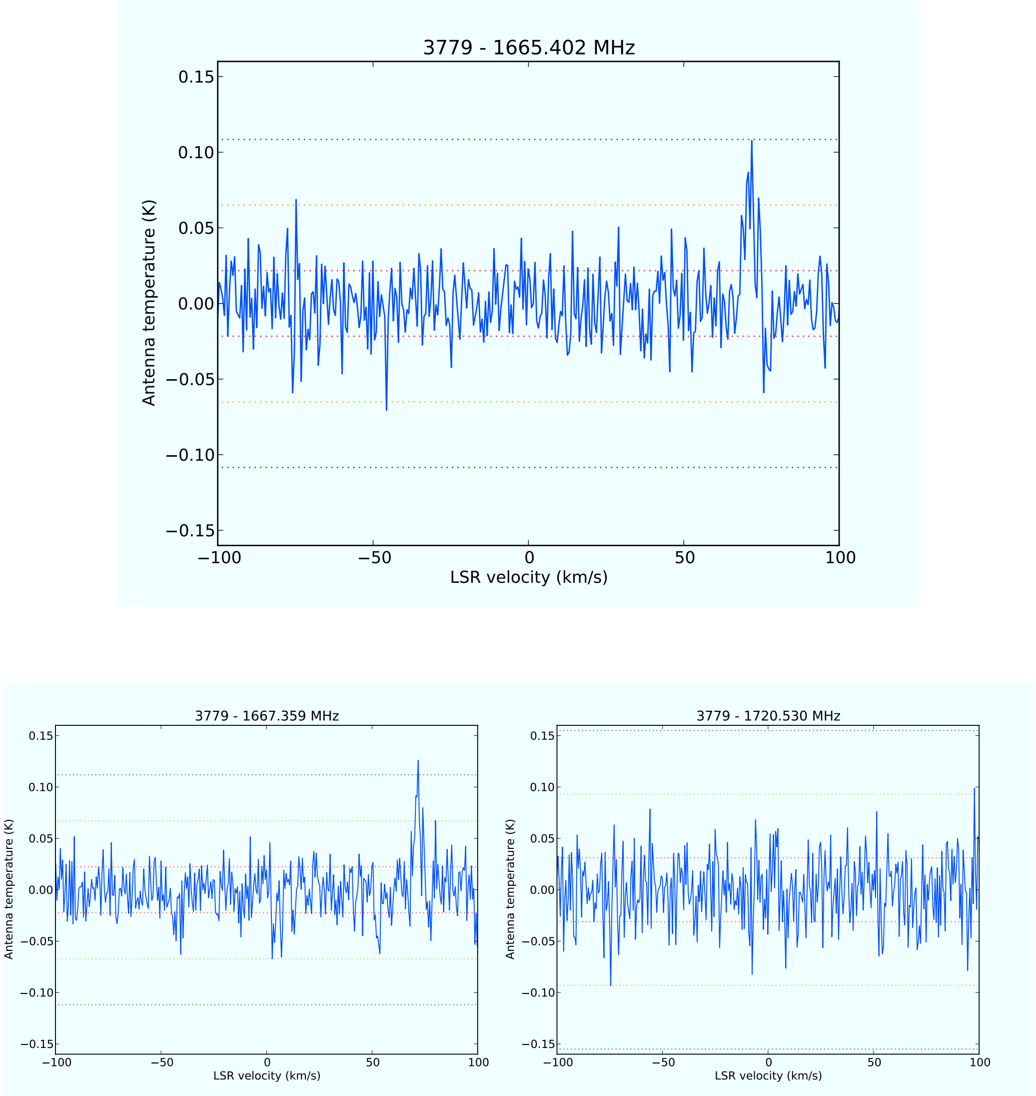

Figure D.5: GBT spectra of the bubble 3779. The spectrum around 1612 MHz was heavily corrupted by RFI.

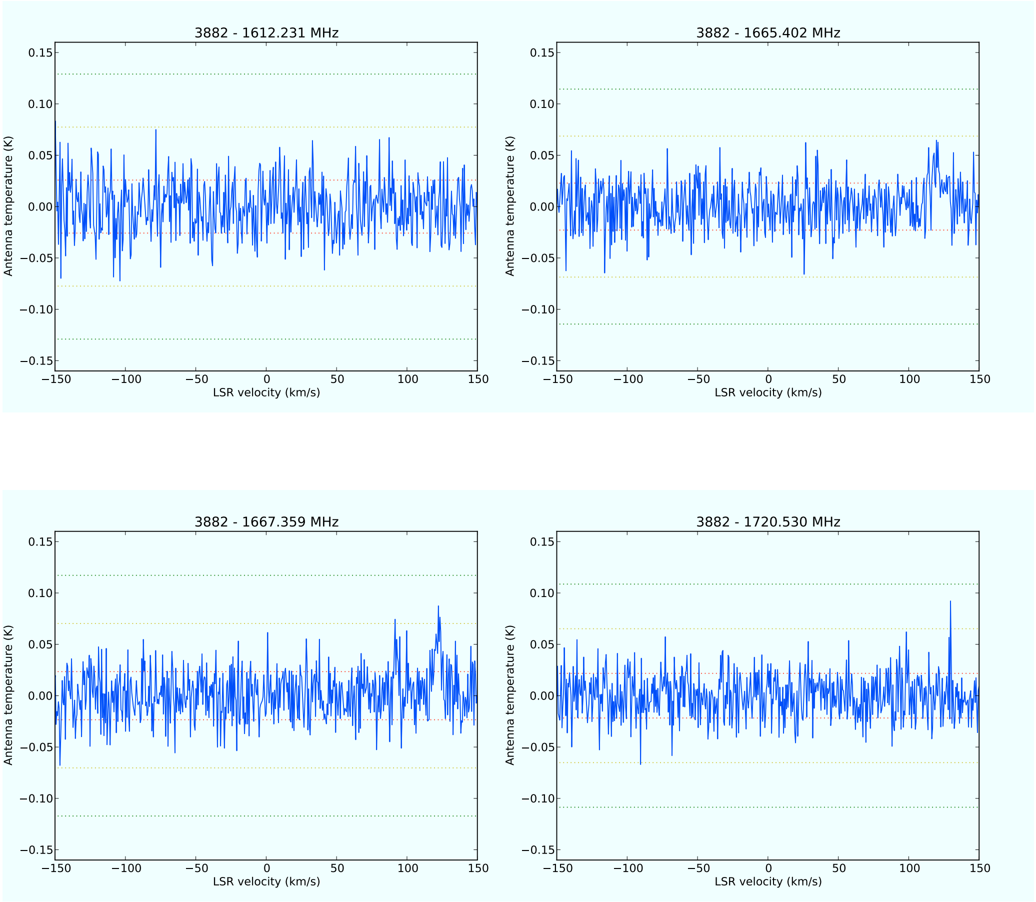

Figure D.6: Complete spectrum of the bubble 3882.

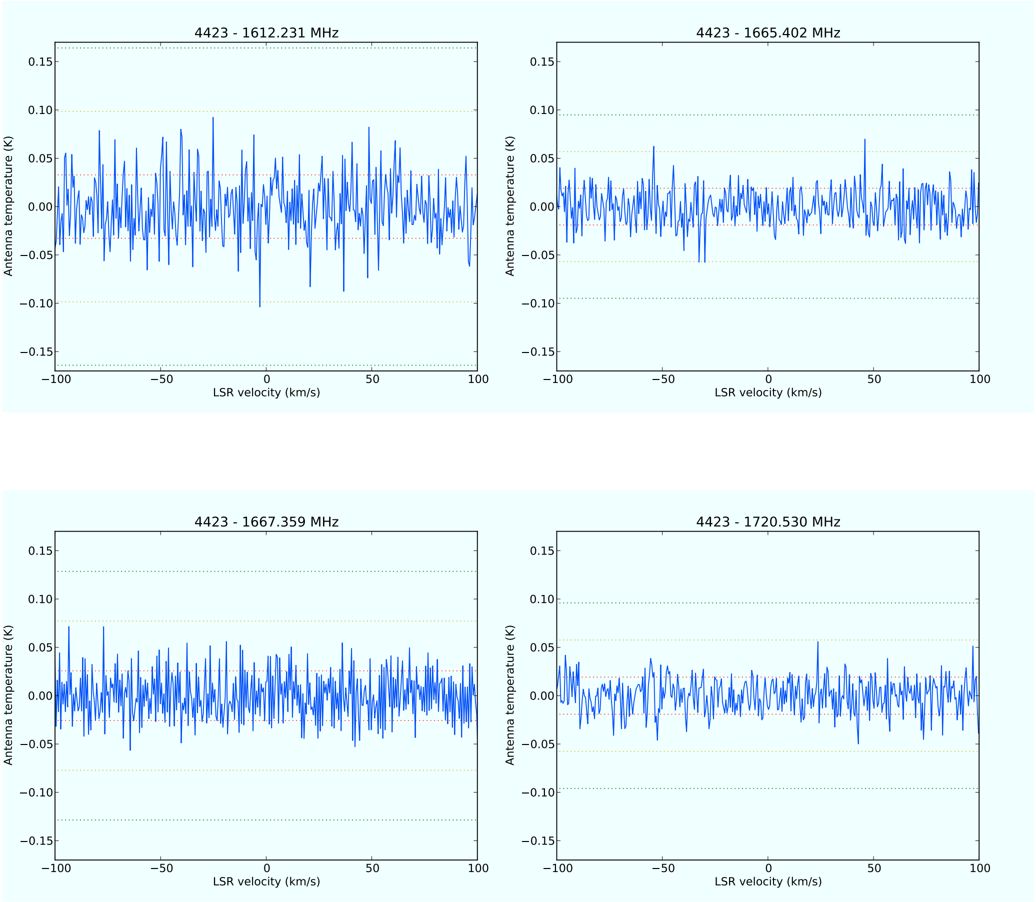

Figure D.7: Complete spectrum of the bubble 4423.

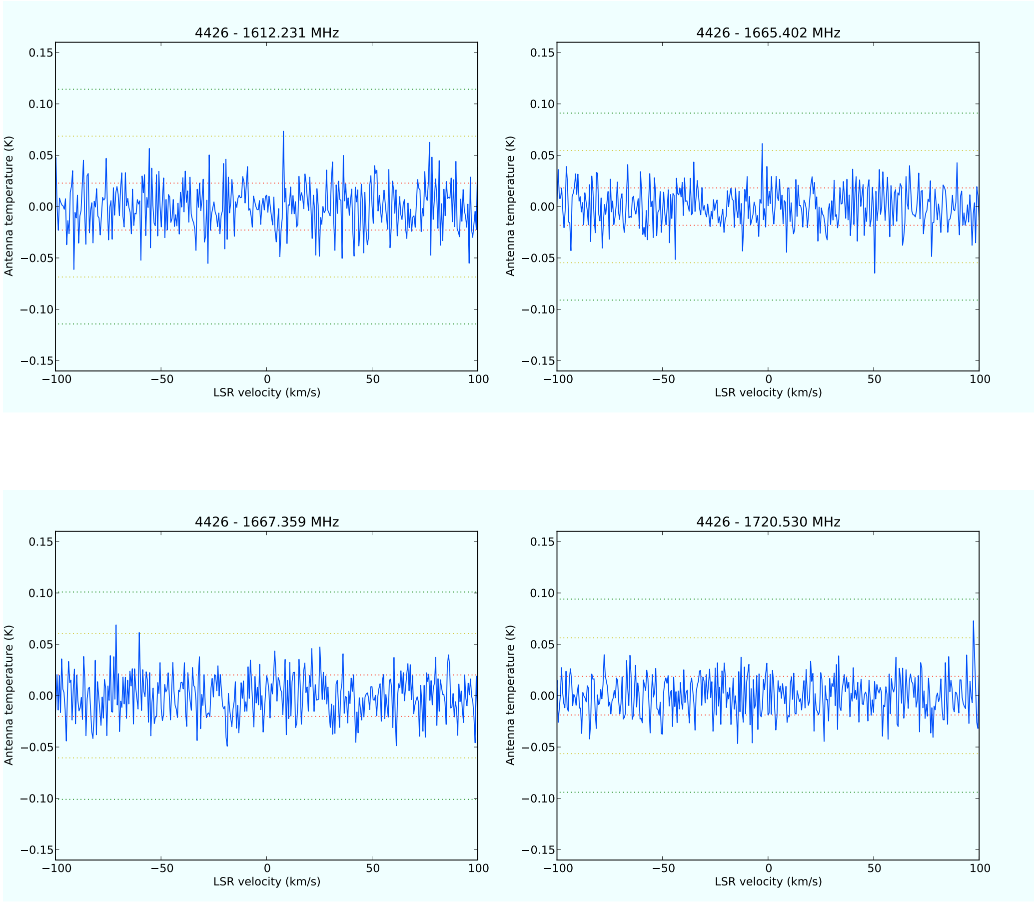

Figure D.8: Complete spectrum of the bubble 4426.

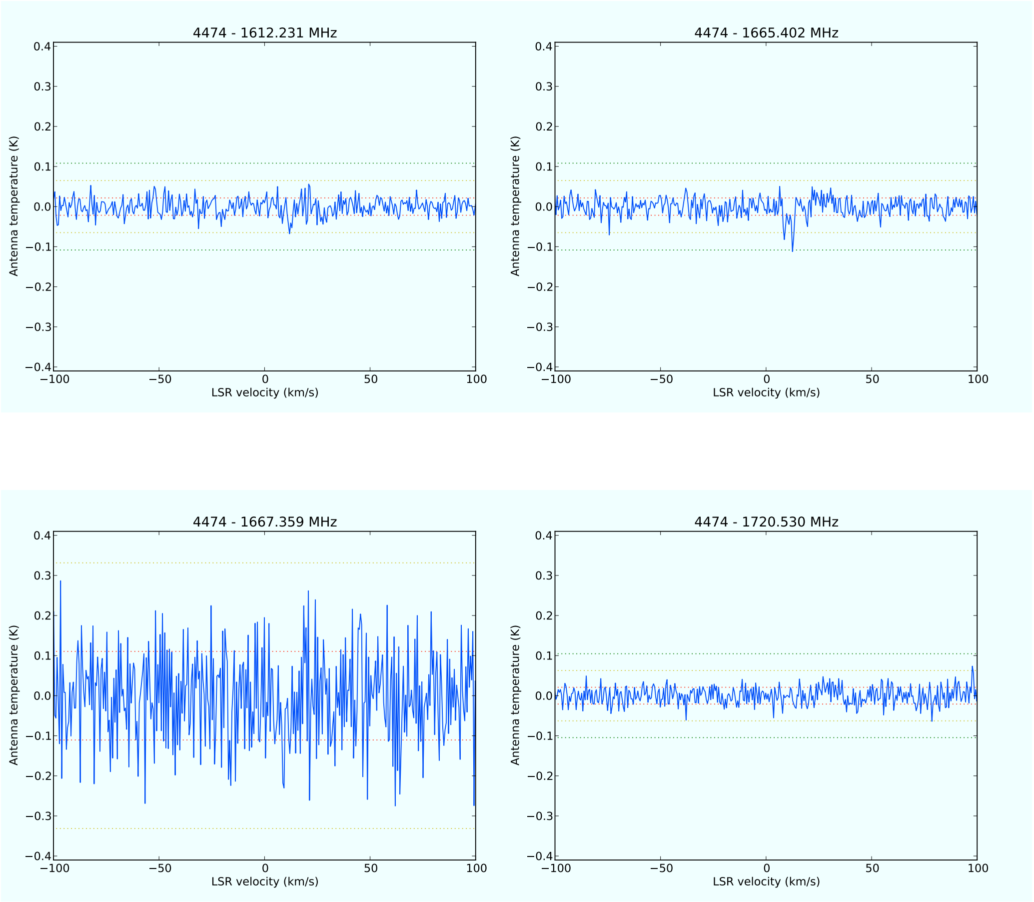

Figure D.9: Complete spectrum of the bubble 4474.

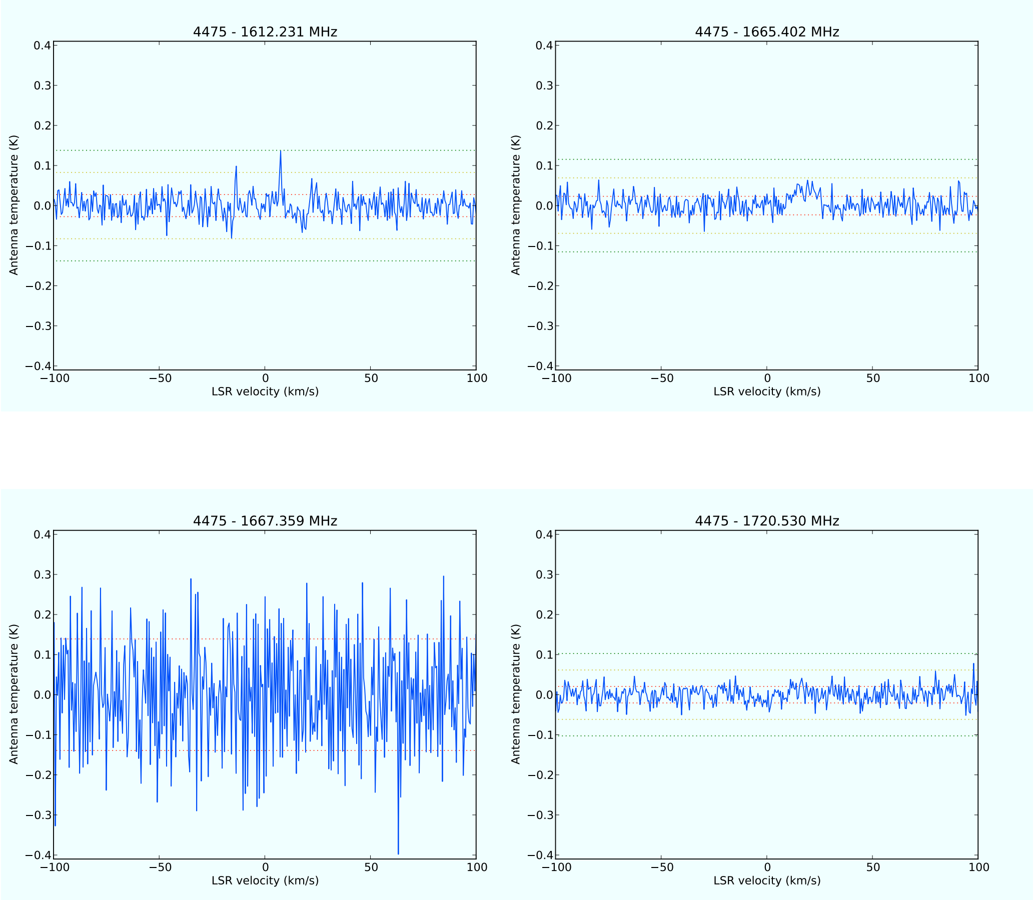

Figure D.10: Complete spectrum of the bubble 4475.

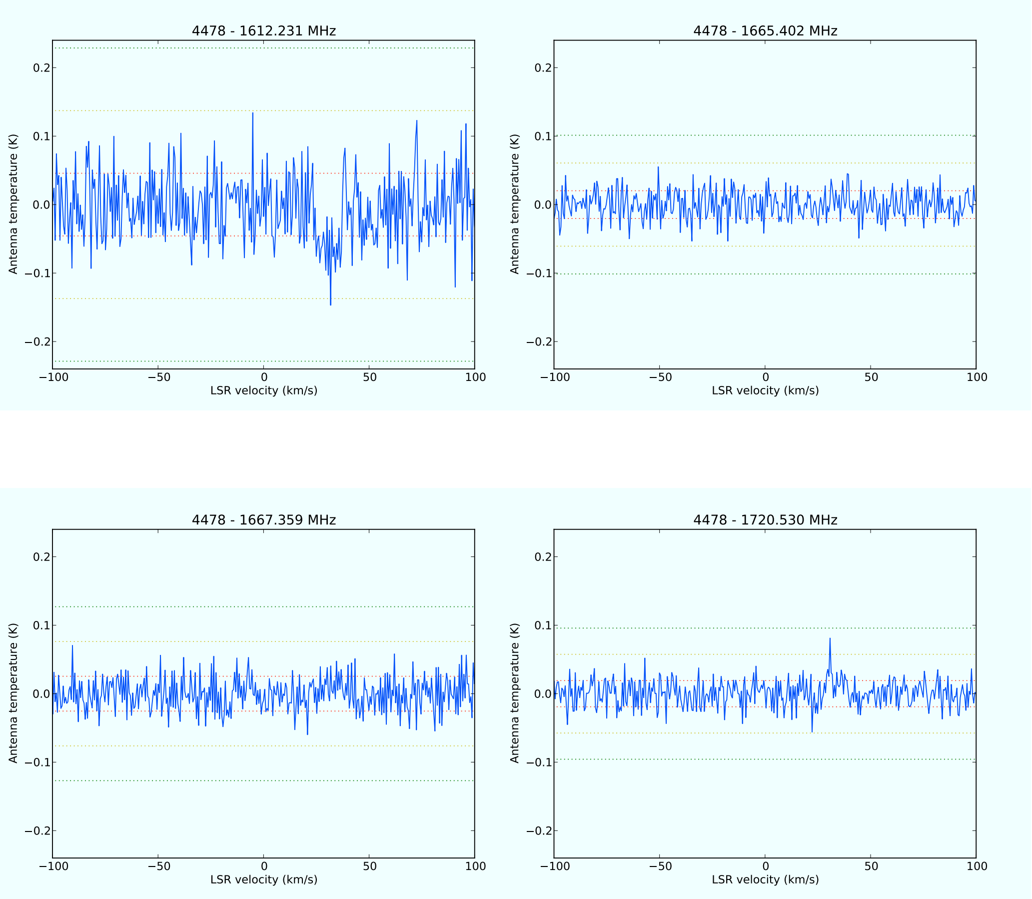

Figure D.11: Complete spectrum of the bubble 4478.

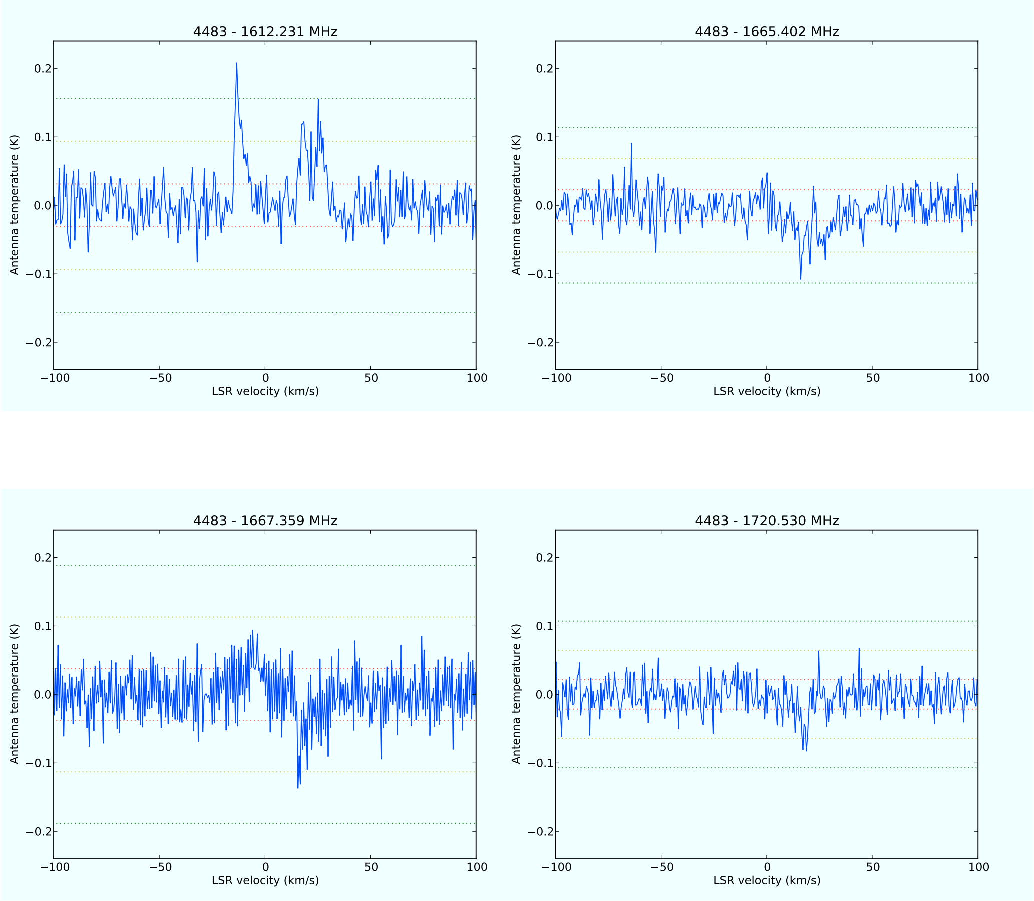

Figure D.12: Complete spectrum of the bubble 4483.

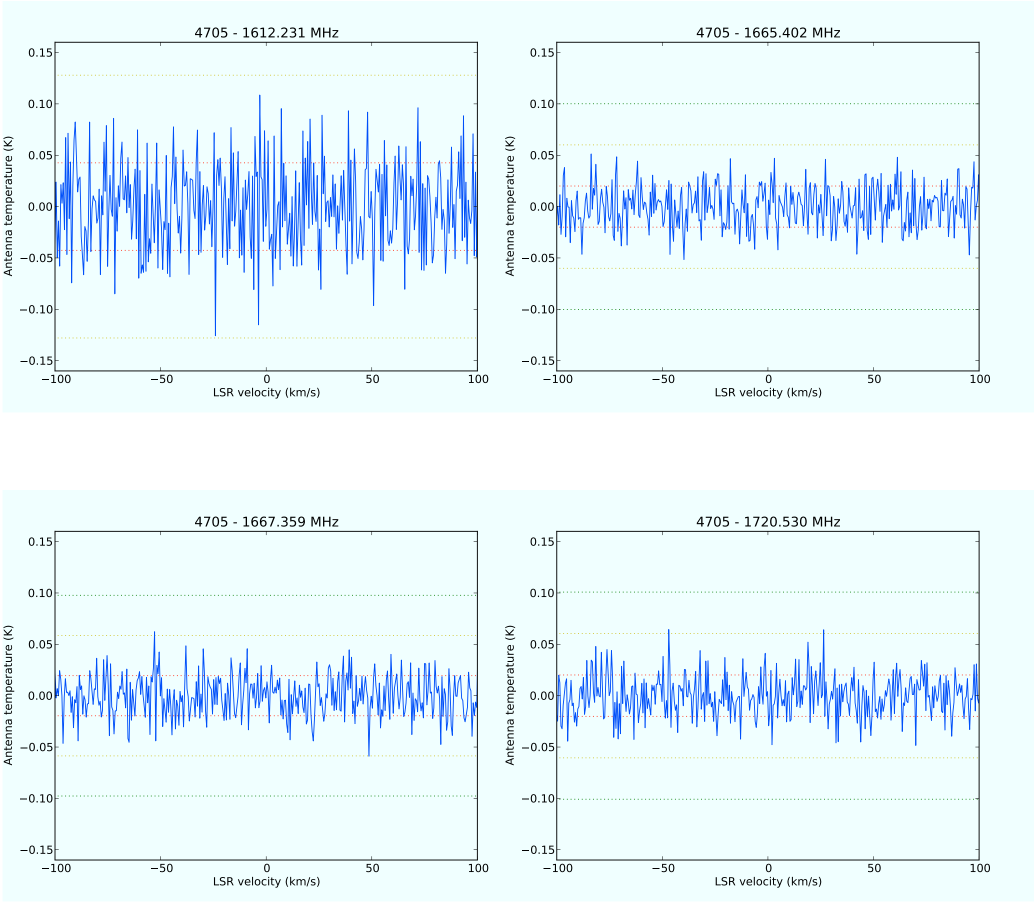

Figure D.13: Complete spectrum of the bubble 4705.

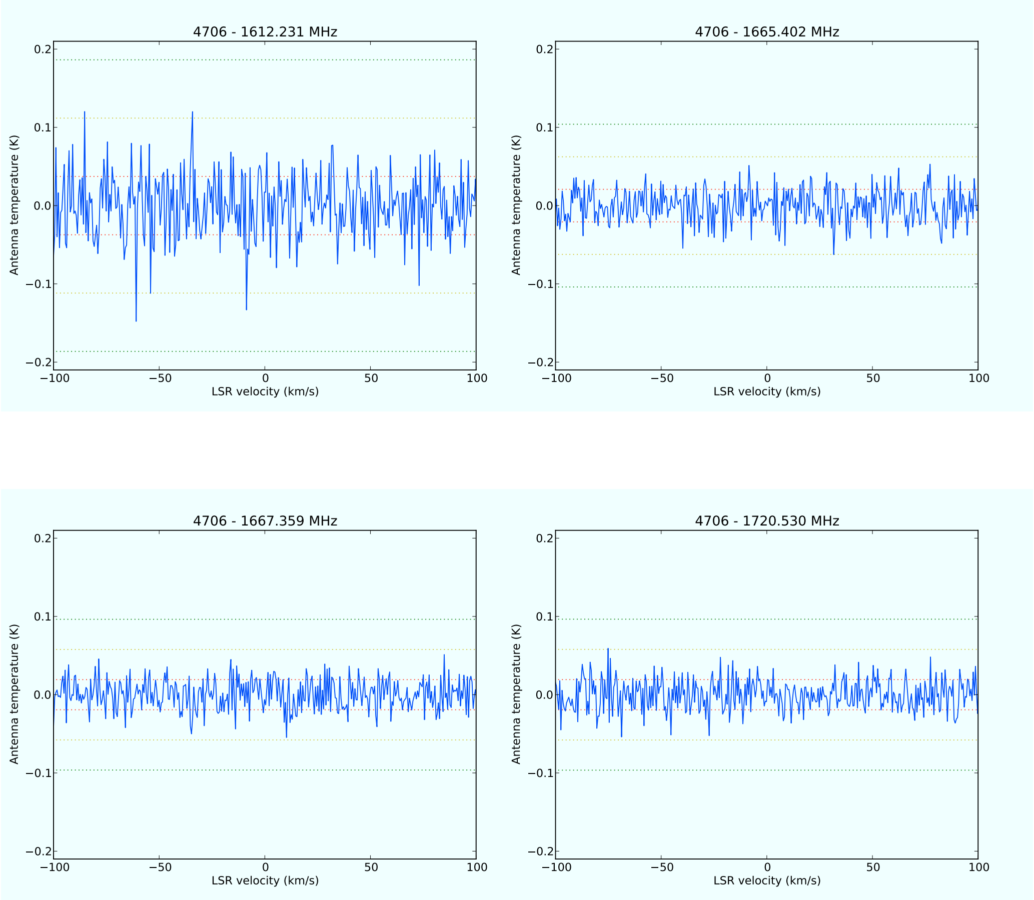

Figure D.14: Complete spectrum of the bubble 4706.

Bibliography

[1] D. R. Mizuno, K. E. Kraemer, N. Flagey, N. Billot, S. Shenoy, R. Paladini, E. Ryan, A. Noriega-Crespo, and S. J. Carey. A Catalog of MIPSGAL Disk and Ring Sources. *The Astronomical Journal*, 139:1542–1552, April 2010.

[2] S. J. Carey, A. Noriega-Crespo, D. R. Mizuno, S. Shenoy, R. Paladini, K. E. Kraemer, S. D. Price, N. Flagey, E. Ryan, J. G. Ingalls, T. A. Kuchar, D. Pinheiro Gonçalves, R. Indebetouw, N. Billot, F. R. Marleau, D. L. Padgett, L. M. Rebull, E. Bressert, B. Ali, S. Molinari, P. G. Martin, G. B. Berriman, F. Boulanger, W. B. Latter, M. A. Miville-Deschenes, R. Shipman, and L. Testi. MIPSGAL: A Survey of the Inner Galactic Plane at 24 and 70 μm. *Publications of the Astronomical Society of the Pacific*, 121:76–97, January 2009.

[3] D. R. Mizuno, S. J. Carey, A. Noriega-Crespo, R. Paladini, D. Padgett, S. Shenoy, T. A. Kuchar, K. E. Kraemer, and S. D. Price. Processing for the MIPSGAL 24 μm Survey of the Inner Galactic Plane. *Publications of the Astronomical Society of the Pacific*, 120:1028–1042, September 2008.

[4] http://irsa.ipac.caltech.edu/data/spitzer/mipsgal.

[5] N. Flagey, A. Noriega-Crespo, N. Billot, and S. J. Carey. Spitzer/InfraRed Spectrograph Investigation of MIPSGAL 24 μm Compact Bubbles. *The Astrophysical Journal*, 741:4, November 2011.

[6] S. Wachter, J. C. Mauerhan, S. D. Van Dyk, D. W. Hoard, S. Kafka, and P. W. Morris. A Hidden Population of Massive Stars with Circumstellar Shells Discovered with the Spitzer Space Telescope. *The Astronomical Journal*, 139:2330–2346, June 2010.

[7] P. W. Morris, S. Stolovy, S. Wachter, A. Noriega-Crespo, T. G. Pannuti, and D. W. Hoard. Tentative Discovery of a New Supernova Remnant in Cepheus: Unveiling an Elusive Shell in the Spitzer Galactic First Look Survey. *The Astrophysical Journal*, 640:L179–L182, April 2006.

[8] V. V. Gvaramadze, A. Y. Kniazev, and S. Fabrika. Revealing evolved massive stars with Spitzer. *Monthly Notice of the Royal Astronomical Society*, 405:1047–1060, June 2010.

[9] J. S. Clark, V. M. Larionov, and A. Arkharov. On the population of galactic Luminous Blue Variables. *Astronomy and Astrophysics*, 435:239–246, May 2005.

[10] J. L. Hora, M. Cohen, R. G. Ellis, M. Meixner, R. D. Blum, W. B. Latter, B. A. Whitney, M. R. Meade, B. L. Babler, R. Indebetouw, K. Gordon, C. W. Engelbracht, B.-Q. For, M. Block, K. Misselt, U. Vijh, and C. Leitherer. Spitzer Sage Observations of Large Magellanic Cloud Planetary Nebulae. *The Astronomical Journal*, 135:726–736, February 2008.

[11] L. D. Anderson, A. Zavagno, M. J. Barlow, P. García-Lario, and A. Noriega-Crespo. Distinguishing between HII regions and planetary nebulae with Hi-GAL, WISE, MIPSGAL, and GLIMPSE. *Astronomy and Astrophysics*, 537:A1, January 2012.

[12] A. A. Zijlstra and S. R. Pottasch. On the scale height of planetary nebulae. *Astronomy and Astrophysics*, 243:478–482, March 1991.

[13] S. R. Pottasch, R. Olling, C. Bignell, and A. A. Zijlstra. Planetary nebulae near the galactic center. I - Method of discovery and preliminary results. *Astronomy and Astrophysics*, 205:248–256, October 1988.

[14] *Herschel Observers' Manual.* September 2012.

[15] www.nrao.edu.

[16] D. J. Helfand, R. H. Becker, R. L. White, A. Fallon, and S. Tuttle. MAGPIS: A Multi-Array Galactic Plane Imaging Survey. *The Astronomical Journal*, 131:2525–2537, May 2006.

[17] B. G. Clark. An efficient implementation of the algorithm “CLEAN”. *Astronomy and Astrophysics*, 89:377–+, September 1980.

[18] J. A. Högbom. Aperture Synthesis with a Non-Regular Distribution of Interferometer Baselines. *Astronomy and Astrophysics Supplement*, 15:417–+, June 1974.

[19] The GBT proposer’s guide.

[20] The GBT observing guide.

[21] D. T. Emerson and R. Gräve. The reduction of scanning noise in raster scanned data. *Astronomy and Astrophysics*, 190:353–358, January 1988.

[22] ?

[23] P. Goldreich and N. Scoville. OH-IR stars. I - Physical properties of circumstellar envelopes. *The Astrophysical Journal*, 205:144–154, April 1976.

[24] B. M. Lewis. The chronological sequence of circumstellar masers - Identifying proto-planetary nebulae. *The Astrophysical Journal*, 338:234–243, March 1989.

[25] S. Etoka and A. M. Le Squeren. OH spectral evolution of oxygen-rich late-type stars. *Astronomy and Astrophysics*, 420:217–223, June 2004.

[26] C. L. Brogan, W. M. Goss, J. S. Lazendic, and A. J. Green. OH (1720 MHz) Maser Search toward the Large Magellanic Cloud. *The Astronomical Journal*, 128:700–708, August 2004.

[27] http://www.aperturephotometry.org.

[28] J. J. Condon, W. D. Cotton, E. W. Greisen, Q. F. Yin, R. A. Perley, G. B. Taylor, and J. J. Broderick. The NRAO VLA Sky Survey. *The Astronomical Journal*, 115:1693–1716, May 1998.

[29] R. L. White, R. H. Becker, and D. J. Helfand. New Catalogs of Compact Radio Sources in the Galactic Plane. *The Astronomical Journal*, 130:586–596, August 2005.

[30] G. G. Fazio, J. L. Hora, L. E. Allen, M. L. N. Ashby, P. Barmby, L. K. Deutsch, J.-S. Huang, S. Kleiner, M. Marengo, S. T. Megeath, G. J. Melnick, M. A. Pahre, B. M. Patten, J. Polizotti, H. A. Smith, R. S. Taylor, Z. Wang, S. P. Willner, W. F. Hoffmann, J. L. Pipher, W. J. Forrest, C. W. McMurty, C. R. McCreight, M. E. McKelvey, R. E. McMurray, D. G. Koch, S. H. Moseley, R. G. Arendt, J. E. Mentzell, C. T. Marx, P. Losch, P. Mayman, W. Eichhorn, D. Krebs, M. Jhabvala, D. Y. Gezari, D. J. Fixsen, J. Flores, K. Shakoorzadeh, R. Jungo, C. Hakun, L. Workman, G. Karpati, R. Kichak, R. Whitley, S. Mann, E. V. Tollestrup, P. Eisenhardt, D. Stern, V. Gorjian, B. Bhattacharya, S. Carey, B. O. Nelson, W. J. Glaccum, M. Lacy, P. J. Lowrance, S. Laine, W. T. Reach, J. A. Stauffer, J. A. Surace, G. Wilson, E. L. Wright, A. Hoffman, G. Domingo, and M. Cohen. The Infrared Array Camera (IRAC) for the Spitzer Space Telescope. *Astrophysical Journal Supplement Series*, 154:10–17, September 2004.

[31] R. A. Benjamin, E. Churchwell, B. L. Babler, T. M. Bania, D. P. Clemens, M. Cohen, J. M. Dickey, R. Indebetouw, J. M. Jackson, H. A. Kobulnicky, A. Lazarian, A. P. Marston, J. S. Mathis, M. R. Meade, S. Seager, S. R. Stolovy, C. Watson, B. A. Whitney, M. J. Wolff, and M. G. Wolfire. GLIMPSE. I. An SIRTF Legacy Project to Map the Inner Galaxy. *Publications of the Astronomical Society of the Pacific*, 115:953–964, August 2003.

[32] www.ipac.caltech.edu/2mass/overview/about2mass.html.

[33] http://en.wikipedia.org.

[34] M. Cohen. High-resolution Mid-Infrared Images of the ISM from the MSX Satellite. In A. R. Taylor, T. L. Landecker, and G. Joncas, editors, *New Perspectives on the Interstellar Medium*, volume 168 of *Astronomical Society of the Pacific Conference Series*, page 97, 1999.

[35] S. L. Lumsden, M. G. Hoare, R. D. Oudmaijer, and D. Richards. The population of the Galactic plane as seen by MSX. *Monthly Notice of the Royal Astronomical Society*, 336:621–636, October 2002.

[36] http://wise.ssl.berkeley.edu/mission.html.

[37] http://www.ir.isas.jaxa.jp/akari.

[38] D. Ishihara, T. Onaka, H. Kataza, A. Salama, C. Alfageme, A. Cassatella, N. Cox, P. Garcia-Lario, C. Stephenson, M. Cohen, N. Fujishiro, H. Fujiwara, S. Hasegawa, Y. Ita, W. Kim, H. Matsuhara, H. Murakami, T. G. Muller, T. Nakagawa, Y. Ohyama, S. Oyabu, J. Pyo, I. Sakon, H. Shibai, S. Takita, T. Tanab, K. Uemizu, M. Ueno, F. Usui, T. Wada, H. Watarai, I. Yamamura, and C. Yamauchi. AKARI/IRC mid-IR all-sky Survey (ISAS/JAXA, 2010). *VizieR Online Data Catalog*, 2297:0, April 2010.

[39] I. Yamamura, S. Makiuti, N. Ikeda, Y. Fukuda, S. Oyabu, T. Koga, and G. J. White. AKARI/FIS All-Sky Survey Point Source Catalogues (ISAS/JAXA, 2010). *VizieR Online Data Catalog*, 2298:0, 2010.

[40] http://www.ukidss.org.

[41] R. M. Cutri, M. F. Skrutskie, S. van Dyk, C. A. Beichman, J. M. Carpenter, T. Chester, L. Cambresy, T. Evans, J. Fowler, J. Gizis, E. Howard, J. Huchra, T. Jarrett, E. L. Kopan, J. D. Kirkpatrick, R. M. Light, K. A. Marsh, H. McCallon, S. Schneider, R. Stiening, M. Sykes, M. Weinberg, W. A. Wheaton, S. Wheelock, and N. Zacarias. *2MASS All Sky Catalog of point sources.* June 2003.

[42] M. P. Egan, S. D. Price, and K. E. Kraemer. The Midcourse Space Experiment Point Source Catalog Version 2.3. In *American Astronomical Society Meeting Abstracts*, volume 35 of *Bulletin of the American Astronomical Society*, page 1301, December 2003.

[43] R. M. Cutri and et al. WISE All-Sky Data Release (Cutri+ 2012). *VizieR Online Data Catalog*, 2311:0, April 2012.

[44] J. S. Urquhart, A. L. Busfield, M. G. Hoare, S. L. Lumsden, R. D. Oudmaijer, T. J. T. Moore, A. G. Gibb, C. R. Purcell, M. G. Burton, L. J. L. Maréchal, Z. Jiang, and M. Wang. The RMS survey. ^{13}CO observations of candidate massive YSOs in the northern Galactic plane. *Astronomy and Astrophysics*, 487:253–264, August 2008.

[45] J. S. Urquhart, M. G. Hoare, C. R. Purcell, S. L. Lumsden, R. D. Oudmaijer, T. J. T. Moore, A. L. Busfield, J. C. Mottram, and B. Davies. The RMS survey. 6 cm continuum VLA observations towards candidate

massive YSOs in the northern hemisphere. *Astronomy and Astrophysics*, 501:539–551, July 2009.

[46] L. D. Anderson, T. M. Bania, D. S. Balser, and R. T. Rood. The HII Region Discovery Survey (HRDS). II. (Anderson+, 2011). *VizieR Online Data Catalog*, 219:40032, August 2011.

[47] D. G. Monet, S. E. Levine, B. Canzian, H. D. Ables, A. R. Bird, C. C. Dahn, H. H. Guetter, H. C. Harris, A. A. Henden, S. K. Leggett, H. F. Levison, C. B. Luginbuhl, J. Martini, A. K. B. Monet, J. A. Munn, J. R. Pier, A. R. Rhodes, B. Riepe, S. Sell, R. C. Stone, F. J. Vrba, R. L. Walker, G. Westerhout, R. J. Brucato, I. N. Reid, W. Schoening, M. Hartley, M. A. Read, and S. B. Tritton. The USNO-B Catalog. *The Astronomical Journal*, 125:984–993, February 2003.

[48] K. A. van der Hucht, P. S. Conti, I. Lundstrom, and B. Stenholm. The Sixth Catalogue of galactic Wolf-Rayet stars, their past and present. *Space Science Reviews*, 28:227–306, 1981.

[49] R. H. Becker, R. L. White, D. J. Helfand, and S. Zoonematkermani. A 5 GHz VLA survey of the galactic plane. *Astrophysical Journal Supplement Series*, 91:347–387, March 1994.

[50] T. Murphy, T. Mauch, A. Green, R. W. Hunstead, B. Piestrzynska, A. P. Kels, and P. Sztajer. The second epoch Molonglo Galactic Plane Survey: compact source catalogue. *Monthly Notice of the Royal Astronomical Society*, 382:382–392, November 2007.

[51] http://www-wfau.roe.ac.uk/sss/halpha/index.html.

[52] A. Acker, J. Marcout, F. Ochsenbein, B. Stenholm, R. Tylenda, and C. Schohn. *The Strasbourg-ESO Catalogue of Galactic Planetary Nebulae. Parts I, II.* 1992.

[53] J. J. Condon, D. L. Kaplan, and Y. Terzian. Infrared Planetary Nebulae in the NRAO VLA Sky Survey. *Astrophysical Journal Supplement Series*, 123:219–232, July 1999.

[54] L. Kohoutek. Version 2000 of the Catalogue of Galactic Planetary Nebulae. *Astronomy and Astrophysics*, 378:843–846, November 2001.

[55] D. Pierini, C. C. Popescu, R. J. Tuffs, and H. J. Völk. The far-infrared/radio correlation in the ISO era. The warm and cold far-infrared/radio correlations. *Astronomy and Astrophysics*, 409:907–916, October 2003.

[56] D. Pinheiro Gonçalves, A. Noriega-Crespo, R. Paladini, P. G. Martin, and S. J. Carey. The MIPSGAL View of Supernova Remnants in the Galactic Plane. *The Astronomical Journal*, 142:47, August 2011.

[57] J. C. Mauerhan, S. Wachter, P. W. Morris, S. D. Van Dyk, and D. W. Hoard. Discovery of Twin Wolf-Rayet Stars Powering Double Ring Nebulae. *The Astrophysical Journal Letters*, 724:L78–L83, November 2010.

[58] M. Cohen, Q. A. Parker, A. J. Green, T. Murphy, B. Miszalski, D. J. Frew, M. R. Meade, B. Babler, R. Indebetouw, B. A. Whitney, C. Watson, E. B. Churchwell, and D. F. Watson. Spitzer IRAC Observations of Newly Discovered Planetary Nebulae from the Macquarie-AAO-Strasbourg Hα Planetary Nebula Project. *The Astrophysical Journal*, 669:343–362, November 2007.

[59] M. Cohen, Q. A. Parker, A. J. Green, B. Miszalski, D. Frew, and T. Murphy. Multiwavelength diagnostic properties of Galactic planetary nebulae detected by the GLIMPSE-I. *Monthly Notice of the Royal Astronomical Society*, 413:514–542, May 2011.

[60] T. Murphy, M. Cohen, R. D. Ekers, A. J. Green, R. M. Wark, and V. Moss. Ultra- and hyper-compact HII regions at 20 GHz. *Monthly Notice of the Royal Astronomical Society*, 405:1560–1572, July 2010.

[61] A. G. G. M. Tielens. Interstellar Polycyclic Aromatic Hydrocarbon Molecules. *Annual Review of Astronomy & Astrophysics*, 46:289–337, September 2008.

[62] E. Peeters, S. Hony, C. Van Kerckhoven, A. G. G. M. Tielens, L. J. Allamandola, D. M. Hudgins, and C. W. Bauschlicher. The rich 6 to 9 vec mu m spectrum of interstellar PAHs. *Astronomy and Astrophysics*, 390:1089–1113, August 2002.

[63] E. Peeters, N. L. Martín-Hernández, F. Damour, P. Cox, P. R. Roelfsema, J.-P. Baluteau, A. G. G. M. Tielens, E. Churchwell, M. F. Kessler,

J. S. Mathis, C. Morisset, and D. Schaerer. ISO spectroscopy of compact H II regions in the Galaxy. I. The catalogue. *Astronomy and Astrophysics*, 381:571–605, January 2002.

[64] K. Volk and S. Kwok. ISO Spectra of Planetary Nebulae. In S. Kwok, M. Dopita, and R. Sutherland, editors, *Planetary Nebulae: Their Evolution and Role in the Universe*, volume 209 of *IAU Symposium*, page 303, 2003.

[65] G. Umana, A. Ingallinera, C. Trigilio, C. S. Buemi, P. Leto, C. Agliozzo, A. Noriega-Crespo, N. Flagey, R. Paladini, and S. Molinari. Identifying Type IIn SN progenitors in our Galaxy: the circumstellar environment of the Galactic LBV candidate Gal 026.47+0.02. *Monthly Notice of the Royal Astronomical Society, accepted.*

[66] http://www.aoc.nrao.edu/ rurvashi/tfcrop/tfcrop.html.

[67] C. J. Davis, M. D. Smith, T. M. Gledhill, and W. P. Varricatt. Near-infrared echelle spectroscopy of protoplanetary nebulae: probing the fast wind in H_2. *Monthly Notice of the Royal Astronomical Society*, 360:104–118, June 2005.

[68] P. S. Conti. Mass loss from early-type stars. In P. M. Gondhalekar, editor, *Mass Loss from Astronomical Objects*, pages 45–58, 1984.

[69] J. S. Clark, M. P. Egan, P. A. Crowther, D. R. Mizuno, V. M. Larionov, and A. Arkharov. Dusty ring nebulae around new candidate Luminous Blue Variables. *Astronomy and Astrophysics*, 412:185–198, December 2003.

[70] G. Umana, C. S. Buemi, C. Trigilio, and P. Leto. Current day mass loss rate for Luminous Blue Variable IRAS 18576+0341. *Astronomy and Astrophysics*, 437:L1–L5, July 2005.

[71] S. M. White. The Radio Nebula around HR Carinae. *The Astrophysical Journal*, 539:851–857, August 2000.

[72] N. Panagia and M. Felli. The spectrum of the free-free radiation from extended envelopes. *Astronomy and Astrophysics*, 39:1–5, February 1975.

[73] D. Buckley and S. E. Schneider. The Ionized Masses of Planetary Nebulae. *The Astrophysical Journal*, 446:279, June 1995.

[74] P. Morris, Morris, and Spitzer WRRINGS Team. Infrared Tracers of Mass-Loss Histories and Wind-ISM Interactions in Hot Star Nebulae. In F. Bresolin, P. A. Crowther, and J. Puls, editors, *IAU Symposium*, volume 250 of *IAU Symposium*, pages 361–366, June 2008.

[75] D. J. Hillier, P. A. Crowther, F. Najarro, and A. W. Fullerton. An optical and near-IR spectroscopic study of the extreme P Cygni-type supergiant HDE 316285. *Astronomy and Astrophysics*, 340:483–496, December 1998.

[76] N. Panagia. Some Physical parameters of early-type stars. *The Astronomical Journal*, 78:929–934, November 1973.

[77] A. Pastorello, S. J. Smartt, S. Mattila, J. J. Eldridge, D. Young, K. Itagaki, H. Yamaoka, H. Navasardyan, S. Valenti, F. Patat, I. Agnoletto, T. Augusteijn, S. Benetti, E. Cappellaro, T. Boles, J.-M. Bonnet-Bidaud, M. T. Botticella, F. Bufano, C. Cao, J. Deng, M. Dennefeld, N. Elias-Rosa, A. Harutyunyan, F. P. Keenan, T. Iijima, V. Lorenzi, P. A. Mazzali, X. Meng, S. Nakano, T. B. Nielsen, J. V. Smoker, V. Stanishev, M. Turatto, D. Xu, and L. Zampieri. A giant outburst two years before the core-collapse of a massive star. *Nature*, 447:829–832, June 2007.

[78] O. D. Fox, R. A. Chevalier, M. F. Skrutskie, A. M. Soderberg, A. V. Filippenko, M. Ganeshalingam, J. M. Silverman, N. Smith, and T. N. Steele. A Spitzer Survey for Dust in Type IIn Supernovae. *The Astrophysical Journal*, 741:7, November 2011.

[79] J. E. Andrews, G. C. Clayton, R. Wesson, B. E. K. Sugerman, M. J. Barlow, J. Clem, B. Ercolano, J. Fabbri, J. S. Gallagher, A. Landolt, M. Meixner, M. Otsuka, D. Riebel, and D. L. Welch. Evidence for Pre-existing Dust in the Bright Type IIn SN 2010jl. *The Astronomical Journal*, 142:45, August 2011.